TU Delft

Delft University of Technology

Miniature sensorized platform for engineered heart tissues

Dostanic, M.

DOI
10.4233/uuid:0f61f871-7c9c-47fc-a542-10883fb2d4de

Publication date
2023

Document Version
Final published version

Citation (APA)
Dostanic, M. (2023). *Miniature sensorized platform for engineered heart tissues*. [Dissertation (TU Delft), Delft University of Technology]. https://doi.org/10.4233/uuid:0f61f871-7c9c-47fc-a542-10883fb2d4de

Important note
To cite this publication, please use the final published version (if applicable).
Please check the document version above.

Copyright
Other than for strictly personal use, it is not permitted to download, forward or distribute the text or part of it, without the consent of the author(s) and/or copyright holder(s), unless the work is under an open content license such as Creative Commons.

Takedown policy
Please contact us and provide details if you believe this document breaches copyrights.
We will remove access to the work immediately and investigate your claim.

This work is downloaded from Delft University of Technology.
For technical reasons the number of authors shown on this cover page is limited to a maximum of 10.

MINIATURE SENSORIZED PLATFORM FOR ENGINEERED HEART TISSUES

MINIATURE SENSORIZED PLATFORM FOR ENGINEERED HEART TISSUES

Proefschrift

ter verkrijging van de graad van doctor
aan de Technische Universiteit Delft,
op gezag van de Rector Magnificus Prof. dr. ir. T.H.J.J. van der Hagen,
voorzitter van het College voor Promoties,
in het openbaar te verdedigen op dinsdag 6 juni 2023 om 10:00 uur

door

Milica DOSTANIĆ

Master of Science in Electrical Engineering, University of Belgrade, Serbia
geboren te Kragujevac, Serbia.

Dit proefschrift is goedgekeurd door de

promotor: Prof. dr. ir. P. M. Sarro
copromotor: dr. M. Mastrangeli

Samenstelling promotiecommissie:

Rector Magnificus,	voorzitter
Prof. dr. ir. P. M. Sarro,	Technische Universiteit Delft
Dr. M. Mastrangeli,	Technische Universiteit Delft

Onafhankelijke leden:

Prof. dr. ir. R. Dekker,	Technische Universiteit Delft
Prof. dr. C. L. Mummery,	Leids Universitair Medisch Centrum
Prof. dr. ir. J. M. J. den Toonder,	Technische Universiteit Eindhoven
Prof. dr. A. D. van der Meer,	Technische Universiteit Twente
Prof. dr. M. Rasponi,	Politecnico di Milano, Italië
Prof. dr. P. J. French,	Technische Universiteit Delft, reservelid

Keywords: *Engineered heart tissue, Heart-on-chip, Organ-on-chip, Microfabrication, Polymer processing*

Printed by: *Proefschrift specialist*

Front & Back: *nero.by.s*

Copyright © 2023 by M. Dostanić

An electronic version of this dissertation is available at
http://repository.tudelft.nl/.

CONTENTS

Summary ix

Samenvatting xi

1 Recapitulating heart physiology in vitro: Heart-on-chip 1
- 1.1 Background and motivation . . . 2
  - 1.1.1 The complexity of human cardiac muscle . . . 2
  - 1.1.2 A solution within the Organ-on-Chip technology . . . 4
  - 1.1.3 Engineered heart tissue as a promising *in vitro* model . . . 5
  - 1.1.4 Current challenges . . . 6
- 1.2 Main question and thesis objectives . . . 8
- 1.3 Outline of the thesis . . . 9

2 The baseline: EHT platform with straight pillars 13
- 2.1 The importance of mechano-transduction . . . 14
  - 2.1.1 HeartDyno as a starting point . . . 15
- 2.2 Design of the EHT platform . . . 16
  - 2.2.1 Anisometric downscaling . . . 16
- 2.3 Microfabrication of the platforms . . . 19
  - 2.3.1 Microfabrication techniques . . . 19
  - 2.3.2 Process flow . . . 20
  - 2.3.3 Addition of focus features . . . 23
- 2.4 Mechanical properties of the EHT platforms . . . 25
  - 2.4.1 Numerical model of straight pillars . . . 25
  - 2.4.2 Analytical model of straight pillars . . . 27
  - 2.4.3 Mechanical characterization . . . 28
- 2.5 Inclusion of cardiac cells . . . 29
- 2.6 Conclusion and Discussion . . . 34

3 Mechanical enhancement: the EHT platform with tapered pillars 37
- 3.1 The "jumping off" issue . . . 38
- 3.2 Design upgrade: tapered pillars . . . 39
  - 3.2.1 Mechanical confinement of the tissues . . . 39
  - 3.2.2 Dimensions of pillars . . . 40
  - 3.2.3 Design requirements . . . 41
- 3.3 Microfabrication of tapered pillars . . . 42
  - 3.3.1 Tapered etching profile . . . 42
  - 3.3.2 Process flow . . . 45
  - 3.3.3 Critical fabrication steps . . . 48
  - 3.3.4 Critical process parameters . . . 51

3.3.5 Angle measurement . . . 52
3.4 Mechanical properties of tapered pillars . . . 54
3.4.1 Finite-element model of tapered pillars . . . 54
3.4.2 Analytical model derivation . . . 56
3.4.3 Nanoindentation measurement . . . 60
3.5 Biological validation of platforms . . . 61
3.5.1 Tissue culture . . . 62
3.5.2 Tissue position measurement . . . 63
3.5.3 Comparison between straight and tapered design . . . 63
3.6 Discussion and Conclusion . . . 64

4 Optical readout of tissue contractile properties 67
4.1 The importance of contractile force assessment . . . 68
4.1.1 Rectangular and circular EHT platform . . . 69
4.2 *ForceTracker* implementation . . . 70
4.2.1 Shape-detection and tracking algorithm . . . 70
4.2.2 Data Analysis . . . 73
4.2.3 Software layout . . . 75
4.3 Software validation . . . 77
4.3.1 Formation of EHTs using hiPSCs . . . 77
4.3.2 Imaging of the EHTs . . . 78
4.3.3 *ForceTracker* application on two EHT platforms . . . 78
4.4 Discussion and Conclusion . . . 81

5 Integrated force sensing 85
5.1 Strategies for electrical contractile force readout . . . 86
5.2 Substrate deformation analysis . . . 87
5.2.1 Analytical model . . . 87
5.2.2 Numerical analysis . . . 90
5.2.3 Optimal sensor position . . . 90
5.3 Capacitive sensing of pillar displacement . . . 92
5.3.1 Sensing strategies . . . 92
5.3.2 Capacitive sensing: working principle . . . 93
5.3.3 Spiral co-planar capacitive sensor . . . 94
5.3.4 Numerical simulations . . . 97
5.4 Fabrication . . . 100
5.4.1 Process flow . . . 100
5.4.2 Critical steps . . . 103
5.5 Portable electronic readout . . . 104
5.5.1 Available architectures . . . 104
5.5.2 Commercial solutions . . . 105
5.5.3 AD7746 working principle . . . 106

5.6 Assembly of the measurement setup . . . 107
5.6.1 PCB design . . . 107
5.6.2 Sensor transfer . . . 108
5.6.3 Wire-bonding . . . 108
5.6.4 Well addition and encapsulation . . . 110
5.6.5 Assembly challenges . . . 110
5.7 Sensor characterization . . . 112
5.7.1 Electrical characterization . . . 112
5.7.2 Mechanical characterization . . . 112
5.8 Biological validation . . . 114
5.8.1 Tissue culture . . . 114
5.9 Discussion and Conclusions . . . 116

6 Integrated pacing microelectrodes 119
6.1 The importance of electrical stimulation for EHTs . . . 120
6.2 Design of the pacing electrodes . . . 121
6.2.1 Electric field distribution: numerical analysis . . . 122
6.2.2 Electrodes and interconnects design . . . 123
6.3 Fabrication of the platform with integrated pacing microelectrodes . . . 124
6.3.1 Microfabrication techniques . . . 124
6.3.2 Process flow . . . 126
6.3.3 Critical fabrication steps . . . 131
6.3.4 Wire-bonding . . . 138
6.4 Electrical characterization of the electrodes . . . 139
6.4.1 Sheet-resistance measurements . . . 139
6.4.2 Post-fabrication resistance measurements . . . 140
6.5 Design of the external pacing setup . . . 141
6.5.1 Electrical circuit model of EHT . . . 141
6.5.2 Electronics design . . . 142
6.5.3 Testing . . . 145
6.6 Biological validation of the platforms . . . 147
6.6.1 EHT generation . . . 147
6.7 Discussion and Conclusions . . . 148

7 A multi-well plate for single heart-on-chip platforms 151
7.1 Multiplexing single-chip OoC devices . . . 152
7.2 Multiplexed pacing platform . . . 153
7.2.1 Platform assembly . . . 153
7.2.2 External electronic connection and user interface . . . 156
7.2.3 Assembly flaws . . . 158
7.2.4 Testing of the platform . . . 159
7.3 Modular platform . . . 159
7.4 Discussion and future outlook . . . 160

8 Conclusions and Future perspectives **163**
8.1 Conclusions . . . 164
8.2 Future work . . . 168
8.2.1 Finding the optimal stiffness of pillars . . . 168
8.2.2 Real-time force analysis . . . 169
8.2.3 Improvements of the assembly process . . . 169
8.2.4 Multiplexing . . . 169

List of Publications **185**

Acknowledgements **187**

SUMMARY

The high death toll of cardiovascular diseases worldwide and the lack of effective treatments for them are the main motivation for developing alternative and more efficient models for cardiac drug development and disease research. The missing link between current laboratory research on static *in vitro* and animal models and the clinical stage research on human patients could be created using the rapidly emerging Organ-on-Chip (OoC) technology. The microphysiological models developed within OoC research combine devices made of biocompatible, soft materials and human-origin organ-specific cell types, which are then exposed to flow, chemical, electrical or biomechanical stimuli.

Modeling a human cardiac *in vivo* environment in an artificial model represents quite a challenge from several aspects. First, cardiac tissue *in vivo* is exposed to a strong coupling between different biomechanical and electrical stimuli that need to be faithfully captured by an *in vitro* model. Furthermore, such an *in vitro* model should recapitulate the complexity of cell-cell and cell-extracellular matrix (ECM) interactions between different cardiac cell types, while obtaining physiologically relevant responses. This thesis addresses the first challenge, in an attempt to engineer a dynamic, artificial microenvironment, suitable for the growth, monitoring, and stimulation of hiPSC-based engineered cardiac tissues (EHTs).

First, the development and optimization of the mechanical support for EHT culture are described. An existing platform for EHT culture was taken as the starting point. The platform consists of a pair of micropillars with rectangular cross-sections within an elliptic microwell. Upon seeding the cell/ECM mixture within the elliptic microwell, cells self-assemble into tissue-like bundles around the micropillars and start spontaneously contracting. The initial platform was anisometrically downscaled to 1, 2, and 3 μL volume of the elliptic microwell, to reduce the number of cells per tissue while providing the same passive load for the tissues in all platforms. The platform was fabricated by PDMS moulding into the cavities in the Si wafer. The initial study showed that tissues formed successfully and remained functional, regardless of the platform size, without significant differences among them. Platform downscaling enabled the reduction of the number of cells used per tissue, as well as the compatibility of the micropillar size with the standard wafer thickness (500 μm). However, a direct comparison of the tissue performance in different platforms was not possible due to the arising issue of tissue position variation along micropillar length and jumping off the micropillars with the increase in the force of contraction.

The issue of jumping tissues was solved by upgrading the geometry of micropillars. Micropillars with hourglass profiles were designed and fabricated to enable spatial confinement of the tissues within the indented area by providing mechanical resistance to tissue movement. Two versions of tapered micropillars were successfully fabricated by PDMS moulding into a Si wafer. The mould was created using a combination of anisotropic deep reactive ion etching (Bosch process) and isotropic etching of Si. The tis-

sue confinement efficiency of the upgraded micropillars was confirmed in experiments with EHTs by comparing the performance of two tapered micropillar geometries with that of straight micropillars. The tapered design improved the experiment yield by solving the problem of tissue position variation and therefore represents a more convenient geometry for further use within the EHT platform.

One of the high-priority readouts to obtain from EHT platforms is tissue contractile force and kinetics. To measure both, two methods were implemented: optical and electrical. Optical measurement of tissue contractile performance was achieved via the newly developed stand-alone, Python-based software *ForceTracker*, which detects and tracks the displacement of micropillar tips throughout the recorded videos of contracting tissues. The software was developed as a versatile tool, able to analyze multiple data formats and aiming at standardizing the analysis across differing EHT platforms. Its performance was validated on two different EHT platforms with micropillars of rectangular and circular cross-sections, respectively. An electrical force assessment was proposed and attempted with an integrated co-planar capacitive sensor of micropillar displacement. The pair of spiral capacitors was integrated underneath each rectangular micropillar, within the 3 µL platform, to detect the tension and compression in the substrate upon micropillar bending. The capacitive sensors were incorporated into the EHT platform using a combination of standard micromachining and polymer processing. A highly sensitive readout system, based on a commercially available electronic component, was developed to measure capacitance change in the aF range. The characterization of static and dynamic sensor behavior was successfully performed and demonstrated agreement with the predicted values. Due to the problems with the assembly process, extensive analysis and experiments with tissue culture are yet to be performed.

To complement electrical sensing, *in situ* electrical stimulation of the tissues was implemented by integrating a pair of TiN microelectrodes at the bottom of the elliptic microwell, in proximity to the tissue. The platform with integrated pacing electrodes was fabricated using the same technology as in the case of capacitive sensors. The electrical properties of the platform were assessed upon completing the wire-bonding and assembly process. In parallel, electronic circuitry for the generation of biphasic rectangular pulses for tissue stimulation was developed and implemented. Test with cardiac cell inclusion demonstrated the biocompatibility of the platform. The tissue pacing efficiency is yet to be proven due to problems with leakage and system assembly.

Finally, following up on the single-chip development, a multi-well plate system was developed to multiplex the pacing of the tissues to up to 32 individual EHT platforms with integrated electrodes. The well plate is composed of a custom-made printed circuit board (PCB) at a bottom of a standard 96-well plate frame. This PCB contains single-chip footprints, contact pads, and interconnects to the external pacing circuitry and it is protected with an acrylic plate with cell culturing wells. Control of the pacing signal and individual well selection was realized via a custom-made software application.

The achievements presented in this thesis are meant to contribute to the development of a miniature sensorized platform for culturing, monitoring, and stimulating EHTs. The functional modules developed in this thesis can be combined in a single platform and represent the basis for the future development of a multiplexed system with closed-loop control of the tissue culturing environment.

SAMENVATTING

Het hoge sterftecijfer door hart- en vaatziekten wereldwijd en het gebrek aan effectieve behandelingen zijn de belangrijkste beweegredenen voor de ontwikkeling van alternatieve en efficiëntere modellen voor onderzoek naar en medicijn ontwikkeling voor hart- en vaatziekten. De ontbrekende schakel tussen huidig laboratoriumonderzoek op statische *in vitro* en diermodellen en het klinische onderzoek op menselijke patiënten kan worden gecreëerd met behulp van de snel opkomende Organ-on-Chip (OoC) technologie. De microfysiologische modellen, die binnen OoC-onderzoek worden ontwikkeld, combineren chips gemaakt van biocompatibele, zachte materialen en menselijke orgaanspecifieke celtypen, die in deze chips vervolgens worden blootgesteld aan stroming, chemische, elektrische of biomechanische stimuli. Het modelleren van een menselijke *in vivo* cardiaal weefsel in kunstmatig modelen is gezien meerdere aspecten een behoorlijke uitdaging. Ten eerste wordt cardiaal weefsel *in vivo* blootgesteld aan een combinatie van verschillende biomechanische en elektrische stimuli die nauwkeurig moeten worden gerecreëerd door het *in vitro* model. Bovendien moet zo'n *in vitro* model de complexiteit van cel-cel en cel-extracellulaire matrix (ECM) interacties tussen verschillende cardiale celtypen nabootsen, terwijl fysiologisch relevante informatie wordt verkregen. Deze scriptie richt zich op het ontwerpen van een dynamische, kunstmatige micro-omgeving, die geschikt is voor de groei, monitoring en stimulatie van hiPSC-gebaseerde gekweekte cardiale weefsels (Engineered Heart Tissues, EHT's).

Allereerst wordt de ontwikkeling en optimalisatie van de mechanische ondersteuning voor EHT-cultuur beschreven. Een bestaand platform voor EHT-cultuur werd als startpunt genomen. Dit platform bestaat uit een paar micropilaren met een rechthoekige doorsnede binnen een elliptische microwell. Na het zaaien van de cel/ECM-mix in de microwell, groeien de cellen uit tot een weefselachtige bundel rond de micropilaren en beginnen spontaan samen te trekken. Het oorspronkelijke platform werd anisometrisch verkleind tot een well volume van 1, 2 en 3 µL om het aantal cellen per weefsel te verminderen terwijl dezelfde passieve belasting aan de weefsels in alle platforms wordt geboden. Het platform werd gefabriceerd door PDMS-molding in de holtes van de Si-wafer. De initiële studie toonde aan dat weefsels succesvol werden gevormd, functioneel waren en onderling geen significante verschillen vertoonden ongeacht de grootte van het platform. De verkleining van het platform maakte het mogelijk om het aantal cellen per weefsel te verminderen en zorgde hierbij voor goede compatibiliteit van de micropilaargrootte met de standaard wafer dikte (500 µm). Een directe vergelijking van de weefselprestaties in verschillende platforms was echter niet mogelijk vanwege het probleem van variatie in weefselpositie langs de hoogte van de micropilaar en het afspringen van de weefsels van de micropilaren bij toename van de contractiekracht.

Het probleem van de afspringende weefsels werd opgelost door de geometrie van micropilaren te verbeteren. Micropilaren met zandloperprofielen werden ontworpen en gefabriceerd om ruimtelijke constrictie van de weefsels in het taps toelopende gebied

mogelijk te maken door mechanische weerstand te bieden tegen weefselbeweging. Twee versies van taps toelopende micropilaren werden met succes gefabriceerd door PDMS-molding in een Si-wafer. De mal werd gemaakt met behulp van een combinatie van anisotrope diep reactieve ion etching (Bosch-proces) en isotrope etsen van Si. De efficiëntie van de weefsel constrictie op de geoptimaliseerde micropilaren werd onderzocht door de prestaties van twee taps toelopende micropilaargeometrieën te vergelijken met die van rechte micropilaren. Het taps toelopende ontwerp verminderde de variatie in weefselpositie en verbeterende hierdoor de experimentele opbrengst. Deze geometrie is dus meer geschikt voor het gebruik in het EHT-platform.

Een van de belangrijkste data punten, die te verkrijgen is uit EHT-platforms, is de contractiele kracht en kinetica van de weefsels. Om beide te kunnen meten, werden twee methoden geïmplementeerd: een optisch en elektrisch meting. De optische meting van de contractiele prestaties van weefsels werd bereikt door de ontwikkeling van *ForceTracker*, een nieuw ontwikkeld en stand-alone Python programma. Dit programma detecteert de verplaatsing van micropilaartips en volgt deze in de opgenomen video's van samentrekkende weefsels. De software is ontwikkeld als een veelzijdige tool en is in staat om meerdere gegevensformaten te analyseren om zo de analyse van verschillende EHT-platforms mogelijk te maken en te standaardiseren. De prestaties ervan werden gevalideerd op twee verschillende EHT-platforms met micropilaren van respectievelijk rechthoekige en cirkelvormige doorsneden. Een elektrische meting van de contractiele kracht is ontwerpen en uitgevoerd met een geïntegreerde coplanar capacitieve sensor van micropilaarverplaatsing. Een paar spiraalvormige condensatoren werd geïntegreerd onder elke rechthoekige micropilaar (3 µL platform) om de spanning en compressie in het substraat bij micropilaarbuiging te detecteren. De capacitieve sensoren werden in het EHT-platform geïntegreerd met behulp van een combinatie van standaard micromachining en polymeerverwerking. Er werd een zeer gevoelig uitleessysteem ontwikkeld, gebaseerd op commercieel verkrijgbaar elektronisch componenten, om capacitieve verandering in het aF-bereik te meten. De karakterisering van statisch en dynamisch sensorgedrag werd succesvol uitgevoerd en toonde overeenstemming met de voorspelde waarden aan. Vanwege problemen met het assemblageproces moeten uitgebreide analyses en experimenten met weefselkweek nog worden uitgevoerd.

Om elektrische metingen te complementeren is er *in situ* elektrische stimulatie geïmplementeerd. Dit is gedaan door een paar TiN microelektroden op de bodem van de elliptische microwell aan te brengen, dichtbij het weefsel. Het platform met geïntegreerde pacing elektroden is gefabriceerd door middel van dezelfde technologie als de capacitieve sensoren. De elektrische eigenschappen van het platform zijn bepaald na het voltooien van het wire-bonding en assemblageproces. Tegelijkertijd zijn elektronische schakelingen om biphasic rectangular pulses voor weefsel stimulatie te genereren ontwikkeld en geïmplementeerd. Testen met hartspiercellen hebben biocompatibiliteit van het platform aangetoond. De efficiëntie van de weefsel-pacing moet echter nog aangetoond worden door problemen met lekkages en systeemassemblage.

Om elektrische metingen te complementeren is er in situ elektrische stimulatie geïmplementeerd. Dit is gedaan door een paar TiN microelektroden op de bodem van de elliptische microwell aan te brengen, dichtbij het weefsel. Het platform met geïntegreerde pacing elektroden is gefabriceerd door middel van dezelfde technologie als de

capacitieve sensoren. De elektrische eigenschappen van het platform zijn bepaald na het voltooien van het wire-bonding en assemblageproces. Tegelijkertijd zijn elektronische schakelingen om biphasic rectangular pulses voor weefsel stimulatie te genereren ontwikkeld en geïmplementeerd. Testen met hartspiercellen hebben biocompatibiliteit van het platform aangetoond. De efficiëntie van de weefsel-pacing moet echter nog aangetoond worden door problemen met lekkages en systeemassemblage.

Ten slotte werd na de ontwikkeling van de single-chip een multi-well plate ontwikkeld om de pacing van de weefsels te multiplexen tot maximaal 32 individuele EHT-platforms met geïntegreerde elektroden. De well plaat bestaat uit een op maat gemaakt printplaat (PCB) aan de onderkant van een standaard 96-well plate. Deze PCB bevat single-chip footprints, contactpads en interconnects naar de externe pacing-circuit en wordt beschermd door een acrylaat plaat met cell culture wells. De controle van het pacing-signaal en de individuel wellselectie werd gerealiseerd via een op maat gemaakte software toepassing.

De prestaties die in deze scriptie worden gepresenteerd, zijn bedoeld om bij te dragen aan de ontwikkeling van een geminiaturiseerd platform met sensoren voor het kweken, monitoren en stimuleren van EHT's. De functionele modules die in deze scriptie zijn ontwikkeld, kunnen worden gecombineerd in een enkel platform en vormen de basis voor de toekomstige ontwikkeling van een gemultiplexeerd regelsysteem van de weefselkweekomgeving.

CHAPTER 1

RECAPITULATING HEART PHYSIOLOGY IN VITRO: HEART-ON-CHIP

1.1. BACKGROUND AND MOTIVATION

THE fast-advancing, modern society in which we are living presently is a great testimony of human intelligence, evolution, and endurance. Even though its progress rate is increasing with each coming decade, the seemingly comfortable lifestyle we are enjoying today comes at times with a high price for our health. In the entire world, stressful daily routines, bad life habits, long working hours, and poor diets with the lack of nutrients are taking a toll on our organisms. All these factors, combined with genetic predispositions are still keeping cardiovascular diseases (CVDs) as the leading cause of death worldwide [1, 2]. The discomforting statistics show that, despite the rapid progress in medicine, biology and technology, the number of people affected by CVDs will only continue to rise in the future.

CVDs manifest through the disruption in cardiac muscle function, which is directly affecting the vascular web entangled to it. It is well known that the heart is one of the most important organs, and certainly the most important muscle of the human body. It is the main "power supply" for the entire organism, as its restless contractions provide oxygenated blood, replenished with nutrients, to the most remote parts of the human body. This continuous flow of blood throughout the complex vascular web, including oxygen and nutrient delivery, is a crucial mechanism for keeping a human organism alive. Even a minor malfunction of this well-coordinated pumping machinery can have fatal consequences. Therefore, any disease related to the cardiovascular system has a major influence on the well-being and life expectancy of an individual. With such a substantial impact, CVDs impose a heavy burden on healthcare systems worldwide. It is therefore of a high social priority to better understand the underlying mechanisms behind the pathogenesis of CVDs, as well as to find efficient treatments for them.

Currently, the main bottleneck in the disease modeling and the drug-development process is the use of non-adequate testing models during the pre-clinical research phase which fail to faithfully recapitulate human (patho)physiology [3]. That is the reason why most drug trials end up being discarded in the clinical stages when reaching human patients. The complexity of human cardiac physiology is often underestimated and oversimplified with the use of static *in vitro* models, such as cell monolayers, or animal *in vivo* models [4]. Even though they are still inevitably used during pre-clinical trials, both static cell monolayers and animal models fail to mimic precisely the complex *in vivo* environment of human myocardium. Consequently, there is a large translational gap between the results obtained from the studies using such *in vitro* and animal models, and the responses obtained from human patients. To bridge this gap, it is required to **develop more advanced and complex *in vitro* models that can accurately capture human cardiac (patho)physiology.**

1.1.1. THE COMPLEXITY OF HUMAN CARDIAC MUSCLE

To understand to which extent is needed to increase the complexity of static cell cultures and how exactly those physiologically relevant *in vitro* models should perform, we first need to delve deeper into the structure and function of human cardiac tissue.

The heart is a highly complex pluricellular organ composed of cardiomyocytes (CMs) and non-myocyte cells (e.g., fibroblasts, endothelial cells, smooth muscle cells, and immune cells) [5]. Myocytes (Fig.1.1B) participate in electrical conduction and contractile

force generation, while the other cell types contribute to building the surrounding extracellular matrix (ECM) together with supporting vasculature, and injury responses [6]. Functional heart muscle tissue is characterized by cells highly organized and structured into muscle bundles with tightly packed myofibrils (Fig.1.1C). Such an organized environment supports the strong electro-mechanical coupling of its main building blocks – CMs.

A single contraction cycle starts with the cell membrane depolarization due to the action potential, which stimulates the inflow of Ca^{2+} into the cardiomyocyte and activates muscle contraction. Followed by a calcium-induced calcium release within the cell, troponin C binds to calcium, moves from the actin-binding sites, and frees actin to be bound by myosin (Fig.1.1D) [7]. This interaction is responsible for sarcomere shortening, as the myosin head pulls actin filaments, resulting in muscle contraction.

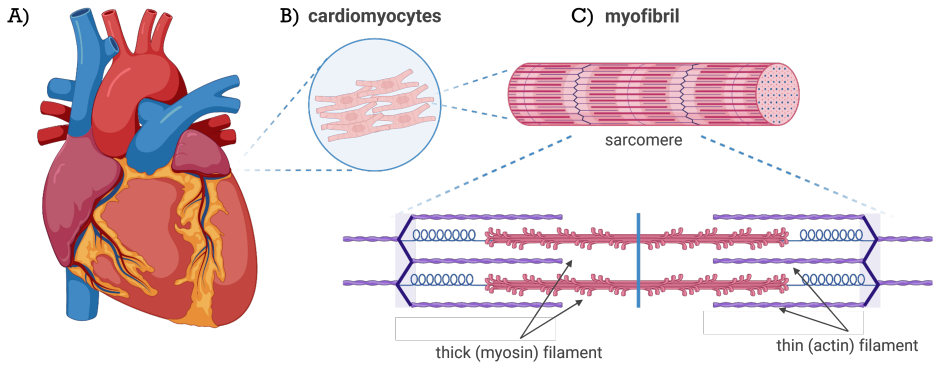

Figure 1.1: The structure of a human heart: a) Close-up view of one of the main building cells of cardiac tissue: cardiomyocytes; b) A cross-section of a cardiomyocyte muscle fiber; c) A single myofibril structure within a muscle fiber; d) Enlarged sarcomere structure consisting of thick and thin filaments responsible for the contraction force generation.

Such a fine-tuned interplay between electrical input and mechanical output of the cardiac muscle is complemented by the whole spectrum of biomechanical and chemical signaling accompanying the cardiac function. This is just a small glimpse into the complexity of cardiac pumping machinery, on a tissue level, which needs to be recapitulated in an equally complex and dynamic artificial microenvironment. In addition to the basic electro-mechanical coupling during contraction cycles, there are several other intrinsic mechanisms involved in the regulation of cardiac responses. The most relevant to mention is the Frank-Starling mechanism, which captures the ability of the heart to respond to increasing load requirements by generating higher contraction force, and the force-frequency relationship, which regulates the increase in Ca^{2+} transients and force of contraction with increasing pacing frequency [8].

To summarize, a robust and physiologically predictive *in vitro* model of adult human cardiac tissue should be able to capture the complex 3D multicellular architecture and cell-cell interactions, achieve functional and synchronized electro-mechanical coupling of CMs, and obtain the physiological responses comparable to the native myocardium.

1.1.2. A SOLUTION WITHIN THE ORGAN-ON-CHIP TECHNOLOGY

Recapitulation of such a finely tuned *in vivo* environment within an artificially fabricated platform poses a difficult challenge on many fronts. On one hand, it requires innovation and creativity from the engineering perspective. For example, it should involve the development of soft, 3D constructs made of biocompatible materials with mechanical properties equivalent to the human heart. Additionally, it should include built-in readouts and biomechanical stimuli with a high degree of control and automation. The second aspect is the biological counterpart, which might pose an even greater challenge. It requires finding the ideal composition ratio and interaction of various cell types within 2D or 3D cultures that could achieve connections and physiological responses comparable to those measured in adult humans. In conclusion, the realization of such a complex system, both biologically and technologically, requires symbiotic efforts of scientists from the fields of biology, chemistry, electrophysiology, physics, and engineering.

An example of a promising *in vitro* model that aims to mimic the complexity of *in vivo* cardiac tissue is currently being developed within the Organ-on-Chip (OoC) field [9–13]. Both engineers and biologists, among other scientists, are joining forces in the rapidly expanding OoC field to mimic the small functional units of different human organs within artificial dynamic microphysiological systems. Great progress has already been made and many of the developed systems have managed to recapitulate the function and physiological responses of different organs up to a certain extent. For example, lung-on-chip devices recreated cyclic deformation of the alveolar-capillary interface during the breathing cycle [14]. Both sheer stress and peristaltic motion effect on gut epithelium have been implemented and studied in gut-on-chip models [15]. For neural activity recordings and analysis, 2D and 3D microelectrode arrays (MEAs) became the golden standard, and their designs are rapidly improving [16, 17]. Furthermore, many systems were developed for analyzing the integrity of the blood-brain barrier using trans-epithelial resistance measurements [18], which is crucial for the drug-delivery process in neurological disorders. Some of the mentioned examples are illustrated in Fig.1.2.

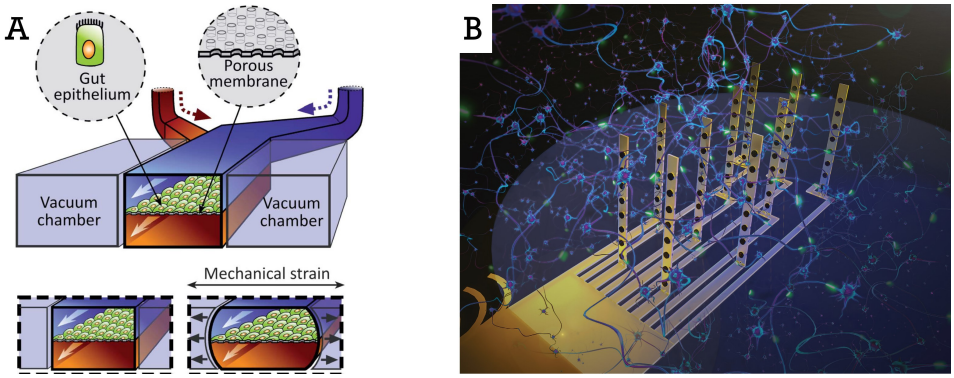

Figure 1.2: A) An example of a Gut-on-Chip model mimicking peristaltic motion within the two-channel system and vacuum chambers for channel actuation [15]. B) An example of a 3D MEA system for recording neural activity in 3D Brain-on-Chip models [16].

1.1.3. ENGINEERED HEART TISSUE AS A PROMISING *in vitro* MODEL

When it comes to cardiac 3D *in vitro* modeling, one that showed great potential to mimic phenotype and (patho)physiology of adult human myocardium is engineered heart tissue (EHT) [19–21]. The EHTs are engineered 3D constructs of cardiomyocytes combined with other supportive cardiac cell types (fibroblast, endothelial, and smooth muscle cells) within an ECM. The tissues of such origin typically self-assemble into muscle bundles around two or multiple anchoring points. The anchoring points are commonly made of soft, elastic polymers and provide mechanical support in the form of passive stretch (preload) during the tissue formation, and the mechanical load during the tissue contraction cycles.

EHT APPROACH

Within the EHT approach, the first step towards obtaining a complex microenvironment of human cardiac tissue was made with the transition from 2D cell cultures to 3D tissue-like constructs. In this way, intracellular crosstalk between CMs, as well as the crosstalk of CMs and non-myocyte cells within the ECM became possible. Communication of different cell types was achieved in all three dimensions. Moreover, being organized within the tissue-like structure reduced cell proliferation and allowed long-term cultures. Both are essential for disease modeling and long-term drug effect studies.

Another advantage arising from the tissue suspension between two or more anchoring points in 3D models is the passive force acting upon cells during the tissue-formation process. The passive force proved to be very efficient in aligning CMs and sarcomeres in parallel with the force direction. This alignment is crucial for the optimal function of the cardiac muscle and efficient electro-mechanical coupling of CMs due to the high degree of organization. In this way, there is no further need for introducing additional patterns or 3D features on the cell culturing substrates for the alignment of CMs in 2D layers.

Lastly, one important advantage of the EHT approach is the versatility and accuracy of contractile properties measurement that can be obtained from the tissue suspended between two or more anchors. It gives ample opportunities to incorporate precise force readouts and to assess the contractile kinetics of the tissues.

The second very important step in the development of EHTs as physiologically relevant *in vitro*

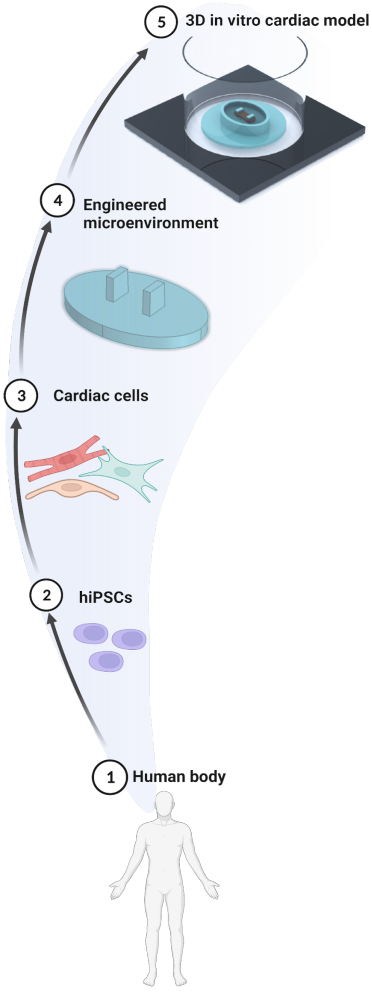

Figure 1.3: The roadmap towards building the physiologically relevant 3D *in vitro* cardiac model.

cardiac models was the inclusion of human induced pluripotent stem cell (hiPSC) technology into building these models [22, 23]. The hiPSC technology enabled the use of human-origin cells of different organs obtained from specific patients, for building complex multicellular cultures. Different cell types, present in cardiac tissue, can be derived from hiPSCs and mixed together to form tissue-like constructs. These tissues are then cultured in biocompatible microenvironments with the goal of creating 3D *in vitro* models with physiological responses close to adult human patients (Fig.1.3). The use of hiPSC-derived cell types steered the OoC field toward the final application in personalized medicine. By using cells obtained with this technology, we are not only able to build more physiologically relevant *in vitro* models but also to obtain patient-specific disease models and disease treatments.

1.1.4. CURRENT CHALLENGES

Even though mentioned advantages give a lot of hope that EHT is a path to take towards creating a physiologically relevant *in vitro* cardiac model, there are still some major challenges to overcome on the way, before EHTs reach their full potential of being used in personalized medicine and for drug discovery purposes [24–26].

BIOLOGY

One of the main drawbacks of the current models is that hiPSC-derived CMs (hiPSC-CMs) are structurally and functionally immature, expressing fetal-like behavior rather than adult CMs. Compared to adult human CMs, which are elongated and rod-shaped, hiPSC-CMs are smaller in size, with more spherical morphology. The cell surface area is also smaller than in the adult stage, which has a significant effect on the cell's functionality (e.g., impulse propagation, action potential depolarization velocity, total contractile force, and membrane capacitance). Sarcomeres in hiPSC-CMs are 25–30 % shorter than in adult CMs, with a lower degree of organization and sparse spatial distribution. Similarly, the mitochondria of hiPSC-CMs are smaller in size, which affects their efficiency in energy conversion. In terms of gene expression as well, hiPSCs are more similar to fetal than to adult CMs. This, together with the non-uniform Ca^{2+} handling, results in low contractile function compared to the adult stage. For all the mentioned reasons, the drug responses of EHTs made of hiPSC-CMs might differ from the physiological responses in adult humans.

In addition to the lack of maturation of hiPSC-CMs, there are also several other issues to address [27, 28]. For example, it is still particularly challenging to obtain very dense tissue, with muscle sheets one next to the other. Furthermore, it has been proven that the stiffness of the ECM significantly affects tissue formation. Very soft matrices will result in less compact and not dense tissues, while rigid environment will restrict cell movement and prevent tissue formation. Therefore, the optimal stiffness of the ECM must be found. Another aspect to consider is the optimal preload that the cardiac tissue should experience during formation and culture, which is defined by the shape and elasticity of anchoring points. This preload should be tuneable to different values for healthy and disease models. Finally, the heart consists of fibroblasts, endothelial cells, and CMs, raising the question of the ratio of these three cell types that should be present in the tissue construct. The optimal combination of all three cell types has yet to be determined.

THE MISSING LINK BETWEEN TECHNOLOGY AND BIOLOGY

To lead the research forward, all of the mentioned aspects should ideally be addressed. As the lack of maturation is one of the main drawbacks of EHT models, it is needed to develop a robust tool to induce and promote cell maturation. There are already examples demonstrating that maturation can be improved by including **electrical** and **mechanical stimulation** into the models [29] and by tuning the **stiffness** and **topology** of the substrates to improve cell organization. Furthermore, **long-term culture** [30] and inclusion of **different cell types** showed also a positive effect on the CMs maturation [31–33]. All these factors should be incorporated into the EHT models to allow the identification of the optimal parameters of the dynamic microenvironment of *in vitro* cardiac tissues (Fig.1.4).

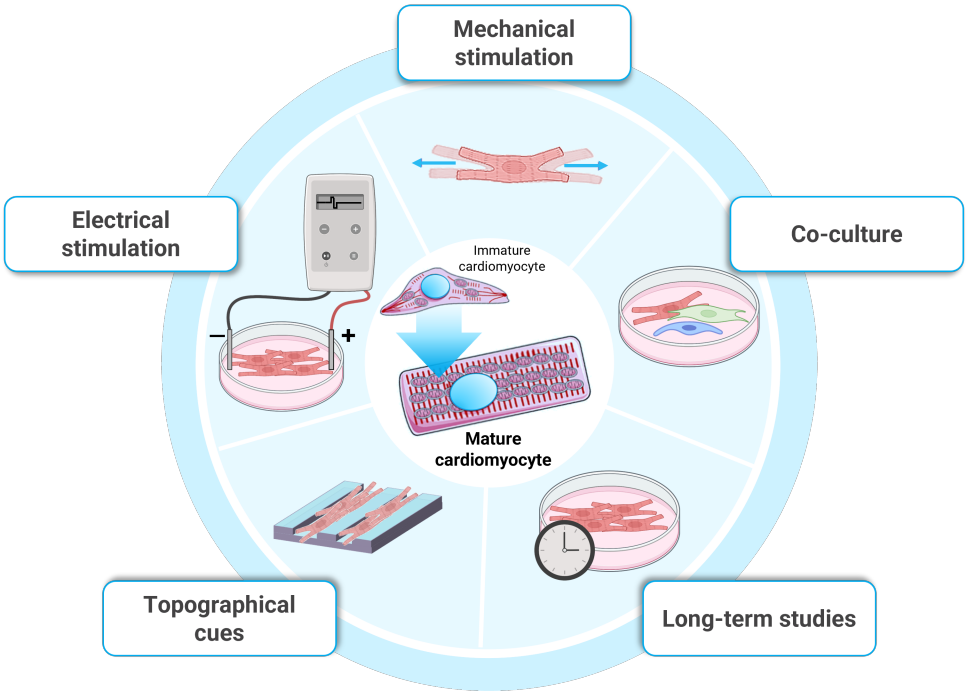

Figure 1.4: Factors involved in promoting the maturation of iPSC-CMs.

Until now, many of the developed EHT models and platforms addressed one or multiple of the mentioned challenges [34–40]. However, most of them are still in the initial phase of development, providing mainly mechanical support for the tissue formation and cell organization. The level of platform complexity is still low, as there are not many sensory readouts or stimulation systems integrated within. Most of the mechanical and electrical stimulations are performed with external systems. Therefore, the automated regulation of experimental conditions and the precise control over the EHT *in vitro* environment is still very limited.

1.2. MAIN QUESTION AND THESIS OBJECTIVES

To achieve a step closer toward a physiologically relevant *in vitro* cardiac model, this thesis aims to answer the following main question:

How can we create an on-chip dynamic microenvironment, with integrated sensing and stimulation, to guide the maturation and development of EHTs?

In order to tackle the main objective of the thesis we need to start by answering smaller questions. First, we need to understand what are the main physiological features that would be significant to model and study with our system. Next, we need to build our model starting from a simple 3D environment that allows tissue formation and understanding how the material and topography themselves influence the 3D tissue organization and function. Once a suitable substrate is developed, further upgrades can follow. The complexity of the entire system should slowly increase with the integration of electrical stimuli and force readouts, as those are the crucial parameters carrying information about tissue well-being and the maturation stage. At each step along the way, it is important to carefully study and understand how each of the introduced changes in the tissue microenvironment affects its physiological responses. Lastly, the developed platform should provide precise mechanical and electrical stimuli to the tissue culture with high automation and control levels. In the end, we should be able to obtain more insights into the parameters and properties of the microenvironment that are most suitable for the development of an *in vitro* cardiac model and how to further improve the development of such an environment.

THE APPROACH OF THIS RESEARCH

To address the research questions and develop the EHT platform, from an engineering perspective, we had to delve into mathematical models that can describe the effect of the platform design on the tissue. By using analytical and numerical modeling we could study the mechanical properties of the 3D topography and the potential effect of the latter on the tissue contractile properties. Furthermore, we could estimate the optimal design for the electrodes delivering electrical pacing by studying the electric field distribution throughout the tissue. From the modeling and platform design, we proceeded to fabrication. By using a combination of standard microfabrication techniques and polymer processing we could create a large number of platforms on a wafer level. With standard dry etching techniques, it was possible to obtain 3D structures with various profiles and sophisticated details etched into the silicon. Additionally, using lithography and different material deposition techniques, we could pattern metal, oxide, or polymer layers on top of silicon wafers with high accuracy. Combining this well-established technology in the Else Kooi laboratory of TU Delft with novel techniques of polymer processing made it possible to manufacture soft, transparent, biocompatible platforms, suitable for cell culture with integrated sensors and electrodes. Once the platforms were made and characterized, the biological counterpart came into play. All the cell culture experiments and analyses were performed in close collaboration with researchers from Leiden University Medical Centre (LUMC). The experiments with cell culturing assessed the tissue formation and functionality in different stages of the platform development.

1.3. OUTLINE OF THE THESIS

This dissertation is structured into eight chapters, including Introduction (**Chapter 1**), Conclusions and Future perspectives, describing the initial development and functional evolution (in time) of the platform for culturing and inducing maturation of EHTs.

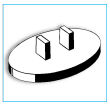

Chapter 2 is the first building block on the road towards a dynamic microenvironment for hosting EHT formation and culture. It starts from the concept of mechano-transduction and explores suitable three-dimensional structures for supporting the formation and growth of the tissues. The initial platform consists of two rectangular micropillars within an elliptic microwell. We start with three different sizes of the platform to study the effect of mechanical load on tissue formation and function. After rounds of characterization, both mechanical and biological, the optimal design choice is made. However, as we delve further into the accuracy of the readouts that we want to obtain from the platform, as well as the reproducibility of the experiments, the need for a design upgrade emerges.

In **Chapter 3** we address the drawbacks of the platform developed within Chapter 2 by implementing a novel design of micropillars. Tapered pillars with the hourglass profile are fabricated and characterized. Such design, with the sides inclined towards the middle of pillars, provides mechanical resistance to the tissue movement outside of the constraining areas. In this way, we achieve spatial confinement of the tissues in predefined positions along the pillars' height, which results in increased reproducibility, experiment yield and force measurement accuracy.

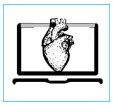

Once the 3D mechanical support for the tissue formation and growth is established, with precise positioning and confinement, in the next chapters we can focus on the functional readouts we want to obtain from the platform. One of the most important parameters to measure in EHT models is the force of contraction. It is a hallmark of its maturation and an indicator of a number of diseases. In **Chapter 4** we describe the automated tool we developed for the optical assessment of contractile properties of the tissue. The python-coded standalone app *ForceTracker* was developed to track the displacement of the pillar tips throughout the recorded videos of tissue contractions. This displacement is further correlated to the force applied upon pillars by the tissue. We validate the functionality of the software on two different EHT platforms and compare it to the alternative contractile assays.

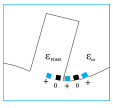

Optical measurement is a commonly used method for force assessment in most of the EHT platforms, but certainly not the optimal technique. **Chapter 5** explores the possibility of using electrical readout from integrated capacitive sensors measuring the deformation of the substrate below the displaced pillars. This deformation is attributed to the bending of pillars upon the contraction of adhering tissue. To capture it, a spiral capacitive displacement sensor is integrated into the PDMS layer below the pillars. The differential capacitive measurement is read-out with a portable UTI system developed at TU Delft.

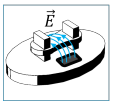

To achieve a dynamic microenvironment for tissue culture and to contribute to the maturation process, we need a range of different mechanical and electrical stimuli, as explained earlier. One of the most important inputs for steering the maturation of iPSC-CMs is electrical pacing. **Chapter 6** describes the integration of a pair of TiN electrodes within the previously developed EHT platform.

The electrodes are positioned near the micropillars, to apply electric field perpendicular to the suspended tissue. Additionally, a custom-made electronic board is developed to provide a variety of biphasic rectangular pulses for stimulating the tissues.

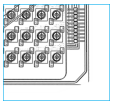

Performing a high-throughput analysis in an up-scaled and standardized manner is the final goal of the developed platform. **Chapter 7** describes the incorporation of the platform with integrated electrodes into a 96-well plate format, which allows multiplexing of the pacing experiments with automated selection of individual chips. This chapter also discusses the multifunctionality of the platform and its flexibility to incorporate force or additional readouts in the same multiplexed manner.

Finally, in **Chapter 8** (Conclusions and Future perspectives) all the results obtained within the thesis are summarized and analyzed in detail. Additionally, encountered limitations of the model are discussed while giving recommendations and suggestions for the continuation of the model development.

CHAPTER 2

THE BASELINE:
EHT PLATFORM WITH STRAIGHT PILLARS

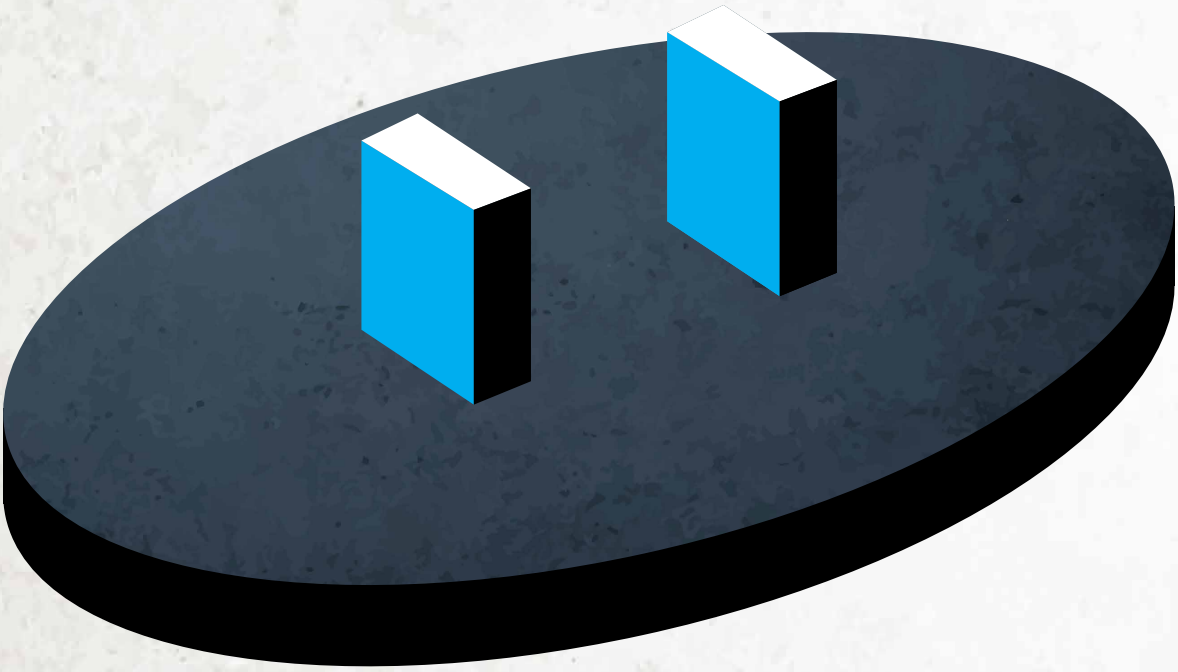

|part of this chapter have been published in *Journal of Microelectromechanical Systems* 29,5(2020)|40

2.1. THE IMPORTANCE OF MECHANO-TRANSDUCTION

THE first step towards the development of a dynamic microenvironment for the growth and maturation of EHTs is the substrate definition, by means of its mechanical properties and topography. Most human cells are known to be mechanosensitive, in the sense that the mechanical cues from their native environment are converted into biological responses. [42, 43] Hence, mechano-transduction has an important role in steering the formation and development of EHT models in a dynamic artificial environment.

In the case of cardiac cells organized into a tissue-like construct within the EHT approach, as has been already discussed in the introductory part, the optimal stiffness of the extracellular matrix supporting the tissue formation has yet to be determined. Moreover, the effective mechanical resistance to the tissue contraction is defined by the stiffness of the anchoring points around which tissues self-organize. This is yet another relevant parameter requiring optimization. Additionally, the shape and dimensions of these anchors determine the efficiency of cell compaction and alignment within the tissue, as well as the passive load applied to the cells during the self-assembly process. [25] For this reason, the design of the substrate of suitable mechanical properties and corresponding topography is the starting point in the design of a platform for culturing EHTs. This chapter will, however, focus only on passive mechano-transduction and the effect of substrate stiffness and topology on cell behavior. The active mechanical stimulation of tissues, involving actuation of the substrate, is left for future work.

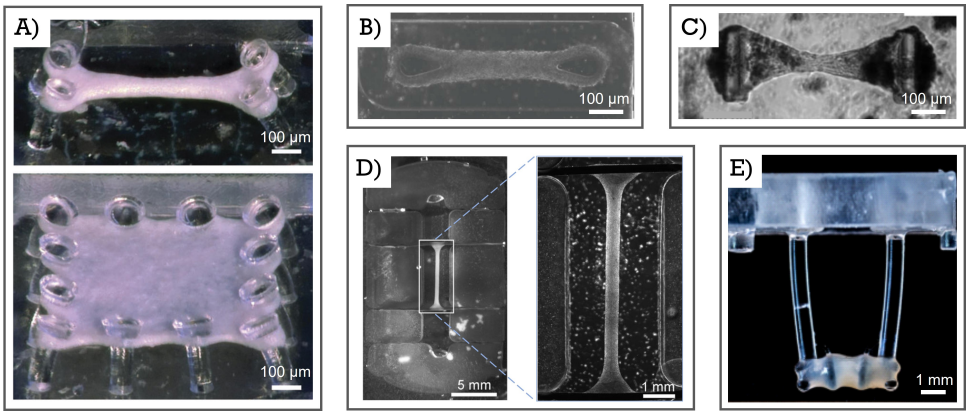

Figure 2.1: Examples of different Heart-on-Chip platforms: A) multi-anchor platform [44]; B) tear-drop shaped pillar platform [45]; C) rectangular pillar platform [34]; D) biowire platform [40]; E) upside-down tissue culture platform [46].

Many research groups explored different approaches trying to answer this question and came up with multiple designs of the anchoring points for tissue formation.[34, 40, 44–46] The designed platforms differ in the number of anchors, geometry, and size, as well as the position of tissue attachment along their length. [19, 35–37, 47] The most representative examples are shown in Fig.2.1. Still, the question of finding the optimal microenvironment for tissue self-assembly remains open. For example, the force developed by human ventricular CMs is approximately 50 mN/mm^2. [48] Similar values were

confirmed from *ex vivo* experiments, where the force per cross-section area (i.e. contractile stress) of the tissue remains in the same range independent of the tissue thickness. However, in existing human induced pluripotent stem cell (hiPSC)-based tissue models reported up to date, measured contractile stress is much lower ($4 mN/mm^2$) [49]. One of the reasons is certainly the lack of maturation of hiPSCs-CMs, but also the need for optimization of the biomechanical cues of the tissues microenvironment.

2.1.1. HEARTDYNO AS A STARTING POINT

The platform design starts from a previously developed system that reported some of the highest contraction force values measured in EHTs up to date (300 µN). The system called HeartDyno was developed by the research group from QIMR Berghofer Medical Research Institute, and it consists of two rectangular micropillars surrounded by an elliptic well of the same height as the micropillars. [50] The micropillars are anchors providing structural support to the tissue, while the elliptic well confines a known volume of cell/ECM mixture from which the tissue is formed. The entire platform is made of PDMS – a biocompatible elastomer and the most common material for the fabrication of OoC systems.

In addition to the high values of the measured force, the HeartDyno system was chosen as a starting point for the design since it is a relatively small PDMS-based platform, potentially compatible with upscaled cleanroom fabrication and sensor integration. Furthermore, the platform is compatible with a standard, stand-alone 96-well plate, which allows its easy adoption by pharma in existing robotic pipelines as well as by research laboratories within academia.

The main shortcomings of the HeartDyno system are its current manufacturing methods by manual PDMS moulding, use of relatively high cell numbers per tissue, and optical-only readout. By downscaling the original platform and making it compatible with batch cleanroom-based fabrication, the first two shortcomings can be addressed in this Chapter. Later on, in Chapter 5 integration of the force readout will be introduced. As it will be shown in this thesis, the representation of the PDMS platform with EHT formed around the micropillars, at the bottom of a 96-well plate, is depicted in Fig2.2.

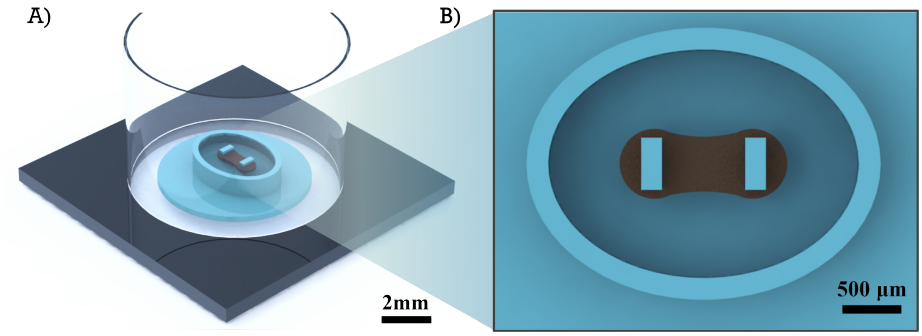

Figure 2.2: A) 3D model of the EHT platform; PDMS structure (in blue) at the bottom of a single well of a 96-well plate, with the tissue (brown) formed around two micropillars, surrounded by an elliptic microwell. B) Close-up image of the tissue within the elliptic microwell.

2.2. DESIGN OF THE EHT PLATFORM

2.2.1. ANISOMETRIC DOWNSCALING

The geometry of the original HeartDyno system was anisometrically downscaled to reduce the number of cells required per EHT and to make the fabrication compatible with batch wafer-level processing while retaining the original pillar stiffness. The HeartDyno's original volume of 3,5 µL, containing approximately 50.000 cardiac cells in the confining microwell, was scaled down respectively to 3, 2, and 1 µL in three distinct versions of the platform. As will be shown, the anisometric scaling ensured that the stiffness of the pillars remained constant in all cases, so that the tissues could effectively experience the same load in all chip sizes.

The idea of platform downscaling has on one side the purpose to study the effect of the mechanical properties of the environment on tissue formation and contractile performance - particularly, to understand better the relation between generated force of contraction and the size of the tissue, number of cells and its cross-section. There are still gaps in knowledge about contractile force behavior as a function of mentioned parameters, therefore the nature of the force generated by iPSC-CMs in EHT models has yet to be fully characterized. Another interesting aspect, which has been studied somewhat more extensively, is the effect of substrate stiffness and the preload of anchors on tissue formation and function. In addition to these more fundamental questions, downscaling is also relevant for practical reasons to ensure compatibility of the fabricated platforms with the standards of microfabrication technology and potential mass production. The main guidelines to achieve platform downscaling were:

- Preserving the stiffness from the initial HeartDyno system;
- Keeping the pillars vs. medium volume ratio to not affect tissue formation protocol;
- Choosing the minimum well volume of 1 µL, to allow reproducible manual pipetting.

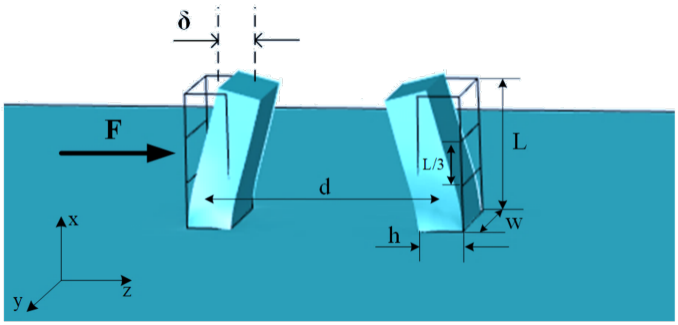

Figure 2.3: Illustration of the pillars' deformation when the force is applied in the *z* direction.

The principle of a bending cantilever in beam theory can be used to describe the behavior of elastic pillars upon tissue contraction. The beam theory for small displacement can be applied with several assumptions: beam cross-section remains undeformed along the entire neutral axis and the transverse strain can be neglected in the bending curve derivation. [51] Given this, the pillars' behavior is described by a one-end fixed bending beam, i.e. cantilever, to determine the downscaling factors. An illustration of the bend-

ing pillars upon force application is shown in Fig.2.3. Here, h, w, and L are the thickness, width, and length of pillars, respectively; d is the distance between pillars, while δ is the tip displacement resulting from the force F acting upon the side of the pillar. For small deflections ($\delta << L$), the force applied upon the pillar is related to the pillar's displacement via the effective stiffness k.

$$F = k \cdot \delta \tag{2.1}$$

The stiffness of the rectangular beam, when a point load force is applied, is defined with the equation:

$$k = \frac{6E_Y I}{(-x^3 + 3Lx^2)} \tag{2.2}$$

where E_Y is Young's modulus of the material, x is a position on the beam where the force is applied, along the X axis from Fig.2.3, L is the length of the beam (in this case length of the pillar), and I is the moment of inertia which for a beam of rectangular cross-section is defined with Eq.2.3:

$$I = \frac{wh^3}{12} \tag{2.3}$$

Combining Eq.2.2 and Eq.2.3, Eq.2.1 becomes:

$$F = \frac{E_Y wh^3}{2(-x^3 + 3Lx^2)}\delta \tag{2.4}$$

It is assumed that the tissue applies a point load in the middle of the length of the pillar, therefore, when $x = \frac{L}{2}$ Eq. 2.4 becomes:

$$F = \frac{4E_Y wh^3}{5L^3}\delta \tag{2.5}$$

The stiffness of pillars experienced by the tissue adhering to the middle of the pillars length is then defined as:

$$k = \frac{4E_Y wh^3}{5L^3} \tag{2.6}$$

There are many possibilities to achieve anisometric downscaling of all the pillar dimensions while preserving the same stiffness as in the HeartDyno system. However, the main assumption is that the final shape of tissues formed around the pillars is determined by the thickness h and width w of the pillars, so the ratio between the two should remain constant by applying the same downscaling factor S. The additional condition comes from the fact that the length of the pillars L is determined by the thickness of silicon wafers used for fabrication, as it will be shown later. The idea is to reduce the length of pillars as much as possible to make them compatible with standard microfabrication techniques and wafer sizes, therefore, the length of the pillar is downscaled with a different factor S_L. Accordingly, Eq.2.6 can be written in the following form:

$$k = \frac{4E_Y wh^3 S^4}{5L^3 S_L^3} \tag{2.7}$$

Since the k is kept constant, and E_Y is Young's modulus determined by the material properties, the relation between different scaling factors is:

$$S_L = S^{4/3} \tag{2.8}$$

The second condition of keeping the ratio of medium volume and pillar volume constant can be expressed as:

$$\frac{V_{medium}}{V_{pillar}} = C \tag{2.9}$$

where $V_{medium} = V_i$ takes values of 3, 2 and 1 µL and w_i, h_i and L_i correspond to the pillar dimensions for each of the volume variations, for i = 1,2,3. Now, using Eq.2.7 and 2.9 we can obtain the relationship between the length of the pillar L and its thickness h, after downscaling:

$$L_i = \sqrt[4]{\frac{4V_i E_Y}{5Ck}}\sqrt{h_i} = N\sqrt{h_i} \tag{2.10}$$

Combining the Eq.2.7, 2.10 and knowing the ratio between L and h before scaling (3.5), it is possible to derive the expression for the scaling parameter S_i, while the scaling coefficient S_{L_i} is then easily calculated using the Eq.2.8.

$$S_i = \left(\frac{1}{3.5\sqrt{h}}\sqrt[4]{\frac{4V_i E_Y}{5Ck}}\right)^5 \tag{2.11}$$

This scaling factor depends on the media volume defined by condition (3), as the rest of the parameters are known constants. Table 2.1 gives the overview of all the downscaled parameters, pillar dimensions and original dimensions of the HeartDyno system.

Table 2.1: Design parameters for the EHT platforms.

Symbol	Description	HeartDyno	3µL platform	2µL platform	1µL platform
w [µm]	pillar's width	500	487	427	352
h [µm]	pillar's height	200	210	176	151
L [µm]	pillar's length	700	700	560	460
d [mm]	pillars' distance	1	0.97	0.85	0.7
a [mm]	semi-minor axis of elliptic wall	1.1	1.05	0.93	0.76
b [mm]	semi-major axis of elliptic wall	1.5	1.43	1.27	1.03
t [µm]	thickness of the elliptic wall	/	200	200	200

2.3. MICROFABRICATION OF THE PLATFORMS

2.3.1. MICROFABRICATION TECHNIQUES

Three different sizes of EHT platforms were fabricated at the wafer level using silicon-based micromachining and polymer moulding techniques. Some of the techniques used during fabrication are plasma-enhanced chemical vapour deposition (PECVD) of SiO_2, photolithography, reactive (RIE) and deep reactive ion etching (DRIE).

PECVD

Thin layers of SiO_2 can be deposited on a wafer surface as a product of condensation and chemical synthesis occurring from the gas phase of SiH_4, N_2O and N_2 in the low-pressure chambers at elevated temperatures [52]. If the process is additionally enhanced by plasma, which provides energy during deposition, allows for reduced process temperature, and improves the layer structural integrity and uniformity, it is then called PECVD. [53] Thin and uniform layers of oxides and nitrides can be obtained using this method. The quality of the PECVD oxide layer is lower than the one obtained from thermal growth, but still very useful in microfabrication as a protective layer during wet and dry etching.

PHOTOLITHOGRAPHY

Photolithography is a technique of patterning photosensitive layers (i.e. photoresists (PRs)) on top of a silicon wafer using UV light. [54] The incident light is blocked in a controlled way by passing through a glass mask patterned with chromium and placed between the light source and the wafer. The exposed parts of PR undergo chemical changes and become either hardened or softened depending on the type of photoresist. The final stage of the process is PR development in which exposed (positive PR) or non-exposed (negative PR) parts are removed so that the mask pattern is transferred to the residual PR

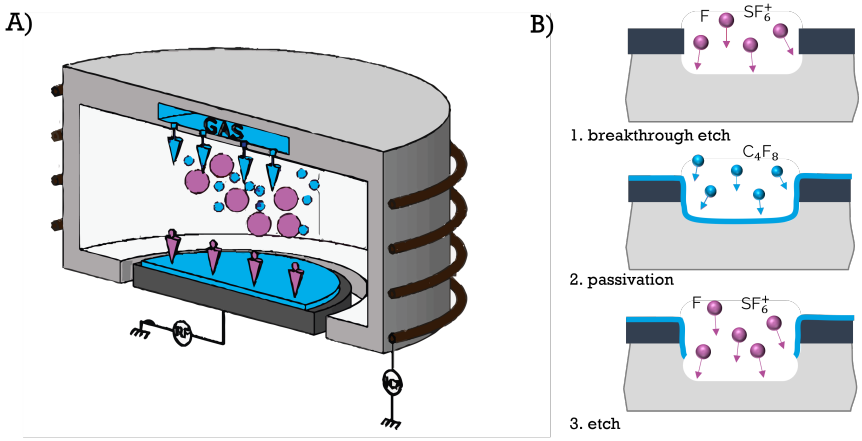

Figure 2.4: Sketch of deep reactive ion etching: A) A reactor chamber of DRIE etcher in which inductively coupled plasma is generated; B) Illustration of the Bosch process in three steps: breakthrough etch, passivation, etching.

on the wafer surface. The patterned layers of PR are used as selective protection for the material below during wet or dry etching.

RIE

Reactive ion etching (RIE) uses a reactor with a parallel plate capacitor configuration to generate plasma in an inert gas (Ar) atmosphere and low-pressure conditions. In our case, RIE is used to etch SiO_2 layer protected with patterned PR. The wafer is placed on one of the electrodes and cooled down with He during the entire process. Upon plasma ignition, DC voltage drives positively charged ions toward the electrode with the wafer, where the chemical reaction with SiO_2 occurs. All SiO_2-on-Si dry-etch processes are based on fluorocarbon plasmas, with SiF as the volatile product [53, 55].

DRIE

Anisotropic etching of silicon wafers to achieve deep cavities of high aspect ratios is performed using DRIE, also known as the Bosch process. The process utilizes a high-density inductively coupled plasma (ICP) source and alternating gas chemistry for the controlled steps of reactive ion etching (RIE) and polymer deposition. An additional RF source is used to generate DC bias to attract ions to the wafer and achieve better directionality of the etching (Fig.2.4). The process consists of three steps: breakthrough, passivation and etching. During passivation cycles, a thin Teflon layer C_4F_8 is conformally deposited over the wafer and the sidewalls of etched structures. In the subsequent etching cycle, the fluorocarbon polymer is etched from the bottom of the cavities and partially from the sidewalls. Since the ion flux is lower, the polymer on the sidewalls is removed much slower than on the bottom of the structures in the plasma direction, minimizing the lateral etch of silicon. This allows further in-depth etching of silicon by fluorine radicals released from SF_6 plasma. Before removing the polymer completely, the deposition is repeated and the cycles continue until the desired depth is achieved [53, 56, 57].

2.3.2. PROCESS FLOW

Fabrication of the platforms starts with the deposition of SiO_2 on 1 mm-thick, double-side polished, 4-inch Si wafers. PECVD oxide is deposited on the wafer surface, on top of 50 nm of previously grown thermal oxide (Fig.2.5A). The oxide layer is patterned using standard lithography steps and RIE, to serve as a hard mask during the DRIE of silicon (Fig.2.5B). The patterned Si wafer was etched using the Bosch process, to precisely define the depth of cavities for PDMS moulding of the pillars and elliptic microwell (Fig.2.5C). A different number of cycles defined three different cavity depths of 423, 560, and 660 µm, respectively.

After the DRIE process, three different depths of cavities are obtained for the three versions of the platform. Prior to PDMS spin-coating the wafers were functionalized with a perfluorinated anti-adhesion self-assembled monolayer (SAM) to ease PDMS removal (Fig.2.5D). The anti-adhesive layer was formed by evaporation of a few droplets of perfluorooctyl-trichlorosilane in a vacuum chamber for two hours. As a result, the silicon dioxide-covered surface of the Si wafer became highly hydrophobic, which was confirmed using water contact angle measurements ($117 \pm 3°$).

As an alternative treatment to silane deposition, it is possible to use fluorocarbon deposition (C_4F_8), i.e. teflon, which is the second step of the Bosch etching process, as

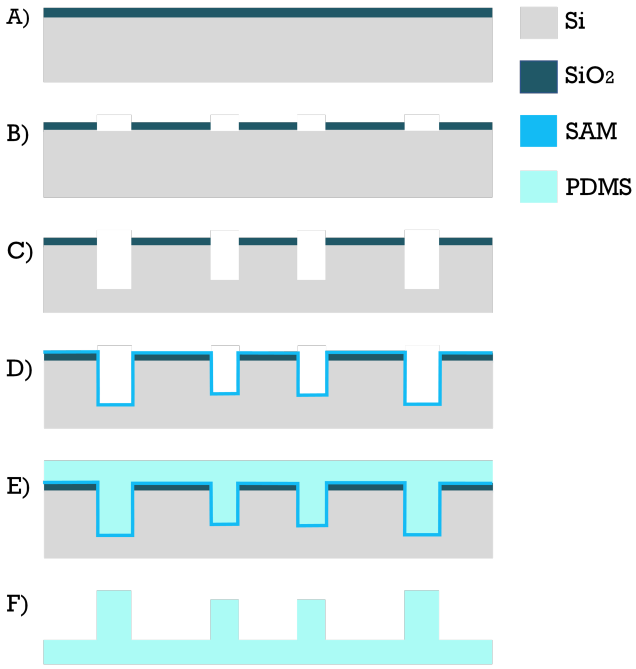

Figure 2.5: Process flow for the fabrication of the platforms for culturing EHTs with straight pillar design.

an anti-adhesion layer on top of Si wafers. In the case of teflon deposition, the roughness of the side of the cavities is increased and the deposited layer is approximately 300 nm thick. Regarding hydrophobicity, SAM and teflon both gave comparable results and therefore can be successfully used as anti-adhesion layers.

An uncured PDMS mixture of Sylgard 184 elastomer and its curing agent (ratio 10:1) was spin-coated using a two-step process (Fig.2.5E). The first step was used to ensure the deep cavities in the wafer were filled with PDMS. The second spin-coating step defined the final thickness of the PDMS substrate supporting the pillars (~ 300 µm). In between the two spin-coating steps, the wafers were degassed under vacuum to make sure that the PDMS reached the bottom of the cavities without trapping air. The PDMS was then cured in an oven at 90 °C for 1 hour and peeled off the wafer easily (Fig.2.5F). After demoulding, the platforms were manually cut out of the PDMS substrate and transferred to the bottom of the wells in a 96-well plate.

Profile measurements of the final PDMS structures as well as the etched mould in Si wafer were measured with a Keyence laser profilometer. Fig.2.6 shows an example of these profile measurements for only one pillar length. It can be noticed that DRIE gives slightly tapered profiles of the etched cavities, which means that the PDMS pillars will have the shape of truncated pyramids instead of parallelepipeds. Shortening of the top cross-section surface area of the pillar compared to the bottom one is measured to be ≈ 5%. In order to obtain the stiffness of the final structures as precisely as possible, this effect was taken into account in the numerical model. (Section 2.4.1) A comparison

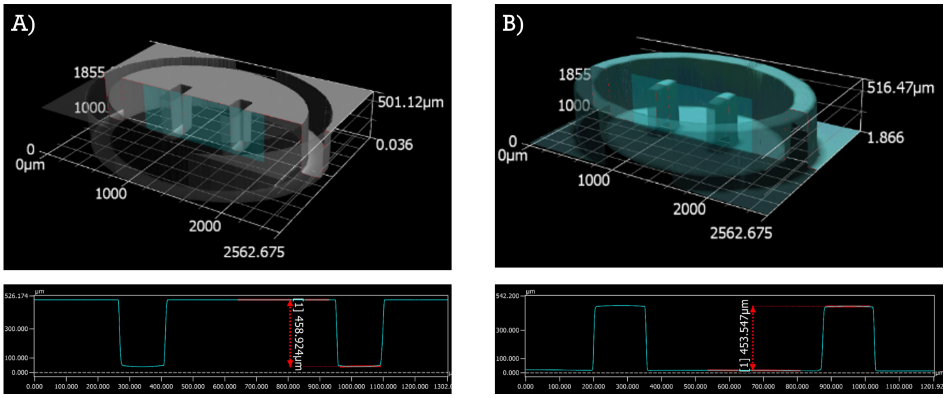

Figure 2.6: Profile measurements of the A) Si mould of pillars and microwell and B) de-moulded PDMS structures. The line measurements (bottom) evidence tapering in the etched structures and consequently in the PDMS pillars.

of the cuboid-like structures with the truncated pyramid-like structures gave negligible difference in the stiffness calculations (≈ 0.02 N/m).

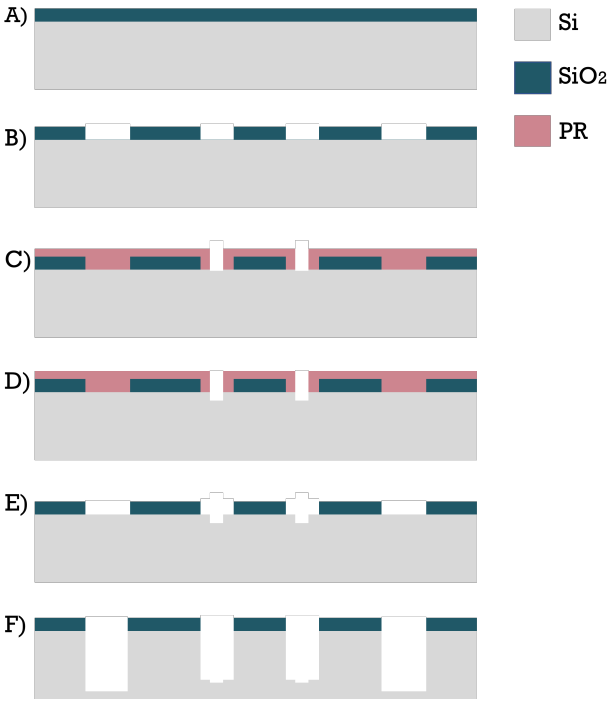

Figure 2.7: Process flow for the fabrication of rectangular patterns at the bottom of cavities for pillar moulds.

2.3.3. ADDITION OF FOCUS FEATURES

Upon pillar fabrication, biological experiments were performed as will be presented later. During the experiments, tissue contractile properties were measured by optically tracking the displacement of PDMS pillars with custom-made software. (Chapter 5) For this purpose, 10 s videos of contracting tissues were recorded with the focus of the optical microscope on top of the pillars to capture their displacement. It was noticed that focusing on the top of the pillars becomes quite challenging due to the pillars optical transparency as well as the fact that cells often end up covering parts of the pillars tips. As focusing exactly on the tips of the pillars is crucial for the software working principle (Chapter 5), the idea was suggested to introduce additional rectangular patterns on the pillars tips as focusing features.

To facilitate the inclusion of additional rectangular patterns on the tips of the pillars, the fabrication flow has been slightly modified. The idea is to create a rectangular pattern at the bottom of the cavities in the Si wafer, which will be translated into a pattern on top of the pillars after PDMS moulding. The rectangular shape is created by using a two-step mask for silicon etching (Fig.2.7), which enabled first the transfer of small rectangles into the Si wafer and later the etching of the pillars and the microwell. The two-step mask was made by adding a patterned photoresist with small rectangular features (Fig.2.7C) on top of the previously patterned SiO_2 hard mask for pillars and wells (Fig.2.7A,B). In this process, dry etching of SiO_2 was performed with a soft landing to make sure not to damage the silicon layer below the oxide. This is a very important step, as every defect or non-uniformity at the Si wafer surface would introduce micro-masking for the later DRIE of rectangular shapes.

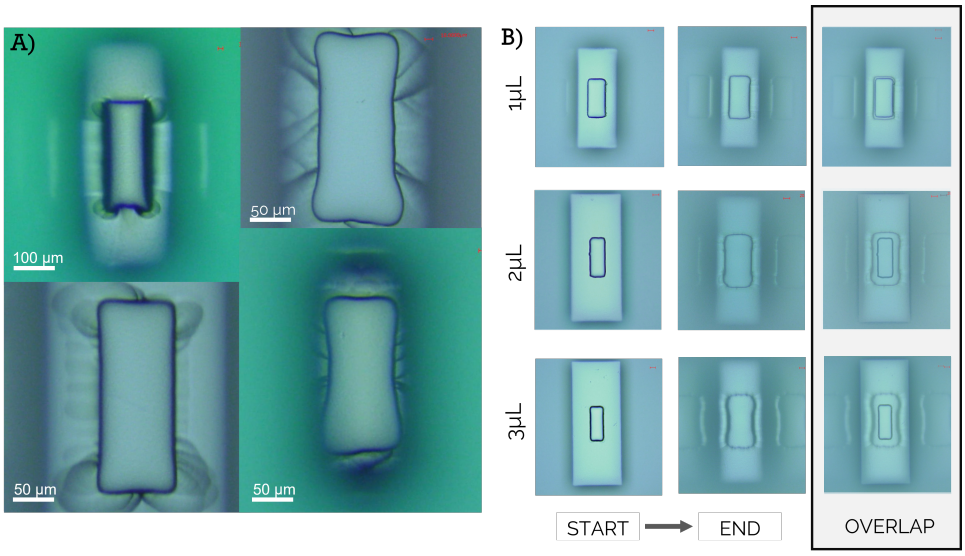

Figure 2.8: A) Examples of damaged rectangular patterns at the bottom of deep cavities, due to the non-optimized parameters of the Bosch process; B) Rectangular patterns etched at the bottom of three different Si moulds, showing their comparison at the beginning and at the end of the etching process.

First, small rectangles of 20 µm depth were etched into the Si with the PR mask (Fig.2.7D). After PR removal and cleaning of the wafer, SiO_2 hard mask remained for the DRIE of pillars and wells (Fig.2.7E,F). However, to make sure that the shape of small and shallow rectangles at the bottom of the bigger cavities can be preserved and transferred to the desired depths, the parameters of the standard Bosch process had to be adjusted.

The slopes and wall roughness of deep cavities made with the Bosch process is determined by the fine-tuning duration of the passivation step and the final etch step in each cycle. In the case of shallow patterns at the bottom of deep cavities, the lateral etch rate of C_4F_8 on the 20 µm large walls is much higher than on the walls of pillars. Therefore, the polymer layer is almost entirely consumed during the last etching step, creating distorted patterns with damaged walls. Some of the examples of damaged shallow rectangular structures are shown in Fig.2.8A. To address this issue, the deposition time of C_4F_8 was extended from 2 s to 2.2 s per cycle, while at the same time, the etching duration was reduced from 1.5 s to 1 s per cycle. These changes made sure that there is enough protective polymer layer during the last etching step of the Bosch process to ensure the preservation of the shallow rectangles until the final depth of the pillars is reached. In addition to process parameter adjustment, the sharp edges of the rectangular patterns were rounded off to reduce the deformation at the corners.

There is a significant difference between the starting rectangular shapes and the final ones obtained at the end of the etching. The most challenging pattern transfer was in deepest cavities (3 µL EHT platforms) where the most prominent geometry broadening can be noticed. This effect is seen in Fig.2.8B, where patterns at the bottom of different depth cavities are shown at the beginning and at the end of the etching process. The overlapping of starting and final patterns is also shown.

After successfully etching cavities of three different depths in the silicon wafer, with rectangular patterns at the bottom, the moulds were made hydrophobic using SAM of (perfluoro)silane. The PDMS moulding followed, in the same way as in the case of pillars without patterns. A 3D image of the Si mould in case of 1 µL platform and the corresponding de-moulded PDMS structure is shown in Fig.2.9.

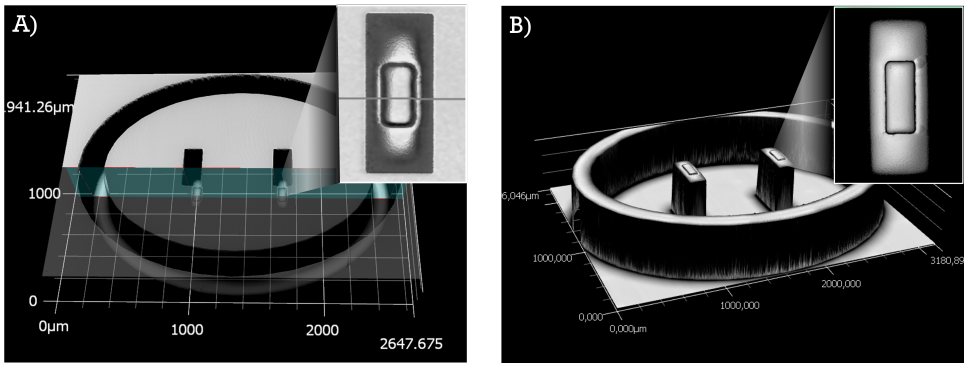

Figure 2.9: A) 3D optical image of Si mould of 1 µL platform with focusing features etched at the bottom of the cavities; B) 3D optical image of PDMS structures of 1 µL platform with focusing features transferred on top of the pillars.

2.4. MECHANICAL PROPERTIES OF THE EHT PLATFORMS

2.4.1. NUMERICAL MODEL OF STRAIGHT PILLARS

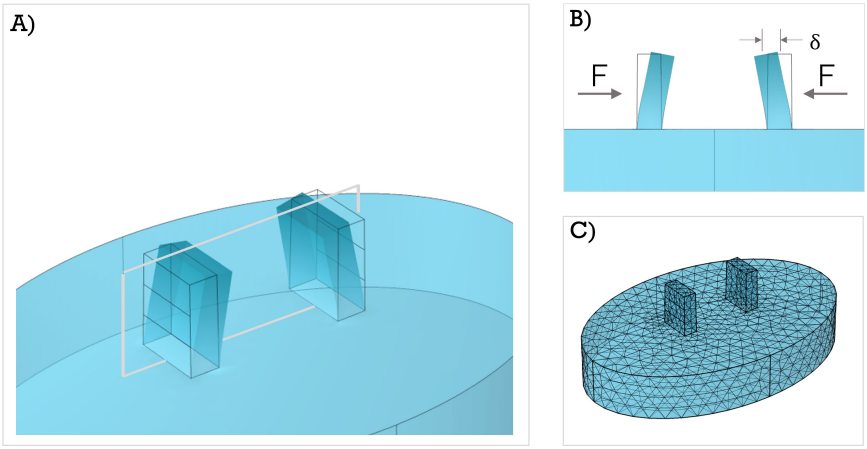

Figure 2.10: Implementation of straight pillar design in Comsol Multiphysics: A) 3D geometry of pillars on the soft substrate; B) deformation of pillars upon force application on the sides; C) geometry meshing to define equation nodes.

Prior to the fabrication of three different EHT platforms, theoretical and numerical modelling was performed. A model of a bending cantilever was used to simulate the behaviour of the elastic pillars when the force is applied by the contracting tissue. Numerical simulations were performed in COMSOL Multiphysics, using a finite element method within the Solid Mechanics module. The 3D geometry of pillars on a soft substrate was generated in Comsol and is shown in Fig.2.10A. The force applied by the tissue was modelled as a load distributed on a rectangular area in the middle of the pillars for all three sizes. The width of this rectangular area was set to 1/3 of the micropillar's length to approximate the estimated tissue thickness. The assumption about the position of adherence of the tissue along the micropillar's height was adopted from literature [58]. Due to the applied force, elastic pillars bend, and by quantifying the displacement of the pillars while knowing their mechanical properties, it is possible to estimate the applied force (Fig.2.10B). The relationship between applied force and the pillar displacement was defined with the Eq.2.1.

Whereas analytical bending cantilever theory assumes rigid support for the cantilever, and as such was used to define downscaled platform dimensions, the numerical model implemented in Comsol Multiphysics more faithfully reproduces the realistic situation, where pillars are attached to the elastic PDMS substrate. The difference in the pillars' tip displacement, when the same force applies to the pillars attached to a rigid versus elastic substrate, is shown in Fig.2.11.

To confirm model agreement with the HeartDyno system, the analysis of pillar mechanical properties was carried out in the following manner. Using the Solid Mechanics module in Comsol, the load of 14 μN was applied on the sides of the pillars and the tip displacement was measured. As the expected stiffness of the pillar, when the point

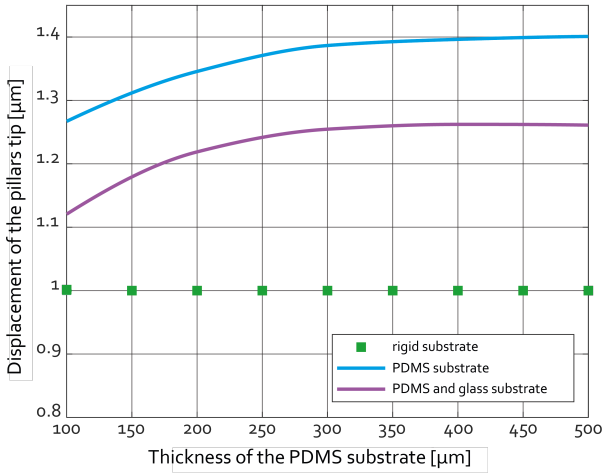

Figure 2.11: Comparison of the substrate effect on the pillar displacement, in case of a soft and rigid connection between pillars and the substrate.

force is applied in the middle of its length, is $k = 14$N/m, consequential tip displacement should be 1 µm. The tetrahedral mesh was generated for the entire geometry, with the refinement features around the pillar connection to the substrate (Fig.2.10 C). The mesh density determines the number of differential equations the model uses to converge toward a single solution. The momentum balance equation in the form:

$$0 = \mathbf{F}_V + \nabla \mathbf{P}^T \tag{2.12}$$

was used to obtain the values of displacement components u,v,w. Here, the term $\mathbf{F}_V$ represents volume forces acting on the undeformed material, while $\mathbf{P}$ is the first Piola-Kirchoff stress tensor which relates forces acting in the spatial directions to areas in the undeformed configuration [51]. The flow of the FEM study is illustrated in Fig.2.12. Table 2.2 shows the resulting stiffness of pillars in three different platforms, for the estimated E_Y = 1.4 MPa, which is the value used for the HeartDyno system. The pillar geometry used in calculations is corrected for the truncated pyramid effect.

Table 2.2: Effective stiffness calculation from numerical simulations.

Symbol	Description	HeartDyno	3µL platform	2µL platform	1µL platform
k [µN]	effective stiffness	14 N/m	13.98 N/m	14.58 N/m	13.52 N/m

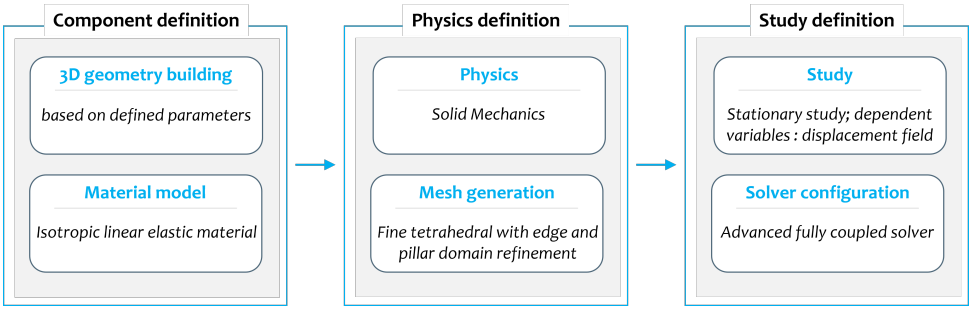

Figure 2.12: Computational flow of mechanical response study of straight pillars using FEM implemented in Comsol Multiphysics.

2.4.2. ANALYTICAL MODEL OF STRAIGHT PILLARS

As mentioned previously, the analysis of pillar deformation was carried out using the beam theory. When a straight beam is loaded and the action is elastic, assuming the small displacement $\delta << L$, the longitudinal centroidal axis of the beam becomes a curve defined as an "elastic curve." The elastic curve of the beam when the force F is applied at the position a is defined with the following set of equations:

$$y = \frac{Fx^2}{6E_Y I}(3a - x), 0 < x < a \tag{2.13}$$

$$y = \frac{Fx^2}{6E_Y I}(3x - a), a < x < L \tag{2.14}$$

From these equations, the maximal tip displacement used previously can be derived for $x = L$, and therefore the corresponding effective stiffness (Eq.2.2). However, to validate

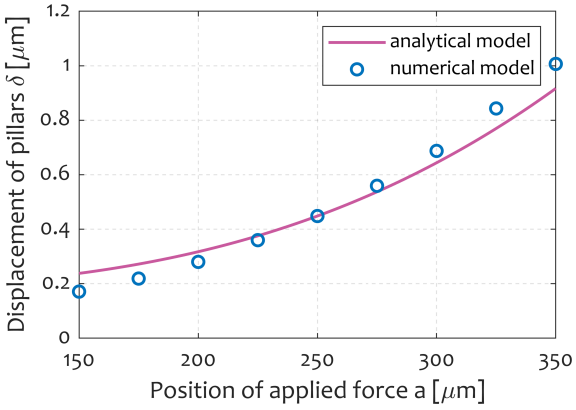

Figure 2.13: Comparison of the analytical and numerical model of the pillar displacement, when force is applied on different positions along pillar length.

the theoretical and numerical model, the comparison with mechanical characterization must follow. For this purpose, the theoretical model was fitted to the numerical to facilitate precise calculation of pillars' mechanical properties. A comparison of the analytical and numerical model of the pillar displacement at the position of applied force is shown in Fig.2.13. Both calculations were carried out for E_Y = 1.4 MPa. In Fig.2.13 only a comparison for 1µL EHT platform is shown since graphs are similar in all three cases.

It is worth noticing that there is a slight mismatch between these two models, since the numerical one accounts for the truncated pyramid shape and the load distribution on a rectangular surface area, while the theory assumes straight pillars with point force approximation. The effect of the soft substrate and its addition to the pillar displacement was included in the theoretical model via additive constant C = 0.1 µm derived based on function fitting in Matlab.

2.4.3. MECHANICAL CHARACTERIZATION

A FemtoTools Nanomechanical Testing System (FT-NMT03) was used for the mechanical characterization of the fabricated PDMS platforms. The nanorobotic system is designed to test the mechanical properties of micro/nanostructures and is equipped with a micro-force sensing probe with a silicon tip that can apply a specific force and measure the displacement of the tip. The PDMS substrate with micropillars was mounted onto a holder next to the sensing probe. The silicon tip was positioned at a predetermined height along the micropillar length with nanometer precision, as shown in Fig.2.14.

During the measurement, the force was applied to the micropillar by the silicon tip and the displacement of the tip was continuously measured with a high-resolution piezo-scanner. After a pre-determined displacement of the probe or after the defined force limit had been reached, the elastic micropillar started returning to the initial position, thereby exerting the restoring elastic force onto the silicon tip. This movement of the tip was again measured with the piezo-sensors and the force-displacement curve was obtained. The stiffness of the micropillar is represented by the slope of the force-displacement curve during the micropillar's return to its initial position. Measurements were performed at five distinct micropillar positions for all three different platforms.

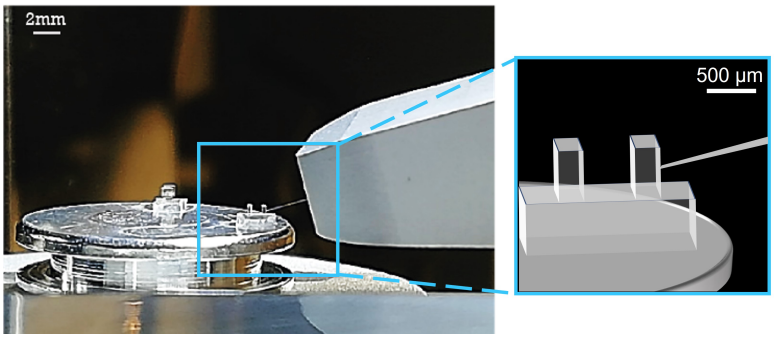

Figure 2.14: Setup for the mechanical characterization of the PDMS micropillars using nanoindentation. The blue frame highlights a single pair of micropillars cut out from the wafer-sized PDMS substrate, as well as the sensor tip of the nanoindentation tool.

Comparison between measured data and data from numerical simulations showed curves with very similar slopes and only slightly shifted apart. The same trend and very similar graphs were obtained for all three micropillar sizes, as demonstrated in graphs Fig.2.15 A-C. In order to fit the simulations to the measured values, an analytical function was introduced to precisely describe the model of bending pillars on the elastic substrate, which could not be approximated using only Eq.2.2. The fitting function in Eq.2.15 was generated by applying Taylor's expansion to Eq.2.2 for $x = \frac{L}{2}$ and finding the missing coefficients C_i using the least square difference fitting tool in Matlab®.

$$k \sim \frac{4E_Y w h^3}{5L^3}\left(c_1 - c_2\frac{x}{L} + c_3\frac{x^2}{L^2} - c_4\frac{x^3}{L^3}\right) \tag{2.15}$$

Consequently, the value of Young's modulus of PDMS was calculated to be 0.8 MPa in all three cases, which is consistent with the use of the same PDMS mixture for all platform types. This value of E_Y was used in the further contractile force estimation.

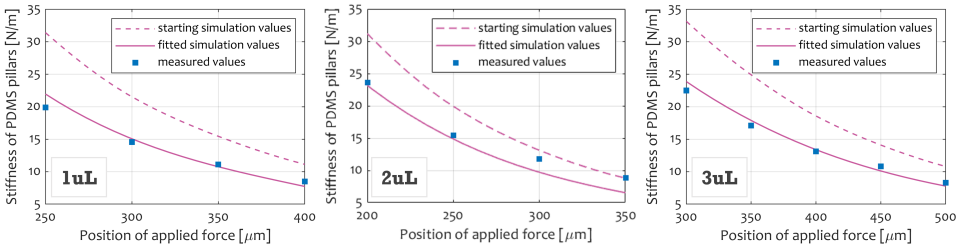

Figure 2.15: Stiffness analysis for the three different platforms with PDMS pillars. Data from finite element simulations (purple) were compared and fitted to the measured data (blue) to estimate Young's modulus of PDMS for the EHT platform.

2.5. INCLUSION OF CARDIAC CELLS

The inclusion of different cell types in fabricated chips, cell differentiation, EHT generation, tissue monitoring and staining during the entire experiment duration, was conducted by collaborators at Leiden University Medical Center. Human-induced pluripotent stem cell (hiPSC) - derived cardiomyocytes (CMs) and hiPSC-derived cardiac fibroblasts (FBs) (4:1 ratio) were mixed in a collagen/Matrigel-based ECM gel and seeded in the three different chips [33]. As a source of differentiated cardiomyocytes and fibroblasts, the LUMC0020iCTRL-06 hiPSC-line was used [59]. For the ECM gel mixture, we used acid-solubilized collagen I and growth factor-reduced Matrigel (2.6 mg/ml collagen I and 9% Matrigel). The number of cells used per chip was approximately 47000 (volume: 3 µL), 31000 (2 µL) and 16000 (1 µL). After pipetting the gel mixture into the PDMS microwells, the 96-well plate was shortly centrifuged to achieve the level and homogenous distribution of the mixture throughout the well, to make sure that the tissue formed around midway along the micropillars length, and to remove any trapped air. Self-assembly and compaction of the tissue around the micropillars were visible within 24 hours, and spontaneous contraction of EHTs started within 72 hours. The formation

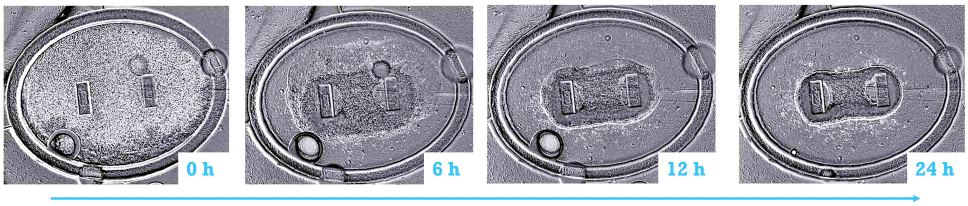

Figure 2.16: Timeline of tissue formation: starting from the cell/gel mixture seeding in the chip (0h) until the compaction into a tissue-like structure after 24h.

process of the tissue over 72h at different time points is shown in Fig.2.16. After approximately 2 hours of gel solidification in a humidified incubator, wells of the 96-well plate were filled with 200 µL formation medium, preventing the tissues from drying out. Formation medium was used during the first 3 days of cell culture and maturation medium thereafter, according to the HeartDyno protocol [50]. Cells were kept in a humidified incubator for the whole time and the medium was refreshed every 3 to 4 days.

All tissues successfully formed regardless of the chip size, demonstrating that the miniaturized design of the elastic micropillars is suitable for the self-assembly of different-sized tissues. Representative images of the three different tissue sizes formed around the micropillars in the PDMS platforms are shown in Fig.2.17. Brightfield images were taken live on day 4 since the beginning of the experiment with a Nikon Eclipse Ti2 optical microscope. Immunostaining of the intracellular sarcomeric structures demonstrated the cellular organization around the flexible PDMS micropillars and sarcomere orientation. The tissues were stained whole–mount and imaged with an Andor Dragonfly 500 fluorescence microscope on day 19 from the beginning of the experiment. Sarcomeres were stained using cardiac-specific antibodies against alpha-actinin (ACTN2) and cardiac troponin T (TNNT); nuclei were stained with DAPI (Fig.2.18).

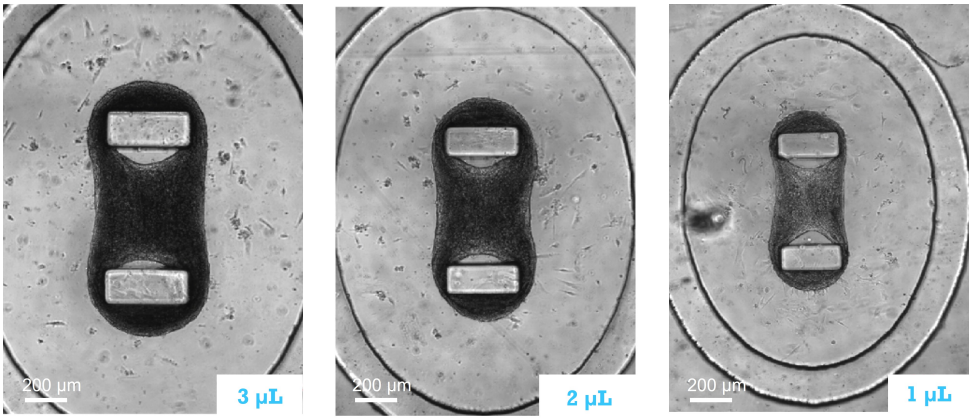

Figure 2.17: Representative images of the three different sizes of hiPSC-based cardiac tissues successfully formed around PDMS micropillars in the miniaturized EHT platforms, taken on day 4 after chip seeding.

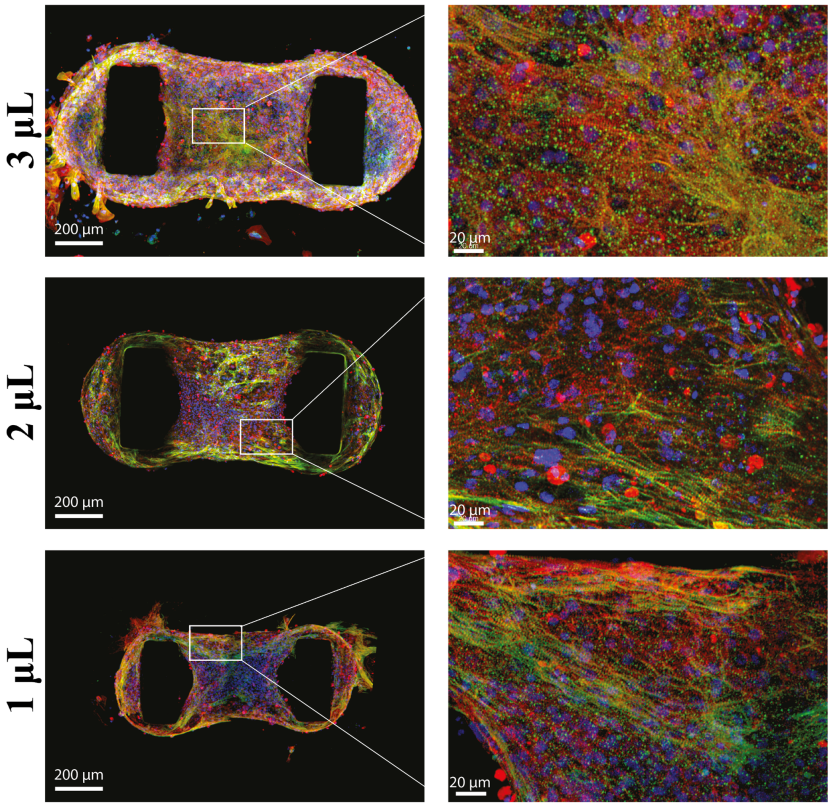

Figure 2.18: Immunostaining of the three tissue sizes for cardiac-specific markers alpha-actinin (αACT) and cardiac troponin T (cTNT). Nuclei were stained with DAPI.

During the 18 days following formation, the contractile performance of the tissues was recorded three times per week and analyzed using custom-made software for tracking the movement of the PDMS micropillars. Recordings of tissues were taken on a Nikon Eclipse Ti with a custom-built environmental chamber at 37°C and 5% CO_2 concentration and equipped with a high-speed camera (Thorlabs). For each data point, 10 seconds of footage was saved at 100 frames per second. Using image processing techniques implemented within a Python-coded custom software (ForceTracker, see Chapter 4) the position of the rectangular tip of the micropillars was tracked throughout all of the frames in recorded videos. The movement of the rectangular tips of the micropillars was measured in pixels and later converted to micrometers. Displacement of the tip of the micropillars is proportional to the tissue's contractile force, which was calculated using the stiffness of micropillars k, Eq.2.15. Using Eq.2.1, and assuming that the tissues adhered to the middle of the micropillars, the contraction force of EHTs could be obtained.

Furthermore, to test the response of the tissues to the electrical stimulation, the EHTs were paced with external platinum electrodes [31]. Voltage in the form of biphasic rect-

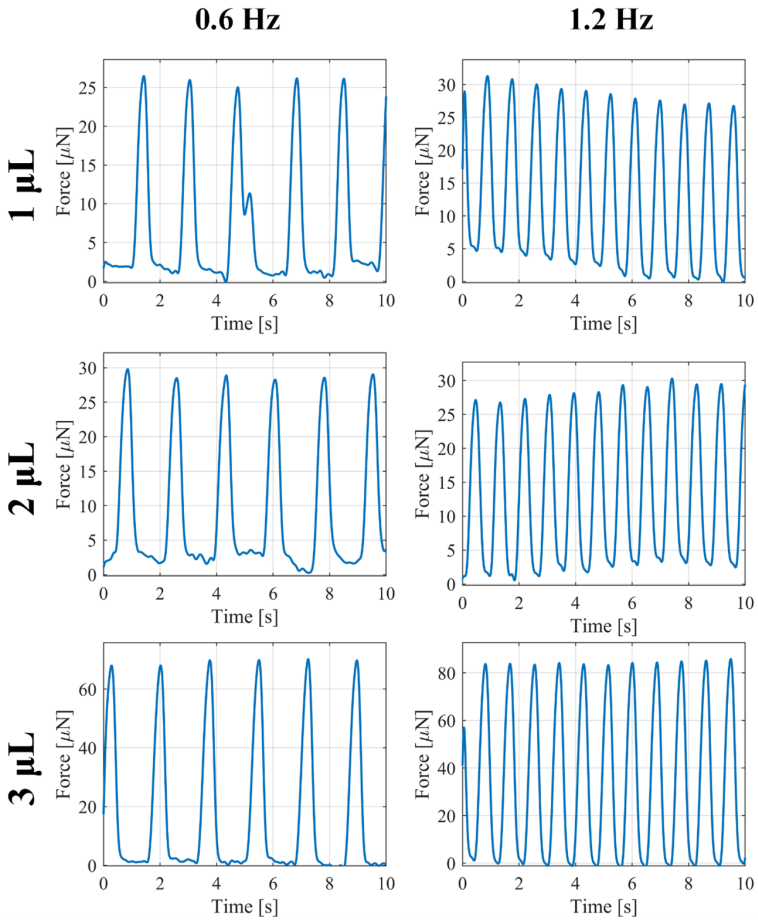

Figure 2.19: Contraction force of 1, 2 and 3 µL-derived EHTs, paced with 0.6 and 1.2 Hz, estimated using software for tracking the displacement of pillars.

angular pulses (40V peak-to-peak) was applied to the tissues, with frequencies ranging from 0.5 to 3 Hz. It was seen that all EHTs followed the pacing frequency up to 2.4 Hz. The output of the software for tracking micropillar motion in the case of pacing at 0.6 and 1.2 Hz on day 11, for all three chip sizes, is shown in Fig.2.19.

The comparison of contractile parameters for the three different chip sizes is shown in Fig.2.20. The measured force is lower than in [58] probably due to the smaller number of cells per tissue. Fig.2.20 shows the comparison for the force of contraction, contraction and relaxation duration, time to reach maximum force as well as 50%-to-50% transient time. It is possible to notice that the variability in force of contraction is large in all three chip sizes, hindering the precise comparison among different-sized tissues. The rest of the contraction parameters are very comparable in all platforms with regard to the value and graph trends. Based on the obtained results, there is no significant differ-

ence between the three chip sizes and therefore no preference from the biological point of view for a certain tissue size. It was thus shown that the downscaling of tissues resulted in the successful formation and function of tissues in all three platform sizes.

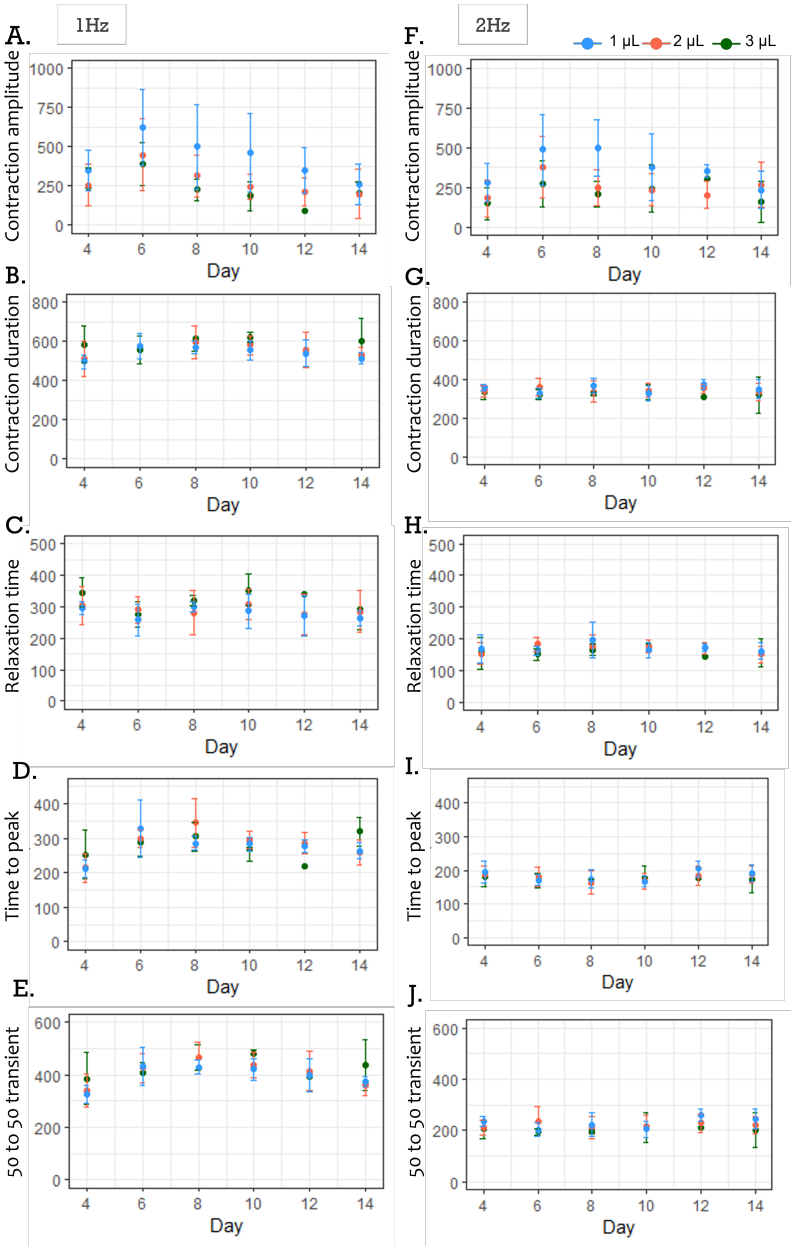

Figure 2.20: Comparison of contractile parameters for 1, 2 and 3 µL platform for culturing EHTs.

2.6. CONCLUSION AND DISCUSSION

This chapter introduced the development of the baseline platforms for EHT culture and formation. Three miniaturized and well-characterized PDMS platforms suitable for EHT formation were described. The PDMS platform for supporting cardiac tissue formation is a downscaled version of the HeartDyno system with three different microwell volume sizes: 3, 2 and 1 µL, respectively. The design of the PDMS platforms containing two pillars with rectangular cross-sections within an elliptic microwell was fabricated by combining wafer-scale silicon- and polymer-based processing. After fabrication, the PDMS chips were mechanically characterized using nanoindentation and finite element simulations, which allowed accurate measurements of the contractile force of the tissues. For cell seeding, the chips were transferred to a standard 96-well plate. Mixtures of hiPSC-CMs and hiPSC-derived cardiac fibroblast were seeded in all three chip sizes. Tissues formed successfully in all wells and were functionally active. Contractile properties of the tissues were evaluated by optically tracking the movement of PDMS pillars. The tissues were viable and functional for at least 18 days. Experiments with electrical stimulation showed that miniaturized EHTs followed the pacing frequency up to 2.4 Hz.

Through this preliminary research, we demonstrated that downscaling the existing HeartDyno system is possible and convenient. The downscaling limit in this work was set by the smallest cell medium volume that could be accurately pipetted manually (i.e., 1 µL). Since fundamental problems were not encountered while downscaling, even smaller devices might be fabricated in the future if handled by pipetting robots or other precision cell culture technologies, until reaching the microfabrication limits. By showing that PDMS platforms could be made using scalable fabrication methods, we came a step closer to high-throughput cardiac drug screening and disease modelling using OoCs.

Finally, cleanroom-based fabrication opened many possibilities for further upgrades, including the integration of electrodes and sensors for platform automation. These aspects will be covered in Chapters 5 and 6. The size that was chosen for further platform upgrade was 2 µL, as a compromise between cleanroom fabrication and ease of manual pipetting.

The main limitation of the developed PDMS platforms is that the exact position of the tissues and their thickness could not be measured during the experiments. Additionally, during N=3 experiments with the three chip sizes, another issue appeared. As seen in Fig.2.19, the variability of the force measurements is quite significant. This variability can be attributed to the variability between tissues, with respect to their composition and formation. Another origin of this variability comes from the variation in tissue position along pillar length, as it is not precisely controlled. All force calculations were carried out with the assumption that tissues are formed exactly in the middle of pillar length and remain there for the entire duration of the experiment, which was seemingly not the case. This hypothesis was confirmed later during the experiment, as tissues started sliding upwards towards the pillars' tips and finally jumped off, evidencing the change in the position in time (Fig.3.1). The new arising issue prompted a restriction to the tissue movement and precise definition of its position along pillar length. A design solution addressing this biomechanical issue is presented in the next Chapter.

CHAPTER 3

MECHANICAL ENHANCEMENT: EHT PLATFORM WITH TAPERED PILLARS

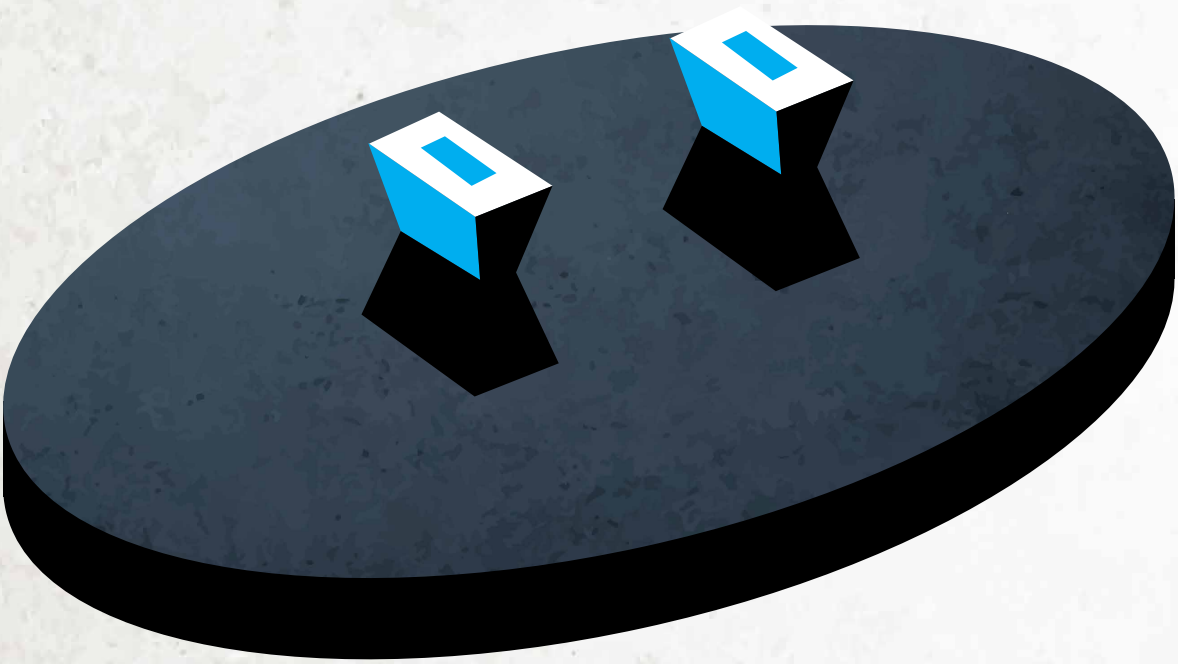

|part of this chapter have been published in *2023 IEEE 36th International Conference on Micro Electro Mechanical Systems (MEMS)*, Jan 2023, pp 374-377,|59

3.1. THE "JUMPING OFF" ISSUE

CHAPTER 2 concluded with the several issues which arose from the experiment with three different sizes of EHT platforms with straight pillars. The main drawback was the lack of tissue position control during the experiments in all three platform sizes, which had three important consequences.

First, the inaccuracy of the estimated tissue position along the length of the pillar introduced uncertainty in contractile force measurements. Initially, it was assumed that after the formation and compaction process, tissues remain positioned in the middle of pillars. However, it was shown that the initial formation position of tissues cannot be accurately predicted and it differs among different platforms and tissue samples. As demonstrated in Chapter I, knowing the exact position at which the tissue applies force is crucial for accurate contraction force calculation. Hence, the variability of the initial tissue formation position introduces uncertainty in force measurement and affects the reproducibility of the experimental conditions. A potential circumvention of this problem would be measuring the position of each tissue at the beginning of the experiment, prior to the assessment of tissue contractile parameters. Such an approach is time-consuming and not an optimal long-term solution for high-throughput experiments.

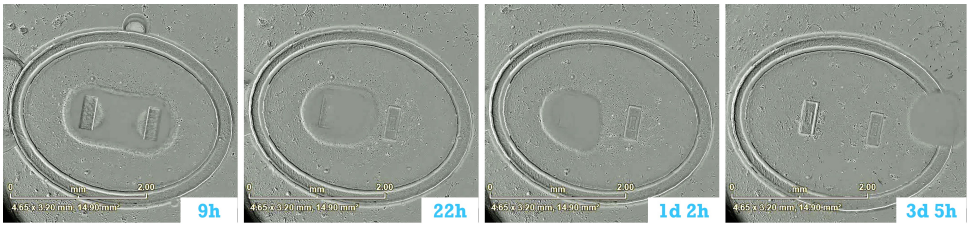

Figure 3.1: The timeline of the tissue jumping off of the straight PDMS pillars

The second problem emerging from the straight pillar design is not only the initial position variation among platforms but also the change in tissue position in time, till the later stages of the experiment. The position variation in time can be attributed to the fact that tissues increase the contractile force until day 6 (Fig.2.22). Since pillars are shaped as PDMS-based, slightly tapered cantilevers with smooth surfaces, the EHTs do not face enough mechanical resistance to remain locked in place. Instead, they tend to slide upwards, towards the tips of the pillars. The entire “jumping off” process is illustrated in Fig.3.1. Similarly to the first issue, the variability and unpredictability of tissue position affect the reproducibility of the experiments and the accuracy of force measurement. As a consequence, significant dispersion of force measurements is demonstrated in Fig.2.21. In an ideal scenario, the only variability in the tissue contractile behavior should have a biological origin, to enable accurate physiological interpretation. Therefore, any variability introduced by the design and mechanical properties of the platform itself should be minimized or completely eliminated. For this reason, it is required to obtain precisely controlled and reproducible conditions for each EHT in the experiment, to support the relevance of the statistical analysis.

Finally, as mentioned previously, the sliding of the tissues toward the tips of the pil-

lars in most cases ends in the complete removal of the tissue from the pillars. This "jumping off" decreases the yield of the experiment down to 15% of the starting amount of tissues within the first week of culture, meaning that a very small percentage of the EHTs reaches the end of the experiment (typically 14 days). This is a limiting factor for long-term drug effect studies and disease modeling.

Mentioned issues are related mostly to straight pillar EHT platforms with upward tissue culture. There are examples of EHT platforms where tissues form upside-down, at the bottom of circular anchors. In this case, pillars have a flange at the tip to localize the tissue and avoid its removal [35, 46]. Other examples involve platforms with wider shapes at the top of the straight pillars to restrict the tissue movement [34]. However, a more general solution that can be applied to all the cases was looked for and identified, still inspired by the bio-mechanical analysis of the issue.

3.2. DESIGN UPGRADE: TAPERED PILLARS

3.2.1. MECHANICAL CONFINEMENT OF THE TISSUES

To address the problem we encountered with the straight geometry of pillars, we considered a design that is more suitable for providing mechanical resistance to tissue movement while confining the tissue in a predefined position. Three designs of pillar cross-section were proposed to tackle the mentioned problem [19, 61]. The advantages and drawbacks of each of them are discussed below.

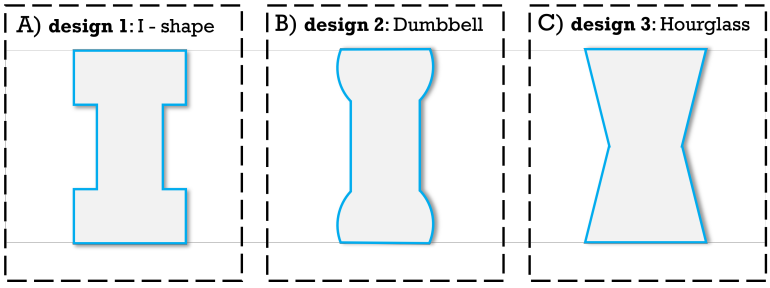

Figure 3.2: Proposed pillar designs for mechanical confinement of the tissues.

The first I-shape design (Fig.3.2A) features a step-wise transition from the narrow to the wide area of the pillar. It provides the most efficient spatial confinement with the highest mechanical resistance to tissue movement outside of the narrow region. However, in this design tissue thickness should be predetermined to fit exactly the indented area. Otherwise, for thinner tissues, the adherence position would still vary within the narrow region. As the exact control of tissue thickness is challenging, this design would still result in a certain level of tissue position uncertainty, therefore it does not represent the optimal design solution. In addition, from the microfabrication aspect, this design is very challenging for moulding, as the sharp transition between wide and narrow regions creates a lot of stress during PDMS de-moulding and is a potential breaking point of the structures. Alternative manufacturing techniques (e.g. 3D printing) might be a better choice if such a pillar design was selected.

The second design (Fig.3.2B) has a rounded dumbbell shape, which makes the moulding of PDMS less challenging than in the previous case, while still providing a good mechanical resistance for the tissue movement. However, the clear separation between narrow and wide areas imposes limitations regarding tissue thickness, similar to the previous design.

Finally, the third design has walls inclined towards the middle of the pillars forming an hourglass-like profile. The confinement accuracy of such a design does not depend on tissue thickness. The tissue would ideally be confined in the central indentation, at the narrow part of the pillar, while experiencing enough mechanical resistance to prevent climbing upwards. In addition, due to the gradual change in pillar width and thickness, the hourglass design is the least challenging for PDMS release. Therefore, this is the design that was chosen for implementation.

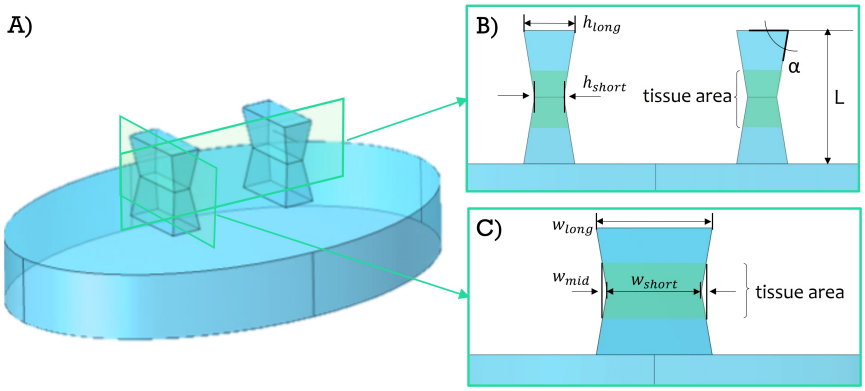

Figure 3.3: Dimensions of tapered pillars: A) 3D representation of tapered pillars geometry on a PDMS substrate; B) cross-section of pillars in y-z plane; C) cross-section of pillars in x-z plane.

3.2.2. DIMENSIONS OF PILLARS

Prior to the fabrication of the selected tapered pillar geometry (Fig.3.2 C: design 3), there are several design constraints to consider to determine the pillar dimensions. Fig.3.3 shows all the relevant dimensions of tapered pillars that need to be defined. Here w_{long} and h_{long} are width and thickness at the lowest and highest position along the length of the pillar, while w_{short} and h_{short} correspond to the dimensions of the narrowest part of the pillar. Since the assumption is that the tissue forms in the middle of the pillar, in the indentation, w_{mid} represents the hypothetical tissue thickness and its adhering region (Fig.3.3 B,C). The thickness of the tissue is supposed to be approximately $L/2$, where L is the pillar length. The tapering angle α is defined as the angle between the pillar's sidewalls and the top plane, assuming perfect symmetry with respect to the center of the pillar.

The pillar dimensions are related as follows:

$$\tan(\alpha) = \frac{L}{(w_{long} - w_{short})} \tag{3.1}$$

$$\frac{(w_{long} - w_{short})}{(w_{mid} - w_{short})} = \frac{L/2}{L/4} = 2 \tag{3.2}$$

Combining equations 3.1 and 3.2 we can express w_{long} and w_{short} as functions of the tapering angle α, thickness of the tissue w_{mid} and pillars length L.

$$w_{short} = w_{mid} - \frac{L}{2\tan(\alpha)} \tag{3.3}$$

$$w_{long} = w_{short} + \frac{L}{\tan(\alpha)} \tag{3.4}$$

$$h_{short} = h_{long} - \frac{L}{\tan(\alpha)} \tag{3.5}$$

3.2.3. DESIGN REQUIREMENTS

As stated in the previous Chapter, from the three different platform sizes the 2 µL one was chosen to be used for further experiments and the platform upgrades. This decision was made as a compromise between downscaling of the tissue size and compatibility with the microfabrication on one side, and the controllability and reproducibility of manual pipetting on the other. The change in the pillar design should not alter the tissue formation and functionality from the previously performed experiments. Therefore, the first requirement is that the stiffness of the tapered pillars should remain similar to that of the 2 µL design. Additionally, tissue formation and final shape should not be affected by the new pillar design, imposing restrictions on the values for $w_{mid} \approx 423$ µm.

The microfabrication imposes yet another set of constraints for the new pillar design. First, due to the fabrication of desired pillar profile, its length is limited by the thickness of the silicon wafer. As the standard wafer thicknesses are predefined (in this case 500 µm as it is the closest value to that of the previous 2 µL design), the new length of tapered pillars is set to be 500 µm. A second challenge rises from the fact that the etching profile of the pillars is rectangular. The uniformity of isotropic etching is highest for circular structures [61], therefore, the difference in etching along x and y directions, as defined in Fig.3.3, and consequently in the tapering angle, has to be found prior to deciding the dimensions of the final structures. Finally, the tapering angle of the pillars should be the right compromise between a high value, which achieves tissue confinement, and a small value, which allows reliable PDMS de-moulding.

Based on these requirements, two tapering angles were proposed for testing the confinement efficiency of the new pillar design: 75° and 80°. Similarly to the previous design with straight pillars, there needs to be an elliptic well surrounding the pillars and containing the cell volume. In the case of tapered pillars, also the surrounding well will have a tapered profile. This needs to be taken into account when deciding on the well dimensions to make sure it can fit 2 µL volume.

3.3. MICROFABRICATION OF TAPERED PILLARS

3.3.1. TAPERED ETCHING PROFILE

ETCHING STRATEGY

The strategy for wafer-level microfabrication of tapered pillars with the desired wall inclination is to use a combination of anisotropic and isotropic deep reactive ion etching (DRIE) of the silicon substrate used as mould [62]. As explained in Chapter II, anisotropic DRIE is performed using the Bosch process for etching straight holes into a Silicon wafer. The process consists of three steps: polymer deposition, break-through and etch step, where the dominant etching is performed in the third etch step using SF_6 plasma [56]. These three steps compose a single cycle of a Bosch process. The number of cycles determines the final etching depth. Isotropic reactive ion etching is achieved using only the third step of the Bosch process. During the Bosch process, polymer deposition prevents the isotropic nature of etching and preserves the steep profile of the walls. However, if there is no polymer deposition, SF_6 plasma will uniformly etch the silicon wafer in all directions, creating a rounded etching profile.

By tuning the number of Bosch cycles and duration of the iso(tropic) etch process and alternating them, it is possible to achieve a staircase-like etching profile with a precisely defined side angle [63, 64]. The etching principle used for the fabrication of tapered pillars is illustrated in Fig.3.4.

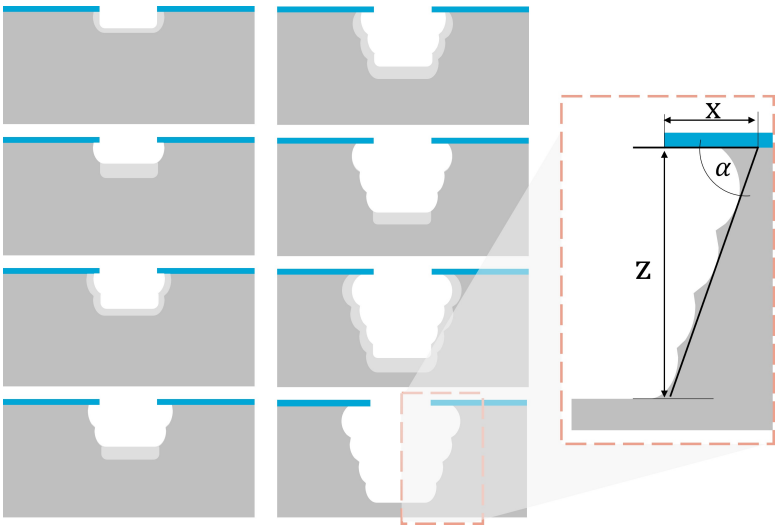

Figure 3.4: Illustration of the etching process by alternating isotropic and anisotropic RIE.

Fine-tuning and precise control of the tapering angle are possible by knowing the etch rates of both isotropic and anisotropic processes. This angle (α) can be calculated from Fig.3.4 in the following manner:

$$\tan(\alpha) = \frac{Z}{X} \tag{3.6}$$

Here X and Z are defined by the etching time and rates in the lateral and vertical directions, respectively:

$$X = (t_{iso} - t_{C_4F_8}) r_{iso}^{\rightarrow}(z) \tag{3.7}$$

$$Z = c_B r_B(z) + t_{iso} r_{iso}^{\downarrow}(z) \tag{3.8}$$

So that:

$$\tan(\alpha) = \frac{c_B r_B(z) + t_{iso} r_{iso}^{\downarrow}(z)}{(t_{iso} - t_{C_4F_8}) r_{iso}^{\rightarrow}(z)} \tag{3.9}$$

Here c_B is the total number of Bosch cycles, t_{iso} is the duration of isotropic etch and $t_{C_4F_8}$ is the time required to remove the residue of C_4F_8 layer from the walls after the Bosch process. Vertical etch rate of the Bosch process, as well as vertical and lateral isotropic etch rates are defined as r_B, $r_{iso}^{\downarrow}$ and $r_{iso}^{\rightarrow}$, respectively. All etch rates are functions of the etching depth, geometry and surface density of the openings and the process temperature [65, 66]. Mentioned effects must be taken into account when defining the number of Bosch cycles and iso etch time in each iteration of the final etching process.

The final process parameters were defined based on several conducted etching tests. Three approaches have been taken to find the best compromise between the etching duration and the number of Bosch-iso etch alternations. The first two examples varied the number of Bosch-iso alternations to reach the final depth (8 and 5 steps, respectively), while the third approach used a Pseudo-KOH recipe in the last step to create a more prominent tapering effect. This recipe mimics the effect of KOH wet etching of silicon which results in an angle of 54.7°, defined by the fixed angle between < 111 > and < 100 > crystal planes of Si. Fig.3.5 shows different etching profiles obtained from the three mentioned approaches.

The first approach (Fig.3.5A) resulted in cavities with straight profile ($\alpha = 90°$) and with prominent scallops on the walls in a staircase-like form in 8 steps. The second approach, with the reduced number of steps from 8 to 5, provided good control of the

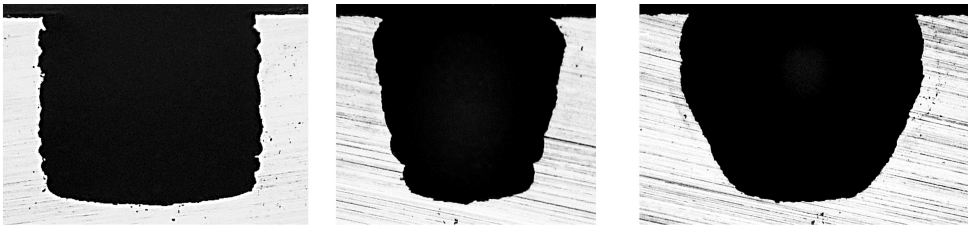

Figure 3.5: Etching profiles of silicon wafer obtained using three different approaches: A) by alternating Bosch and iso etching in 8 steps, B) by alternating Bosch and iso etching in 5 steps, C) by mimicking in dry form the wet etching of silicon with KOH (pseudo-KOH).

tapering angle with a more smooth etching profile. The difference between 8- and 5-step etching is in the duration of the iso etch step. In the first case, with more steps and shorter etching time, the iso etch time becomes insufficient to remove the polymer residues from the walls after the Bosch step and to efficiently broaden the cavities uniformly in all directions. Hence, the profile remains mostly straight. Finally, the third approach with the KOH recipe resulted in very smooth walls, with negligible scallops, but with a minimal angle of 25°, which is still much higher than the desired tapering angles.

As the second approach was chosen for the final process, all the relevant etching parameters were tested and adjusted based on Eq.3.9 to achieve the tapering angles of 80° and 75°.

ETCH RATES

As stated previously with Eq.3.9, etch rates for both isotropic and Bosch etching depend on the etching depth. Therefore, the change of etch rates with depth was obtained from the initial tests and used for further calculations of the final tapering angles. It was found that the etch rate of the Bosch process is very stable and less sensitive to changes in temperature or etching geometry than the isotropic etch rates. On the contrary, the isotropic etch rate declines faster with the increase in depth of the etched cavity. This difference in isotropic etch rate is expected since there is a bigger surface area of silicon exposed to the plasma within deeper cavities. Unlike the Bosch process, where the walls are protected with polymer and dominant etching is directed towards the bottom of the cavity, during iso etching, the interaction between gas and silicon atoms is happening in all directions. Still, there is a significant difference in lateral and vertical isotropic etch rates

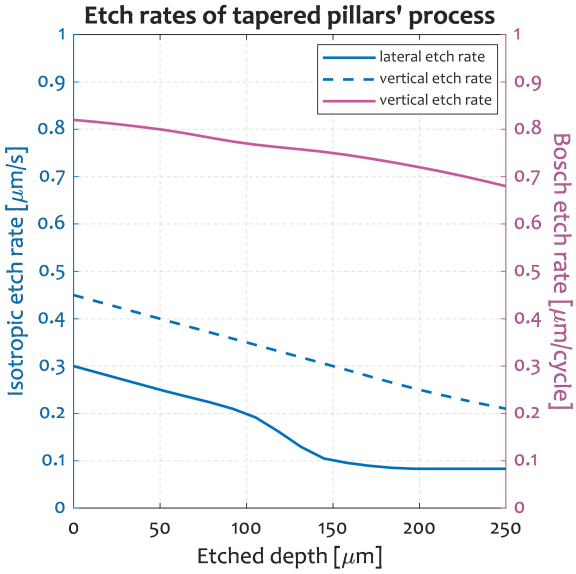

Figure 3.6: The relationship between different etch rates and the etched depth.

since plasma is predominantly biased towards the Si substrate. Fig.3.6 shows measured etch rates of Bosch vertical etching, as well as both lateral and vertical isotropic etching. The graph shown in Fig.3.6 was obtained by interpolating individual measurements from 6 different etching depths. Each value was obtained based on $N > 3$ measurements and the average value was taken for the final interpolation.

3.3.2. PROCESS FLOW

Tapered pillars were made using a combination of standard microfabrication techniques and polymer processing, similar to the fabrication of straight pillars. The end goal was to create cavities in Si wafer as a mould for tapered pillars made of PDMS. The main steps of the described process flow are illustrated in Fig.3.7. The double-side polished, 500 µm-thick Si wafer was etched symmetrically from each side, assuring that the tapering of both sides meets in the middle of the wafer. The first step of the fabrication was the definition of a hard mask for DRIE (Fig.3.7 A). Similarly to the previous process, this mask consists of a 50 nm-thick layer of thermally-grown SiO_2 and 5 µm-thick PECVD oxide. Thin thermal oxide enables a better definition of the etching profile and accurate mask geometry transfer onto the cavities in the wafer, as it is a higher quality layer than PECVD SiO_2. The oxide layer was then patterned using standard photolithography steps: coating, exposure, and development, followed by dry etching of SiO_2. The same process was repeated on each side of the wafer. The oxide layer was patterned in two steps creating a two-level hard mask (Fig.3.8). The first mask is the starting etching mask of narrow

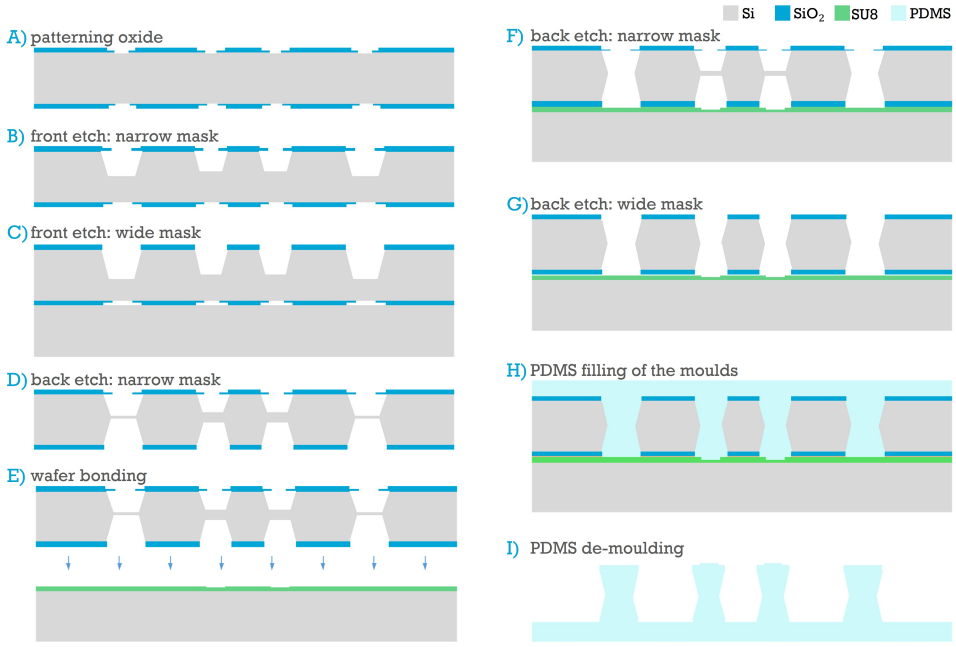

Figure 3.7: Flow of the tapered pillar fabrication process.

rectangular windows which define the middle part of the pillars. The second mask defines the widest parts of the pillars, top and bottom rectangular cross-section, and it is used to finalize etching and compensate for the bowing effect (see Section 3.3.3). After the definition of the hard mask, staircase-like deep reactive ion etching follows.

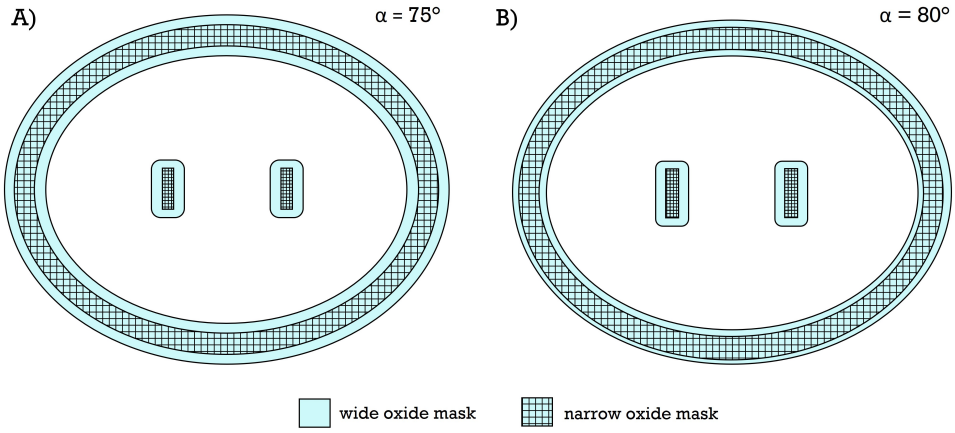

Figure 3.8: Photolithography masks design for the two-step oxide mask patterning, for A) 75 ° and B) 80 ° tapered pillars.

FRONTSIDE

First, the front side of the wafer was etched by alternating the Bosch process and Isotropic etching, until reaching 240 µm depth (Fig.3.7B). In the last 20 µm of the front-side etch, the narrow mask is removed by wet etching of SiO_2 in buffered HF. For this thin oxide removal, the backside needs to be protected with photoresist to make sure that the SiO_2 is not affected. The wet etching should be timed precisely so that only the thin oxide of a narrow mask is removed completely, leaving the second oxide mask unaffected. The front side etching was then finalized by transferring the process wafer to a Si carrier wafer and etching until the middle (250 µm) (Fig.3.7C). The transfer to a carrier wafer is necessary for this step to mimic the same etching conditions in both front and backside processing, as the carrier wafer is required at the end of the backside etching as well. Only in this way, the final shape symmetry can be obtained. The front side etching ended with reaching slightly more than the middle of the wafer (≈ 260 µm) in the center of the cavities, due to the rounded bottom profile. After completing the front side etching, the wafer was removed from the carrier wafer, cleaned in O_2 plasma to remove the polymer residues from the sidewalls deposited during the Bosch process, and in HNO_3 to remove organic as well as metal particles. Table 3.1 shows the etching strategy for both tapered designs for the front side etching. A similar process applies to the backside since the cavities should be symmetric.

BACKSIDE

The backside wafer etching proceeded in the same way as the front side, with alternating Bosch and iso processes (Fig.3.7D). However, etching finalization requires support

Table 3.1: Etching parameters for the tapered pillar fabrication process.

	Tapering angle 80°			Tapering angle 75°		
Number of steps	Bosch cycles	Iso etch [s]	Depth [um]	Bosch [cycles]	Iso etch [s]	Depth [um]
1	35	50	50	18	60	45
2	35	50	100	18	60	90
3	40	65	150	20	80	135
4	40	80	200	20	100	180
5	40	20	240	23	120	220
6	/	/	/	20	20	240

for the etch-through cavities in the wafer by closing them from one side. For this reason, the process wafer needs to be tightly bonded to a support wafer, prior to completely opening the elliptic walls around the pillars. The wafer bonding was performed with a direct wafer bonding technique using an adhesive polymer as an intermediate layer in between the two silicon wafers (Fig.3.7E). In this case, SU8 – an epoxy-based negative resist - was used as the bonding adhesive, because of its good mechanical properties and cross-linking efficiency [67, 68]. A thin layer of SU8 was spin-coated and soft-baked on a support Si wafer. Prior to SU8 coating, 20 µm-deep rectangular shapes were etched into the support wafer to be transferred later as focus features on top of the moulded pillars. Fine alignment of two non-transparent Si wafers was achieved using the IR camera of the wafer bonder EVG500. The bonding was performed by applying 2.5 kN force on the wafers, which enabled the wetting of the Si surface by the SU8 layer. In this configuration, the final cross-linking and hard baking step of SU8 were performed at 120°C, to ensure strong and reliable wafer bonding. The bonding uniformity was quantified with Newton rings, as shown in Fig.3.9.

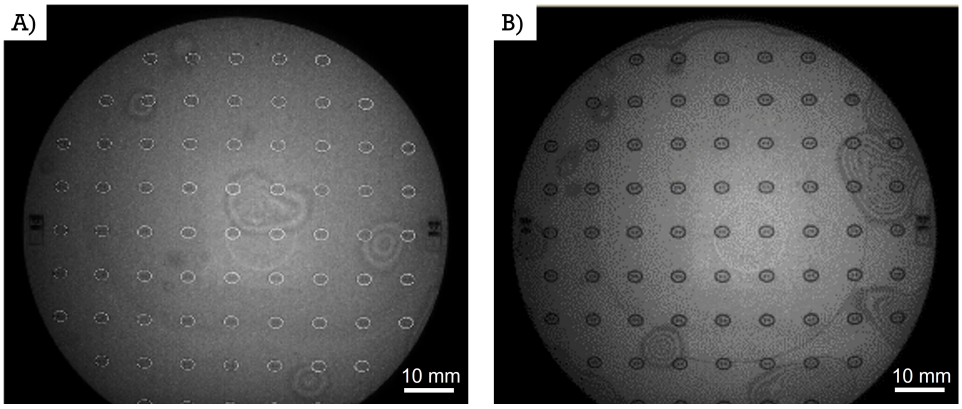

Figure 3.9: Newton rings demonstrating the efficiency of direct wafer bonding for A) 80° and B) 75° tapered pillars.

After wafer bonding, the etching was completed from the backside in the same way as the front. Before connecting the cavities from both sides of the wafer, the narrow oxide mask is removed once again, and the wide rectangles were used to obtain the final tapered profile of pillars (Fig.3.7F, G). In the end, cleaning in oxygen plasma is performed to remove C_4F_8 residues from the cavities in Si.

PDMS

The final step of the fabrication is PDMS moulding (Fig.3.7H). Prior to polymer spin-coating, the wafer surface was made hydrophobic by covering it with a self-assembled monolayer of (perfluoro)silane from the vapour phase. PDMS mixed with the curing agent in a 10:1 ratio was spin-coated for 30 s at 400 rpms on top of the silicon mould. PDMS was then degassed for at least 20 minutes within a vacuum chamber, to ensure the release of the trapped air bubbles and complete penetration of PDMS into the tapered structures. PDMS was cured at 90° C for 1h. Finally, the PDMS structures were released from the silicon mould with the assistance of the capillary force effect of isopropyl alcohol (IPA) (Fig.3.7I).

3.3.3. CRITICAL FABRICATION STEPS

There are several steps of the process flow very critical for the fabrication success. They are discussed in more detail below.

1. Bowing effect

The first challenge encountered during the fabrication process is the step after removing the first SiO_2 mask of narrow windows to finalize the etching process and define the top and bottom shape of pillars. The second mask used in this case contains wide rectangular windows, as illustrated in Fig.3.8. During the staircase-like etching process, the isotropic etch gives a rounded profile of the cavities, resulting in a significant under-etched part below the oxide mask. This etched region underneath the first oxide layer has a rounded profile, as shown in Fig.3.10A, and it is called the bowing effect [69]. The formed curvature in Si, below the first oxide mask, is beneficial in this case, as it will define the slope of the final tapered structures. However, the Si residue between the widest part of the cavity and the second oxide mask needs to be removed (shown in light

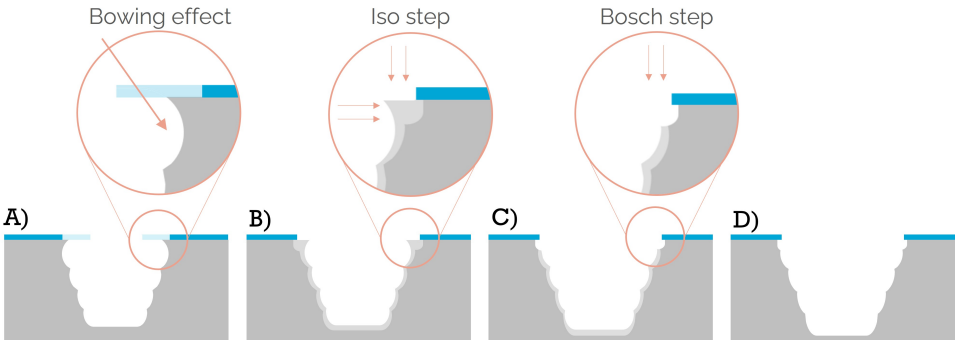

Figure 3.10: Illustration of the bowing effect during etching finalization.

gray in Fig.3.10B). For this reason, a second oxide mask is needed to expose this Si part to plasma etching and to fine-tune the final slopes of tapered pillars. The etching after the first oxide mask removal starts with an isotropic step (Fig.3.10 B). This etching step will consume most of the Si residue, with a very small undercut below the second oxide mask. In this way, the top and bottom shapes of the final structures are well-defined with the second oxide mask. The iso etching step is followed by a Bosch process (Fig.3.10 C), to smoothen out the sidewall underneath the second oxide mask and to fine-tune the tapering angle. Additionally, the final Bosch step enables the merging of the cavities at 250 µm depth. In case the reverse approach was applied, first Bosch and then Iso etch, the Bosch process would remove all the leftover Si below the first oxide mask and elongate the etched profile, reducing the tapering angle. Iso etch would then compensate for the angle reduction, but the bowing effect would be prominent in this case, creating again significant undercut below the second oxide mask and affecting the final shape of tapered cavities.

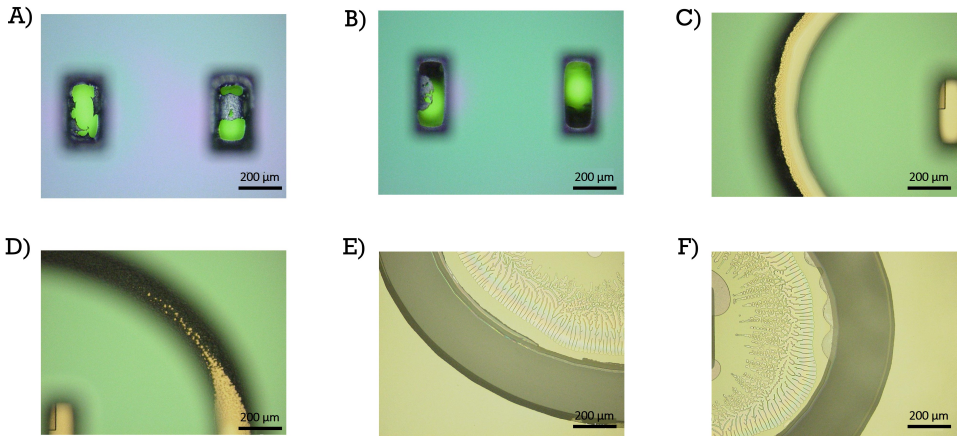

Figure 3.11: Examples of polyimide bonding issues.

2. Wafer bonding

The second critical step worth mentioning is the bonding of the process wafer to the support wafer to provide the enclosure of pillars and wells from one side. Similar to the straight pillar design, a rectangular focus feature was imprinted on the top of the final PDMS tapered pillars (Fig.3.710). To achieve this patterning, small rectangles were etched into the supporting Si wafer in correspondence with the tapered cavities. This step imposes an additional challenge for the wafer alignment during bonding.

Polyimide bonding

To overcome the alignment challenge, the first approach was to bond a transparent wafer with focusing features to the process wafer using uncured polyimide as the bonding adhesive. The alignment was performed optically with a specially designed mechanical wafer aligner. Aligned wafers were cured at 90° C, under the bonding pressure. This approach showed several drawbacks :

- First, the uncured polyimide under pressure was pushed into the opened holes on random spots across the wafer. The polyimide that reached the middle of the cavity from the backside of the wafer interfered later with the final etching of the Si to merge cavities from both sides. (See Fig.3.11A, B)
- Second, PI that covered the supporting wafer was consumed during the last steps of DRIE, in the exposed areas of pillars and wells. The uneven PI residues were visible on the bottom of the opened structures, especially walls in Fig.3.11 C, D. Removal of these residues is possible with CF_4 plasma. However, this plasma treatment also affects the cured polyimide layer that bonds two wafers, resulting in wafer detachment if exposure to plasma is too long. Therefore, a compromise was found between the cleaning of the exposed parts of the bottom wafer and affecting the PI bond.
- Finally, the applied pressure during wafer bonding and curing was controlled manually, which had a negative influence on bonding uniformity (Fig.3.11 E, F). As a result, several Si islands with holes detached completely from the supporting wafer, decreasing the fabrication yield.

Direct wafer bonding

Direct wafer bonding was explored only as the second approach due to the alignment and contamination issues originating from the available tool in the cleanroom. Nevertheless, with the soft baked SU8 as an adhesive layer, two Si wafers were bonded together, after 16h of the bonding process at 120° C temperature and 2.5 kN applied force. The problem of polymer penetration into the pillar area was solved completely since the used SU8 was already soft-baked. Also, the bottom of the opened pillars and wells were completely free of residues, as shown in Fig.3.12. Additionally, the good bonding uniformity resulted in increased fabrication yield to 100% for both 80° and 75° pillars.

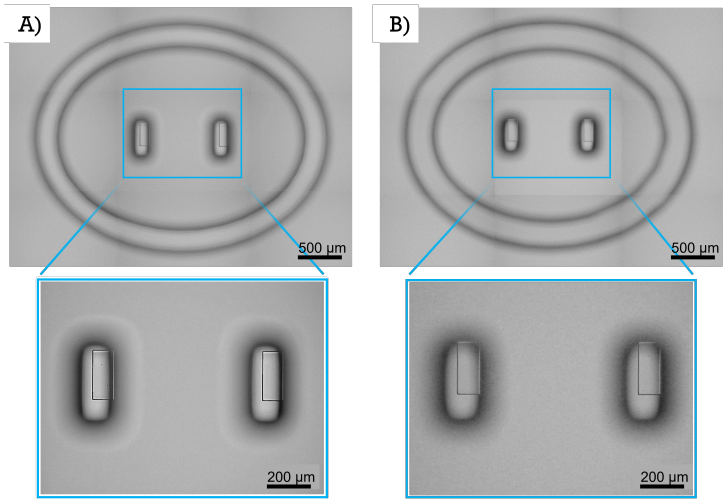

Figure 3.12: Examples of the bottom of the structures in Si wafers at the end of the fabrication process, after using direct wafer bonding with SU8 for A) 80° and B) 75° tapered pillars.

3.3.4. CRITICAL PROCESS PARAMETERS

Several fabrication parameters influenced the process optimization and determined the final design of the tapered pillars. The most relevant among them will be mentioned in more detail.

1. Etch rate dependency on geometry

An important aspect of the fabrication process is the effect of the mask geometry on the etching profile. This effect was already known and taken into consideration during the design process, however, it could have been quantified only during the process development.

During isotropic etch the efficiency and uniformity of gas interaction with the Si atoms is the highest for circular geometries, while it decreases for sharp edges and narrow trenches [65]. This effect was noticed in the case of isotropic etching with a rectangular oxide mask. The final difference in lateral isotropic etching along x and y direction, as defined in Fig.3.3, was found to be $\approx 10\,\mu m$ by the end of the process. As a consequence, the final tapering angle was different on each side of the pillars.

Not only does the etching depend on the geometry of the hard mask, but the feature size also influences the etching efficiency. For this reason, besides the difference in lateral isotropic etching, there is a significant difference in both anisotropic (Bosch) and isotropic vertical etching between pillars and the elliptic well. The etching area in the case of the well is much larger than the pillar area, which allows more interaction of the SF_6 plasma with the exposed Si atoms. Due to this effect, elliptic wells were etched faster than the pillars, resulting in a 50 µm depth difference when reaching the middle

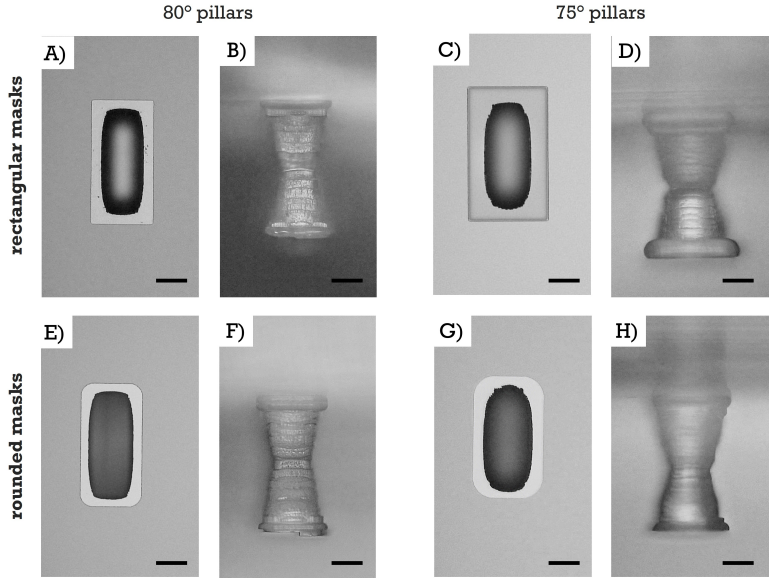

Figure 3.13: Comparison between rectangular and rounded masks used for etching finalization for both versions of tapered pillars. Scale bar 100 µm.

of the wafer. For this reason, the support wafer had to be included in the process very soon after the beginning of the backside etching, to avoid well opening and detachment of the islands with pillars before the end of the process.

The etch rate was also slightly affected by the different etching conditions in the front and the backside of the wafer. During the backside etching, the cooling was less efficient, due to the air present in the holes of the previously etched pillars. This effect increased the isotropic etch rate by 16 ± 3 % while the Bosch process remained stable.

2. Wide mask geometry

The initial design assumed perfectly rectangular cross-sections both in the middle and the top and bottom of the pillars, and the masks for oxide layers were designed accordingly. However, due to the nature of the isotropic etching process - more precisely, the bowing effect and the non-uniformity of the etching along x and y directions - the mask design had to be modified. At the end of the first etching part using narrow rectangular windows as the oxide mask, the top view of the formed cavity in Si was closer to an ellipse than a rectangle (Fig.3.13A, C). The second etch with the initial oxide mask resulted in the addition of wide rectangular shapes at the top and the bottom of the pillars, which disrupted the tapered geometry and affected the removal of the final PDMS structures (Fig.3.13B, D). To circumvent this issue, the final mask for the second part of the etching included rectangular windows with rounded corners to match better the shape of obtained cavities (Fig.3.13E-H). This approach increased the yield of the fabrication to 100%.

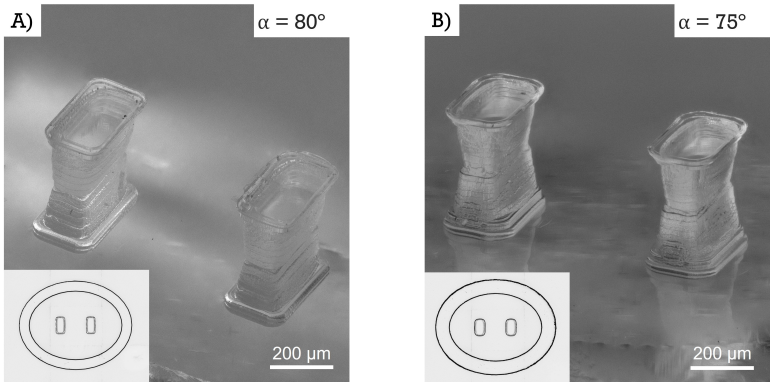

Figure 3.14: Optical inspection of the PDMS structures of both A) 80° and B)75° tapered pillars.

3.3.5. ANGLE MEASUREMENT

After PDMS moulding, the released tapered pillars were optically characterized to inspect the final dimensions and geometry. The Keyence laser profilometer with the movable microscope was used for imaging tapered pillars at 60° view angle. The images of both designs are shown in Fig.3.14.

In addition, scanning electron microscopy (SEM) was used to closely inspect the surface properties of the holes etched into the Si wafer. Fig.3.15A shows the cross-section of the diced Si wafer with both visible pillars of 75° tapering angle, while Fig.3.15B shows

a close-up image of the top half of the etch cavity with clearly visible roughness and the staircase-like structures on the wall.

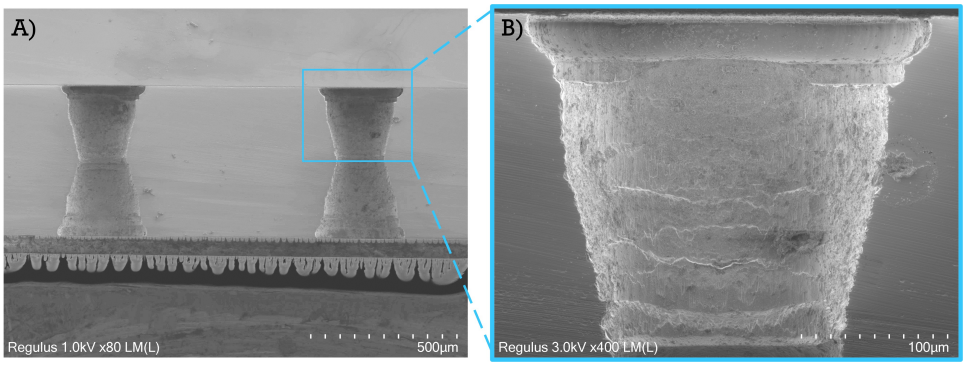

Figure 3.15: SEM imaging of the 75° tapered holes etched into Si wafer.

Due to the previously mentioned difference in lateral isotropic etch rate in x and y directions, it was expected that the final tapering angles would differ in both directions. This was confirmed by final inspection and measurements of both PDMS structures and cross-section of Si moulds. Obtained dimensions and accurate tapering angles were further implemented in numerical model simulations for the characterization of pillars' mechanical properties. (see next Section) The dimensions of the final masks and fabricated PDMS structures are given in Table 3.2.

The large difference in dimensions of the masks and final structures originates from the final etching steps. The isotropic etch is making the middle part of the pillars wider, as well as introducing additional undercut in the top and bottom parts. For this reason, the patterns of the masks were designed much smaller than expected structures to take into account all the overetching.

Table 3.2: Designed and final dimensions of tapered pillars.

	Tapering angle 80°		**Tapering angle** 75°	
	mask design	*PDMS structures*	*mask design*	*PDMS structures*
α_x	80°	78°	75°	75°
α_y	80°	82°	75°	78°
$w_{long}[um]$	446	471	406	447
$h_{long}[um]$	222	252	234	280
$w_{short}[um]$	345	383	290	367
$h_{short}[um]$	100	142	70	157

3.4. MECHANICAL PROPERTIES OF TAPERED PILLARS

Prior to designing the masks for fabrication and determining the final dimensions of pillars, a numerical model was created using Comsol Multiphysics to perform the analysis of the mechanical properties of the tapered pillar design. Further design upgrade followed, after determining fabrication parameters and final dimensions of pillars. This version was used for the comparison of mechanical characterization to numerical analysis.

3.4.1. FINITE-ELEMENT MODEL OF TAPERED PILLARS

The initial design of the tapered pillars and all the dimensions used during microfabrication were taken from numerical modelling of the pillars' mechanical properties. Numerical analysis was performed using the finite-element method (FEM) in Comsol Multiphysics. Similar to the analysis of straight pillars, FEM was used to simulate pillar deformation upon the force acting at the pillar's side, mimicking the contraction of suspended tissues. In the case of tapered pillar design, 3D geometry was first created in SolidWorks, a 3D modelling software, and then imported into Comsol as a Parasolid file. SolidWorks was especially useful for creating complex geometry with rounded pillar edges in the final design. The second model included all the effects obtained after microfabrication and therefore was the most accurate representation of the final PDMS structures.

Initially, the pillars were designed with rectangular cross-sections along the z axis. The desired stiffness was obtained by tuning the h_{short} and the mask dimensions were extracted from this model following Eqs. (3.1-3.5). The 3D geometry of the pillar model is shown in Fig.3.16A.

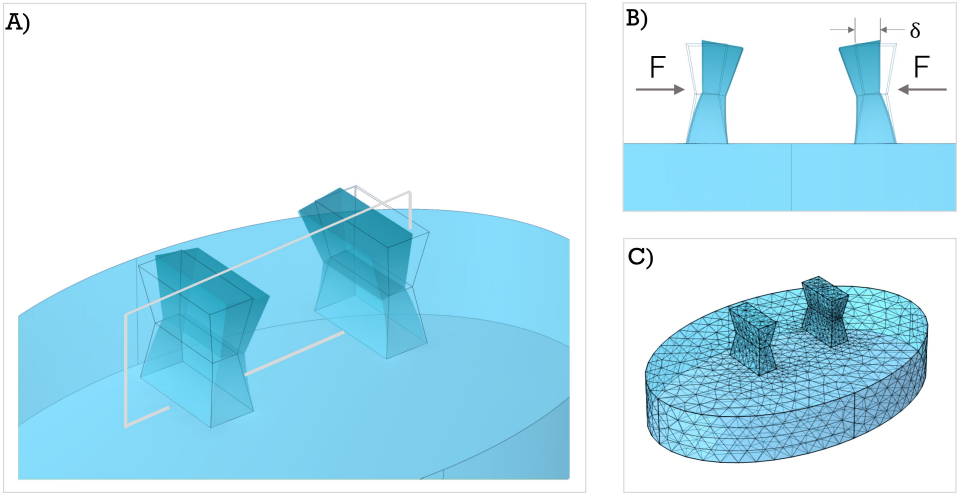

Figure 3.16: The initial design of tapered pillar geometry implemented in Comsol Multiphysics: A) 3D geometry of pillars on the soft substrate; B) deformation of pillars upon force application on the sides; C) geometry meshing to define computation points.

Using the physics of the Solid Mechanics module in Comsol, a uniform load was applied to the 50x50 μm^2 rectangular area on the wide side of the pillars. The load was applied along the x direction, on different positions along the z axis (Fig.3.16B). The load distribution on the rectangular surface was used to mimic the nanoindentation setup, which was used later to confirm the mechanical properties of the pillars. The material for the pillars and substrate below was defined as *Linear Elastic Material*. The viscoelasticity of PDMS was neglected, as the displacement of pillars and the material deformation was very small, and therefore still in the linear region. Young's modulus of PDMS was assumed to be 1.2 MPa, which is in accordance with the previous measurements performed in our group. However, E_y was later precisely calculated during mechanical characterization. The next step of the model building was the definition of the points for which the set of differential equations in matrix form would be solved. These points are defined by each node of extra fine tetrahedral mesh with the refined connection between pillars and substrate area (Fig.3.16C). The momentum balance equation [70, 71] in the form:

$$\rho_0 \frac{\mathrm{d}^2\mathbf{u}}{\mathrm{d}t^2} = \mathbf{F}_V + \nabla[(\mathbf{I} + \nabla\mathbf{u})\mathbf{S}] \tag{3.10}$$

in a stationary study $\frac{\mathrm{d}^2\mathbf{u}}{\mathrm{d}t^2} = 0$ was used to converge the matrix solution towards the values of displacement components u,v,w. Here, the term $\mathbf{F}_V$ represents volume forces acting on the undeformed material, while the second term represents the divergence of the first Piola-Kirchoff stress tensor, relating forces acting in the spatial directions to areas in the undeformed configuration [51]. The flow of the FEM study is illustrated in Fig. 3.17.

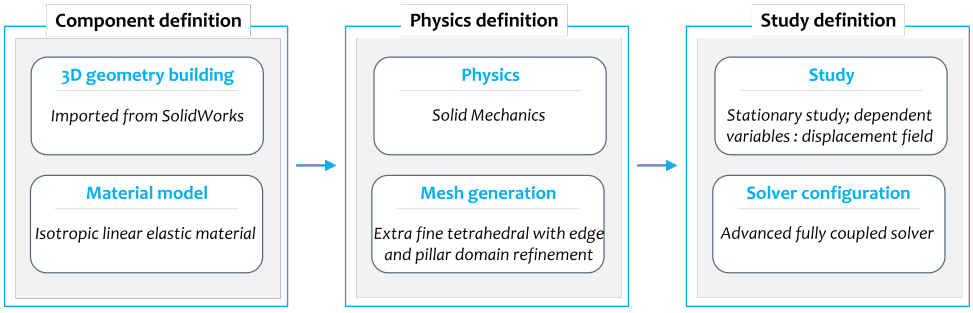

Figure 3.17: Computational flow of FEM study of tapered pillar deformation implemented in Comsol.

Boundary load of F = 20 μN was applied on the defined rectangular areas along the pillars' length. The resulting deformation of pillars is shown in Fig.3.16B. This deformation (δ) was estimated from the computation output and the effective stiffness of pillars (k) was determined based on the equation:

$$F = k \cdot \delta \tag{3.11}$$

Geometry dimensions from these simulations were used for the initial mask definition. However, after the fabrication of tapered pillars, the design from Comsol was updated according to the fabrication constraints and finally obtained dimensions. The

more realistic, new geometry was further used to estimate the stiffness of pillars and to compare it with nanoindentation measurements. Final pillar geometry, and the resulting pillars' displacement, as well as the meshing of the geometry, are illustrated in Fig.3.18.

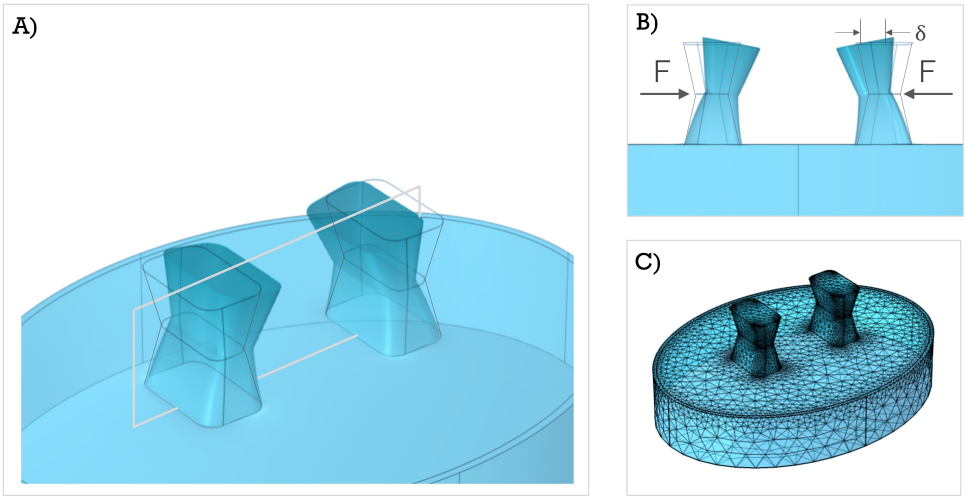

Figure 3.18: Final design of tapered pillar geometry based on fabrication results, implemented in Comsol Multiphysics: A) 3D geometry of pillars on the soft substrate; B) deformation of pillars upon force application on the sides; C) geometry meshing to define computation points.

3.4.2. ANALYTICAL MODEL DERIVATION

For straight pillars, the analytical model was imported from the standard linear beam theory. However, the case of tapered beams requires a different approach. There are several analyses of deformation and stiffness calculation for single tapered members [72–74]. The concept from those studies can be extended to find the approximate deflection curve in the specific case of symmetrically tapered pillars. This analysis still assumes small beam displacement, and for this reason, the theory of equivalent systems was used to simplify the problem [75]. This theory applies in cases where the structure has a variable moment of inertia in the plane normal to the neutral bending axis of the beam. The cross-section of the pillar along the longitudinal axis, with the bending principle used in this model, and the relevant dimensions are shown in Fig.3.19.

The analysis starts from the moment-curvature equation, which is a second-order differential equation describing the beam curvature, for small beam displacement, when the load is applied in x direction:

$$\frac{\mathrm{d}^2 y}{\mathrm{d}x^2} = -\frac{M_x}{E_Y I} \tag{3.12}$$

By double integration of Eq.3.12, the deflection curve y is obtained in the following form:

$$y = \frac{1}{E_Y I}\int \left[-\int M_x dx\right] dx + C_1 \int dx + C_2, \tag{3.13}$$

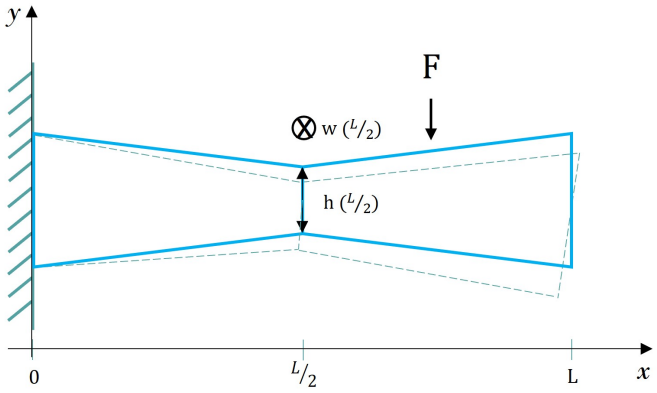

Figure 3.19: Illustration of the tapered beam model with one fixed end and the deformation as a consequence of the applied point force F.

where C_1 and C_2 are integration constants determined by the boundary conditions, E_Y is Young's modulus of the beam material, I is the second moment of cross-sectional area and M_x is the bending moment acting in the direction of the applied load. The term $E_Y I$ describes the resistance of the beam to bending. In case of variable stiffness or beam cross-section, this term becomes a function of x, where x is the bending axis of the beam:

$$E_Y I = E_Y(x) I(x) \tag{3.14}$$

In the case of tapered pillars, Young's modulus is constant, while the second moment of cross-sectional area about the bending axis I is varying across the pillars' length. It can be expressed in the following manner:

$$I(x) = I_{L/2} f(x), \tag{3.15}$$

where $I_{L/2}$ is the value of I in the middle of the pillars, where the cross-section is minimum. Eq.3.13 becomes:

$$y = \frac{1}{E_Y I_{L/2}} \int \left[-\int \frac{M_x dx}{f(x)} \right] dx + C_1 \int dx + C_2, \tag{3.16}$$

The resultant bending moment at any cross-section is defined as:

$$M_x = -F(L - x) \tag{3.17}$$

The equation for the second area moment for a beam with a uniform rectangular cross-section is:

$$I_x = \frac{w h^3}{12} \tag{3.18}$$

However, in our case, both w (width) and h (thickness) are functions of x. Therefore:

$$I_x = \frac{w(x)h(x)^3}{12} \tag{3.19}$$

Eq. 3.16 can be solved by dividing the problem into two separate segments and connecting them with boundary conditions. It is possible to define linear functions for both $w(x)$ and $h(x)$ on these two regions:

$$w(x) = \begin{cases} \left(1-\frac{2x}{L}\right)w(0) + \frac{2x}{L}w\left(\frac{L}{2}\right), & 0 < x < \frac{L}{2} \\ \left(\frac{2x}{L}-1\right)w(L) - \left(\frac{2x}{L}-2\right)w\left(\frac{L}{2}\right), & \frac{L}{2} < x < L \end{cases} \tag{3.20}$$

$$h(x) = \begin{cases} \left(1-\frac{2x}{L}\right)h(0) + \frac{2x}{L}h\left(\frac{L}{2}\right), & 0 < x < \frac{L}{2} \\ \left(\frac{2x}{L}-1\right)h(L) - \left(\frac{2x}{L}-2\right)h\left(\frac{L}{2}\right), & \frac{L}{2} < x < L \end{cases} \tag{3.21}$$

By including these functions in the Eq.3.19, $I(x)$ becomes a fourth-degree polynomial function. To simplify the computation of the analytical solution of Eq.3.19, $I(x)$ is approximated with a second-degree polynomial using function fitting tools of Matlab. $I(x)$ becomes:

$$I(x) = \begin{cases} (p_1x^2 + p_2x + p_3)I\left(\frac{L}{2}\right), & 0 < x < \frac{L}{2} \\ (m_1x^2 + m_2x + m_3)I\left(\frac{L}{2}\right), & \frac{L}{2} < x < L \end{cases} \tag{3.22}$$

Coefficients p_i and m_i, i= 1,2,3, for both 75° and 80° tapered pillars, are given in Table 3.3.

Table 3.3: Fitting coefficients for the second moment of inertia. $I(x)$

	i	1	2	3
75°	p_i	$7.3\cdot10^{-9}$	$-4.47\cdot10^{-12}$	$8.1\cdot10^{-16}$
75°	m_i	$7.3\cdot10^{-9}$	$-2.7\cdot10^{-12}$	$3.5\cdot10^{-16}$
80°	p_i	$5.6\cdot10^{-9}$	$-3.5\cdot10^{-12}$	$6.23\cdot10^{-16}$
80°	m_i	$5.6\cdot10^{-9}$	$-2.01\cdot10^{-12}$	$2.7\cdot10^{-16}$

The approximation of $I(x)$ with the second-degree polynomial is shown in Fig.3.20, proving the good agreement with the exact values obtained using the Eqs.3.19-3.21 at 10 positions along each segment. Fig.3.20A shows only $I(x)$ fitting for 80° tapered pillars since the slopes are similar for both designs.

By including this approximation into the Eq.3.16 it is possible to obtain a set of equations for bending curve of tapered pillars on two specified segments:

$$y(x) \approx \begin{cases} \frac{1}{E_Y I_{L/2}} \int \left[\int \frac{F(L-x)dx}{(p_1x^2+p_2x+p_3)} \right] dx + C_1 \int dx + C_2, & 0 < x < \frac{L}{2} \\ \frac{1}{E_Y I_{L/2}} \int \left[\int \frac{F(L-x)dx}{(m_1x^2+m_2x+m_3} \right] dx + C_1 \int dx + C_2, & \frac{L}{2} < x < L \end{cases} \tag{3.23}$$

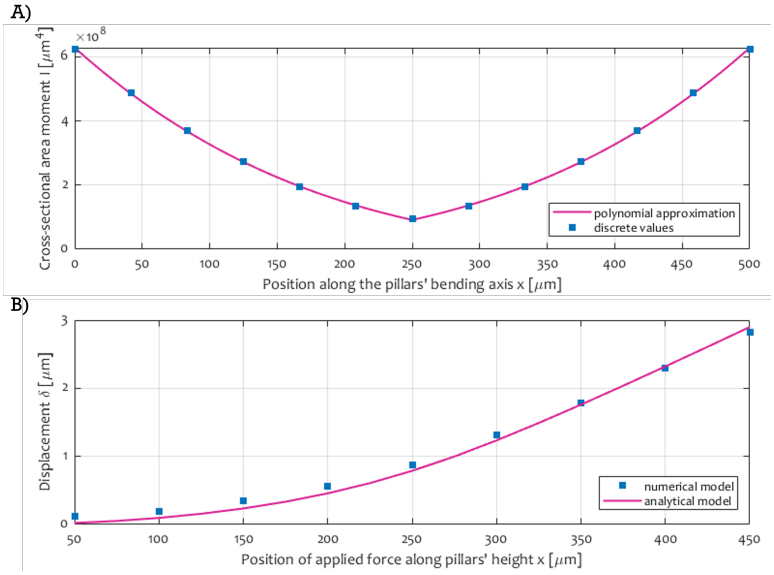

Figure 3.20: A) Fitting the discrete values of $I(x)$ based on analytical expression to the second degree polynomial approximation; B) Comparison of numerical and analytical models for the displacement of 80° tapered pillars tip, for different positions of applied force along the length of the pillar.

The solution for the bending curve can be obtained with the set of boundary and matching conditions to calculate integration constants. First boundary conditions are defined at the fixed end of the beam ($x = 0$), assuming that both deflection and slope are zero:

$$y(0) = 0 \tag{3.24}$$

$$\frac{\mathrm{d}y}{\mathrm{d}x} = 0 \tag{3.25}$$

These two boundary conditions provide the solution for the first segment $x \in (0, \frac{L}{2})$. For the second segment, the continuity in mechanical behaviour applies, assuming the continuity of the slope and matching deflection at the junction of two intervals. Therefore, matching conditions are defined as follows:

$$y\left(\frac{L^-}{2}\right) = y\left(\frac{L^+}{2}\right) \tag{3.26}$$

$$\frac{\mathrm{d}y}{\mathrm{d}x}\left(\frac{L^-}{2}\right) = \frac{\mathrm{d}y}{\mathrm{d}x}\left(\frac{L^+}{2}\right) \tag{3.27}$$

The solution for the bending curve was obtained using *dsolve* function in Matlab for corresponding boundary conditions. Finally, the maximum displacement of the beam ($Y_{max} = y(x = L)$) was calculated for different positions of applied point force along the beams' length.

The results obtained from the analytical model were compared to Comsol simulations for both types of tapered pillars. To reduce calculation complexity, a rigid surface was assumed as the contact point at the bottom of the pillars and the effect of substrate deformation was not taken into account for analytical analysis. For the sake of the model comparison, the same conditions were implemented in Comsol, assuming that pillars are attached directly to the rigid surface. In Fig.3.20B the comparison of the numerical and analytical model is shown. The calculated correlation coefficient (R = 0.999) shows very good agreement between the two models.

The analytical model development enabled direct calculation and fitting of E_Y, to the experimental values obtained from mechanical characterization, as it will be shown in the next section. Later on, the accuracy of the value obtained with the analytical model is compared to FEM analysis, which takes into account the more realistic geometry of pillars and replicates measurement conditions.

3.4.3. NANOINDENTATION MEASUREMENT

In the same way as previously described in Chapter II, FemtoTools Nanomechanical Testing System (FT-NMT03) was used for the mechanical characterization of the tapered pillars. Silicon cantilever with a flat circular tip, 50 µm in diameter, was used to apply force, with 15° orientation angle, on different positions along pillar length. The setup is illustrated in Fig.3.21. Measurements were performed on 3 different positions, on each pillar. The measurements were repeated for 3 samples of both 75° and 80° tapered pillars. The maximum applied force was 80 µN and the pillars were displaced accordingly. A corresponding displacement–force curve was obtained by measuring pillar displacement with a piezo-scanner. The stiffness of the pillars was obtained from the unloading curve upon the pillars' return to the initial position.

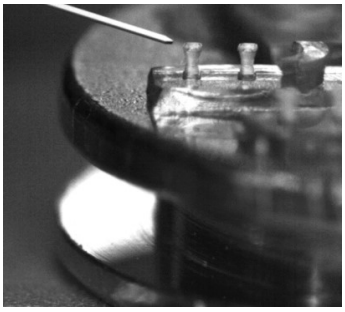

Figure 3.21: Nanoindentation setup for mechanical characterization of tapered pillars. Tapered pillars in PDMS mounted on a metal base with the sensor tip next to it.

MODEL FITTING: YOUNG'S MODULUS CALCULATION

The nanoindentation measurements were used to calculate the exact Young's modulus of PDMS and to compare their elastic curve to the ones obtained from the numerical and analytical analysis.

Both analytical and numerical models assumed E_Y = 1.2 MPa. The condition from the experimental setup was recreated in the numerical model, as mentioned earlier. The disagreement between modelling and measured values is evident from the graphs, therefore, correction for E_Y was performed. The analytical equations were solved from the $E_Y \in \{500, 1300\}$ KPa in 500 points. The new E_Y was selected as the value for which a minimal square difference between experimental and analytical data was obtained, for both pillar types. The updated value for E_Y was 900 KPa which is the value implemented into the numerical model as well. A comparison of the two models to the experimental values, before and after the E_Y correction, is shown in Fig.3.21. The value for E_Y is

slightly higher than the one obtained in Chapter 2 (800 KPa), which can be attributed to the difference in thickness of PDMS below pillars between different measurements.

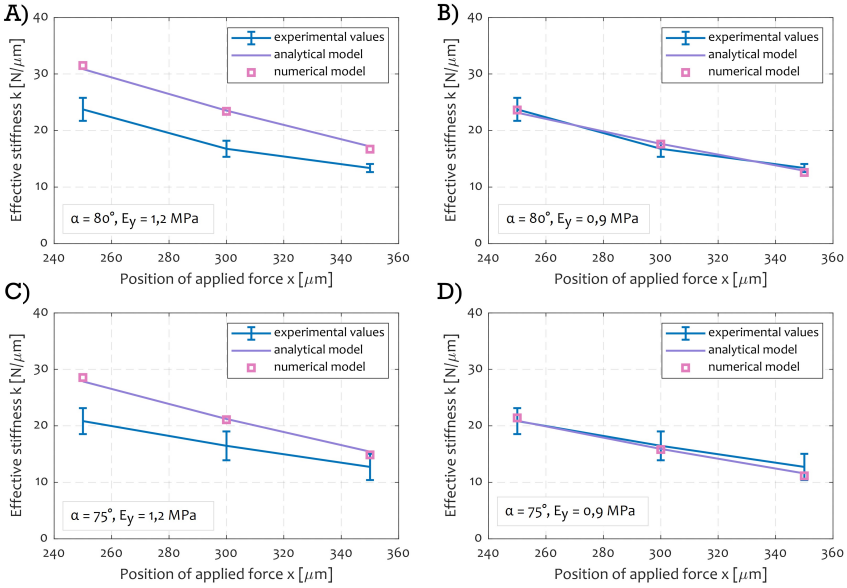

Figure 3.22: Comparison of the numerical, analytical and experimental data A) before and B) after E_Y correction for 80° tapered pillars and C) before and D) after E_Y correction for 75° pillars.

3.5. BIOLOGICAL VALIDATION OF PLATFORMS

The assessment of the efficiency of the novel pillar design was performed by culturing EHTs on both tapered pillars and comparing them to the tissue performance in the case of straight pillars. The main questions of the study were the efficiency of tissue confinement in tapered design and its effect on the tissue contractile properties, the yield of the experiment and the dispersion of the results.

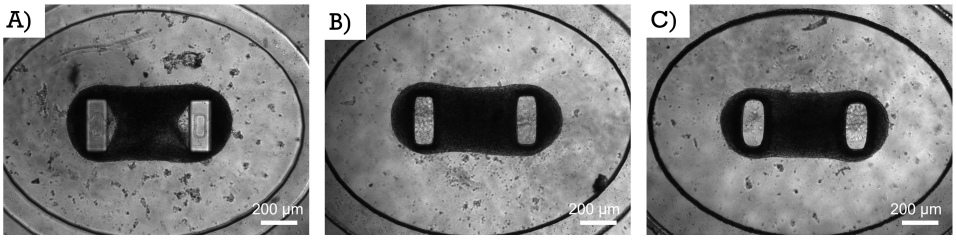

Figure 3.23: Representative images of EHTs formed around A) straight, B) 80° tapered, and C) 75° tapered pillars.

3.5.1. TISSUE CULTURE

For EHT formation on tapered pillars, a similar protocol was used as reported in Chapter 2, with the addition of endothelial cells. Briefly, three different cell types: cardiac fibroblast (cFB), endothelial cells (ECs) and cardiomyocytes (CMs) were derived from hiPSC line (LUMC0020iCTRL-06). The hiPSCs were differentiated into CMs as described previously [33, 41]. The EHTs were composed of 70% hiPSC-CMs,15% hiPSC-derived cFB and 15% ECs. For the ECM gel mixture, 41% of acid solubilized collagen I (3.3 mg/mL), 5% of DMEM (10X), 6% of NaOH, 9% of growth factor reduced Matrigel and 39% of formation medium were used. The EHTs were cultures in formation medium for 72h combined with VEGF (50 ng/mL) and FGF (5 ng/mL). After 72h the culture medium was switched to BPEL+ VEGF (50 ng/mL)+ FGF (5 ng/mL) and maintained in culture for 14 days. The tissues were successfully formed in all three different pillar designs. Representative images of tissues formed around straight, 80° tapered and 75° tapered pillars are shown in Fig.3.23. Brightfield images were taken live on day 7 since the beginning of the experiment with a Nikon Eclipse Ti2.

From Fig.3.23 it is possible to notice the difference in tissue formation among different platforms. In the case of straight pillars, it is common to have a triangular-shaped area without cells called a "V-neck" [76], next to the pillars. This means that, in the case of straight pillars, the tissue does not adhere completely to the pillar area, which creates challenges for the optical force readout, as will be explained in Chapter 4. In the case of both tapered designs, there is no evidence of a "V-neck" appearance.

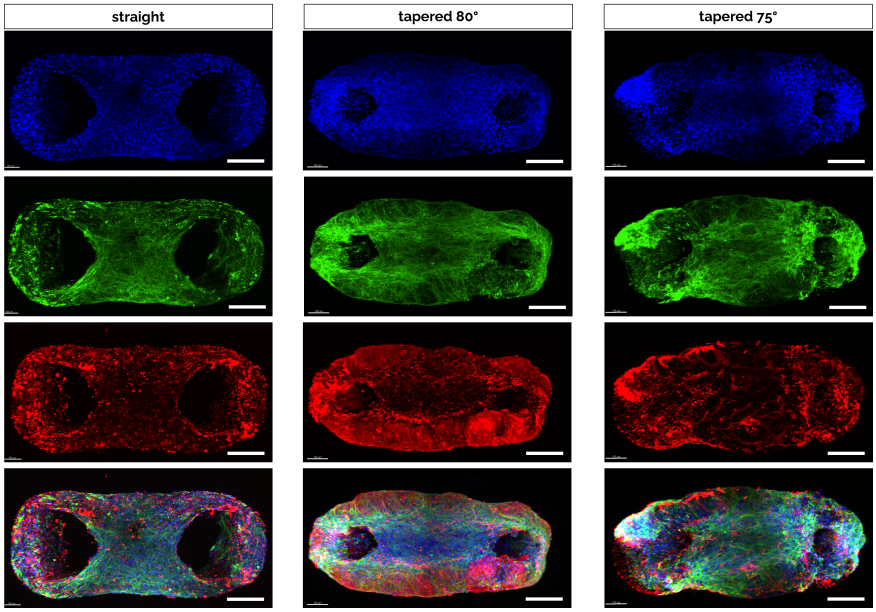

Figure 3.24: Immunostaining of the tissues in three different platforms for cardiac-specific markers: alpha-actinin (red), and cardiac troponin T (green). Nuclei were stained with DAPI (blue). The superposition of all three color channels is shown in the last figure (Courtesy of Laura Windt, LUMC). Scale bar 200 µm.

Immunostaining of the intracellular sarcomeric structures demonstrated the cellular organization around all three versions of pillars and sarcomere orientation. The tissues were stained whole–mount and imaged with an Andor Dragonfly 500 fluorescent microscope on day 15 from the beginning of the experiment. Sarcomeres were stained using cardiac-specific antibodies against alpha-actinin (ACTN2) and cardiac troponin T (TNNT), while nuclei were stained with DAPI (Fig.3.24).

3.5.2. TISSUE POSITION MEASUREMENT

To assess tissue confinement with the tapered geometry, the tissue positions along pillar length were measured for both designs. Optical images were taken using a Keyence VHX-900F microscope at 60° view angle. The imaging was performed at the end of the experiment, after fixing the tissues on the pillars. The measurements were repeated for a minimum of three tissues of each tapered pillar design and the confinement in the middle of pillars was seen in all of them. In Fig.3.25 representative examples of tissue confinement in the middle area of both tapered pillar designs are shown. By visual inspection, it was determined that the new geometry successfully provided mechanical constraints on the tissue movement outside the narrow area in the middle of the pillars. However, the exact measurement of tissue thickness from the obtained images is still challenging, due to the evaporation of excess liquid once the elliptic well is disrupted.

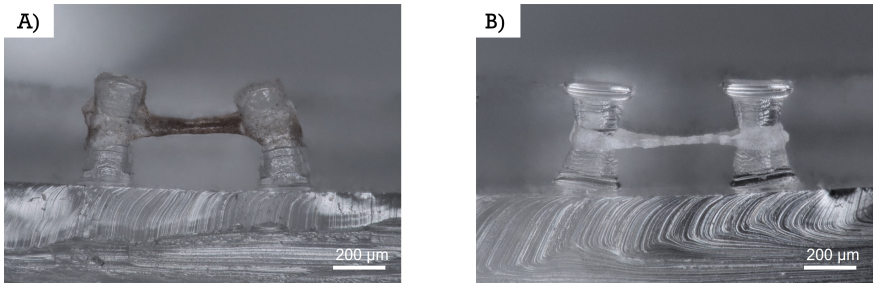

Figure 3.25: Optical images of tissue confinement in the middle of A) 80° and B) 75° tapered pillars.

3.5.3. COMPARISON BETWEEN STRAIGHT AND TAPERED DESIGN

The comparative study between tapered and straight pillar designs was performed based on the yield of the experiment and contractile tissue parameters.

The yield of the experiment significantly improved from 15% for straight design to 100% for both 80° and 75° tapered pillars. This means that all tissues on tapered pillars reached the end point of the experiment, proving that spatial confinement solved the problem of jumping off and enabled long-term cell culture. The duration of the experiment was 14 days.

The contractile parameters of tissues in different pillars were measured. The videos of contracting tissues were recorded on days 4, 7 and 11, during spontaneous contraction as well as during electrical pacing at 1 Hz and 2 Hz. Videos of contracting tissues of 10 s duration were recorded using an inverted optical microscope (Nikon Eclipse Ti2) with a high-speed camera. Videos were analyzed using ForceTracker (Chapter 4), the custom-

made standalone app for tissue contractile performance assessment. The results of the analysis and comparison of all three designs on day 7 are shown in Fig.3.26.

It is possible to notice from the graphs that the variability in the contractile behavior is significantly reduced in the case of both tapered pillar designs compared to the straight ones (85%). The other parameters describing contractile kinetics, such as contraction and relaxation time to reach 10% and 90% of the upstroke and downstroke of the contraction cycle, are comparable in all three designs. It is yet to be determined to which extent can the decrease in variability of contractile properties be attributed to the new pillar design and tissue confinement. Another factor that needs to be taken into account before making any conclusion is the difference in pillar stiffness between all three designs, which can also have an influence on the contractile force generation and reduction of output variability.

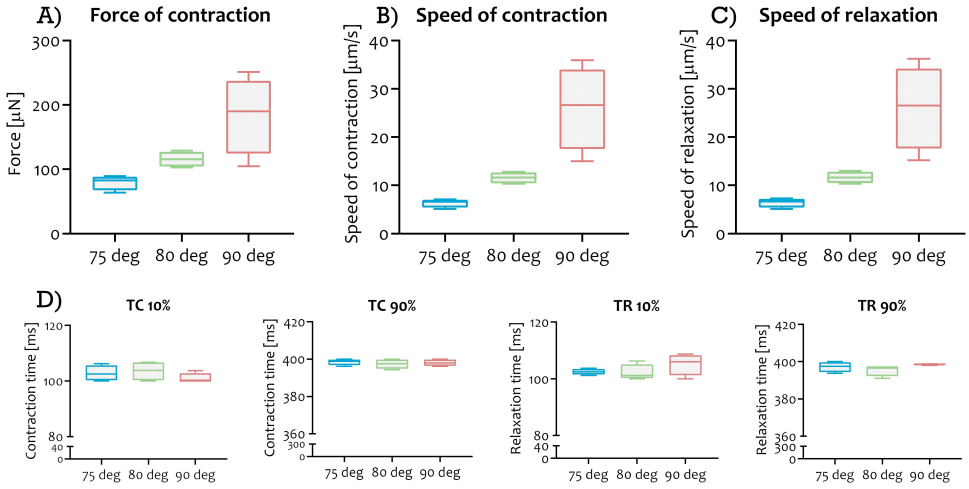

Figure 3.26: Contractile performance analysis of EHTs in straight and tapered pillars: A) Contractile force of EHTs. Contraction kinetics, specifically B) contraction and C) relaxation speed over time; D) Time of contraction to reach 10% and 90% of the upstroke and downstroke of the contraction cycle.

3.6. DISCUSSION AND CONCLUSION

In this Chapter, a novel design of PDMS pillars for tissue self-assembly in EHT platforms was introduced. The design is meant to increase the control over tissue position over time and consequently reproducibility of contraction force measurements. PDMS-based pillars were designed and fabricated in an hourglass shape, with symmetric tapering, producing a restriction in the middle of the pillars' length. Such design was shown to provide precise and predictable confinement of EHTs around the pillar restriction, as it presents mechanical resistance to tissue movement. Additionally, the issue of "jumping off" was successfully addressed with the tapered design, resulting in an increased yield of the experiment. The pillars were made with two different tapering angles: 75° and 80° to test their confinement efficiency.

The design, modelling and microfabrication of both pillar variations were described in detail. The final dimensions were achieved through several iterations due to many fabrication challenges. Even though the final measured tapering angle corresponded to the anticipated values, there is still the possibility for further optimization to reduce the broadening of the initial mask dimensions and to achieve better control of the final structures. One difficulty in achieving this is the limitation imposed by the isotropic etching of narrow trenches. By reducing the width of rectangular windows in the first oxide mask to compensate for the structure broadening until the end, the uniformity of isotropic etch reduces. For this reason, there is a trade-off between the smallest value for the h_{short} that can be achieved and the final difference in tapering angles in x and y directions. Both affect the stiffness of the pillars, therefore tuning of dimensions has to be performed with consideration of mentioned effects.

Additional improvement of the process must be implemented for better inclusion of focus features on top of the pillars, as these are crucial for optical imaging and use in software for contractile force analysis. These features were initially etched in the support silicon wafer before bonding with SU8. However, the etched cavities were not deep enough to be transferred as a rectangular pattern on top of pillars during PDMS moulding, since the SU8 layer on top reduced their step height. This is something to be adjusted in the future fabrication process.

In addition, the mechanical characterization of both tapered designs was performed using a nanoindentation measurement system. This resulted in the correction of the assumed Young's modulus and consequently precise measurements of the force of contraction. It was discovered that the stiffness of new designs is higher than expected by the design because of the geometry widening and fabrication limits. This is something that can be fine-tuned by reducing the number of final etching steps with the second oxide mask or with a slight change in geometry.

The efficiency of tapered designs in tissue confinement was tested by performing a comparative study between straight and tapered pillars. It was noticed that the tissue formation was unaffected by the new pillar design. Additionally, the "V-neck" was absent for tissues in tapered pillars, meaning that the tissue adheres entirely to the indented pillar area in the middle [76]. This is very beneficial for imaging purposes since the elimination of the "V-neck" shape improves the efficiency of pillar displacement tracking.

Tissue confinement was confirmed optically for both tapered designs. Consequently, the yield of experiments significantly increased as the jumping-off issue was solved. It is yet to be determined whether the confinement of the tissue originates only because of the tapering geometry or the effect of higher stiffness has a significant influence as well. This will be tested in the future by reducing the stiffness of tapered pillars and analyzing the confinement efficiency.

Furthermore, the effect of the tapered design on tissue contractile properties was analyzed. A decrease in variability for the contractile force measurements was noticed, while the other contractile kinetics parameters were comparable in all three designs.

To conclude, all the drawbacks of the previous straight pillar design were successfully addressed with the tapered approach. Further experiments and analysis of the tissue contractile behavior will lead to more concrete biological conclusions about the exact influence of pillars' mechanics and geometry on tissue contractile performance.

CHAPTER 4

OPTICAL READOUT OF TISSUE CONTRACTILE PROPERTIES

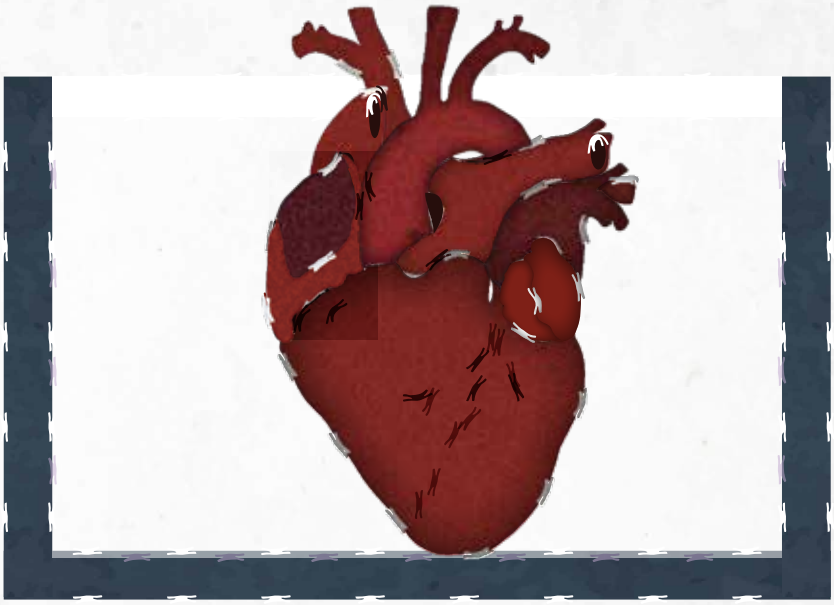

|This cahpter has been submitted to *ACS Biomaterials Science & Engineering*

4.1. THE IMPORTANCE OF CONTRACTILE FORCE ASSESSMENT

A fundamental function of the heart is the development of contractile force to push blood flow in the body. Cardiac contraction is the result of a fine-tuned interplay between electrical activation, calcium handling, and myofilament activation [7]. There are several intrinsic mechanisms that regulate this fine interplay and adjust the response of the cardiac muscle according to electrical or mechanical stimuli. For example, the Frank-Starling [FS] mechanism adjusts the contraction force to the load applied to the cardiac muscle, while the force-frequency relationship [FFR] enables response to the rapidly changing requirements of blood supply by an increase in force [8]. These mechanisms are just two examples that demonstrate the importance of contractile force regulation in a healthy heart. Moreover, there is a spectrum of cardiovascular diseases (e.g. cardiomyopathy, myocardial infarction, hypertrophy) directly affecting the contractile function of the heart. Hence, measurement of cardiac contractile kinetics is crucial to assess the level of recapitulation of the human physiology and pathophysiology in an *in vitro* model. Specifically, in the case of hiPSC- based *in vitro* models, the force of contraction represents one of the most important hallmarks of tissue maturation towards the adult-like myocardium.

Among many benefits of using the engineered heart tissue (EHT) approach, the one that stands out is the ease of contractile force assessment in these models. Upon the tissue enclosure around the micropillars, the formed healthy tissue starts spontaneously contracting in a rhythmical manner, as described previously. The force of contraction causes the bending of elastic pillars and can be correlated to the consequential displacement of the pillars' tips. Due to the small pillar displacement, the torsion of the pillar is neglected and only bending is taken into account for the force calculation. The main principle of pillar deflection upon the contraction of the tissue is illustrated in Fig.4.1.

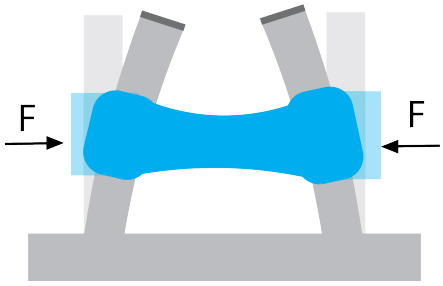

Figure 4.1: Principle of posts (gray) bending upon tissue (blue) contraction.

Various EHT platforms have been developed and used across different research groups [19, 34–36, 41, 45, 77]. Many of them are based on the model of cardiac tissue suspended between two or more elastic pillars. These platforms differ in the shape and size of pillars, the distance between them, and the shape and size of the tissues formed around them. The most representative examples are shown in Fig.4.2. One aspect they all have in common is the measurement principle used to obtain contractile parameters of the tissues [37, 78, 79]. Typically, deflection of pillars is optically tracked over time and later converted into the force applied by the tissue. To assess the pillars deflection, different

research groups use custom-made and platform-specific image processing algorithms [80]. Used programming languages vary, and most of the developed tools are not openly available to the scientific community. The mentioned drawbacks prevent the cross-comparison of the results between different research groups, making the standardization of tissue contractile measurements in EHT platforms particularly challenging.

Together with the collaborators from the University of Twente, within the Netherlands Organ-on-Chip initiative, we identified the need for the development of a robust, platform-independent, easy-to-use, and standalone software tool for assessing contractile properties of tissues in different EHT platforms. To address this need we propose *ForceTracker*, a standalone application developed in Python that provides a time-efficient and robust analysis of EHT contractile dynamics, from multiple video formats and different EHT platforms. The core of the standalone application is a shape-detection algorithm that tracks the deflection of tips of elastic pillars throughout all the frames of a video recording of a contractile assay. The detection is implemented in a shape-independent manner with respect to the geometry of the pillars and currently operates for circular and rectangular shapes, as those are the most common shapes of pillar cross-sections used in EHT platforms.

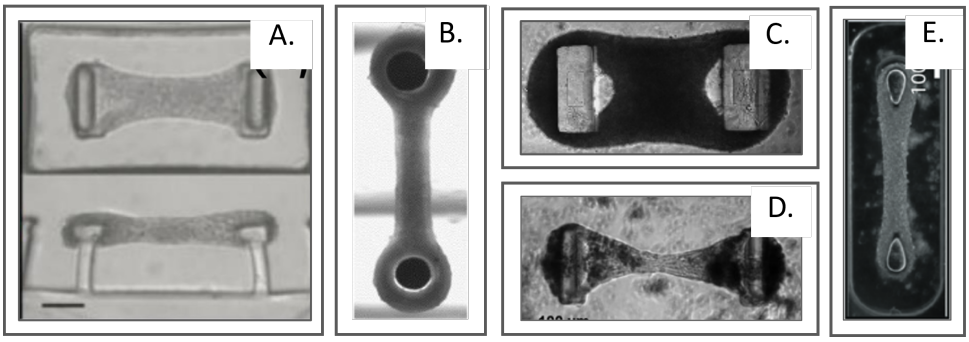

Figure 4.2: Examples of different EHT platforms:(A-B) Platform with a pair of rectangular pillar cross-sections with a constraining feature on the top [19]; (B) Platform with circular pillar cross-section [35];(C-D) Platforms with rectangular cross-section culturing the microtissues (without the constraining feature) [34, 41]; (E) Platform with (two-step) droplet-shaped pillars [45].

4.1.1. RECTANGULAR AND CIRCULAR EHT PLATFORM

The current implementation of *ForceTracker* was benchmarked through two specific EHT platforms, as relevant representatives of the platforms used across the field (Fig.4.3). The first of these EHT platforms was developed at the University of Twente by Ribeiro et al. and will be referred to in this chapter as the *circular platform* [35]. This platform hosts tissues suspended between two cylindrical 3 mm-long polydimethylsiloxane (PDMS) pillars, which fit into individual holders made by micro-milling polymethyl methacrylate (PMMA) (Fig.4.1A). The platform is designed to fit in a 12-well plate format, with three tissues per well (Fig.4.3B-C). The second EHT platform is the platform with rectangular micropillars, (i.e. *rectangular platform*), whose design and development were explained in detail in previous chapters. (Fig.4.3D-F).

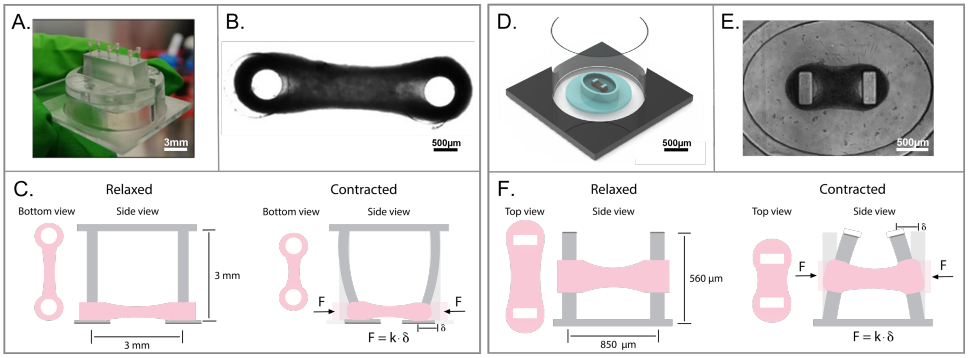

Figure 4.3: Engineered heart tissue (EHT) platforms used for the *ForceTracker* implementation. (A-C) Circular platform: (A) Image of three EHTs formed around cylindrical pillars on a single-well holder. (B) Brightfield image of a single EHT bottom view in a 12-well plate format. (C) Illustration of the bending principle of elastic cylindrical pillars upon tissue contraction. (D-F) Rectangular platform: (D) 3D model of the EHT platform within a single compartment of a 96-well plate, with the PDMS structure in blue and cardiac tissue in brown. (E) Brightfield image of an EHT top view in a 96-well plate format. (F) Illustration of the bending principle of rectangular elastic pillars upon tissue contraction. F= Force of contraction, k=pillars stiffness, and δ = pillars deflection.

4.2. *ForceTracker* IMPLEMENTATION

The implementation of *ForceTracker* can be divided into three parts. In the following, the first and the second part describe the two most important building blocks of the software: the shape-detection and tracking algorithm, and the data analysis block. Finally, the overall structure and user interface of the software are described in the last part.

4.2.1. SHAPE-DETECTION AND TRACKING ALGORITHM

The core of the developed software is a shape-detection and tracking algorithm. The algorithm extracts the positions and shapes of pillars' tips from each frame of the recorded videos and tracks their displacement throughout all the consecutive frames. In addition to pillars' displacement, the algorithm also measures and tracks the change in the size of the tissue during the contraction cycles. The displacement of pillars is measured in pixels and later converted to micrometers. Further calculations correlate this displacement to the tissue's contractile performance. The shape-detection and tracking algorithm is coded in Python, using built-in functions of *openCV* and *skimage* libraries [81]. The shape-detection and tracking algorithm was implemented in three steps: image pre-processing, thresholding, and shape tracking. All the steps of the algorithm are depicted in Fig.4.5 and detailed below.

IMAGE PRE-PROCESSING

Several image transformations are applied to ensure low noise and robust shape detection. Firstly, each frame is converted to a grayscale image, decreasing the image complexity from three color channels to one, while preserving the information about pixel luminosity. The latter is quite important, as it is the concept that many downstream image processing algorithms rely on. The second step of image pre-processing is the re-

moval of small noise and glitches in pixel intensity. Bilateral filtering is used for this purpose. Unlike standard blurring and smoothing techniques which only remove noise by blurring the entire image, bilateral filtering also preserves object edges and shapes [82]. This is made possible by considering only pixels with similar intensity values among neighboring groups of pixels.

However, bilateral filtering only removes small noise and reduces glitches, which is often not enough to avoid larger artifacts (e.g., shadows, air bubbles, or cells/ECM residues). In that case, morphological transformations are implemented to achieve higher-level filtering [83]. First, image erosion is performed to eliminate small objects from the image and clear out the defects around the edges of bigger objects. It results in a reduction in object size in the image, as all the boundary pixels are 'cleared out.' To bring the eroded objects back to their initial dimensions, the complementary transformation to erosion, i.e. image dilation, is performed. Image dilation expands the objects by assigning value '1' to the surroundings of remaining active pixels by following the pattern inferred from the transformation itself. The combination of these two morphological transformations removes most of the small defects from the original image. Additionally, it is very efficient in decreasing or even eliminating shadows of pillars from the images. The effect of each step of image pre-processing and its importance for the final detection result is demonstrated in Fig.4.5A-B.

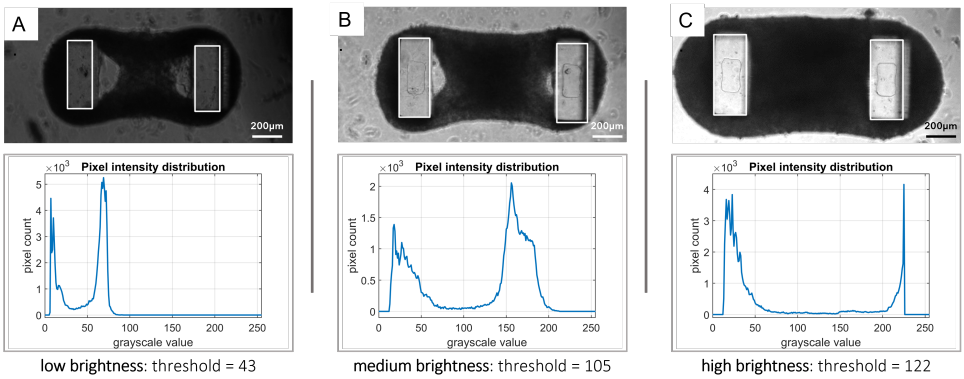

Figure 4.4: Pixel intensity distribution. (A) Low brightness distribution. (B) Medium brightness distribution. (C) High brightness distribution.

THRESHOLDING

Videos that are targeted for analysis with *ForceTracker* depict rhythmical contraction and relaxation cycles of 3D tissue-like constructs of cells, densely compacted around a pair of elastic pillars. In both platforms of interest, the pillars are made of PDMS, a material transparent in the visible range of the electromagnetic spectrum. In the context of image processing, this transparency translates into high-brightness pixel areas representing the PDMS pillars, surrounded by low-brightness pixel areas of opaque tissue. This condition of imaging made the Otsu thresholding method the most suitable approach to distinguish transparent (pillars) from opaque (tissue) frame areas. The Otsu algorithm

extracts the high-intensity objects from dark backgrounds by finding the optimal pixel threshold intensity value [84, 85].

In our case, we binarize the image using the Otsu threshold, by converting all the pixels belonging to the pillars' tips into white areas, and all the pixels belonging to the tissue into black areas. The algorithm first finds the distribution of pixels per gray-scale intensity. An example of pixel intensity distribution for different brightness levels in videos is illustrated in Fig.4.5. This distribution is affected by the contrast, pixel intensity, and amount of bright and dark areas in an image. Regardless, in the pixel intensity distribution of each frame, it is possible to clearly distinguish two peaks belonging to two classes of pixels. Low-intensity pixels in the first peak belong to the tissue area, while the high-intensity pixels of the second peak represent transparent pillars and the bright part of the image outside of the tissue area. The Otsu threshold is then calculated by maximizing the variance between the two classes of pixels and finding the pixel intensity value for which the overlap of two peaks is negligible. This output value is further used for binary thresholding the image into the white areas corresponding to the pillars and the black area representing the tissue. Examples of final frames, after performing thresholding, are shown in Fig.4.5.

SHAPE DETECTION

Shape detection and tracking start by dividing the frame vertically into two symmetric parts. Each part of the image contains one pillar and approximately half of the tissue. After the Otsu threshold is obtained, the image binarization is performed on both parts of the original image, resulting in two black-and-white images. The accuracy of final shape representation after binarization is strongly dependent on the quality of previously performed filtering and thresholding. Once the white pillar tip areas are extracted from the black background, detection can be performed. Using a contour detection function, the edges of each object in the image can be found by calculating the maximum intensity difference between neighbouring pixels [86, 87]. Ideally, at this step, only the tissue and two pillars should be detected, as all the other artifacts should be filtered out of the frame. The exact areas of pillars are differentiated from the tissue contour with a dimension sorting algorithm. In this method, the detection of pillar contour is shape-independent, as the contours can be found for any shape in the image. Depending on the shape of the cross-section of the pillar, the detected contours are approximated with circles or rectangles. Approximation with rectangles or circles is only implemented for the ease of further processing and contractile properties calculations (Fig.4.5D). This means that the software can easily be expanded for tracking different pillar geometries.

It is relevant to mention that in the case of the platform with rectangular pillar cross-section, an additional shape often appears in the videos, between the tissue and pillars, previously described as "V-shape" [76]. This shape originates from the inner area without cells, as the tissue does not adhere completely to the pillars from the inner side. Due to its transparency and therefore high-intensity pixels, this area becomes white and gets merged to the one side of the rectangle. Additional masking steps are implemented to exclude the area with no cells from the final shape detection and to ensure that only rectangles are selected for tracking.

For each detected pillar, a shape centroid is found using image moments. In this way, the geometric center of both pillars is obtained, and its relative movement can be

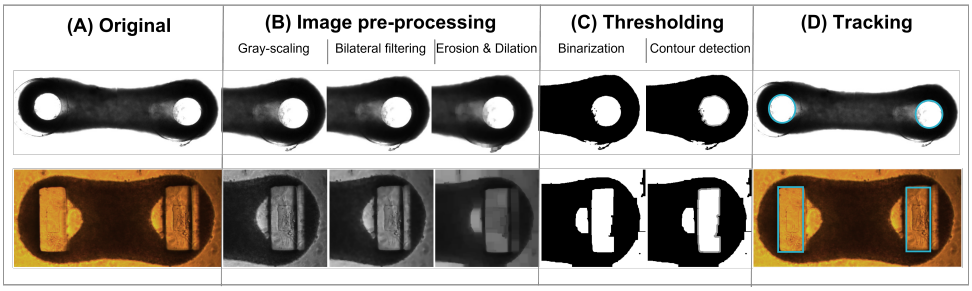

Figure 4.5: Algorithm detection steps. (A) Original image of circular (top) and rectangular platforms (bottom). (B) Pre-processing. The images are converted to grayscale, processed by the bilateral filter, and lastly by complementary morphological transformations (erosion and dilation). (C) Thresholding step of combining binarization and contour detection. (D) Tracking of the pillars from both platforms (light blue contours).

tracked throughout all the frames of a video. Absolute displacement of pillars relative to each other is found by calculating the Euclidian distance between the centers of the detected shapes. This calculation is repeated for every frame of a video, finally resulting in the periodic data series depicting the rhythmical contraction of the tissue. The displacement is measured in pixels and later converted to micrometers for further force calculations. In addition to the pillar tip displacement, the change in tissue surface area is also measured in each frame. In this way, we are able to quantify the change in tissue surface area during the tissue's contraction cycles.

For each detected pillar, a shape centroid was found using image moments. In this way, the geometric center of both posts is obtained, and its relative movement can be tracked throughout all the frames of a video. The relative displacement of posts towards each other is found by calculating the Euclidian distance between centers of detected shapes. This calculation is repeated for every frame of a video, finally resulting in sinusoidal-like data depicting the rhythmical contraction of the tissue. The displacement is measured in pixels and later converted to micrometers (μm) for further force calculations. All the steps of the detection algorithm are shown in Fig.4.5.

Except for the pillar tips displacement, the change in the tissue area is also extracted from the videos. The surface of the tissue area is measured based on the detected contour around the tissue. In this way, we can quantify the change in tissue size during the contraction cycle.

4.2.2. Data Analysis

The contraction wave of the tissues is the output of the shape detection algorithm, and it is used to further calculate the physiological hallmarks of the EHTs. An absolute force of contraction (FoC) is the main readout of the software, as it can be directly correlated to the performance of the CMs and their level of maturation [21]. Furthermore, FoC output allows identifying the effect of different drug compounds on the CMs, a disease mechanism, or the response to external stimuli, which can be related to the *in vivo* situation [24, 88].

To calculate the FoC, mechanical properties of each platform must be known (e.g., Young's modulus of the pillar material, the position of the tissue adherence to the pillars,

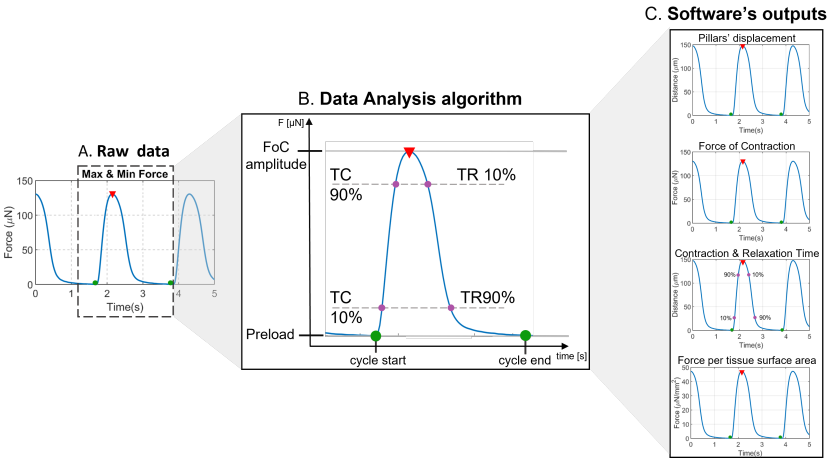

Figure 4.6: *ForceTracker* graphs output. (A) Force of contraction (FoC) graph with the explanation of contraction cycle with maxima and minima, and the time to achieve 10% and 90% of contraction and relaxation (B). (C) *ForceTracker*'s four output time series graphs: pillar displacement, FoC, contraction and relaxation time, and force per surface area.

and the geometry of the pillars). For each platform, the FoC generated by the tissues was calculated using previously described methods [35, 41]. In addition to the FoC generated during contraction cycles, a resting tension acts upon pillars during tissue formation. This tension imposes a preload on the pillars, and it is calculated as the difference between the position of the unloaded and loaded pillars. The baseline of the contraction cycle was set to zero by subtracting the resting tension from the measured force values.

Even though the FoC is a major hallmark of cardiac function, contractile kinetics also provides significant insights into cardiac (patho)physiology [21, 24, 88]. There are examples where pathological effects can be hindered by the preserved amplitude of contractile force but are clearly expressed in the alterations of contractile kinetics [89]. Also in the intrinsic regulatory mechanisms of the myocardium, such as the FFR and the FS, contractile kinetics are up or downregulated.

The analysis of the contractile kinetics of EHTs can be performed only across a complete contraction cycle. This is implemented in *ForceTracker* in a robust way, by analyzing the data between two minima surrounding a peak value of the contraction. In the cases when the brightfield video starts or ends in the middle of a contraction cycle, this data is discarded. Further on, the speed of contraction and relaxation is calculated from each contraction cycle. Additionally, the time to reach 10% and 90% of the up-stroke and downstroke of the contraction cycle is also obtained.

Another relevant contractile parameter is the FoC per cross-section area of the tissue. However, in previous studies, obtaining this value requires an additional histological step for every analyzed tissue, and can be performed only at the end of the experiment [39, 90–93]. Instead, as alternative information, the measured surface area of the tissue was used to calculate the force per tissue surface area. The data analysis output graphs and illustration of the contractile parameter calculation are shown in Fig.4.6.

4.2.3. SOFTWARE LAYOUT

The complete *ForceTracker* app is composed of multiple building blocks. Each of the building blocks facilitates an important part of the video analysis process. The main ones are: shape detection, tracking algorithm, and data analysis, which were previously detailed. However, there are additional layers required to run a robust standalone app. They are all interconnected through the user-friendly graphical interface (GUI)(Fig.4.7). The software GUI was implemented using built-in functions of *PySimpleGUI* library. This library enabled us to develop an interactive environment with relevant feedback and pop-up error messages for the users [94]. The GUI contains three separate tabs requiring specific input from the user, prior to starting the analysis.

First, the algorithm requires general information such as the format of video files and the location of the folder containing files for analysis. (Fig.4.7A) This information can be inserted via the Main Menu tab (Fig.4.7A-B). Currently, the algorithm can process videos in .avi,.tiff, and .nd2 formats. The second step is the definition of detection parameters within the Settings tab (Fig.4.7C). Here the user selects the cross-section of the pillars and specifies its dimensions in micrometers (Fig.4.7D) together with mechanical properties (Fig.4.7E). In the last tab Data Analysis (Fig.4.7F) the user makes a selection of the graphs that will be stored in the output folder after completing the analysis. The available output graphs show the displacement of pillars, the force of contraction, contraction and relaxation speed, and the force of contraction per tissue area.

The automatic video analysis starts by pressing the button “Start Analysis” in the Main Menu, once all the input parameters are defined (Fig.4.8A-B). The computation first runs Shape-detection and tracking algorithm for every available video. The video analysis is done in parallel, using a multithreading approach (Fig. 4.8C). This method maximizes the speed of data processing as it uses in parallel all available cores of a personal computer (PC) to execute the program. In our case, using a high-end PC (Intel Core i7) computation time for 50 videos (each video of approximately 10 s) without multithread processing was 14 min 20 s, while multithreading reduced this time to 4 min 23 s (3.3 times). During the ongoing analysis, the user is regularly updated on the remaining percentage of computation via a progress bar in the Main Menu. The outputs of the shape-detection and tracking algorithm are the displacement of pillar tips and the change in tissue surface area for each video. The raw data are forwarded to the low-pass filter implemented as *signal.iirfilter* in Python. Filter parameters are set according to the data frequency, which is extracted from the raw data using Fourier transform. Filtered data become the input for the calculation of contractile parameters within the Data Analysis block. This computational block outputs four .png graphs and two excel files, one containing all the details of the video analysis for every video and the second one with the summary of all the files analyzed (Fig.4.8D-E).

MANUAL DETECTION

The described algorithm flow applies in the case when an automatic analysis is possible, i.e. if the parameters defined at the beginning of the analysis remain valid for all the videos. However, there are normally outliers and unpredictable artifacts for which manual correction of detection parameters is needed. For example, low brightness and contrast make Otsu threshold calculation challenging, as demonstrated in Fig.4.4. Hence,

the value of the Otsu threshold can be manually adjusted by the user to improve detection quality. Furthermore, in the case of very prominent shadows which cannot be removed during image pre-processing, it is possible to manually increase the number of dilation and erosion iterations to enhance filtering. Both options for detection improvement are available to users by choosing the Manual detection correction mode from the Settings tab. A new window appears showing detection for the currently processed video and all the parameters available for the real-time detection adjustment (Fig.4.7G).

Feedback is provided to the user while defining input parameters via pop-up error messages. As additional feedback, verification of the detection quality is implemented. For each video, a .png image showing shape detection on a single frame is stored in the main folder. In this way, a fast inspection can be performed to determine the detection efficiency for all the videos.

STANDALONE APPLICATION

Pursuing the goal of making a versatile tool for standardized assessment of tissue contractile properties in EHT platforms across different research groups, the ForceTracker algorithm was compiled into a standalone application. The algorithm was compiled using Nuitka [95], a Python compiler that allows compiling all the libraries and modules into a C-level program. Within this module we included *multiprocessing*, *tkinter*, *numpy*

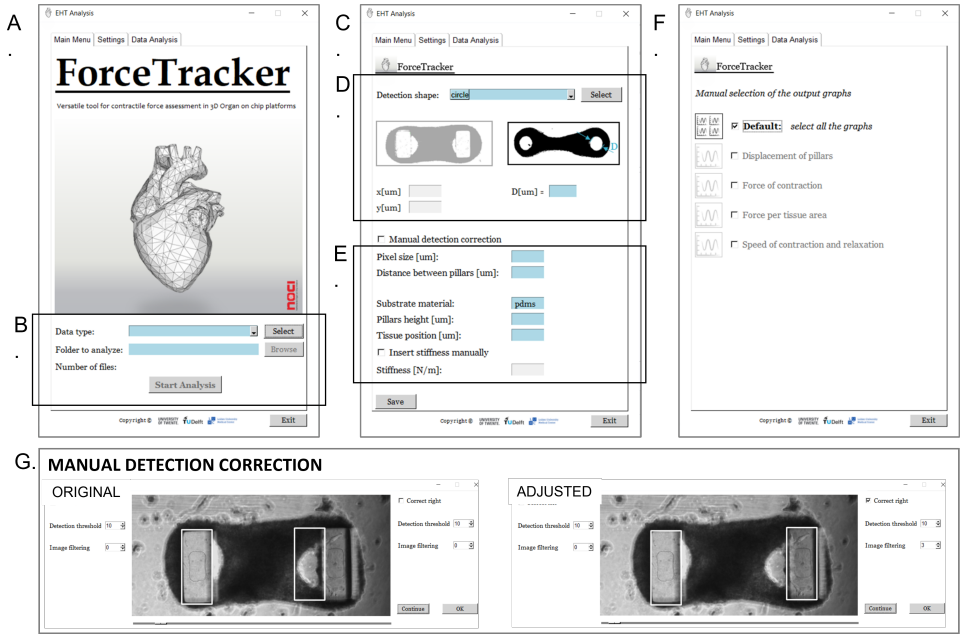

Figure 4.7: *ForceTracker* graphical user interface (GUI). (A) The Main window of the standalone application. (B) Section to select the type of data, the location of the files to be analyzed, and the start button to start the automatic analysis. (C) The secondary window for the settings. (D) Selection of the platform and important dimensions. (E) Specifications on the material and location of the 3D tissue. (F) Data analysis window to select the output graphs of interest.

and *pyside2* libraries. Additionally, Mingw64 [96] was used as the C compiler. Compiling into the standalone app was executed using Python in the command prompt.

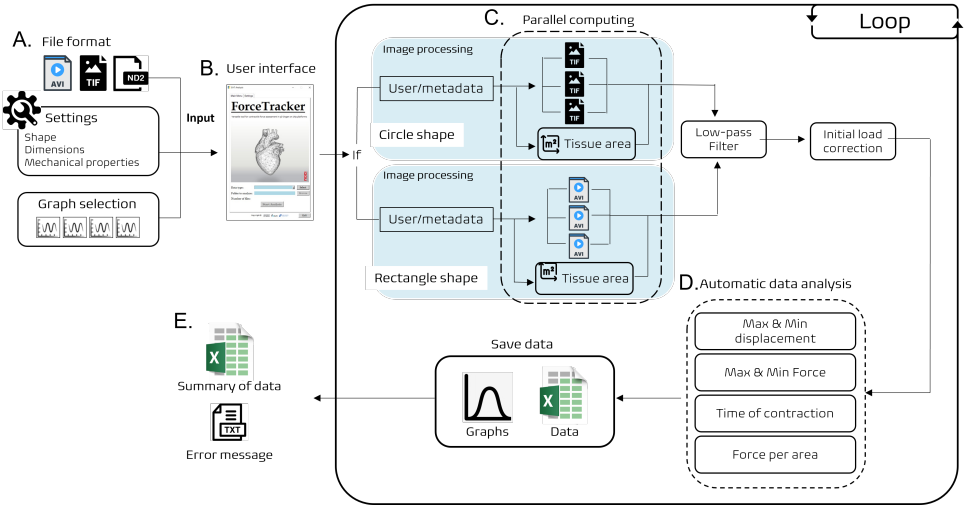

Figure 4.8: *ForceTracker* structure and computational flow. (A) Input files (.avi,.tif, or .nd2), settings, and selections of the output data. (B) Easy-to-use user interface. (C) Internal shape detection and tracking using parallel computing. (D) Automatic data analysis on the contraction wave generated by the tracking. (E) The output of the *ForceTracker*. Summary data and .txt log file in case of any problem with the analysis.

4.3. SOFTWARE VALIDATION

4.3.1. FORMATION OF EHTS USING HIPSCS

The validation of the developed software was conducted by means of the mentioned EHT platforms using the same hiPSC line (LUMC0020iCTRL-06)[18]. The hiPSCs were differentiated into CMs as described previously [33, 35, 41]. Briefly, in *circular platform*, three tissues were formed per well in a 12-well plate format, using hiPSC-CMs and 3% of human adult cardiac fibroblasts (hCFs) from Promocell (C-12375). Cells at a final concentration of 16.8 x10^6 cells/mL were mixed with an ECM mixture consisting of 2X Maturation medium, fibrinogen (final concentration 2 mg/mL, Sigma-Aldrich F8630), Matrigel (final concentration 1 mg/mL), aprotinin (final concentration 2.5 µg/mL, Sigma-Aldrich, A1153) and 0.6 U/mL of thrombin (Sigma, T7513). For the *rectangular platform*, all the experiments including cell culture were conducted by researchers from LUMC, as part of a collaboration. The EHTs for the *rectangular platform* were composed of 70% hiPSC-CMs, 15% hiPSC-derived cardiac fibroblasts, and 15% hiPSC-derived endothelial cells [19]. For the ECM gel mixture, 41% of acid solubilized collagen I (3.3 mg/mL), 5% of DMEM (10X), 6% of NaOH, 9% of Matrigel (final concentration 1 mg/mL) and 39% of formation media, as previously described in [58], were used. The number of cells used per tissue was approximately 31 x 10^3 (in 2 µL volume).

4.3.2. IMAGING OF THE EHTS

Brightfield videos of both platforms were taken at 37 °C in an atmosphere of 5% CO_2, using an inverted microscope (Nikon Eclipse Ti2) with a high-speed camera, respectively Prime BSI express from Photometrics at the University of Twente and DCC3260C - High-Resolution from ThorLabs at the Leiden University Medical Center (LUMC). Contractile measurements were performed every 2 days from day 4 to day 14 after tissue formation at the University of Twente for the *circular platform* and at LUMC for the *rectangular platform*. Videos were recorded for 5-10 s approximately with a frame rate of 100 fps and a bit depth of 11-bit. In both platforms tissues were electrically stimulated at 2 Hz with bipolar rectangular pulses of 10 ms, 3–5 V/cm, using a custom-made pacing device connected to a pair of electrodes immersed into the well with tissues.

4.3.3. *ForceTracker* APPLICATION ON TWO EHT PLATFORMS

To test the versatility of *ForceTracker*, brightfield videos of tissues from the two aforementioned EHT platforms (circular and rectangular) were analyzed. More precisely, for both platforms, the tissues were analyzed under different conditions to demonstrate the software's capability to extract contractile parameters from a signal in the relevant frequency range. In the first case, spontaneous contractions of the tissues were recorded, as an example of low-frequency behavior, and in the second case tissues were electrically stimulated at 2 Hz. We successfully tracked and analyzed the contractile performance of hiPSC-EHTs from both EHT platforms. Representative graphs of contraction are in Fig.4.9. Each experiment was performed at least three separate times per platform.

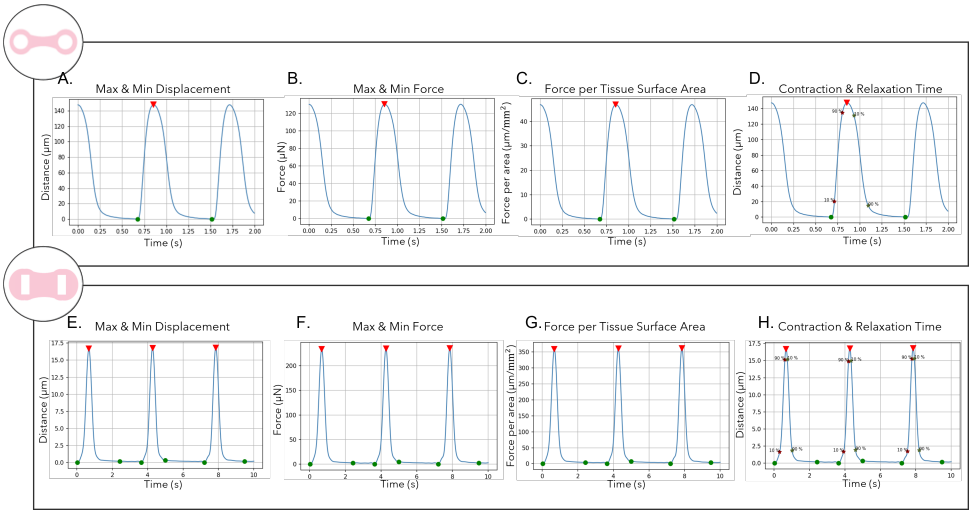

Figure 4.9: *ForceTracker* representative contractile graphs. (A-D) Circular platform. (A) Tissue displacement over time. (B) FoC over time. (C) Force per surface area over time. (D) Time of contraction to reach 10% and 90% of the upstroke and downstroke of the contraction cycle. (E-H) Rectangular platform. (E) Tissue displacement over time. (F) FoC over time. (G) Force per surface area over time. (H) Time of contraction to reach 10% and 90% of the upstroke and downstroke of the contraction cycle.

In the case of *circular platform*, we observed an increase in FoC from day 4 to day 6, which then remained constant until day 8. Later, the force reached the minimum value on day 10 and continued to increase slowly until the end of the experiment. On day 14 the value of the force was nearly as high as on day 6. All the tissues were able to follow

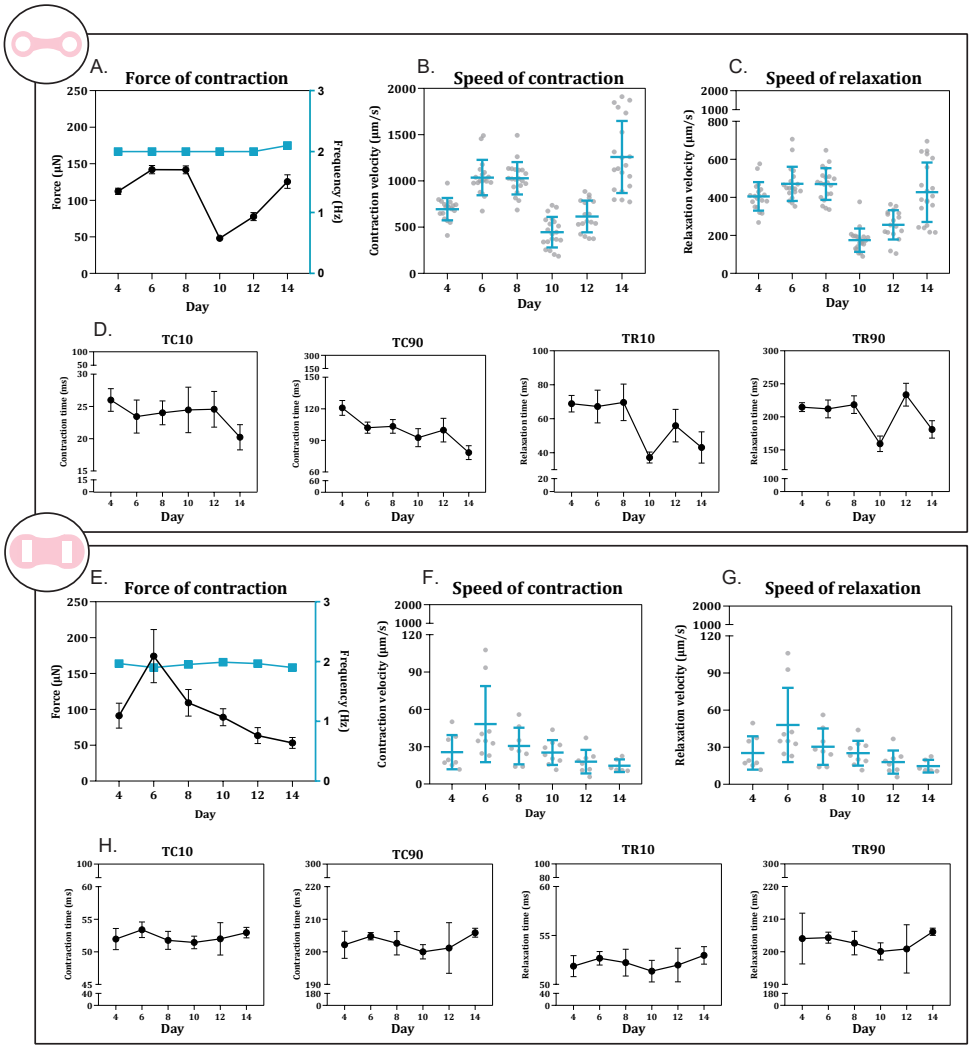

Figure 4.10: *ForceTracker* contractile performance analysis of two EHT platforms. (A-D) Circular platform. (A) FoC of EHTs and contraction frequency. Contraction kinetics, specifically, contraction (B) and relaxation velocity (C) of EHTs over time. (D) Time of contraction to reach 10% and 90% of the upstroke and downstroke of the contraction cycle. (E-H) Rectangular platform. (E) FoC of EHTs and contraction frequency. Contraction kinetics, specifically, contraction (F) and relaxation velocity (G) of EHTs over time. (H) Time of contraction to reach 10% and 90% of the upstroke and downstroke of the contraction cycle. All the measurements were done on days 4, 6, 8, 10, 12, and 14. Values are expressed as means ± SEM for N= 3. TC = time of contraction, and TR = time of relaxation

the stimulation frequency of 2 Hz (Fig.4.10A). The observed change in contractile performance over the 14 days was correlated with the contraction kinetics and contraction times output (Fig.4.10B-D).

The tissues formed in *rectangular platform* showed an increase in contractile performance from day 4 to day 6 when the maximum value was reached. A continuous decrease in force value followed until the endpoint of the experiment (day 14) (Fig.4.10E). In terms of contraction kinetics, a pattern similar to the FoC was observed, with the maximum speed of contraction and relaxation on day 6 (Fig.4.10F-G). On day 10 the lowest times to reach upstroke and downstroke of contraction were observed (Fig.4.10H).

Additionally, we analyzed the spontaneous contractions of the same tissues, prior to electrical stimulation. On average we observed that the contraction frequency of the tissues was 1.2 Hz for the tissues formed around circular pillars and 0.6 Hz for the tissues on rectangular pillars. In the case of spontaneous frequency, a similar pattern in the contractile behavior to the stimulated tissues was noticed, with a lower value of the speed of contraction and relaxation (Fig.4.11).

Finally, we evaluated the segmentation accuracy of *ForceTracker* by comparing the tissue surface area calculation with manually segmented tissues using the image processing software package ImageJ. For each time point, the first frame of the brightfield videos was used to compare the accuracy of segmentation. It is important to mention that during manual measurements the pillars' area was subtracted from the calculated surface area, as the same principle is used by *ForceTracker*. We found that the surface area relative error of *ForceTracker* is below 5% in both platforms. Specifically, in the circular platform, the accuracy is 98% on average, while for rectangular, where a high level

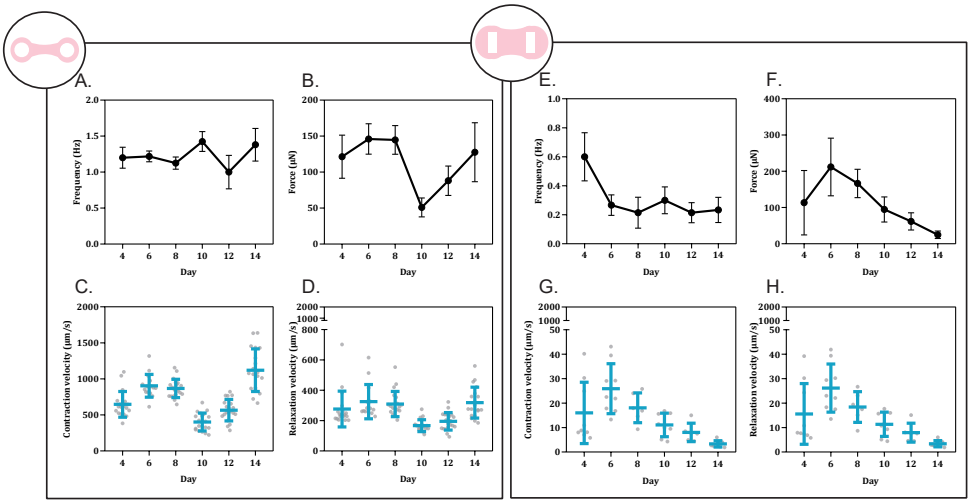

Figure 4.11: *ForceTracker* spontaneous contraction analysis. (A-D) Circular platform. (A) Contraction frequency. (B) FoC. Contraction kinetics, specifically, contraction (C) and relaxation velocity (D)of EHTs over time. (E-H) Rectangular platform. (E) Contraction frequency. (F) FoC. Contraction kinetics, specifically, contraction (G) and relaxation velocity(H) of EHTs over time. All the measurements were done on days 4, 6, 8, 10, 12, and 14. Values are expressed as means ± SEM. (N= 3).

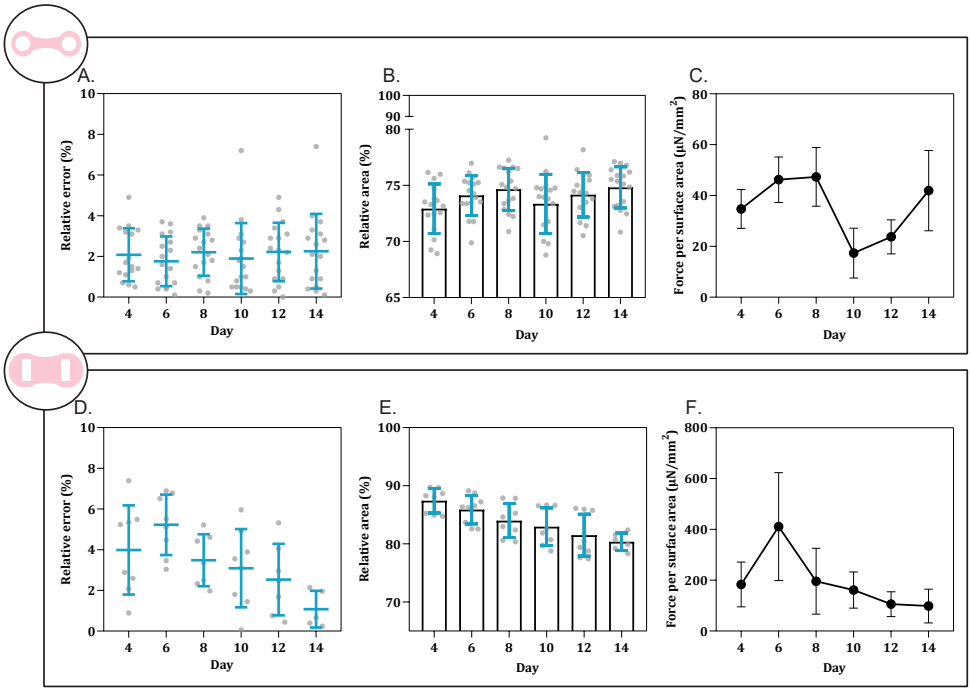

Figure 4.12: *ForceTracker* tissue surface area analysis. (A-C) Circular platform. (A) *ForceTracker* relative error tissue surface area segmentation compared to the tissue area measured manually using Image J. (B) Relative tissue compaction compared to day 0. (C) Force per surface area over time. (D-F) Rectangular platform. (D) *ForceTracker* relative error tissue surface area segmentation compared to the tissue area measured manually using Image J. (E) Relative tissue compaction compared to day 0. (F) Force per surface area over time. All the measurements were done on days 4, 6, 8, 10, 12, and 14. Values are expressed as means ± SEM. (N= 3).

of background noise was observed, the software has an accuracy on average of 97%. Moreover, based on the surface area calculations, the relative change of tissue surface area compared to day 0 showed that during the first 5 days after tissue formation, there is prominent tissue compaction in both platforms. Lastly, the force per surface area was calculated for each platform (Fig. 4.12).

4.4. DISCUSSION AND CONCLUSION

This chapter describes the implementation and validation of *ForceTracker* as a versatile tool for the assessment of 3D cardiac tissues cultivated in different EHT platforms using hiPSCs. By analyzing the contractile performance in two different platforms, we showed that *ForceTracker* can be implemented and independently used across different laboratories without further software development. We demonstrated the robust and stable performance of the software over the course of the experiments, and in various conditions. Parallel computational approach and high level of automation enabled time-efficient analysis of large data sets. *ForceTracker*'s detection and tracking showed low sensitivity to common incidental defects, such as alteration of tissue shape or air bub-

bles. The shape detection accuracy has been verified via comparison to manual measurements using the software ImageJ.

ForceTracker fills the gap of a missing software for contractile performance analysis of tissues in 3D platforms, with reference to the most used pillar shapes (rectangle and circle). By using a shape-independent algorithm and an easy-to-use user interface, the application has the advantage of automatically analyzing multiple videos in an unbiased way, taking into account the geometry and mechanical specifications of each platform. The software demonstrated robustness and stability of detection over large amounts of data. Additionally, *ForceTracker* is not dependent on the symmetric position of tissues in all the frames, as each pillar is tracked independently. However, the main challenge for the detection arises from the variability of brightness and contrast among videos. To circumvent this drawback, critical image pre-processing steps were successfully implemented. Nevertheless, there is still occasionally the need for manual detection correction, as the range of artifacts and variations in videos that can be anticipated by the algorithm is necessarily limited. In the future, optimal camera settings can be found and recommended to the users for video recordings.

The current outputs of the software are graphs showing the displacement of pillars, the tissue force of contraction, as well as the detailed contraction kinetics analysis. We also incorporated the analysis of changes in tissue surface area over time, as an additional readout of force per tissue surface area [97]. This information complements the contractile performance analysis of 3D cardiac tissues. While this readout provides information about the tissue compaction over time and during each contraction, it does not replace force per cross-section area measurements. The tissue cross-section area measurement requires an additional histological step which puts an end to the experiment and therefore limits the throughput.

The versatility of *ForceTracker* was demonstrated by analyzing over time the contractile performance of EHTs under electrical stimulation and during spontaneous contraction. We analyzed tissues from two different EHT platforms in collaboration between three research groups (LUMC, Delft University of Technology, and University of Twente). The findings we presented correspond to what was previously shown in each platform, even though a direct comparison between the platforms could not be conducted in this experiment because of differences in cell types used for tissue formation. Nevertheless, it is important to mention that by using the same hiPSC line we could observe that between day 4 and day 6 the EHTs showed the highest force of contraction in both platforms. Additionally, a significant difference in the speed of contraction was observed between the two platforms, even though the force values are comparable (Fig.4.10). This is related to the difference in pillar size and the mechanical properties of each platform. Particularly, in the *circular platform* tissue displacement during the contraction cycle is larger than in the *rectangular platform* (Fig.4.9). However, the effective stiffness experienced by the tissues is lower for circular-shaped pillars than for rectangular ones, which explains the contractile performance.

Overall, *ForceTracker* represents a milestone toward standardized analysis of contractile tissue performance in 3D *in vitro* models that use flexible anchoring points. These models are not only limited to cardiac physiology. 3D tissue-like constructs are often used also on e.g. skeletal muscle platforms [98, 99]. *ForceTracker* can be applied

not only for standardized contractile measurements in EHT platforms but also to extend the measurement principle to all OoC platforms hosting suspended tissues, in which generated contraction force or applied load is a required readout. The contractile performance measurements obtained in this way provide valuable quantitative data to evaluate disease models and drug responses.

CHAPTER 5

INTEGRATED FORCE SENSING

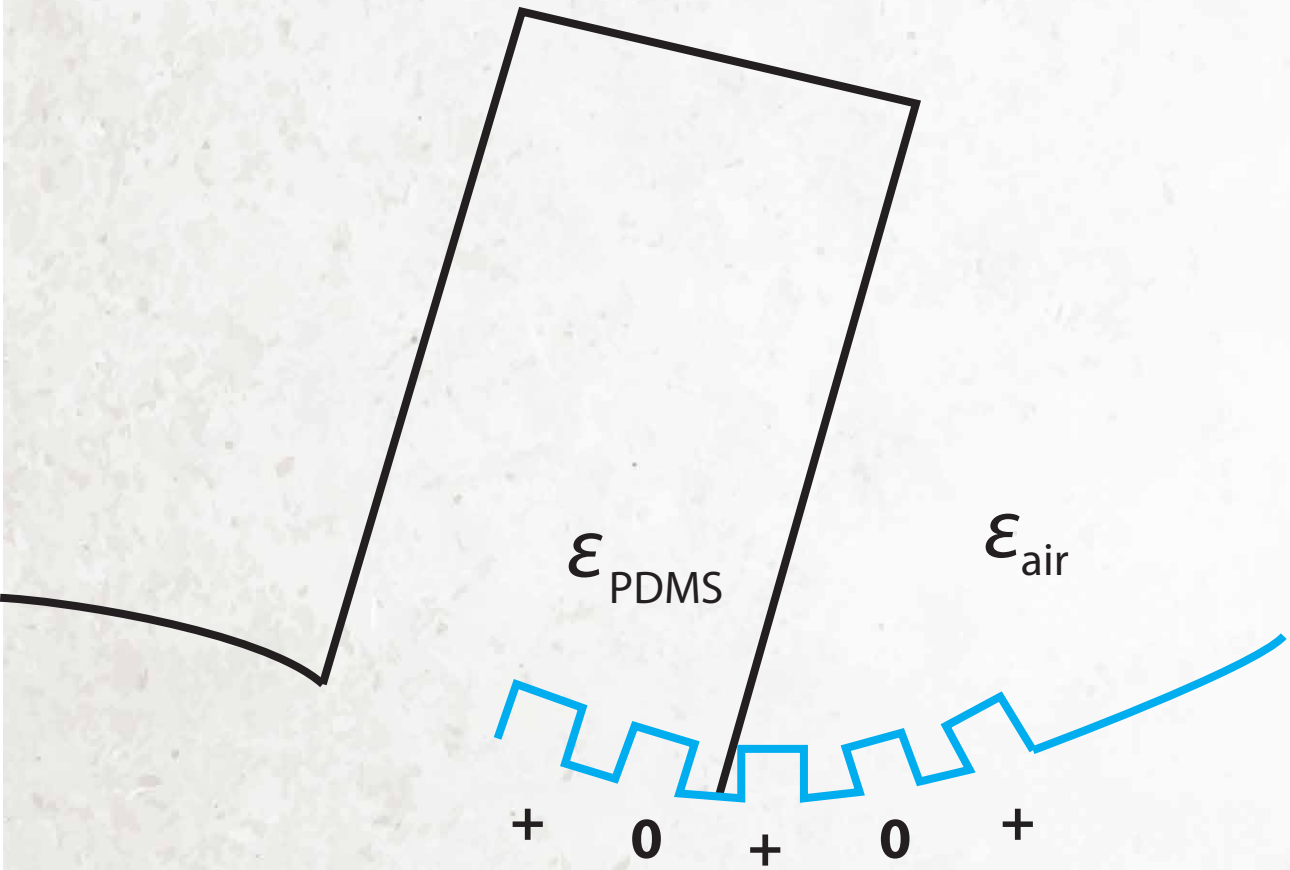

|part of this chapter have been published in *22nd International Conference on Solid-State Sensors, Actuators and Microsystems (TRANSDUCERS 2023)*, June 2023

5.1. STRATEGIES FOR ELECTRICAL CONTRACTILE FORCE READ-OUT

THE importance of assessment of tissue contractile performance in the developed EHT platform was previously discussed in a detailed manner. Until now, the optical method has been implemented as the golden standard for measurements of tissue contraction force in EHT platforms. However, the procedure is laborious, and cannot be conducted in real-time in most cases. Automation and high control of EHT microenvironments can therefore be achieved only by integrating force sensors within the platforms. An electrical force readout would allow real-time monitoring of the tissue contractile performance and enable closed-loop control systems for e.g. pacing and mechanical stimulation.

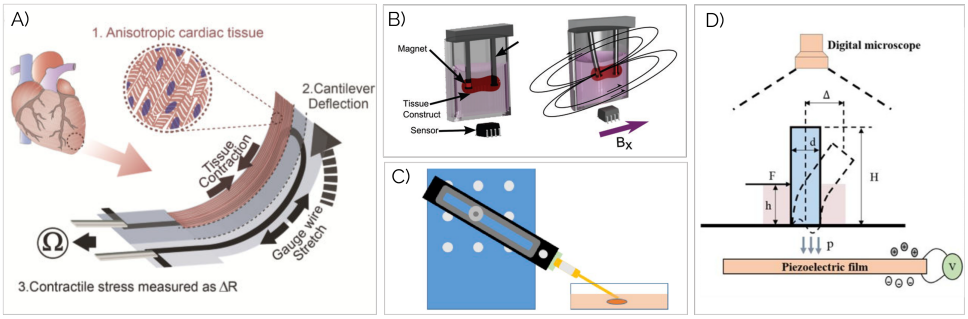

Figure 5.1: Examples of force sensing in cardiac tissue platforms: A) Strain gauge embedded in polymer-based cantilever for measuring cardiac tissue contraction [1]; B) Magnetic sensing of cardiac tissue contraction [2]; C) Piezoelectric cantilever sensor probe for force measurement [3]; D) Detection of micro-pillar array deformation via digital image processing and piezoelectric sensing techniques [4].

There are several examples of the use of different sensing techniques to assess the contractile properties of cardiac tissues electrically, as shown in Fig.5.1. Some of them are even implemented in a configuration similar to the EHT platform developed in this thesis. One of the most common force measurement techniques is traction force microscopy. Via high-resolution microscopes and sophisticated image processing algorithms, displacements produced in the platform are translated to forces. This is very useful when the platform under consideration is an array of micropillars. Furthermore, strain sensing techniques have been widely used for contractile force assessment of thin cell layers via integrated piezoresistive strain gauges (Fig.5.1A)[100]. However, there is still a lack of application of this sensory mechanism in 3D platforms. Another example is magnetic force sensing, whereby the displacement of micropillars with embedded magnets causes an alteration in the electrical output of the magnetoresistive sensor below (Fig.5.1B) [101]. In this case, the sensor is separate and placed outside of the tissue culturing chamber. One of the few integrated solutions includes piezoelectric materials. These sensors have been exploited for measurement of the force applied by the tissue on thin piezoelectric layers integrated below the micropillar arrays or on the cantilever sensor probes (Fig.5.1C, D)[102, 103].

With many available techniques and advancing integration and fabrication methods,

the requirement for integrated sensing solutions in OoC platforms becomes achievable. The advantages of sensor integration are numerous. Besides the previously mentioned need for automation, there is also the high precision in fabrication resulting in sensor reproducibility, accurate transduction capabilities, and a variety of available read-out circuitry for both static and dynamic measurements. Additionally, an integrated sensor may provide the advantage of single-pillar characterization, as opposed to the coupled analysis performed in currently used optical methods.

In the context of the developed platform, assessment of the tissue contractile properties was previously performed indirectly, by monitoring the bending of the elastic pillars. This is a non-invasive method of measuring the force of contraction and contractile kinetics, without interfering with the electro-mechanical coupling of the tissue itself. The same principle can be followed when considering the integration of an electrical force readout. Again, the mechanics of bending pillars can be exploited to relate the resulting deformation to the applied force of contraction. When the force is applied on the pillar side, the maximum bending moment and the maximum stress are generated at the pillar-substrate interface. Since both pillars and the substrate are made of elastic material, the stress is distributed within the substrate causing its deformation. Taking into account this effect as well as the nature of layer-by-layer microfabrication, the idea here proposed is to design a co-planar sensor that can be integrated into the elastic substrate to exploit in the optimal way the deformation occurring upon pillar bending.

5.2. SUBSTRATE DEFORMATION ANALYSIS

5.2.1. ANALYTICAL MODEL

Extensive analysis of the mechanical response of the system of two elastic pillars, attached to the elastic substrate, upon the application of a partially distributed load along the length of the pillars has been conducted. The described system is analog to the developed EHT platform from previous chapters, consisting of two PDMS micropillars,

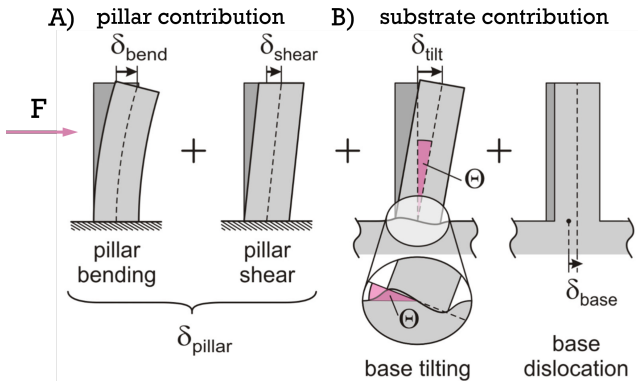

Figure 5.2: Illustration of all the components contributing to the total deflection of pillars when force is applied along its height. A) contribution from bending and shear of the pillar B) contribution of the substrate with base tilting and dislocation.

around which a cardiac tissue compacts and applies cyclic contractions.

It was already mentioned previously that there is a certain contribution to the displacement of pillars originating from the substrate deformation, which was taken into account through the additive constant (Section 2.4.2). Here, this effect will be subjected to analysis and used as a basic mechanism for sensing the pillars' displacement.

When a force is applied in a lateral direction upon elastic pillars (see Fig.5.2), the resulting mechanical response is pillar deflection. This deflection can be attributed to several involved mechanisms. The dominant one, especially in the case of the rigid substrate, originates from the pillar bending and it is defined by Hook's law: $F = k_{bend}\delta$. In linear elastostatics, besides the bending, there is also the effect of shear deformation of pillars with less significant influence in the case of the soft pillars with high aspect ratios [70]. Furthermore, due to the presence of an elastic substrate below the pillars, an additional effect appears, which happens to be essential for the used sensing mechanism. There is an additional component in the total pillar deflection originating from the warping of the substrate and tilting of the pillar centroid axis. This warping is the result of the axial tension in the substrate as a balancing reaction to the torque acting on the beam [104]. Axial tension at the pillar base can be expressed as:

$$\sigma_{zz} = -x\frac{M}{I}, \tag{5.1}$$

where M is the torque at the bottom of the pillar when a force F acts at the top ($M = L \cdot F$), I is the second moment of inertia of the beam, and x is the distance from the point at the pillar cross-section from the neutral axis. As the maximum stress occurs at the edges of the beam, where the distance from the centroid axis is maximum ($x = c$), it is possible to express normal stress σ_{zz} as a function of maximum stress σ_{max}:

$$\sigma_{zz} = -\frac{x}{c}\sigma_{max} \tag{5.2}$$

The tilt of the pillar base upon the force applied along the pillar length is proportional to the substrate deformation and can be described as:

$$\Theta = T_{tilt}(\nu)\frac{\sigma_{max}}{E_y} \tag{5.3}$$

Here $T_{tilt}(\nu)$ is the tilting coefficient derived in [104], which depends only on the Poisson ratio of the material ν, and E_y is Young's modulus of the material. Hence, the contribution to the total pillar displacement from the substrate deformation, for a sufficiently small tilt angle θ, can be expressed as:

$$\delta_{tilt} = L\tan(\theta) \approx L\theta \tag{5.4}$$

Starting from Eq.5.1, it is also possible to derive the distribution of the substrate deformation at the substrate-pillar interface in vertical z direction, as a consequence of the axial tension σ_{zz}. Here, only the final analytical expression is mentioned and the complete derivation can be found in [105]. Now, the analytical function that describes the

out-of-plane displacement u_z of the substrate below the pillar, as a consequence of axial tension, is:

$$u_z = h^2 \frac{3M}{4\pi EI} \int_{\frac{x}{h}-0.5}^{\frac{x}{h}+0.5} ds \int_{\frac{y}{w}-0.5}^{\frac{y}{w}+0.5} dt \frac{\frac{x}{h}-s}{\sqrt{s^2+t^2}} \tag{5.5}$$

Here h and w are the height and width of the pillar, respectively, while M, E_y, and I were previously introduced. The integration is carried out across the lateral cross-section of the pillar.

Table 5.1 gives all the parameters used for calculations. The force is applied as a line load in the middle of the pillar ($M = F \cdot \frac{L}{2}$). The solution for u_z was obtained by double integration using the function *integral2* in Matlab, for every point (x, y) in a square surface area at the pillar-substrate interface in range (-400, 400) µm for both coordinates. The 3D representation of the obtained substrate deformation in z direction (u_z) is shown in Fig.5.3A.

Table 5.1: Parameters used for substrate displacement calculation

Parameter	Description	Value
L	pillar length	700 [µm]
w	pillar width	478 [µm]
h	pillar height	210 [µm]
F	applied force	50 [µN]
E_y	Young's modulus	1.2[GPa]
ν	Poisson's ratio	0.5

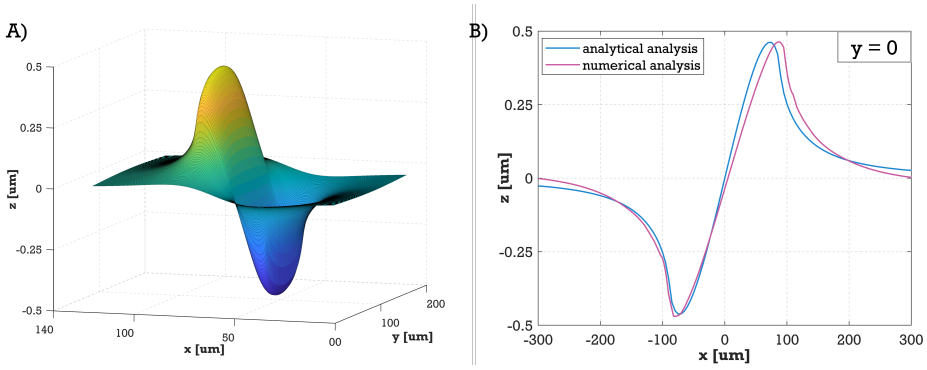

Figure 5.3: A) 3D representation of substrate deformation obtained from the analytical model; B) Comparison of the analytical and numerical model for substrate deformation across the pillar, for $y = 0$. The applied force is 50 µN at the middle of pillar length ($H = \frac{L}{2}$) in both cases.

5.2.2. NUMERICAL ANALYSIS

In addition to analytical modeling, Comsol Multiphysics was used to carry out FEM analysis. The mechanical response of the system with elastic pillars was modeled using the Solid Mechanics module, as described previously (Sections 2.4.1 and 3.4.1). Dimensions of the pillars and all relevant parameters used for the calculations are given in Table 5.1. The simulation flow is described in Fig.5.4.

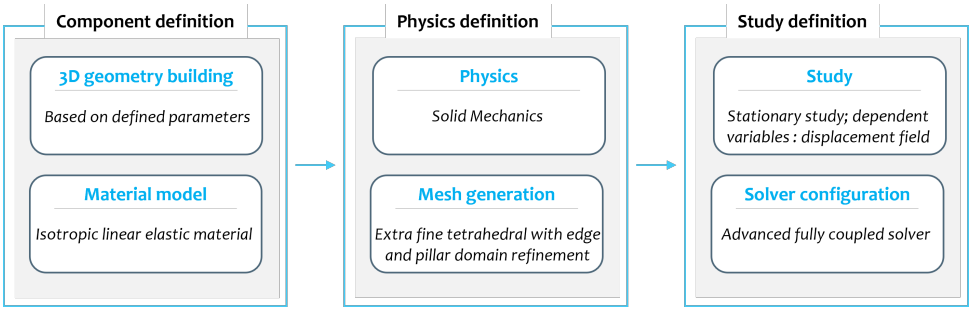

Figure 5.4: Computational flow of FEM study of PDMS substrate deformation below rectangular pillars, upon force application, implemented in Comsol.

At this stage, Comsol simulations were used to compare the analytical analysis of the substrate deformation upon bending of the pillars with the results from FEM analysis. The substrate deformation across the middle of the pillar (x axis) for $y = 0$ was exported from Comsol and compared to the calculations carried out in Matlab using Eq.5.5 for the same conditions. This comparison is shown in Fig.5.3B and it was used to validate the numerical model, which will be used for further substrate analysis and integration of complex sensor geometry. Fig.5.3B shows good agreement of the maximum substrate displacement along the x axis of both numerical and analytical models.

Due to the complexity of the study, the rest of the substrate deformation analysis and search for the optimal sensor placement the studies were performed only using FEM in Comsol.

5.2.3. OPTIMAL SENSOR POSITION

Substrate deformation and consequential strain were examined on multiple positions to explore the possibilities for optimal sensor positioning. The substrate deformation was analyzed along x, y, and z directions on the pillar-substrate interface, by varying the distance from the neutral axis of the pillar. The graphs showing a decline in deformation δ_z with the distance from the center of the pillar for all three directions are shown in Fig 5.5. Fig.5.5A exaggerates the effect of substrate deformation for purpose of graphical representation.

Based on this analysis, conclusions about the optimal sensor position can be drawn. First, the vertical position of the sensor should be in the range of 0-100 µm from the pillar-substrate interface inside the substrate. Outside of this region substrate deformation drops significantly (Fig.5.5D, Fig.5.6A). Further on, based on the change in substrate deformation in the x and y direction from Fig.5.5 B, C the area of pillar deformation can

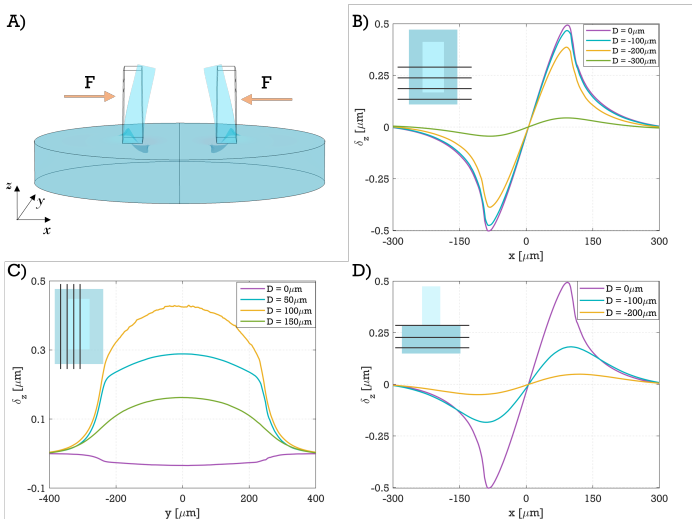

Figure 5.5: Substrate deformation analysis upon force application in the middle of pillars length: A) 3D representation of the mechanical response of the system with two pillars on an elastic substrate when force F is applied; B) Substrate deformation in z direction on different positions along B) x, C) y and D) z axis.

5

be determined. This area is maximized to include every part of the substrate below the pillar subjected to deformation. The top view of these regions is shown in Fig.5.6B and it defines the optimal areas for sensor placement. Ideally, the sensor should be positioned in a way to cover the entire area experiencing deformation, to maximize force detection. Finally, due to the anti-symmetric nature of the substrate displacement and generated strain around the neutral x-axes of the pillars, the optimal arrangement would include two separate sensors detecting opposite strain in the substrate: compressive with the positive substrate deformation in z direction, and tensile in the area with negative substrate deformation. In Fig.5.6 it is indicated with white rectangles the optimal range for sensor positioning both in the $x-y$ plane as well as in-depth.

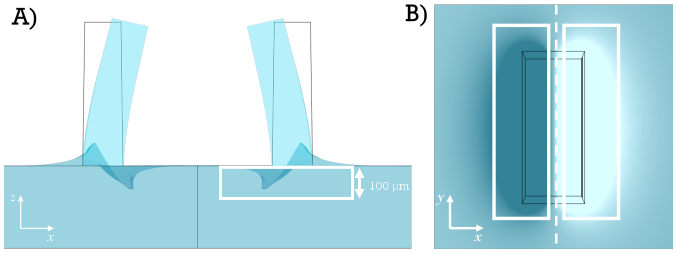

Figure 5.6: Cross-section of the EHT platform with two pillars displaced upon force application, with enlarged resulting substrate deformation and an indication of the optimal range for vertical sensor placement within the substrate; B) top view of single-pillar deformation, with white rectangles indicating the optimal areas for sensor placement in $x-y$ plane.

5.3. CAPACITIVE SENSING OF PILLAR DISPLACEMENT

5.3.1. SENSING STRATEGIES

When choosing the optimal sensing mechanism that would fit such a specific application of force detection in the developed EHT platform, there are several requirements to take into account.

First, the sensor should be able to measure very small substrate deformations, i.e. in the sub-micron range (see Fig.5.5), corresponding to very low strain values ($\sim 10^{-3}$). Therefore, the sensing mechanism should be sensitive to such small perturbations. Furthermore, the desired signal for measurement has quite slow dynamics (0-3 Hz) hence, the sensor should enable high performance in this range of frequencies. As the EHT platform is made using microfabrication techniques, the sensor fabrication should be compatible with the standard micromachining methods. Finally, the complexity of the read-out circuitry is another criteria to consider. The final measurement setup will be used in a cell culturing facility, therefore the need for the development of a compact and portable system emerges. Based on mentioned criteria, several sensing mechanisms were proposed and analyzed in detail for the specific application. Their analysis is elab-

Table 5.2: Comparison of different transduction mechanisms for use in pillar displacement sensing.

sensing mechanism	***Piezoresistive***	***Capacitive***	***Piezoelectric***
sensing objective	strain	substrate displacement	pressure
sensitivity	0.1 Ω/N	1.5-4.8 pF/N	0.05 nV/N
advantages	• Cleanroom compatible • Efficient integration with on-chip electronics • High sensitivity	• Cleanroom-compatible • Suitable for soft-substrate integration • Temperature stability • High sensitivity • Little to no hysteresis	• High sensitivity
disadvantages	• Sensitive to temperature changes • Low suitability for soft substrates integration • Hysteretic output signal • High power consumption	• Presence of parasitic and stray capacitance • Complex read-out electronics • Output non-linearity	• Low resolution • Only for highly dynamic setups • Complex read-out electronics • Not cleanroom compatible

orated within the master thesis project of Mahdieh Shojaei Baghini [106]. Here, only conclusions and final comparisons are presented.

Piezoresistive, piezoelectric, and capacitive sensors were considered as a potential solution, with small fabrication complexity and high dynamic range, for detection of the substrate deformation in the EHT platform [107–112]. It was shown that, even though the piezoelectric approach has the highest sensitivity for detection of very small substrate deformation, its low resolution in low dynamic measurements comes as a significant drawback. The piezoresistive principle demonstrated high compatibility with MEMS fabrication techniques, however, it showed inferior sensitivity compared to the other two sensing mechanisms. Finally, capacitive displacement sensing showed the best overall characteristics, taking into account the previously mentioned criteria. It has the highest sensitivity normalized to the base value of the electrical quantity, it is relatively simple to integrate into the existing EHT platform, and the read-out circuitry is not more complex than for the other two sensing mechanisms. Table 5.2 summarizing these three transduction techniques is shown below.

5.3.2. CAPACITIVE SENSING: WORKING PRINCIPLE

From the aforementioned transduction mechanisms, the co-planar capacitive sensor has been selected as the most suitable for the specific purpose of force assessment in the EHT platform via substrate deformation quantification. This sensing principle relies on the change in the capacitive readout as a consequence of the mechanical displacement of the capacitor plates and the dielectric in between them. The displacement of plates is caused by the substrate deformation and does not depend on the strain transfer efficiency to the sensor itself, unlike in other sensing alternatives discussed previously (piezoelectric and piezoresistive).

The reasons for selecting a co-planar configuration instead of a parallel plate configuration for the capacitive sensor are mentioned below. First, due to the geometry and nature of the co-planar capacitor, the fringing field lines are very prominent, in addition to the direct lines between the capacitor plates [113]. This makes the measured capacitance more sensitive to the change in the dielectric material surrounding the plates, the

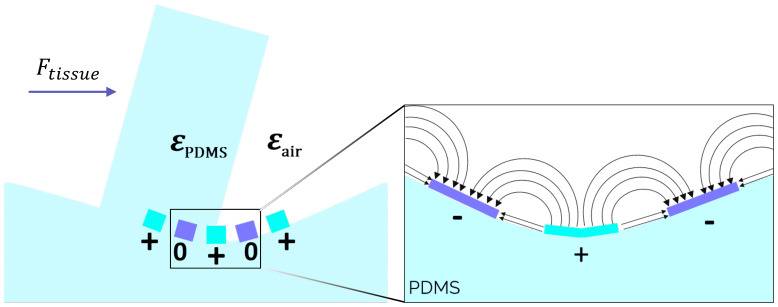

Figure 5.7: Simplified illustration of the co-planar capacitor working principle: Upon pillar bending, capacitor plates are displaced, directly affecting the electric field between them. The electric field distribution, dominantly determined by the fringing field lines, is shown in the close-up insert.

distance, and the tilting of the plates, than in the case of parallel capacitors. Second, since the sensor needs to be integrated within a previously developed EHT platform, its fabrication needs to be compatible with microfabrication techniques. Also in this sense, patterning the metal lines of a co-planar capacitor in a single layer and having contacts in the same plane is much simpler than creating a sandwich-like structure of polymer-metal multilayers to obtain parallel-plate capacitors. For the mentioned reason, a co-planar spiral capacitive sensor was selected for detecting substrate deformation upon tissue contraction in the EHT platform.

For a co-planar capacitor consisting of multiple alternating plates, the total capacitance is a superposition of all the fringing fields between the adjacent plates as well as the parallel plate capacitance, which is negligible in this case. The illustration of the working principle of the co-planar capacitor upon pillar displacement is shown in Fig.5.7 with the enlarged illustration of electric field lines among three planar capacitive plates.

5.3.3. SPIRAL CO-PLANAR CAPACITIVE SENSOR

The idea of co-planar capacitive sensing can be used in various designs, for example in interdigitated or spiral arrangements. It has been shown that the spiral design has a higher base capacitance than the interdigitated one for the same total length of the lines, increasing in this way signal-to-noise ratio [106]. Additionally, with a spiral design, deformation in both x and y directions can be detected via the change in plate distance, hence the spiral design has been selected for integration, although the individual force components along x and y cannot be distinguished.

The geometry of a spiral co-planar sensor consists of two metal plates, organized in a spiral geometry, with N1 and N2 turns respectively. Each metal plate interacts via fringing fields with the neighboring, oppositely charged plates. Two spiral capacitors are positioned below each pillar to exploit the effect of anti-symmetric substrate deformation and enable differential readout of capacitance change. Thus, the final design resulted in

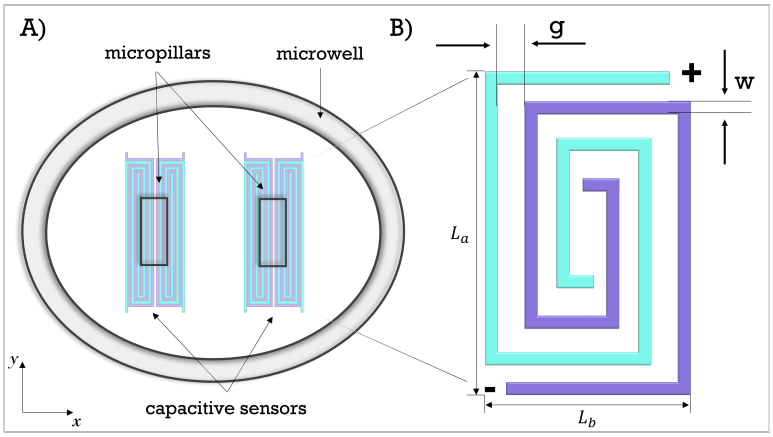

Figure 5.8: A) Top view of the EHT platform with integrated co-planar capacitive sensors. B) Sketch of a single spiral capacitor with the relevant dimensions.

four sensors per EHT platform, with two sensors per pillar. The top view of the platform with integrated sensors is shown in Fig.5.8A. An individual spiral capacitor is shown in Fig.5.8B. Here, w is the width of the metal lines, g is the gap between them, and L_a and L_b are the outer dimensions of the sensor.

The rectangular shape of the spiral configuration was chosen over the circular one, for its higher sensitivity to displacement in a specific direction. In the case of our EHT platform, the force upon pillars is always applied in x or $-x$ direction, depending on the pillar position. Therefore, the dominant substrate deformation with the anti-symmetric shape around the neutral plane (see Fig.5.5B) happens in the same direction. For this reason, the longer plates of the spiral capacitor are perpendicular to the main deformation direction, exposing the dielectric between the plates to the maximum pressure changes. A single spiral sensor is placed at the peak of the compressive or tensile strain, resulting in the increase of the gap between neighboring capacitor plates in case of compression, or a decrease of the plate distance for compressive strain. The resulting displacement of sensor plates upon tension and compression occurring in the substrate is illustrated in Fig.5.9 where the sensor deformation is enlarged in Comsol for clear visual representation.

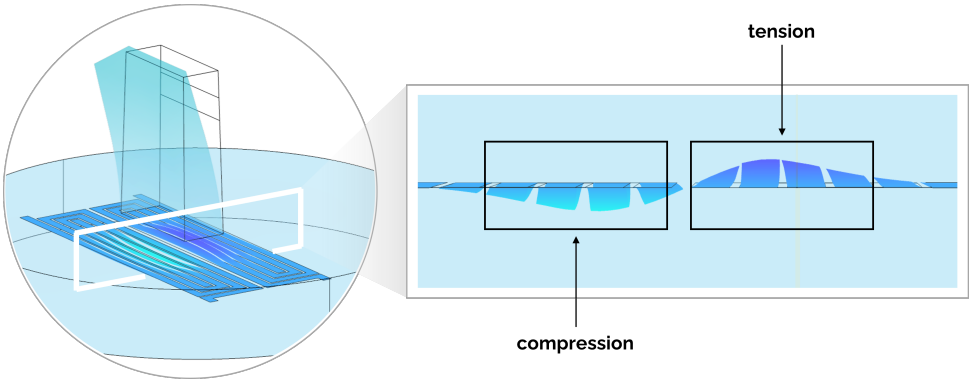

Figure 5.9: Illustration of the sensor plates displacement, in two co-planar capacitors, due to the compression and tension occurring in the elastic substrate upon pillar bending.

The sensitivity and performance of the sensor can be tuned by varying the ratio between metal layer width (w) and the gap between plates (g). This is characterized as a metallization ratio (MR) by the following definition:

$$MR = \frac{w}{w+g} \tag{5.6}$$

By varying the metallization ratio and the number of turns, different sensor configurations can be explored. Four sensor types have been designed and analyzed. The designs were made by keeping the outer dimensions constant and changing the metallization ratio only. Dimensions of all four sensor types are given in Table 5.3.

Based on the given dimensions, a glass-chromium mask was designed for photolithography fabrication steps, as illustrated in Fig.5.10A. All four different sensor types were

Table 5.3: Dimensions of four sensor variations.

parameter	Sensor A	Sensor B	Sensor C	Sensor D
$g[\mu m]$	5	10	5	10
$w[\mu m]$	20	10	5	40
MR	0.8	0.5	0.5	0.8
$L_a[\mu m]$	1200	1200	1200	1200
$L_b[\mu m]$	200	200	200	200

part of the final mask design, and each type occupies a single wafer quadrant. The wafer distribution of sensors with a detailed design of a single wafer die with four sensors and corresponding interconnects and contact pads are shown in Fig.5.10A. A close view of each sensor type and their position with respect to pillars is represented in Fig.5.10B.

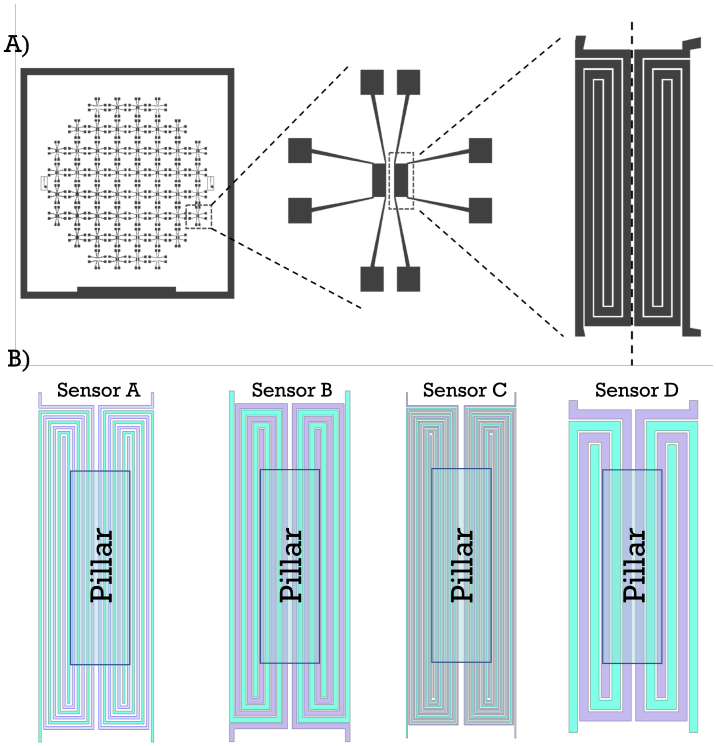

Figure 5.10: A) Photolithography mask including four sensor designs, with the close-up image of a single wafer die containing four sensors with corresponding interconnects and contact pads; B) Illustration of the four sensor designs and their position with respect to the pillar.

5.3.4. NUMERICAL SIMULATIONS

The electrical response of capacitive sensors upon pillar deformation was carried out using FEM analysis in Comsol Multiphysics. A system of two pillars on an elastic substrate, with embedded capacitive sensors, was placed in a spherical air domain to facilitate the analysis of capacitance change as a consequence of the pillar bending and substrate deformation (Fig.5.11A). The inner domain of the sphere was assigned to a moving mesh, to take into account the electric field distortion due to the pillar bending. The outer shell of the sphere was defined as an infinite boundary converging towards the zero charge. The plates of the spiral capacitors were modeled as conductors using Shell physics, for infinitesimally thin metal layers. The actual thickness of capacitor plates is ~1 µm (see Section 5.4.1), which is negligible compared to the other dimensions in the model, making the mesh generation very challenging. Comsol's Shell module seemed to be a valid approach, as computational accuracy is preserved due to fringing fields mostly determining the total capacitance. Additionally, meshing complexity was significantly reduced by avoiding submicron-thin objects. Still, the dimensions of the metal plates were much smaller than the rest of the objects in the model, hence different meshing must be defined for each of these domains. Fig. 5.11B illustrates the meshing of the entire computational model, while Fig.5.11C gives fine details of the delicate meshing of the substrate, pillars, and sensors with more dense and refined elements at the contact between different regions.

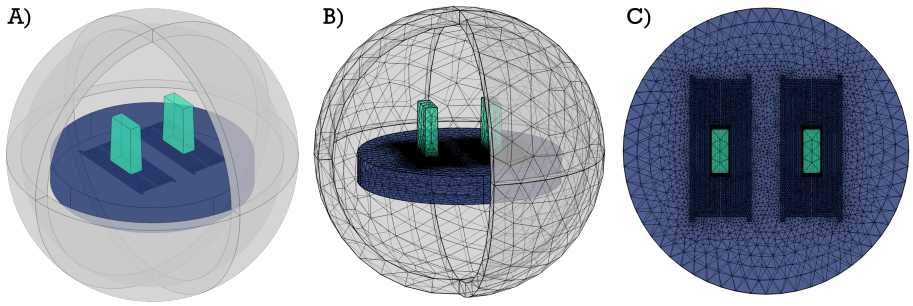

Figure 5.11: 3D Comsol model of the system with pillars with integrated capacitors: A) geometry design of the pair of pillars (green) on an elastic substrate (blue) with integrated pair of spiral capacitors below each pillar (dark blue) within a spherical air domain (grey); B) mesh of the entire geometry to define computational nodes; C) top view of different mesh size for the pillar, substrate, and sensor area.

FEM computation included coupling of the mechanical and electrical response of the system represented in Fig.5.11A. The mechanical response of the system to the force applied along the pillar's length generates displacement of pillar and substrate deformation. The obtained mechanical output and substrate deformation were used to define input for the second computational step, in which capacitance between displaced plates was calculated. The two-step computational model was implemented in Comsol using a Multiphysics approach to couple Solid Mechanics and Electrostatics modules. The computation flow of the model is shown in Fig.5.12.

Sensor performance was characterized based on several carried-out analyses. First, the base capacitance was calculated for all four sensor types in the static case, i.e. when

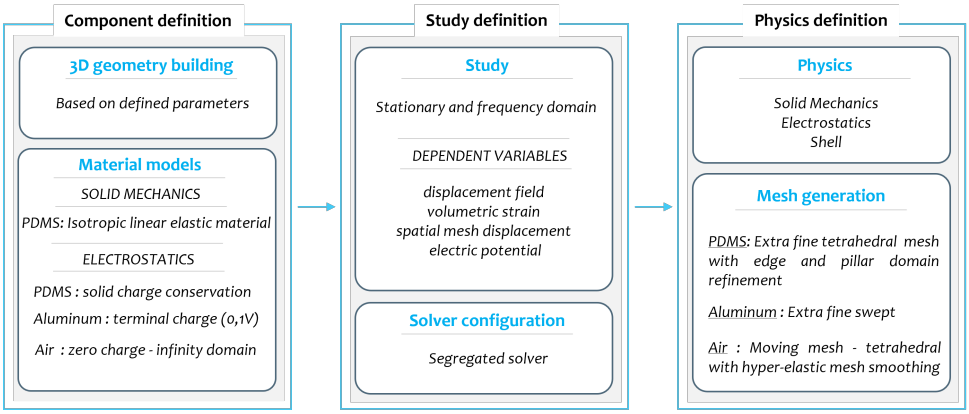

Figure 5.12: Computational flow of FEM study of electric field distortion and capacitance change of spiral co-planar capacitors as a consequence of mechanical response of the system with two PDMS pillars to the force acting along pillar length.

5

there is no force applied on the pillars and therefore no substrate deformation. This is defined as base capacitance C_0.The calculations were made for the sensor integrated at 150 µm depth from the substrate surface. The depth choice was made to ensure that electric field lines are propagating entirely through the PDMS medium, making the comparison to the theoretical model more faithful. Base capacitance for similar conditions was also calculated using the co-planar waveguide (CPW) theory [109, 114]. This theory can be applied to a system of spiral plate capacitors, by mapping it to a standard parallel plate capacitor model, while preserving geometry, with the use of elliptical integrals according to [109]. The model derives capacitance per unit length of a co-planar capacitor embedded into the PDMS substrate, surrounded by air domain, as illustrated in Fig.5.7. The capacitance per unit length of a CPW is defined as:

$$C_{CPW} = \epsilon_{ref} C_p \tag{5.7}$$

Here ϵ_{ref} is the effective relative permittivity of the system depending on the dielectric material around the capacitor ($\epsilon_{air}, \epsilon_{PDMS}$) and the geometry of the metal lines, and C_p is the partial capacitance of the CPW in vacuum. The partial-capacitance method can be applied in multilayered systems, by separating the effect of each layer (air and PDMS in this case) via modified dielectric constant [115]. The influence of spiral geometry in both ϵ_{ref} and C_p is included through elliptic integrals of the first kind. Detailed derivations of ϵ_{ref} and C_p are given in [109], and here only final expressions were used to calculate the capacitance of the sensors. The partial capacitance of the CPW embedded into the PDMS (C_{CPW}) is then translated into the total capacitance of the spiral capacitor by multiplying it with the average path of each spiral plate l_{av}, from Fig.5.8:

$$C_{spiral} = C_{CPW} l_{av} \tag{5.8}$$

This capacitance derivation is considered an approximation for the case of rectangular spiral sensors, and it is used only to give an estimation of the capacitance range for the

four considered sensors, as well as a benchmark for the results obtained from Comsol simulations. A comparison of the base capacitance values is given in Table 5.4.

Table 5.4: Comparison of base capacitance values.

Sensor type	A	B	C	D
$C_{analytical}$ [pF]	0.55092	0.41017	0.73418	0.348655
$C_{numerical}$ [pF]	0.59279	0.43321	0.77640	0.36013
Sensitivity [pF/N]	1.51	3.1	4.864	0.86

Furthermore, the sensitivity of each sensor is obtained from the following equation:

$$S = \frac{C - C_0}{F - F_0} \tag{5.9}$$

where C_0 is the base capacitance when there is no substrate deformation (F=0), and C is the effective capacitance in case of substrate deformation when F = 50 µN is applied upon the pillar. The sensitivity analysis was performed by varying sensor positions within the PDMS substrate in z direction, to understand the sensitivity change with respect to the distance from the pillar-substrate interface. Calculations were performed for all four types of sensors, and are shown in Fig.5.13. It can be noticed in the graphs that sensitivity drops exponentially with the increase in distance from the bottom of the pillars. This is true for all four sensor types, where the fastest drop in sensitivity is noticed for sensor A. The exponential drop in sensitivity is consistent with the previous analysis of the substrate displacement (Fig.5.5D), which also declines abruptly when going deeper into the substrate. Based on the conducted analysis, the expected change in capacitance, for the force of 100 µN is in the range (80 - 500) aF, depending on the sensor type.

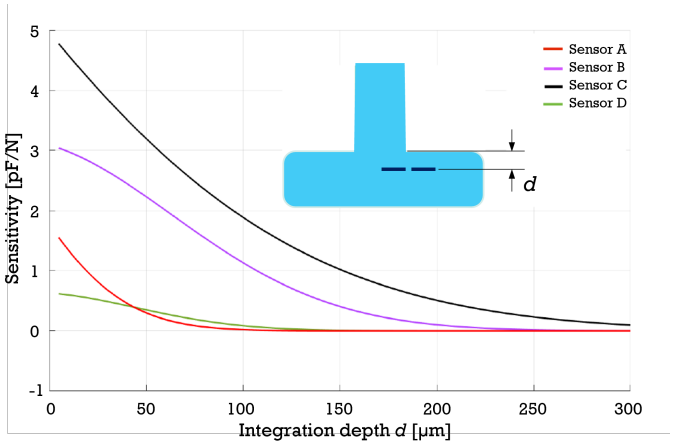

Figure 5.13: Analysis of the change in sensitivity of all four sensor types with the increased integration depth within the PDMS substrate.

Lastly, time-dependent analysis was conducted to analyze sensor response when the cyclic contraction of cardiac tissue is applied upon pillars. To simplify the calculations, only sensor D was subjected to this study, as it contains the least meshing nodes among the four sensors in consideration. For modeling purposes, a sinusoidal signal with frequency f=0.4 Hz and amplitude F_0 =50 µN was applied as a load upon the middle of the pillar length. The resulting capacitance change was estimated for both sensors below a single pillar in positions S_1 and S_2, as shown in Fig.5.15. The sensor in position S_1 experiences positive capacitance change as the plates decrease distance due to the tensile strain in the positive semi-period of the sine-wave function. At the same time, sensor S_2 detects the opposite capacitance change due to the distance increase between capacitor plates as a consequence of compressive strain in the substrate, as previously shown in Fig.5.9. Fig.5.14 demonstrates the anti-symmetric behavior of sensors in different positions below the pillar, which provides arguments for differential force readout from each pillar.

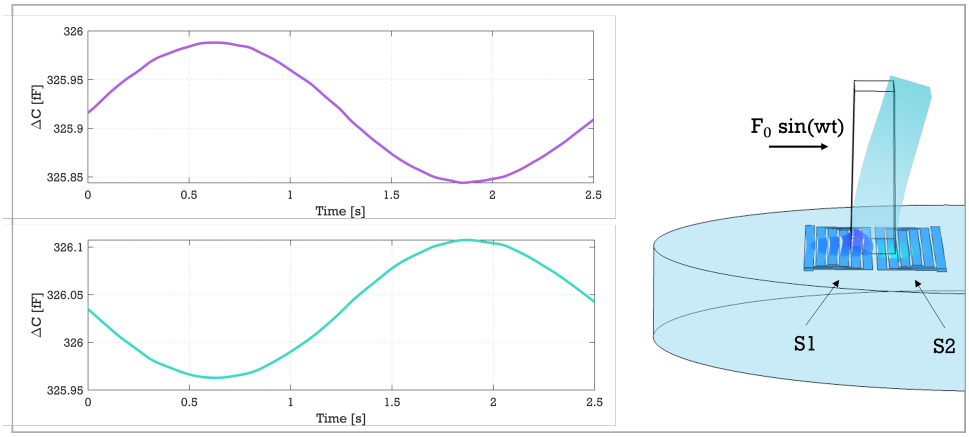

Figure 5.14: Numerical analysis of dynamic sensor behavior with a sinusoidal force acting upon the pillar.

5.4. FABRICATION

5.4.1. PROCESS FLOW

Microfabrication techniques explained in previous chapters were used to fabricate the designed capacitive displacement sensors integrated into the PDMS substrate in close proximity to the bottom of two pillars. Both sensors and interconnects are meant to be integrated entirely within the PDMS substrate, which poses a challenge for fabrication. The microfabrication process uses two 4-inch single-side polished silicon wafers, which are combined and bonded in the end into a PDMS platform with integrated sensors. The flowchart of the fabrication process is shown in Fig.5.15.

First, a 5 µm-thick PECVD SiO_2 was deposited in a Si wafer to be used as a mask for deep reactive ion etching (DRIE). The oxide layer was patterned using 3 µm-thick photoresist and the unprotected areas were dry etched in CHF_3 and C_2F_6 plasma (Fig.5.15A). As mentioned, the patterned oxide layer was used as a hard mask for the DRIE process,

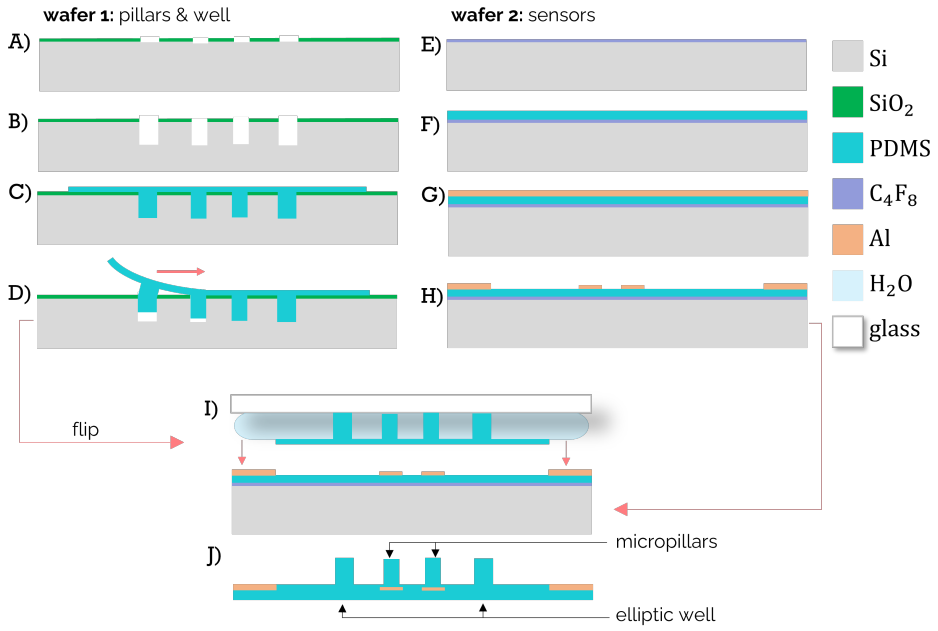

Figure 5.15: Process flow of the fabrication of EHT platform with integrated capacitive displacement sensors.

during which 660 µm-deep cavities for pillars and elliptic wells were etched into the Si wafer (Fig.5.15B). Sensor development was done in parallel to the improvement of the pillar design, therefore the 3 µL platform was initially used for sensor implementation due to the highest pillar displacement, among three different platform sizes, generated by tissue contraction. Prior to PDMS moulding, the wafer was covered with SAM of (perfluoro)silane to ensure hydrophobicity of the Si surface and easy removal of the polymer. The Si mould was finally covered with PDMS by two-step spin-coating to fill in the cavities in Si while obtaining a thin (< 100 µm) layer on top of the wafer (Fig.5.15C). The thickness of the PDMS layer above the cavities in Si should be in the range between 50 and 100 µm. The lower thickness limit is determined by the following process step of PDMS removal from the moulds using an adhesive as assisting layer. On the other hand, the thickness of the PDMS layer should be enough to support the removal of 660 µm-long pillars and wells without causing structural damage. The adhesive used in this case should not be very strong, since it is later removed from the final structures to not disrupt the mechanical properties of the EHT platform and the sensitivity of integrated sensors. The upper limit for the thickness of the PDMS layer on the Si wafer originates from the sensor design and the optimal range for sensor position. As the substrate deformation declines exponentially with increasing distance from the pillar-substrate interface, the optimal sensor position is no further than 100 µm in depth. After the successful removal of PDMS structures from Si mould, contact openings are made in the PDMS layer with a circular biopsy puncher of 1 mm in diameter (Fig.5.15D) to leave the contact pads exposed, upon wafer bonding, for wire-bonding.

The second wafer was coated with Teflon to obtain a hydrophobic Si surface prior to PDMS spin-coating (Fig.5.15E). Next, 80 µm layer of PDMS was spin-coated and cured at 90 °C (Fig.5.15F). After curing, the wafer was kept in a vacuum to avoid gas permeation in the PDMS before metal sputtering. Prior to sputtering, the wafer was exposed to low-power oxygen plasma (75 W for 1 min) to activate the PDMS surface and enhance adhesion between metal and polymer layers. Additionally, a leak-up rate (LUR) test was performed to ensure that the gas leakage from the PDMS layer was within the specified range so that it did not alter sputtering conditions. The aluminum layer was sputtered on top of PDMS, in 4 steps of 250 nm per step, with 3 min of degassing in between. In total, 1 µm of Al was sputtered at 25 °C at low power (1 kW) (Fig.5.15G). Low power is needed to reduce the bombardment energy of Al atoms not to damage the PDMS surface. The sputtering temperature was also limited due to the presence of PDMS and the large difference in thermal expansion coefficient between Al and polymer. In the following steps, sensors were patterned with dry etching using 2 µm-thick photoresist layer as a mask (Fig.5.15H). Four different sensor designs were created in four wafer quadrants. Most of the photolithography steps were conducted with a dedicated procedure. For example, spin-coating was conducted with the manual spinner to avoid contamination of

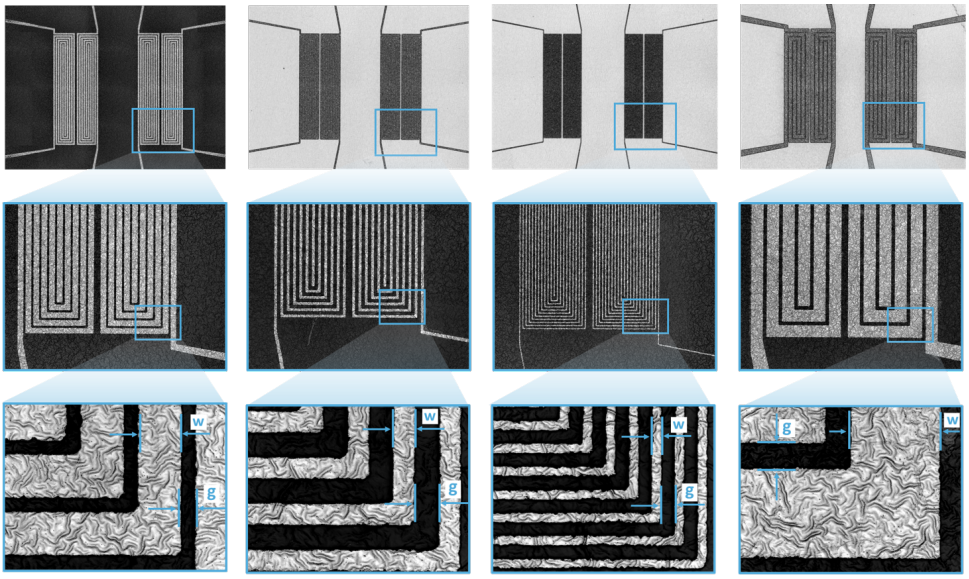

Sensor type	A	B	C	D
g_{mask} [µm]	5	10	5	10
$g_{measured}$ [µm]	6,2	10,8	5,5	10,9
w_{mask} [µm]	20	10	5	40
$w_{measured}$ [µm]	19,1	9,7	4,3	39,1

Figure 5.16: Optical images of the four types of sensors with different metallization ratios, patterned in Al on top of a PDMS layer. Second and third insert show 10x and 20x magnification, respectively, of patterned Al lines.

the automatic tool with PDMS. Further on, since the exposure of Al and PDMS together to high temperatures can cause metal cracking and wrinkling, standard soft and hard baking steps for photoresist (PR) were substituted with baking steps at lower temperatures (90 °C) on the hot plate. After dry etching in Cl and HBr plasma, PR was removed using a combination of low-power O_2 plasma, acetone, and IPA. Finally, optical images of all four sensor types, with close-up images of patterned Al lines on the PDMS layer after PR removal, are shown in Fig.5.16.

The final integration of sensors into the EHT platforms was done by transferring PDMS structures from the Si mould, aligning and bonding them to the wafer with patterned sensors. De-moulded PDMS structures were transferred and aligned using the surface tension of a water droplet on a transparent glass wafer (Fig.5.15I). Attachment to the wafer with sensors was made using uncured PDMS. After alignment, the wafer was cured for an additional 1 hour at 90 °C to ensure bonding of the two cured polymer layers. The bonding and assembly process will be elaborated in more detail when discussing integration with the readout system (Section 5.6).

5.4.2. CRITICAL STEPS

ALUMINUM SPUTTERING

As mentioned previously, metal deposition causes stress in PDMS due to the difference in thermal expansion coefficients, resulting in the formation of wrinkles on the PDMS surface. During Al sputtering, the kinetic energy of metal particles heats up the PDMS surface, resulting in PDMS expansion. PDMS is then uniformly covered with the metal layer while being in such an expanded form. However, after cooling down to room temperature, PDMS shrinks back to the initial state, and wrinkles are formed on the metal-coated surface. The wrinkle formation and inspection of surface properties are shown in Fig.5.17. Here, t is the thickness of the Al layer, S_{al} is the average wrinkle height in the rectangular area on the Al line, while S_{PDMS} is the roughness across the surface of PDMS. In the case of capacitive sensing, these wrinkles are actually beneficial as they slightly increase the surface area of the capacitor plates, contributing to the fringing field lines. However, they might cause disruption in the layer uniformity and crack formation. A potential solution to this issue would be the incorporation of a stress buffer layer between metal and PDMS. Still, the addition of any layer with mechanical properties between Al and PDMS would decrease substrate deformation and therefore the output signal of sensors. Therefore, in the first instance, the buffer layer was not introduced.

PHOTORESIST REMOVAL

Another critical step in the process is the removal of PR after plasma etching of Al. During dry etching in Cl_2 and HBr plasma, PR is bombarded by the plasma ions and therefore hardened. The standard procedure to remove the PR, after dry etching, is by using high-power oxygen plasma to oxidize organic PR. However, high-power oxygen plasma (600 W) results in the formation of a glassy surface layer heavily rich in SiO_x, causing crack formation in the PDMS surface due to the built-up stress [116]. The maximum power for surface treatment of PDMS, without causing damage, is up to 100 W for a very short time, which is not sufficient for PR removal after dry etching. Alternative ways of removing PR from PDMS include a combination of low-power O_2 plasma together with acetone and

IPA rinsing. After 2 min of oxygen plasma (75 W), followed by immersion in acetone and IPA for 10 minutes each, PR is completely removed from the patterned aluminum layer.

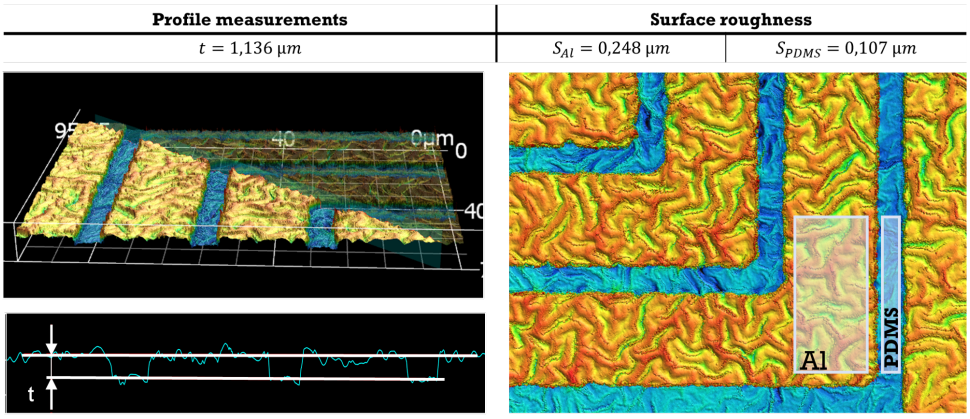

Figure 5.17: Wafer surface roughness analysis after sputtering and patterning aluminum layer on top of PDMS.

5.5. PORTABLE ELECTRONIC READOUT

5.5.1. AVAILABLE ARCHITECTURES

In order to measure the change in capacitance of the spiral co-planar sensors upon tissue contraction it is necessary to develop high-sensitivity, low-noise, portable readout circuitry that is capable of detecting capacitance change in aF range. The requirements regarding readout portability are dictated by the nature of the measurements, conducted within the tissue culturing facility at Leiden University Medical Center. Additionally, as explained earlier, tissues are cultured in an incubator - a humid environment maintained at 37°C and 5% of CO_2 gas concentration. Hence, sensor integration and packaging, as well as the readout circuitry, must comply with such working conditions. High sensitivity and low noise requirements are the consequence of the very small expected signal from the tissue contraction force, in the range of 100 µm.

Several strategies were considered as possible circuit implementations to detect such a small capacitance change. Some of the most relevant solutions convert the capacitance variation into an output signal in the voltage domain (C2V), current domain (C2I), time domain (C2T), frequency domain (C2F), or directly in the digital domain (C2D). Each of these strategies was analyzed in detail within the master thesis project of Filippo Pfaiffer. [117] Table 5.5 provides a summary of mentioned techniques found in literature, compared based on the achieved resolution, as the most critical aspect of the required readout system.

From the listed architectures, the solutions that could achieve resolution in the desired aF range are architectures based on sigma-delta and capacitive-to-voltage converters. However, the goal of designing a portable and discrete readout system rules out the possibility of using very sensitive but bulky instrumentation available in well-equipped engineering laboratories, such as lock-in amplifiers. Moreover, the implementation of

Table 5.5: Comparison of resolution values achieved by capacitive readout methods (from [117]).

topology	resolution	reference
Capacitive to voltage : lock-in	0.065 aF	P.Ciccarella [118]
Capacitive to digital: $\Sigma - \Delta$	5.4 aF	J.Perez Sanjurjo [119]
Capacitive to voltage	54 aF	L.Zhong [120]
Capacitance to time	255 aF	Y. He [121]
Capacitance to current	800 aF	G. Scotti [122]

lock-in amplifiers in a discrete domain is very challenging, as shown in many attempts [123]. For this reason, the remaining options for readout circuitry design are discrete capacitive-to-voltage architectures and $\Sigma - \Delta$ converters.

5.5.2. COMMERCIAL SOLUTIONS

Two commercially available solutions have been identified, that implement the mentioned architectures: Smartec's Universal Transducer Interface (UTI) [124, 125] and Analog Devices AD7746 [126]. More precisely, UTI is based on a voltage-to-period converter with a period-modulated oscillator whose output signal has a period proportional to the measured capacitance. In the case of AD7746, the core of the component is a $\Sigma - \Delta$ capacitive-to-digital converter.

Both components were analyzed and tested in terms of resolution, accuracy, measurement precision, and noise susceptibility. The results showed very similar behavior in both cases, with slightly superior behavior of AD7746 in terms of resolution. Additional advantages of AD7746 include signal routing via coaxial shielded cables, which ensures a low level of noise and external electromagnetic (EM) interference. Furthermore, in the case of UTI, an external reference capacitance must be used for the proper signal measurement, while AD7746 does not require any external reference. Finally, AD7746 was chosen for further implementation as a readout solution for capacitive sensing in aF range.

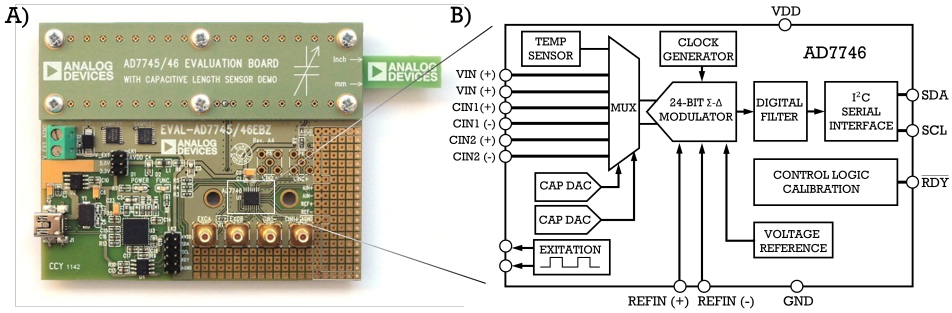

Figure 5.18: Readout electronics for capacitance measurement: A) Evaluation board for the AD7746 integrated circuit; B) Detailed schematic of the architecture of the AD7746 component [126].

5.5.3. AD7746 WORKING PRINCIPLE

Analog Devices AD7746 is an integrated circuit based on a capacitance-to-digital conversion. The component has two capacitive channels and each of them can be configured as single-ended or differential, enabling in total two differential measurements of two pairs of capacitors. The measurement range is ± 4.096 pF with 21-bit readout precision, achieving 4 aF resolution in the best case. Measurement time can be selected between 8 values from 10 to 110 ms, depending on the application. The highest resolution is associated with the longest measurement time. Noise analysis of the AD7746 component resulted in RMS value of 12.2 aF, which is dependent on the measurement conditions and the external EM interference. The component performance in terms of the noise level can be slightly improved with signal chopping at expense of measurement time.

The component architecture consists of a 24-bit $\Sigma-\Delta$ modulator, followed by a third-order digital filter that enables capacitive-to-digital signal conversion and sends it further via serial communication to the microcontroller. The AD7746 is mounted on an evaluation board, containing coaxial connectors, a microcontroller with a USB connection to a PC, and a voltage regulator. The component architecture and the evaluation board are shown in Fig.5.18. A user-friendly interface allows visualization of the measured signal and setup of the measurement parameters within stand-alone software.

Measurements are performed by connecting one of the two excitation outputs (EXC1 or EXC2) to one terminal of the capacitor. The generated excitation is a square wave 32 KHz signal. The second terminal of the capacitor is connected to CIN1(+) or CIN2(+) pins, in case of single capacitance measurement. If a differential measurement is performed, one terminal of two capacitors must be connected to the same excitation signal, while the second terminal of each capacitor is connected to CIN (+) and CIN (-), respectively. An on-chip analog multiplexer connects the two capacitive input signals to the $\Sigma-\Delta$ converter, but since the input of the $\Sigma-\Delta$ is single, only one channel can be converted at a time. Therefore, it is not possible to have the simultaneous conversion of both capacitive channels. This means that additional components must be implemented to enable differential measurement of the signal coming from all four sensors. Available measurement configurations for differential measurements with the current system are shown in Fig.5.19.

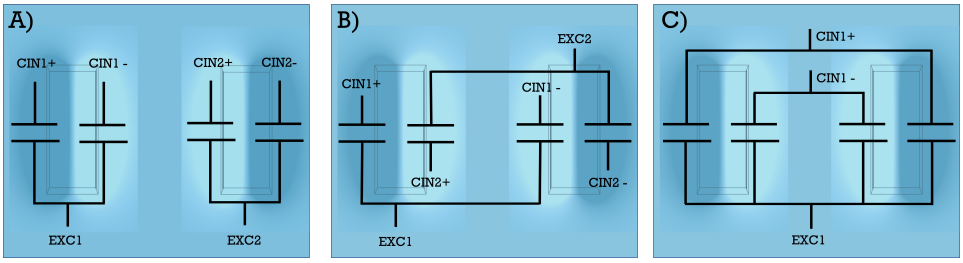

Figure 5.19: Measurement configurations for differential measurements in EHT platforms with integrated sensors: A) differential readout from each pillar, independently; B) Differential readout from both pillars, combining sensors that experience opposite capacitance changes; C) Differential readout of all four sensors, by adding up the effect of the sensors exposed to the same type of capacitance change. Compression and tension of substrate by pillar motion are shown in dark and light blue, respectively.

5.6. ASSEMBLY OF THE MEASUREMENT SETUP

Wafer-level fabricated individual sensors were integrated into the system compatible with the readout circuitry, to allow evaluation of the sensor performance by means of static and dynamic electrical characterization. The assembly of the entire system was carried out in several steps, which will be explained in detail below.

5.6.1. PCB DESIGN

A PCB was designed to allow the connection of the individual sensors to the readout AD system. Since the final application of the sensors is force measurement of EHTs in culture, only the PCB with integrated sensors will be placed in the incubator and exposed to humid conditions at 37 °C temperature. The readout system will remain outside of the incubator and it will be connected to the PCB with sensors and tissues only when performing measurements.

This PCB contains a footprint of a single PDMS chip with sensors (Fig.5.20A), with eight golden bond pads for each spiral plate of four capacitors in total. Metal interconnects are routed from the bond pads to the coaxial connectors and insulated from EM disturbance with two ground planes above and below the traces. One plate of each spiral capacitor was connected to the excitation signal via a single coaxial connector (P1) The other four plates were connected to independent connectors (P2-P5) for output signal connection with the AD board. (Fig.5.20B)

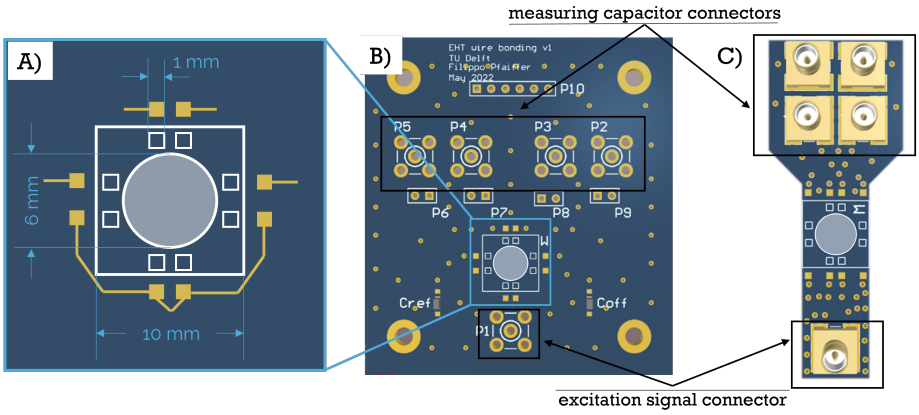

Figure 5.20: A) The footprint of a single PDMS chip and its connection to the PCB; B) Initial version of PCB designed for experiments with cell inclusion; C) Second version of PCB, adjusted for the nanoindentation measurements.

A second PCB was designed for compatibility with the nanoindentation setup used for the electrical characterization of the sensor's dynamic performance when subjected to mechanical deformation. Both PCB designs are shown in Fig.5.20.

5.6.2. SENSOR TRANSFER

A full wafer of sensors patterned on top of the PDMS layer was fabricated as described previously (Fig.5.21A) From a wafer-level stage, individual sensors were cut into 10x10 mm^2 squares using a blade. The top part of the sensors was protected with the laser-cut pressure-sensitive adhesive (PSA). The alignment of the adhesive and transfer of the chip to the wafer surface was achieved using the surface tension of the water droplet on a transparent glass wafer. PSA was laser cut in such a way as to ensure the protection of the Al interconnects while leaving open the circular area around the elliptic microwell. The addition of the PSA layer increased the mechanical rigidity of the thin PDMS with patterned Al and protected the thin metal lines from breaking during the transfer procedure. PDMS pillars with elliptic wells were transferred and bonded to the middle area of the chips, uncovered with PSA. The bonding was performed with a thin layer of uncured PDMS (Fig.5.21B). Detachment of assembled EHT platforms with integrated sensors from the Si wafer was performed using IPA and a thin metal blade. The blade was placed below PDMS chips to provide a stiff substrate during chip transfer to a PCB, minimizing the bending of PDMS. After detachment and evaporation of IPA residues, single chips were bonded to the PCB using uncured PDMS.

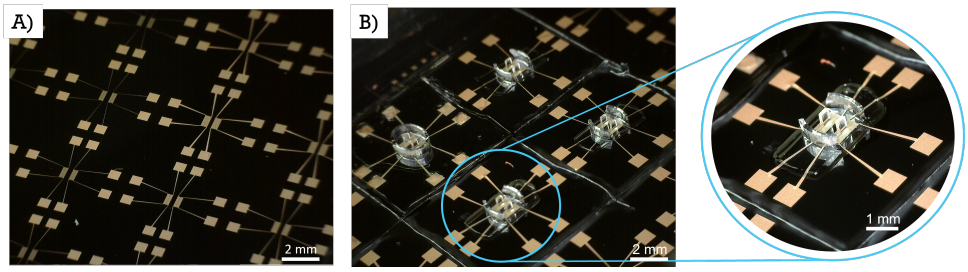

Figure 5.21: A) Wafer-scale sensor patterning on PDMS substrate; B) Assembly of the EHT platforms with integrated sensors on a wafer level with a close-up of an individual PDMS chip.

5.6.3. WIRE-BONDING

The connection of the fabricated chips to the contact pads on the PCB was made by means of wire-bonding. This technique consists of a welding process in which two materials are joined together mediated via pressure, heat, and ultrasonic energy. Here ultrasonic wire-bonding to gold with aluminum wire was utilized. This process is performed at room temperature, while applied force and the amount of ultrasonic (US) energy can be tuned depending on the substrates for bonding. When ultrasonic energy is applied, thin Al wire is brought in contact with the metal pad, as generated mechanical vibrations create the heat that joins two materials together [127, 128]. During wire-bonding process, the connection is first created between the contact pad on the fabricated chip and the Al wire. Afterward, the arc is created and the wire is extended to reach the contact pad on the PCB. Finally, the second bond is made on the PCB pad, creating in this way an electrical connection between a single chip and the PCB. The illustration of the wire-bonding process is shown in Fig.5.22.

Wire-bonding parameters depend on the properties of the substrate on which bond-

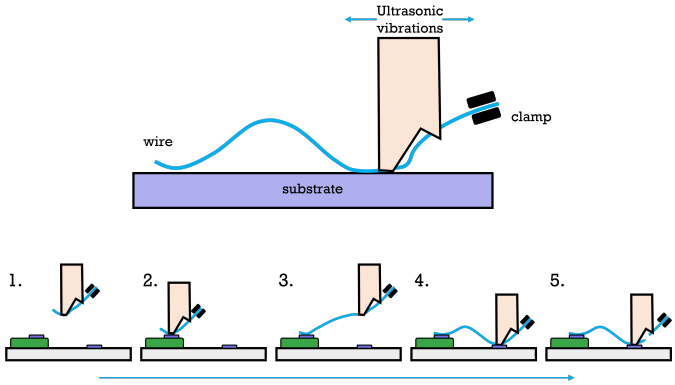

Figure 5.22: Illustration of the wire-bonding process [128]: (1) positioning the wedge at the first contact pad on the substrate; (2) welding on the first contact pad; (3) wire extension to reach the second contact pad on a PCB; (4) welding on the second contact pad; (5) completing the wire-bonding process by wire breaking.

ing is performed. In the case of the platform with integrated sensors, 1 µm-thick Al contact pads are patterned on top of the 80 µm-thick PDMS layer. PDMS is a mechanically soft polymer, meaning that it can absorb a large amount of ultrasonic energy, opposite to mechanically stiff silicon substrates. Therefore, achieving enough mechanical vibrations to weld Al wire to the Al contact on top of the PDMS layer is very challenging. In addition to the absorption issue, mechanical force is applied during wire-bonding as the tip of the wire-bonder with the clamped wire in the middle pushes the bonding surface. Such a thin Al layer by itself is not able to withstand this pressure from the bonder tip without breaking. To circumvent the direct bonding to the Al on PDMS, squared golden shims (0.4 x 0.4 mm^2) were glued to the Al pads using silver conductive paste. The glue was manually dispensed on each contact pad and the shims were gently placed on top using a pick-and-place tool. The glue was solidified by baking at 125 °C for 2h, to create a stable, low-resistance contact between Al pads and the golden shim. The golden shim provided mechanical support that was missing for the successful wire-bonding process.

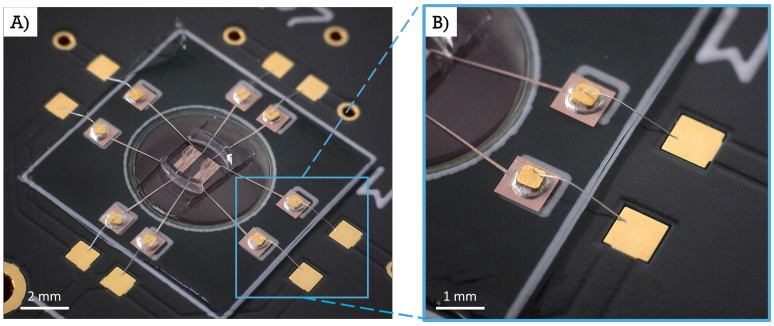

Figure 5.23: Wire-bonding of the EHT platform with integrated sensors to a custom-made PCB; B) Detailed view of the wire-bonded pads, with the golden shims on top of a thin Al later.

Upon glue baking, wire-bonding was successfully performed using the parameters from Table 5.6. Ultrasonic power was still higher than in the case of bonding on top of the Si, due to the soft substrate below the golden shim and the contact pad. The optical images of the final EHT platform transferred and glued to a PCB, with the focus on wire-bonded pads are illustrated in Fig.5.23A and 5.23B respectively.

Table 5.6: Wire-bonding parameters.

	US power [mW]	Time [ms]	Force [mN]
Bond 1 (chip)	1300	850	700
Bond 2 (PCB)	300	350	300

5.6.4. WELL ADDITION AND ENCAPSULATION

As the final application of the sensor is force measurements during tissue culture, an additional well for cell culture medium was mounted on top of the wire-bonded chips and aligned to the circular opening in the PCB. The well was made out of a laser-cut piece of polymethyl methacrylate (PMMA), 8 mm-high with a 1 mm-thick wall, which was bonded to the protective PSA layer using uncured PDMS. The entire system was made leakage-free, which was confirmed by tests with ethanol and DI water prior to cell culture. After mounting the plastic well, the wire-bonds and contact pads were encapsulated with PDMS to insulate them and prevent contact with water and culture medium. The final assembly of the sensors is shown in Fig.5.24.

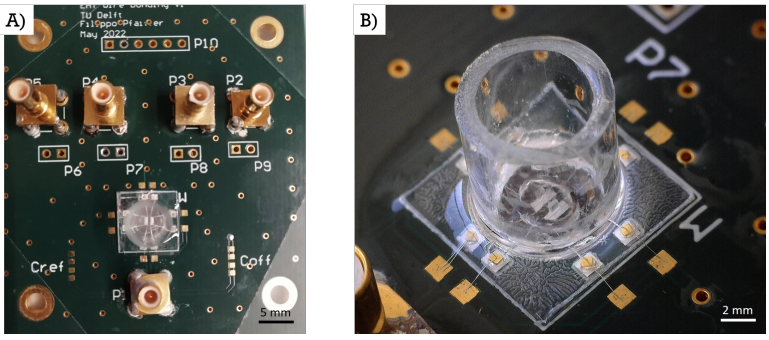

Figure 5.24: A) Assembly of the EHT platform with integrated sensors on top of the custom-made PCB; B) Packaging of the EHT platform by mounting the well for cell culture medium and the wire-bonds encapsulation.

5.6.5. ASSEMBLY CHALLENGES

The assembly process of the fabricated sensors showed to be very sensitive and prone to failures. Only sensor D reached the end of it in the first fabrication attempt. The most critical steps of the assembly process are the transfer to a PCB and the wire-bonding, as will be explained in more detail.

The transfer of PDMS chips with EHT platforms and integrated sensors from a wafer to the PCB was the first reason for the assembly failure. Due to the difference in stiffness between the aluminum layer and PDMS, any extensive bending or substrate deformation causes damage to the very thin metal lines of sensor interconnects (Fig.5.25A). The most critical breaking point was the merging of contact pads and interconnects. Since there is a sharp transition from the large contact pad area into very thin metal lines of interconnects, this spot is the most prone to breaking during the assembly procedure, as shown in Fig.5.25B. Furthermore, PDMS removal from the wafer might result in the bending or rolling of the polymer, which causes wrinkling of the metal lines. After returning PDMS to the initial flat position, the formed wrinkles might result in cracking and interconnect disruption (Fig.5.25C).

Another critical step of the assembly process is wire-bonding on a soft substrate. Unlike in the case of electrode integration, as it will be shown in the next chapter, in the fabrication process of capacitive sensors it was decided not to add a stress buffer layer of polyimide below the deposited metal layer as the first instance. In this case, wire-bonding was performed on Al pads with golden shims, patterned directly on top of a PDMS. Therefore, due to the lack of mechanical support, the assembly process is more sensitive to the pressure occurring during the wire-bonding. If the thickness of the deposited conductive glue is too thick, or the golden shims are not perfectly flat, the pressure of the bonding needle causes cracks around the glue and the golden shim, in the Al contact pad, disrupting the metal connection (Fig.5.25D).

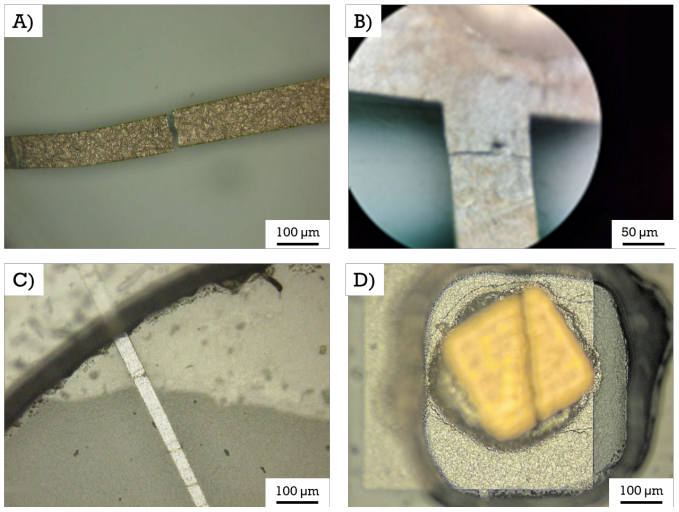

Figure 5.25: Examples of metal connection disruptions during the assembly process. A) broken interconnect during pillar bonding; B) broken connection at the contact pad; C) bent interconnects due to the transfer process; D) crack at the contact pad after golden shim gluing.

5.7. SENSOR CHARACTERIZATION

5.7.1. ELECTRICAL CHARACTERIZATION

Electrical characterization of the sensors was performed by measuring the electrical output of sensors in both static and dynamic conditions. For sensor performance in static conditions, the base capacitance of the fabricated sensors was measured and compared to the estimated values from simulations.

These measurements were performed on a wafer scale, with the PDMS layer patterned with Al sensors only. In this case, as sensors were not fully encapsulated in PDMS, the expected capacitance is smaller than the values obtained from CPW theory and simulations with sensor integration, shown in Table 5.7. Corrected values for the expected capacitance have been calculated, based on the fact that half of the fringing field lines propagate through the air instead of PDMS in this specific case. Table 5.7 gives an overview of the calculated capacitance values for the sensors within the air-PDMS domain, and measured values.

Table 5.7: Base capacitance measurements, yield and comparison with simulations.

Sensor type	A	B	C	D
Simulation value [fF]	374	279	497	231
Measured value [fF]	300 ± 59.4	250 ± 25.9	450 ± 42.6	180 ± 39.9
Measurement yield	81%	87%	62%	85%

As mentioned, the wafer with patterned sensors was divided into four quadrants, where each quadrant contains 12 EHT platforms with 4 sensors of the same type per platform. In total, 48 sensors of each type were measured per wafer quadrant. Measurements were performed on a wafer-scale, using an Agilent 4294A Precision Impedance Analyzer. This instrument was connected to an electromagnetically shielded probe station (Cascade Microtech Summit 12k) with four independent sensing/force probes. The probes were used to make electrical contact with the Al pads patterned on top of PDMS layers. C-V measurements were performed, with voltage sweep from 0 to 5 V. The excitation signal frequency was set at 32 kHz to match the excitation frequency of the AD7746 board. However, measurement results were proven to be stable within a wide range of frequencies.

As shown in Table 5.7, the least number of successful measurements was obtained for sensor C, since patterning of very thin metal lines (5 µm) was the most delicate and prone to breakage. Slightly lower capacitance values compared to the simulations can be explained by the fabrication imperfections, particularly slight over-etching of the metal lines during the dry etch of Al (Fig.5.16).

5.7.2. MECHANICAL CHARACTERIZATION

Mechanical tests were performed to characterize the dynamic behavior of the assembled sensors. The only available sensor for this measurement, after the assembly, was sensor D, with a lower base capacitance than expected (95 fF). Similarly to the previous mechanical characterizations, FemtoTools Nanomechanical Testing System (FT-NMT03)

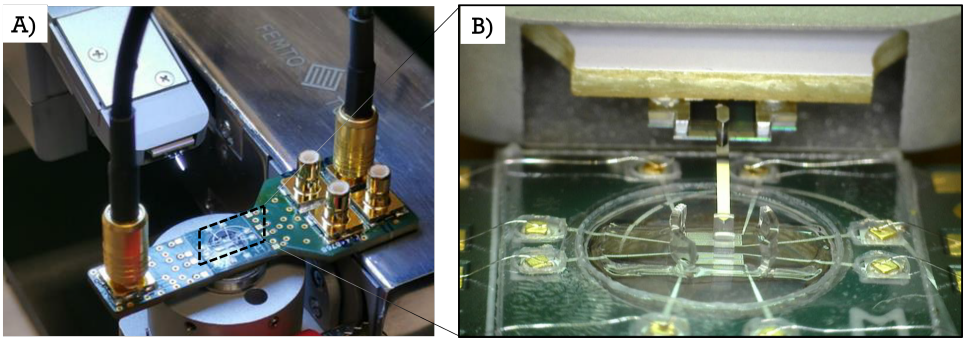

Figure 5.26: A) PCB with wire-bonded sensors mounted on the holder of the nanoindenter for characterization of dynamic sensor behavior; B) Close-up image of the nanoindenter silicon probe applying force along the micropillars length.

was used. The goal was to apply controlled force along the pillar length and simultaneously measure the electrical response of the sensor. The force was applied with a flat circular silicon probe, 50µm in diameter, with a 15° tilt angle from the horizontal plane.

The platform with integrated sensors was wire-bonded to a custom-made PCB (see Fig.5.20C) shown in and Fig.5.26, specifically designed to match the nanoindentation setup. For measurement purposes, the elliptic well of the PDMS platforms was cut from the sides of the pillars, enabling access to the nanoindenter probe. PCB was glued and mounted on a metal holder of the nanoindenter (Fig.5.26). Measurements were performed with high precaution because the silicon tip of the sensor head is very fragile and can easily be damaged if the PCB is not attached well to the metal holder.

The Si probe movement is controlled via a micro-positioning stage, connected to a PC. After mounting the PCB on a metal holder, the AD7746 readout system was connected to the PCB with coaxial cables. For the measurement duration, the readout system was placed in a Faraday box to minimize the measurement noise. Measurements were performed by applying controlled force up to 300 μN, on different positions along

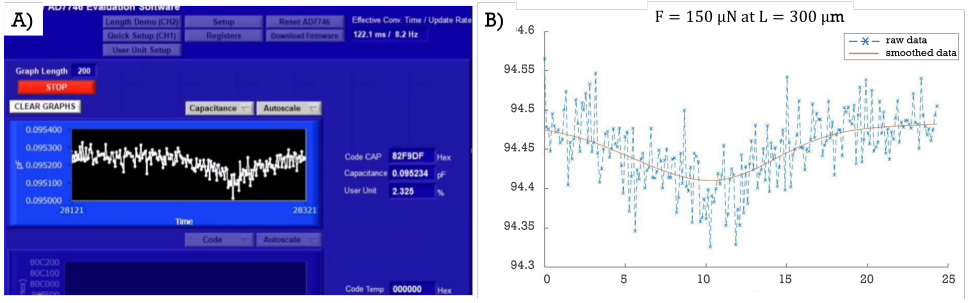

Figure 5.27: A) The user interface of AD7764 software shows real-time capacitance measurement during force application upon pillars; B) Filtering out noise from the raw measurement data using *smoothdata* function in Matlab to extract the change in capacitance.

pillar length (250 µm – 550 µm). The force of the tip was increased continuously until reaching the specified value, followed by the tip return to the initial position. In this way, the applied force profile was mimicking a single contraction cycle of the EHT at a very low frequency. Consequent substrate deformation and therefore capacitance change was monitored in real-time using the AD7746 evaluation software. The user interface of AD7746 software together with the real-time signal recording is shown in Fig.5.27A. As can be seen from Fig.5.27B, even though the measured profile corresponds to the applied force, the signal had still a high noise level. Additional signal post-processing is performed in Matlab using the function *smoothdata* to filter out the noise and extract the information about capacitance change. The raw and filtered data are shown in Fig.5.27B.

The change in capacitance (ΔC) corresponding to the applied force was calculated from the filtered signal and is shown in Fig. 5.28. This figure gives an overview of all the performed measurements with the force in the range of 100 – 300 µN and the point of indentation going from 250 µm until 550 µm from the pillar base. From the graphs, it can be noticed a nearly linear dependency of ΔC from the applied force. The responsivity of the sensors is defined as the ratio between the capacitance change and the applied force and can be calculated as the slope of the obtained curves. The calculated responsivity is in the range from 0.42 fF/µN up to 0.28 fF/µN, which is in agreement with the simulated values for sensor D (Table 5.4). The slightly lower values might be a consequence of the assembly imperfections regarding the alignment of the pillars with sensors.

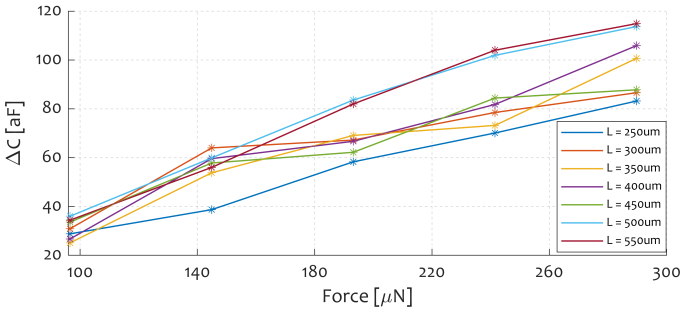

Figure 5.28: Differential measurements of capacitance change upon application of force at 7 different positions along micropillars length, captured through the AD7746.

5.8. BIOLOGICAL VALIDATION

The final validation of the novel sensor design integrated into the EHT platform involved tissue culture and contractile force measurements. Since only two platforms with non-zero base capacitance reached the end of the assembly process (sensors A and D), those samples were used for the trial experiments with cardiac cells.

5.8.1. TISSUE CULTURE

Similarly to previous cases, EHTs were generated using a mixture of iPSC-derived cardiomyocytes (CMs), cardiac fibroblast (cFB), and endothelial cells (ECs). All three cell

types were derived from the hiPSC line (LUMC0020iCTRL-06) [18]. The cells were frozen and kept in liquid nitrogen until 7 days prior to EHT formation. The EHTs were composed of 70% hiPSC-CMs,15% hiPSC-derived cFB, and 15% ECs. For the ECM gel mixture, 41% of acid solubilized collagen I (3.3 mg/mL), 5% of DMEM (10X), 6% of NaOH, 9% of growth factor reduced Matrigel and 39% of formation medium were used. The EHTs were cultured in a formation medium for 72h combined with VEGF (50 ng/mL) and FGF (5 ng/mL). After 72h the culture medium was switched to MBEL+ VEGF (50 ng/mL)+ FGF (5 ng/mL) and maintained in culture for 14 days. Cells were kept in a humidified incubator for the whole time and the medium was refreshed every 3 to 4 days. Bright-field images were taken every day, following tissue formation, since the beginning of the experiment, with a Nikon Eclipse Ti2. The timeline of the tissue formation process in the platform with sensor D is shown in Fig.5.29.

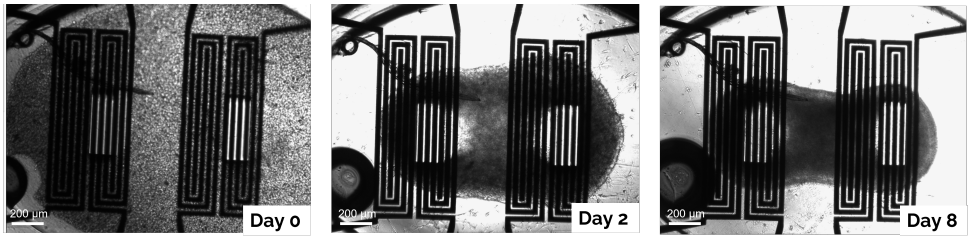

Figure 5.29: Timeline of EHT formation on the platform with integrated sensor D, on days 0,2 and 8.

The tissues remained in culture for 14 days, proving the biocompatibility of the new EHT platform with integrated sensors. Formed tissue in both platforms with sensors A and D on day 9 is shown in Fig.5.30. Unfortunately, both spontaneous and paced contractions of the tissues were insufficient to detect any movement of the pillars, therefore electrical measurements of contraction force could not be performed in this experiment. The reason for the low contractility originates from the cell culturing procedure and timing of critical steps, which can cause cell damage if not followed strictly. Future experiments are necessary to assess the dynamic performance of the sensor for the contractile force recording of cardiac tissues.

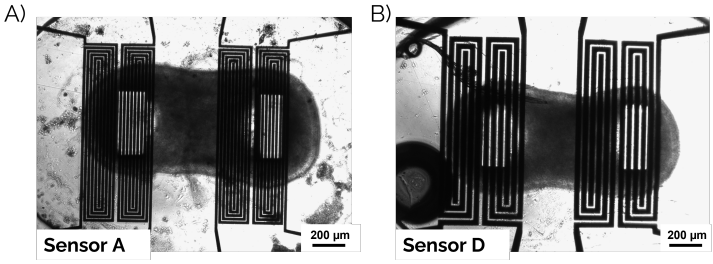

Figure 5.30: EHTs formed in the platform with integrated sensor type A (A) and type D (B).

5.9. DISCUSSION AND CONCLUSIONS

In this Chapter design, modeling, fabrication, and characterization of novel capacitive co-planar displacement sensors for measurement of tissue contraction force were described. The working principle of the sensors exploits the deformation in the substrate below PDMS pillars occurring as a consequence of pillar displacement. Base capacitance change between co-planar metal plates upon their displacement was selected as the optimal sensing mechanism for correlation to the force applied upon pillars, based on the sensitivity and fabrication requirements. A pair of spiral capacitive co-planar sensors were positioned in the areas of maximum substrate deformation, underneath each pillar, to measure both tension and compression occurring in the PDMS substrate. Four different spiral geometries were explored and modeled using Comsol Multiphysics to study the electrical response and responsivity of sensors depending on the capacitor geometry.

Sensors were integrated into the EHT platform using the same fabrication techniques as previously adopted: micromachining of silicon and polymer processing. All four sensor types were successfully patterned and fabricated on a wafer level. However, it was shown that the assembly process of fabricated sensors into an experimental setup is challenging and prone to failures. Both assembly steps: sensor transfer from the silicon wafer and the wire-bonding, demonstrated disruptions in the electrical connection of the sensors. This can be addressed in the future fabrication process by encapsulation of contact pads and interconnects within a stress buffer layer such as polyimide. In this way, the lack of mechanical stability during wire-bonding might be improved. It is important to notice that the polyimide layer was avoided in the first place to not affect the substrate deformation by adding rigidity to the material below the pillars. The same needs to be taken into account when modifying the fabrication process, that the additional polyimide layer is present only in the areas where substrate deformation is zero. The sensors should still be integrated only within the PDMS layer for high sensitivity to substrate deformation.

A readout system based on capacitive-to-digital conversion was developed to measure base capacitance change in the aF range, within a robust, low-noise and portable system. Minimizing noise is one of the main challenges for such a small capacitance change readout system. Even though the system was proven to be suitable for capacitance change upon pillar deflection, all tests were conducted in dry conditions. The noise level originating from the measurements with the tissues around the pillars within the culturing medium is yet to be determined in future experiments. Furthermore, the current readout system can obtain differential measurements from only two capacitors, therefore force measurement from each pillar separately is not possible in this configuration. Additional signal demultiplexing can be implemented into the AD board to facilitate multiple differential measurements.

The sensors that completed the assembly process were characterized by measuring base capacitance, which showed good agreement with the anticipated values from simulations and theory. The dynamic behavior of sensor D was also assessed using the nanoindentation setup by applying force up to 300 μN on different positions along the pillars' height. Based on these preliminary measurements sensor responsivity was found to be 0.35± 0.07 fF/μN, setting the low limit for the measured force with sensor D at 100

μN. More characterization of all four sensor types is required for a proper statistical analysis. The comparison of different sensor types will determine which design is optimal for force measurements in the EHT platform.

Finally, the two assembled sensors were tested for biocompatibility by culturing EHTs for 14 days. Unfortunately, tissues did not show desired contractile performance and the generated force was below the sensor detection range. Repeated experiments will provide more insight into the feasibility of the developed sensors for real-time tissue contraction force monitoring.

At this stage, only single EHT platforms with integrated sensors were tested individually. However, the next step of the system development, after detailed characterization and selection of the optimal sensor geometry, is multiplexing the capacitance measurement and fitting the EHT platform with integrated sensors to the multi-well plate format. Additionally, the fabrication of the platform is compatible with the integration of tapered pillars, which will be implemented in future design.

CHAPTER 5

INTEGRATED PACING MICROELECTRODES

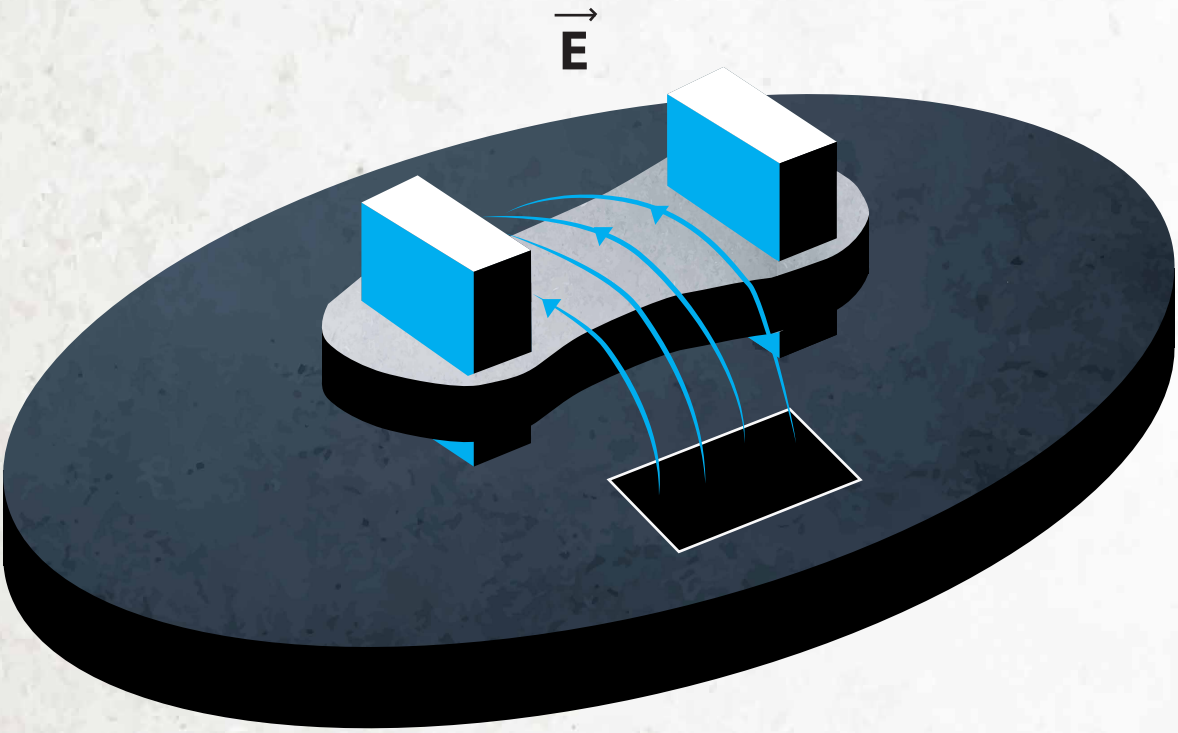

6.1. THE IMPORTANCE OF ELECTRICAL STIMULATION FOR EHTS

An important part of the development of a dynamic microenvironment for EHT culture is the inclusion of electrical stimulation. According to the previous research on cardiac tissue models *in vitro*, electrical stimulation demonstrated improvement in the functional assembly of cardiomyocytes [129–131]. The high importance of electrical stimulation for the maturation of iPSC-CMs has already been elaborated in the Introduction. Multiple studies have demonstrated that EHTs submitted to electric field stimulation express an increase in conduction velocity, enhanced structural organization of sarcomeres, and improved Ca^{2+} handling properties [25, 132, 133]. Furthermore, understanding the effect of a drug dose on the heart rate and contractile properties is crucial for *in vitro* cardiac models used for drug testing and disease modeling [134].

Most electrical pacing systems in *in vitro* 2D and 3D models use pair of electrodes positioned in the proximity of the cell layers and tissues, to deliver electric field stimulation with the electrical impulse propagating through the cell culture. Pacing electrodes are commonly made from carbon or platinum wires, however, carbon has superior current injection characteristics [135]. Some examples of developed systems for electrical stimulation of cardiac cells are shown in Fig. 6.1 [136–139].

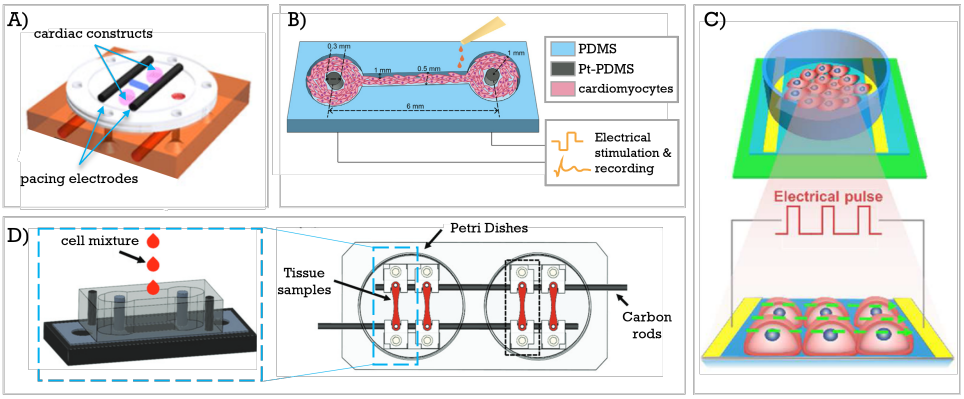

Figure 6.1: Examples of pacing systems for 3D and 2D cardiac tissues: A) Perfusion-stimulation bioreactor with parallel carbon electrodes for tissue stimulation [136]; B) Schematic of a 3D platform with platinum-PDMS pillars as electrodes [137]; C) Plane electrode integration for 2D cell culture stimulation [138]; D) Bioreactor with two Petri dishes and carbon rods for electrical stimulation [139]

.

Adjusting stimulation parameters and electrical signal properties allows cell response to be tuned, depending on the culturing conditions and experimental setup. However, the optimal stimulation regime and pacing parameters for enhancing the maturation of iPSC-CMs are yet to be defined. Most of the research groups used biphasic rectangular pulses for charge-balanced stimulation with frequencies up to 6 Hz, pulse duration shorter than 20 ms and maximum electric field of 8 V/cm [140, 141].

Until now, most of the reported systems for electrical stimulations of cardiac tissues use bulky external pacing electrodes that are either immersed into the wells containing cell culture or placed at the bottom of a culturing bioreactor or Petri dishes, as shown in

Fig.6.1. In all of these cases, the electrodes are part of the external setup, placed manually in the proximity of the tissues, limiting the controllability and reproducibility of the cell culture stimulation. For this reason, in this work, a pair of planar pacing microelectrodes was integrated into the substrate of the previously developed EHT platform, to address mentioned issues by enabling ultimate uniformity, accuracy and precision in controlled *in situ* tissue stimulation. The microelectrodes were integrated into the 3 µL platform for EHT culture with straight pillars, however, the fabrication method is compatible with all platform sizes as well as with the tapered pillar design (Chapter 3).

6.2. DESIGN OF THE PACING ELECTRODES

A pair of rectangle-shaped planar electrodes was integrated into the EHT platform on top of the PDMS substrate, inside of the elliptic microwell and in the proximity of the tissue, to enable electrical stimulations of tissues formed around the pillars. The integrated electrodes create a uniform electric field propagating perpendicular to the tissue formation direction. Such a design was chosen to achieve parallel electric field lines through most of the tissue area, to maximize the uniformity of the field within the tissue and to avoid interference with the PDMS pillars.

When applying electrical stimulation within a biological system, it is important to define stimulation parameters and electrode material carefully, to induce no or minimal damage to the cell culture. The choice of electrode material determines the mechanism of charge transfer to the electrolyte. This mechanism can be non-faradic, defined by charging and discharging the electric double-layer capacitor at the electrode/tissue interface. The second type of charge transfer is faradaic reversible or non-reversible, where actual electron transfer and oxidation occurs on the electrode surface. The non-reversible faradaic transfer should be avoided due to the generation of chemical byproducts and slow degradation of electrodes during stimulation [142]. In the case of the EHT platform with integrated electrodes developed in this chapter, the material chosen for the electrode surface is titanium nitride, which provides a non-faradaic charge transfer mechanism.

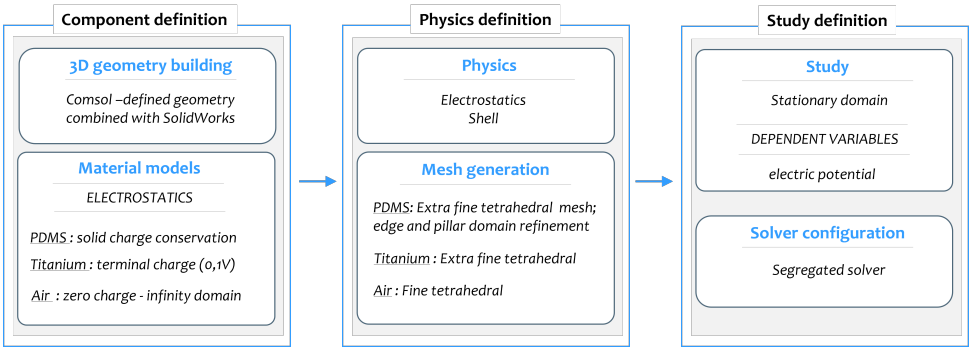

Figure 6.2: Comsol model of the EHT platform with integrated pair of pacing electrodes: A) 3D geometry design with the PDMS elliptic microwell and a pair of pillars (blue), cardiac tissue (brown) and a pair of TiN electrodes (black); B) Mesh of the 3D geometry used for definition of computational nodes in FEM analysis.

6.2.1. ELECTRIC FIELD DISTRIBUTION: NUMERICAL ANALYSIS

The exact shape and position of the electrodes were determined via numerical analysis of the electric field distribution within the system of two elastic pillars, elliptic microwell and two planar electrodes (Fig.6.2A). For this purpose, Comsol Multiphysics was used to create a 3D model of the described system. The microwell, electrodes and substrate were defined using the standard geometry module in Comsol, while the 3D model of tissue adhering to the middle of the pillar length was imported from SolidWorks. The system was placed within a spherical air domain with zero charge at the infinite sphere boundaries. Since the thickness of the integrated electrodes is in the submicron range due to the used microfabrication techniques (see Section 6.3.2), Shell physics was used to represent two TiN plates with infinitesimal thickness. This approximation is valid since all other dimensions in the model are in the hundreds of micron range, therefore the very small electrode thickness would cause a lot of challenges for mesh generation, which is avoided by using the Shell model. Electric field distribution was calculated using the Electrostatics module, where one electrode was defined as a terminal with 1 V electrical potential, while the second electrode was grounded. Platform material was PDMS with relative permittivity of $\epsilon_r = 2.7$, as in all the other models used in previous chapters. The EHT was modelled using properties of a skin-like medium available in Comsol, with $\epsilon_r = 2 \cdot 10^5$. Prior to computation, mesh nods were created to define the set of equations for the finite-element calculation method. The fine tetrahedral mesh was used, with additional refinement at the area of thin electrodes. The meshing of the entire model is shown in Fig.6.2B. The computational flow for FEM analysis is shown in Fig.6.3.

A stationary study with the electric potential as a dependent variable was used to obtain the electric field distribution in the system. The resulting electric field in the middle vertical plane of the tissue, as well as the top view of the elliptic well, are shown in Fig.6.4. It is visible from the graphs that the electric field (E) lines originating from the

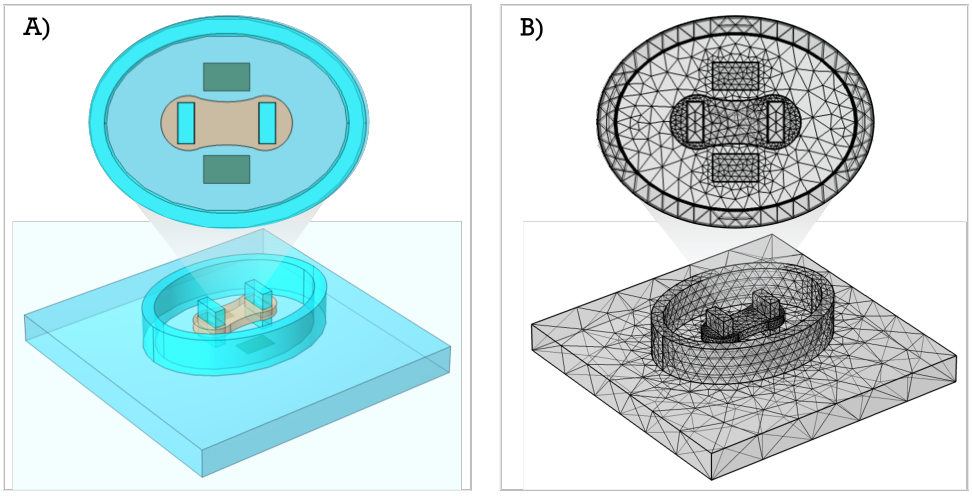

Figure 6.3: Computational flow of FEM study of electric field propagation within the system of EHT platform with integrated pacing microelectrodes.

two planar electrodes positioned on both sides of the tissue are parallel within the tissue. The position of the electrodes was chosen in such a way to achieve parallel distribution of the majority of E field lines through the tissue, creating in this way a uniform field within the EHT. From the graphs is also clear that the E field lines are more densely distributed through the tissue due to the difference in relative permittivity between tissue and PDMS. This model confirms the hypothesis of planar electrodes providing uniform E-field stimulation to the cardiac tissue in the developed EHT platform.

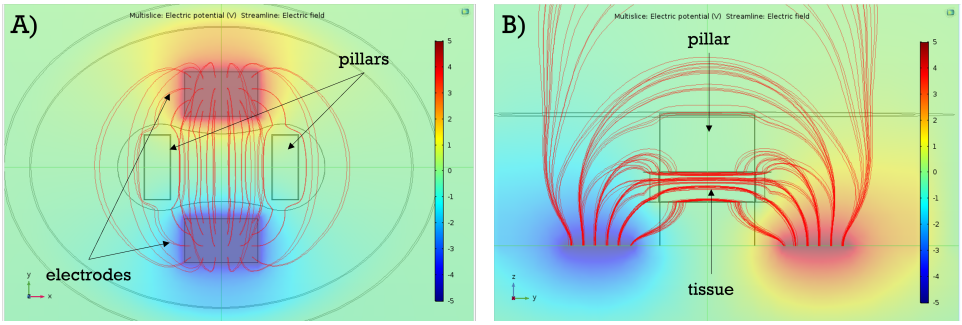

Figure 6.4: FEM simulation of the electric field distribution within the cardiac tissue in an EHT platform with integrated pacing microelectrodes: A) top and the B) side view of the electric field lines.

6.2.2. ELECTRODES AND INTERCONNECTS DESIGN

The pair of TiN electrodes was designed in a rectangular shape with rounded edges to avoid strong E field concentration in the sharp corners and to allow uniform E field distribution through the tissue between the two pillars. The interconnects connecting electrodes to the bond pads outside of the elliptic well were designed in a serpentine shape to preserve the integrity of metal interconnects upon deformation of the substrate. With such a design the strain in the metal lines is reduced by minimizing the metal area in the direction of the maximum strain. This is particularly important for the future upgrades of the platform including mechanical stimulation of the tissues. The final design of the electrodes and interconnects within a single chip layout is shown in Fig.6.5 with the design parameters given in Table 6.1. All the lithography masks for microfabrication were generated based on the designs from both SolidWorks and Comsol which were used for numerical analysis.

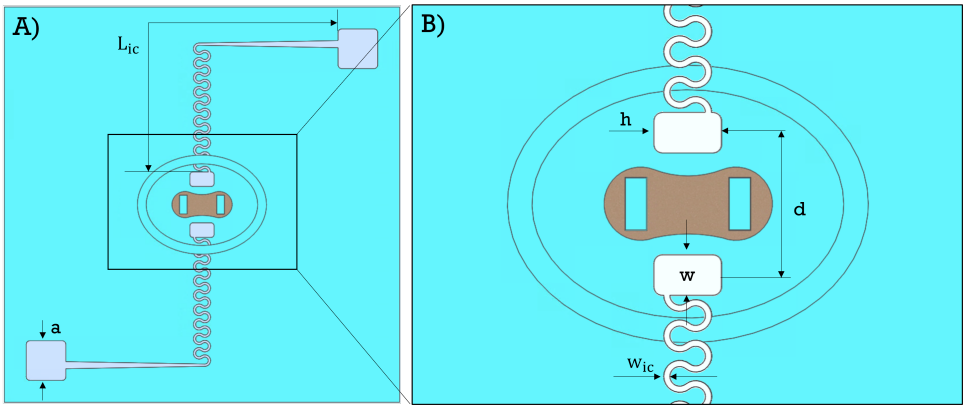

Figure 6.5: Layout of a single chip of EHT platform with integrated pacing electrodes with all relevant dimensions.

Table 6.1: Parameters used for the design of electrodes and interconnects

Symbol	Description	Value
L_{ic}	length of interconnects	11.332 [mm]
w_{ic}	width of interconnects	50 [µm]
a	contact pad size	1 [mm]
h	height of the electrode	550 [µm]
w	width of the electrode	330 [µm]
d	distance between electrodes	11.6 [mm]

6.3. FABRICATION OF THE PLATFORM WITH INTEGRATED PACING MICROELECTRODES

Two fabrication strategies were developed and will be discussed in the next section. Prior to the detailed process step discussion, an overview of used microfabrication techniques will be given.

6.3.1. MICROFABRICATION TECHNIQUES

Fabrication of the EHT platform with integrated electrodes was done using most of the previously described microfabrication techniques and processes such as photolithography, PECVD oxide deposition, reactive and deep reactive ion etching and metal sputtering. Most of these processes were primarily used to process silicon, while the polymer layer was only moulded. Here polymer processing including polyimide and metal patterning will be explained in detail.

METAL DEPOSITION

Uniform thin metal layers can be deposited on top of different substrates by using a technique called sputtering. Metal sputtering is a type of physical vapor deposition (PVD) technique, where ionized heavy ions of inert gases (e.g. argon, neon, xenon) are used to bombard the target metal material (Fig.6.6)[143]. If the energy of incident ions is higher than the surface binding energy of the target material, atoms get ejected out of the target and biased towards the substrate at the opposite side of the process chamber. The quality of the deposited layer is highly influenced by the pressure and temperature in the sputtering system. The highest quality layers of sputtered metal are obtained in a low-pressure atmosphere at high temperatures (e.g., 350 °C). The vacuum increases the mean free path of ejected metal atoms and allows most of them to reach the silicon substrate, which increases the sputtering efficiency [144]. However, if the substrate to be coated by sputtering is polymer, such as PDMS, the temperature of the process is reduced to room temperature, consequently decreasing the quality of the deposited layer. For the process developed in this chapter, sputtered metal layers were aluminum, titanium, and titanium nitride.

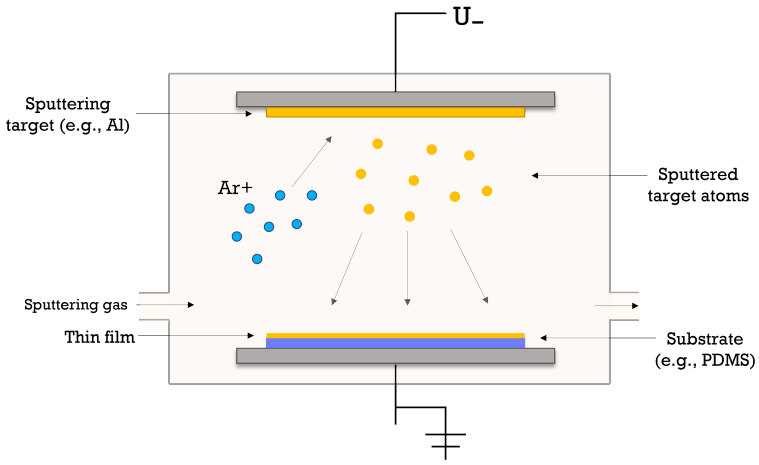

Figure 6.6: Schematic of the metal sputtering process [143].

POLYIMIDE PROCESSING

When depositing metal on top of a low-stiffness polymer layer, an additional polymer can be used as a stress buffer layer. A commonly used polymer for this purpose is polyimide (PI). Polyimide is a high-temperature resistant organic polymer with good thermal, mechanical, and chemical stability. Besides as a stress buffer, it also can be used as an insulation layer due to its high dielectric constant. Polyimide used in the fabrication process developed in this thesis is a photo-sensitive type of polyimide (LTC39) which can be patterned in the same way as a negative photoresist and developed using a cyclopentanone-based developer. It can be cured at low temperature for the soft-baking step, which is enough for evaporating solvent, but for optimal performance and good

adhesion layers, high-temperature bake (350°C) in the atmosphere with low O^2 concentration (~ 20 ppm) is preferable. The main application of PI in the fabrication of integrated pacing electrodes is as a stress buffer layer between PDMS and the sputtered metal layers, as its Young's modulus (~ 2 GPa) value is in between that of stiff metal layers (Al, Ti, TiN) and soft PDMS. The additional purpose of PI is as an insulation layer for the interconnects of the electrodes because of its dielectric properties.

6.3.2. PROCESS FLOW

Two different fabrication strategies were proposed and developed to integrate a pair of pacing microelectrodes into the EHT platform. The first fabrication strategy consists of fully automated process steps and can be easily adapted for standard mass production cleanroom-compatible flows. This strategy entirely relies on standard microfabrication techniques and tools available inside a well-equipped cleanroom environment. However, due to technical difficulties, this process flow was not used for the fabrication of the final devices. Nevertheless, all the steps of the process were tested and their viability was proven, as it will be further discussed in detail.

The second fabrication strategy was envisioned as an alternative process flow, with fewer steps and the use of less costly equipment. This strategy, however, involves manual steps such as wafer alignment, bonding and laser cutting, which are all performed outside of the cleanroom environment. All this makes the second process more challenging for upscaling, even though it was used for the fabrication of final devices.

FABRICATION STRATEGY 1

The fabrication flow of the EHT platform with integrated electrodes can be divided into several parts which will be described below. All the fabrication steps of pacing electrode integration into the EHT platform are shown in Fig.6.7.

1. Silicon mould fabrication

The fabrication process starts with a double-side polished Si wafer with a thin layer of thermal oxide grown on both sides. Additional 5 µm PECVD SiO_2 is deposited on the front side and patterned using standard photolithography steps (Fig.6.7A). The oxide is dry etched in CHF_3 plasma, followed by photoresist removal in ionized O_2. The patterned oxide is used as a hard mask for DRIE of cavities for pillars and wall moulding into the Si wafer using Bosch process (Fig.6.7B). The same approach is used as in Chapter 2, for 2 µL EHT platform. Teflon residues after Bosch process are cleaned in 15 min high-power O_2 plasma. After mould fabrication, SiO_2 used as the hard mask is removed from the wafers using buffered HF. Next, 1μm of SiO_2 is thermally grown on the wafer to ensure conformal covering of deep cavities with a high-quality oxide layer (Fig.6.7C). This oxide layer within the cavities in the Si wafer will protect the PDMS pillars during the final release of the structures by the backside etching of Si. After thermal oxidation, 4 µm of PECVD oxide is deposited on the backside of the wafer and patterned as previously, to create a hard mask for the last step of Si etching (Fig.6.7D).

2. PDMS moulding

From this point, polymer processing starts and the wafer is considered polymer-contaminated, therefore additional cleaning steps must be taken before using standard tools in the cleanroom. The first step of polymer processing is filling in deep cavities in Si with PDMS

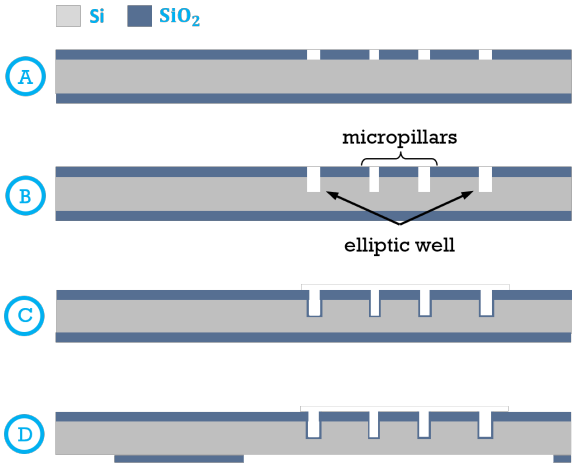

Figure 6.7: Process flow of the first fabrication strategy of EHT platform with integrated pacing microelectrodes: Si mould fabrication for micropillars and elliptic wells.

while obtaining a thin and uniform layer on the wafer surface (Fig.6.8A). The thickness of this PDMS layer should be approximately 20 µm. To make sure that the flat thin layer of PDMS is obtained on the wafer surface, long degassing (3h) is performed prior to curing. PDMS is then cured in a vacuum oven for 2 hours, with slow temperature ramping up from 20 to 80 °C, followed by the final curing at 90 °C for 30 min. Upon curing, the PDMS above the Si cavities is covered with a stress-buffering polyimide layer prior to metal sputtering. This step assures uniform deposition of the Al layer on top of PDMS within deep cavities, preventing metal cracking. Before Al deposition, a leak-up rate (LUR) test is done to check if the gas leakage from the polymer layer is within the allowed range. High gas leakage out of the polymer can affect the sputtering conditions and the controllability of the process. For this reason, PDMS is cured in vacuum and kept there until the LUR test to avoid any gas absorbance. Besides the LUR test, prior to metal sputtering, the surface of PDMS is exposed to low power O_2 plasma to enrich the PDMS surface with hydroxyl groups and improve adhesion between metal and polymer [116]. Sputtering is performed in four steps, with 250 nm Al deposition per step, with 3 min degassing steps in between (Fig.6.8B). The deposited Al layer is patterned using standard photolithography steps, using spray-coating instead of spin-coating due to the high topography present on the wafer. The Al layer is dry etched in chlorine (Cl) and hydrogen bromide (HBr) plasma to create the hard mask for etching contact and electrode openings in PDMS. In the case of PDMS dry etching, Al is used as a hard mask because the etching chemistry attacks the photoresist as well, which therefore cannot be used as a protection. In the following step, 20 µm of PDMS is dry etched in plasma of sulfur hexafluoride (SF_6), carbon tetrafluoride (CF_4) and O_2 until reaching the SiO_2 landing layer (Fig.6.8C). Al hard mask was then removed in PES solution (Fig.6.8D).

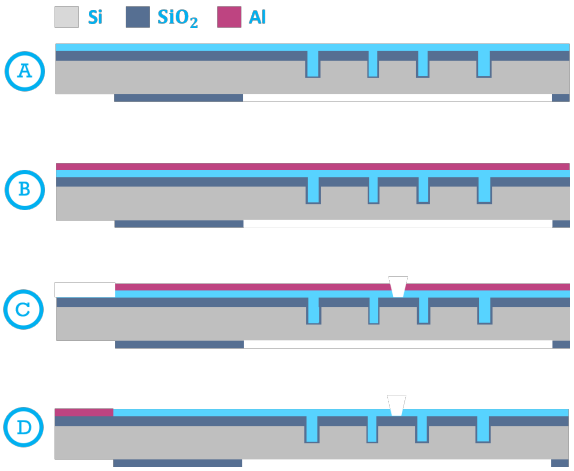

Figure 6.8: Process flow of the first fabrication strategy of EHT platform with integrated pacing microelectrodes: PDMS moulding and etching contact and electrode openings.

3. Electrode patterning

The 1 µm thick PI layer is patterned on top of the PDMS with electrode and contact openings (Fig.6.9A). This is the first insulation layer for the interconnects and a stress buffer for the following metal deposition. To create the pacing electrode, a first Al layer for the contact pads is deposited and patterned using photolithography and dry etching, followed by sputtering of 200 nm Ti and 50 nm TiN layer (Fig.6.9B). Due to the high difference in stiffness between Ti/TiN layer and PDMS, only parts on top of the PI layer are free of wrinkles and cracks. Similarly to Al, the TiN/Ti layer is patterned using spray-coating and standard photolithography steps and etched in Cl/HBr plasma. Coating and patterning of a second PI layer followed, for encapsulation of the interconnect areas (Fig.6.9C).

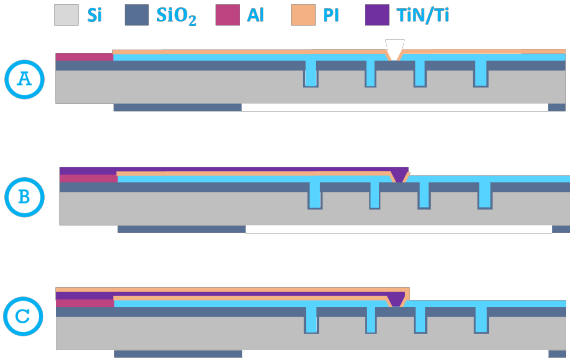

Figure 6.9: Process flow of the first fabrication strategy of EHT platform with integrated pacing microelectrodes: Patterning TiN/Ti/Al electrodes on PDMS, encapsulated in between polyimide layers.

4. Platform release

After electrode encapsulation, an additional 50 µm of PDMS is spin-coated on top to define the substrate for the EHT platform (Fig.6.10A). Again, an Al layer is sputtered on top of the PDMS as protection for PDMS during the last etching step. Finally, the EHT platforms are released by etching silicon from the backside of the wafer using Bosch process (Fig.6.10B). In this step, a circular opening is made in the Si wafer, along with two small squared openings for contact pads. PDMS pillars and elliptical microwell are released during Si etch within the large circular well. Finally, the protective Al layer is removed in PES, while the landing layer of thermal SiO_2 on top of the PDMS pillars and microwells is removed in buffered HF solution (Fig.6.10C).

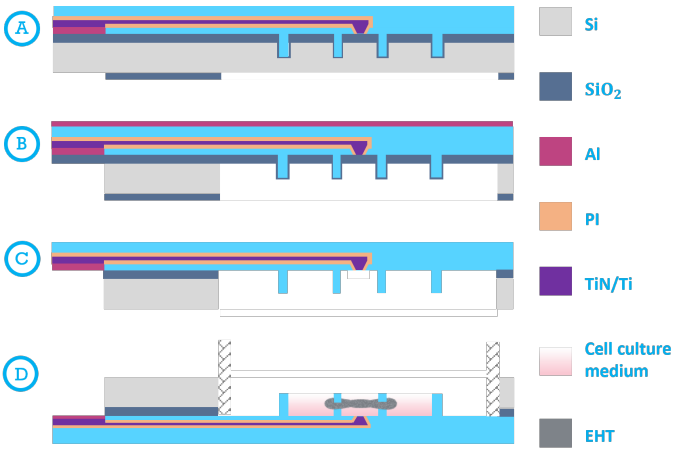

Figure 6.10: Process flow of the first fabrication strategy of EHT platform with integrated pacing microelectrodes: Backside etching of the silicon and final release of the structures.

FABRICATION STRATEGY 2

For the second proposed process flow, many of the solutions were adopted from the first fabrication strategy. However, the process was separated into two individual wafers to decrease the complexity of the fabrication and to avoid the use of cleanroom tools that became unavailable during process development. The illustration of the fabrication process is shown in Fig.6.11.

The first wafer is the silicon mould for PDMS pillars and elliptic wells. All the steps (1-4) are the same as in the first process flow. Briefly, a single-side polished Si wafer was patterned and etched using DRIE to create the mould for PDMS pillars and elliptic wells. Upon etching, the wafer was silanized to assure hydrophobic surface of Si prior to PDMS spin-coating and filling of the cavities in the Si wafer. Polyimide was patterned on top of the PDMS layer to create the stress-buffering layer prior to metal deposition. Aluminum was then sputtered and patterned for contact and electrode openings. Both Al and PDMS were dry-etched to create openings in the PDMS layer. The first wafer processing ended with Al removal in PES.

The second single-side polished Si wafer was silanized prior to spin-coating 80 µm

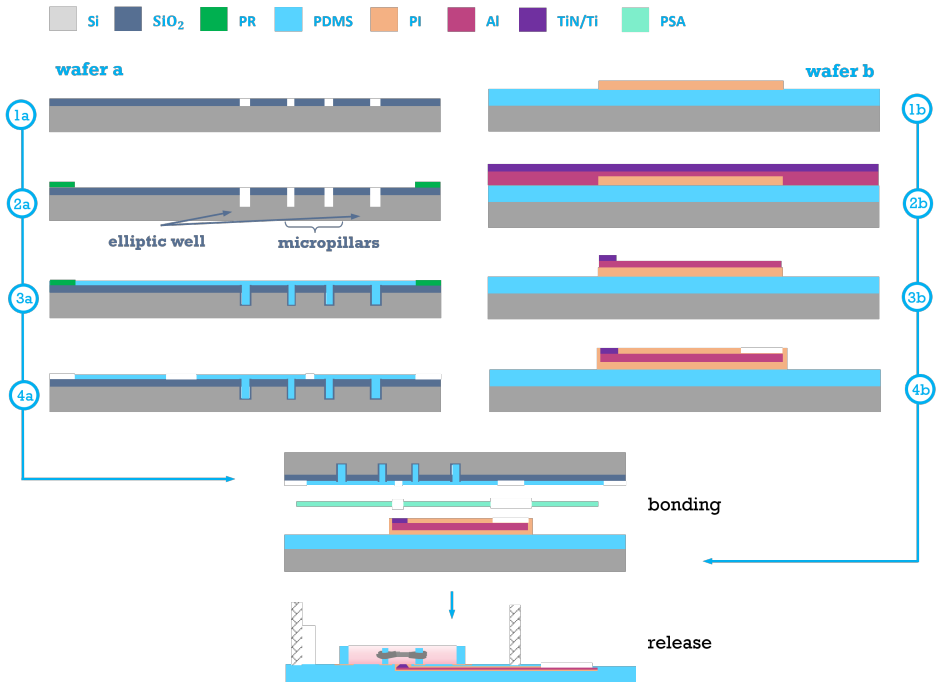

Figure 6.11: Process flow of the second fabrication strategy of EHT platform with integrated pacing microelectrodes

thick PDMS layer. The first PI layer was patterned on top of PDMS to create good and stress-free adhesion between metal layers and the PDMS substrate. Furthermore, 1 µm-thick AlSi, 100 nm-thick Ti and 25nm-thick TiN layers were sputtered on top of PDMS with patterned PI. TiN was the last sputtered metal layer, making it the top layer of the electrodes. This was preferred because of its good properties. TiN does not form an oxide layer, it has a good charge transfer efficiency, and it has high polarization resistance [145]. Electrode areas were patterned first by dry etching selectively only the TiN/Ti layer. Next, Al was patterned for both interconnects and contact pads. Aluminum was used for serpentine interconnects because of its lower stiffness than Ti/TiN, to preserve the integrity of the metal lines upon polymer deformation. The second PI layer was spin-coated and patterned on top of the electrodes for the final encapsulation and protection.

The last step of the fabrication process of the EHT platform with integrated electrodes is bonding of the two wafers. This was done using pressure-sensitive adhesive (PSA) as the bonding layer. PSA was laser-cut in a wafer-scale format to match the contact and electrode openings of the wafer with moulded PDMS. Adhesive protection was removed from one side and aligned to the wafer with PDMS structures. PDMS was peeled off the silicon mould using PSA as a mechanical support. Only by using a very strong adhesive such as PSA, 700 µm-long PDMS pillars and wells on top of a 20 µm-thick PDMS substrate were removed from the silicon cavities without damage. The PDMS layer bonded to PSA was suspended on water droplets on a glass wafer and aligned to

the second wafer with patterned electrodes. Two wafers were finally bonded by removing the second adhesive protection of PSA. After bonding, EHT platforms with integrated pacing electrodes were cut into 9 x 9 mm^2 squares and peeled off the second Si wafer.

Both process strategies result in a pair of TiN/Ti electrodes integrated into the EHT platform. Fig.6.12 demonstrates the final electrode patterning and encapsulation within the PDMS microwell, in the proximity of pillars.

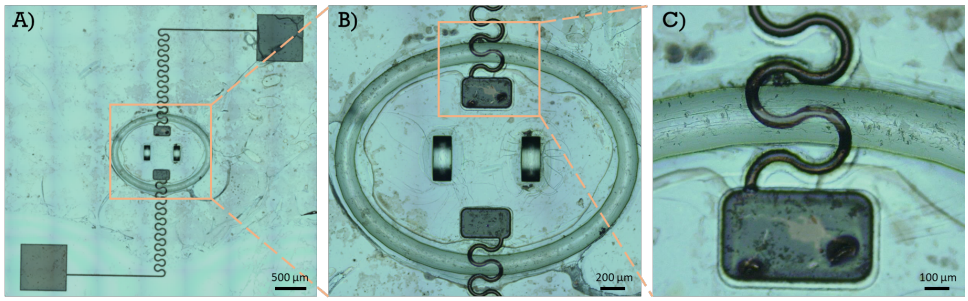

Figure 6.12: Fabricated EHT platforms with integrated pair of pacing microelectrodes. Top view of the final PDMS platform (A) with a close-up view of the elliptic well (B) and the single TiN electrode (C).

6.3.3. CRITICAL FABRICATION STEPS

There are several fabrication steps worth elaborating on in more detail as they were critical for the process flow development.

CONFORMAL PDMS COATING OF THE WAFER WITH DEEP CAVITIES

One of the first challenges of the fabrication of the EHT platform with pacing electrodes was filling the 700 µm-deep cavities in Si with PDMS and obtaining a thin uniform layer of PDMS on top. The standard spin-coating does not work in this case since, due to the centrifugal force, PDMS is removed from cavities during spinning. One of the available coating methods that can be suitable for this specific application is the doctor blade technique [146]. With this technique, low-viscosity material is spread over the substrate with the slow movement of a sharp blade, leaving the uniform layer of desired thickness behind, as illustrated in Fig.6.13A. The blade distance from the substrate is fixed and determines the final layer thickness. The uniformity of the obtained layer depends on many parameters such as surface tension and viscosity of the coating layer, blade material, the speed of the blade movement as well as the angle between the blade and the substrate. When coating substrate with cavities, geometry and density of openings has an influence as well.

The initial tests showed that using a very thin sharp blade for PDMS coating resulted in material removal from the cavities in silicon due to the large angle between the blade and the substrate. Reduction of the coating angle improved the layer uniformity and the process was finally optimized with the use of a glass cylinder instead of the blade. Using a glass cylinder significantly reduced the coating angle, finally creating a flat PDMS layer of uniform thickness across the entire wafer. The resulting thickness of the coated layer was determined by a 20 µm-thick ring of photoresist patterned on the edges of the wafer.

By rolling the glass cylinder on top of it the thickness of the PDMS layer was set to 20 µm, as illustrated in Fig.6.13B.

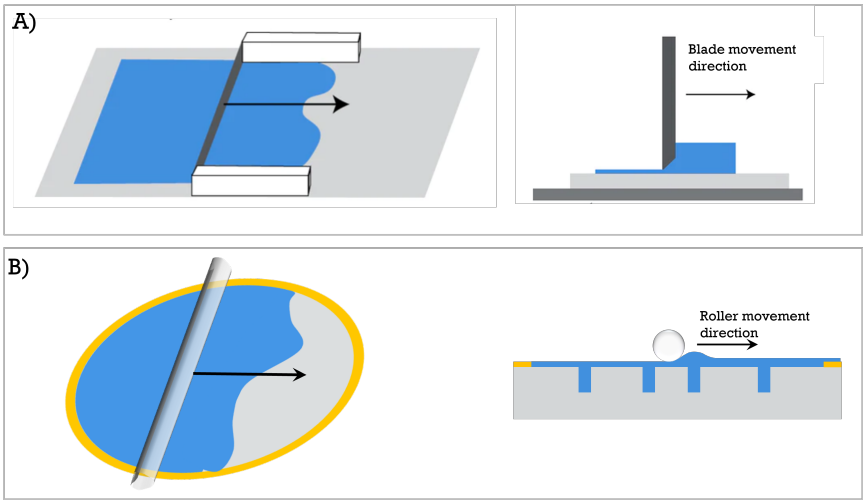

Figure 6.13: Illustration of different coating techniques: A) doctor blade coating by controlled spreading of the low-viscosity liquid on a substrate using a sharp blade; B) glass roller-coating of PDMS on top of a Si wafer with cavities using cylindrical glass roller.

PDMS CURING

After roller coating, the next critical step was PDMS curing. It was found that the concave profile of PDMS above cavities is the most suitable for conformal coating with PI and metal in later steps. In the case of the convex profile, metal sputtering and lithography resulted in damaged interconnects, while a perfectly flat layer was very challenging to obtain. The reason for this is the thermal expansion of PDMS during metal sputtering as well as the low vacuum in the sputtering chamber that pushes out trapped gas from the PDMS in cavities, even if PDMS was cured in a vacuum oven. To obtain the desired concave profile of PDMS above deep cavities prior to metal sputtering, PDMS was first

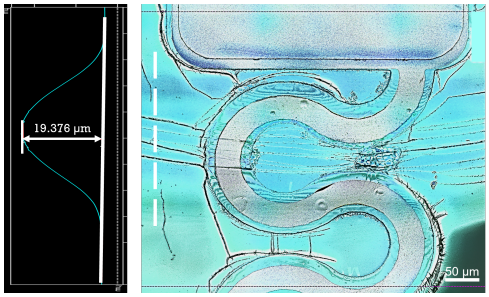

Figure 6.14: Profile measurement above microwell filled with PDMS, with the electrode patterned on top.

cured in vacuum at a lower temperature, with a slow ramping up from 20 to 80°C to remove as much of the trapped air as possible. The first part of curing resulted in a uniform PDMS layer above the deep cavities. The second curing step was done rapidly at a higher temperature (90 °C) to cause thermal expansion of PDMS and create a concave profile above the cavities. The formed hills of polymer were approximately 20-25 µm high, which was not the problem later for lithography and metal patterning. An example of the PDMS concave profile above the cavities in the Si wafer is shown in Fig.6.14.

PI AS A STRESS BUFFER LAYER

Even though the concave profile of PDMS is advantageous for metal sputtering and lithography, as it solved the issue with the large PDMS deformation, still during the sputtering process deep wrinkles and cracks are formed in the areas above the cavities. Wrinkle formation is a consequence of the expansion and compression of the soft polymer during the sputtering process. Especially due to the presence of metal layers with a much higher stiffness than PDMS, the cracks and wrinkles are quite prominent. An example of the PDMS layer after the metal sputtering and removal is shown in Fig.6.15A. Consequently, metal layers are not continuous in the areas above cavities. This step is critical for both fabrication strategies, as the Al layer needs to be sputtered and patterned after PDMS filling of the holes, in both cases. Non-uniform coating of PDMS with Al results in damage of the walls and pillars during dry etching.

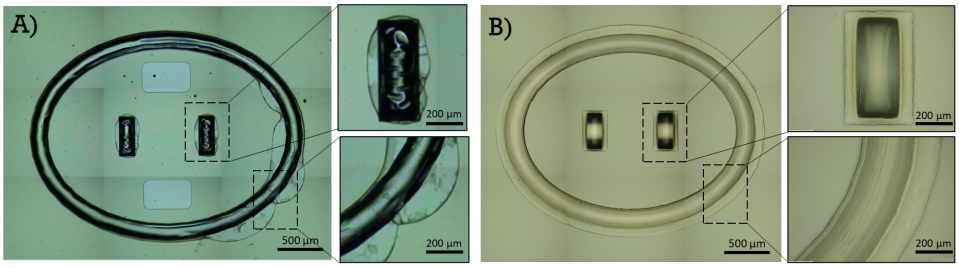

Figure 6.15: Comparison of the filling in deep cavities in Si with PDMS, before (A) and after (B) addition of PI layer on top.

To solve this issue, an additional PI layer was deposited above the cavities prior to any metal deposition, as demonstrated in Fig.6.15B. This layer is a stress buffer that prevents cracking and wrinkling of PDMS in the deep Si cavities and enables the deposition of uniform and conformal metal layers on top. Fig.6.15 shows a comparison between PDMS in cavities, before and after the addition of PI.

This step is particularly relevant for the first fabrication strategy and it is one of the most challenging steps of the process flow. If the layer on top of the walls and pillars is not smooth enough and free of wrinkles and cracks, electrodes and interconnects cannot be patterned. Fig.6.16 shows PI and electrode patterning across the PDMS wall before and after the deposition of an additional PI stress-buffer layer above cavities. This shows that neither PI nor metal could be patterned on top of the PDMS wall without a stress buffer layer. The close-up image of the wall without the PI layer (Fig.6.16A, B) shows prominent wrinkles formed during metal sputtering. Even minimal non-uniformity in

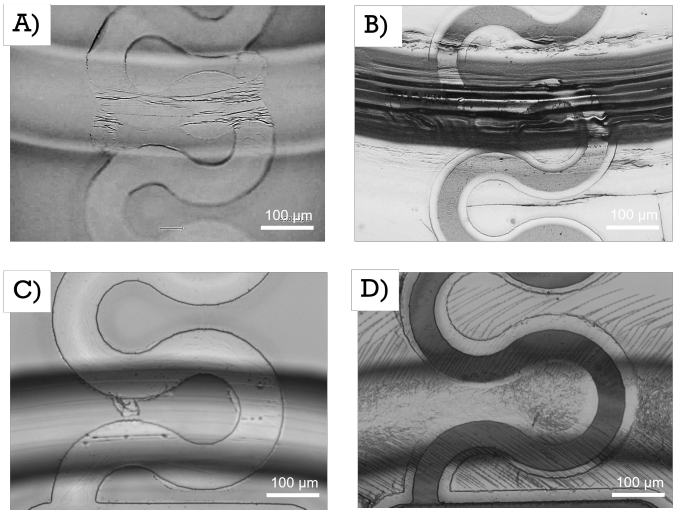

Figure 6.16: Polyimide and metal patterning on top of the elliptic microwell filled with PDMS, before (A,B) and after (C,D) additional PI layer covering the microwell.

Al coverage will increase after dry etching of metal, resulting in pronounced roughness in the PDMS elliptic wells. In the second case (Fig.6.16C, D), after introducing the PI stress-buffer layer, both PI and Al/TiN/Ti patterning and lithography were successful.

A demonstration of the PI role as a stress buffer layer for the electrode patterning on top of PDMS is shown in Fig.6.17. After metal deposition, the cracks due to stress in PDMS become even more prominent, than when only PI was present. Moreover, new cracks form because of the significant stiffness difference between the PDMS and Ti/TiN layers. Fig.6.17A shows the metal deposition on top of a wafer with PDMS and patterned PI structures. After removing metal outside of the electrode area, the role of PI becomes evident. It is possible to notice how the metal layer is uniform and continuous on top of PI protection, while wrinkles and cracks are present only outside of the PI region, at the PDMS-PI interface (Fig.6.17B). Finally, Fig.6.17C demonstrates metal patterning directly on top of a uniform PI layer, which results in a stress-free electrode and its sur-

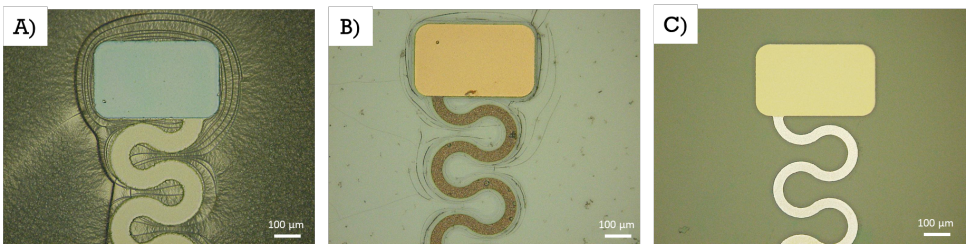

Figure 6.17: The difference in stress distribution after metal deposition (A) and patterning (B) on top of the PDMS layer and on top of the PI layer (C).

roundings. In case when mechanical stimulation of the platform is not needed, therefore substrate elasticity is not critical, the approach of using a uniform instead of pattered PI layer might be adopted to completely avoid stress and consequential crack formation in PDMS.

Another fabrication detail worth mentioning is the curing of PI layers on top of PDMS. Preferably PDMS is used in the final steps of the fabrication process due to its low temperature capacity. Once PDMS is deposited, process temperature should ideally not go above 100 °C to not affect its mechanical properties. However, this process flow requires the curing of the PI layer on top of a cured PDMS. As previously explained, complete polymerization of PI, good adhesion and optimal mechanical properties of the layer are achieved when curing at 350 °C in an atmosphere with low O_2 concentration. On the other hand, PDMS starts decomposing around 250 °C, and its mechanical properties depend highly on the curing conditions [147, 148]. The typical curing temperature used for PDMS was 90 °C. Therefore, the compromise was found between optimal curing of PI and temperature resistance of PDMS, so that the solvent component was removed from the PI layer and delamination is avoided, but also that PDMS was not exposed to very high temperature. The recipe for curing PI at 150 °C was developed and used for curing all the PI layers. This temperature reduction did not show any negative effects on the PI layer, except for the increase in the final layer thickness by 30%. However, the adhesion effects might become apparent once mechanical stimulation is incorporated.

PI CHALLENGES

Several challenges emerged when processing PI on top of PDMS as a stress buffer and electrode insulation layer. First, when spin-coating PI it is very important to achieve good adhesion to the substrate. For this reason, plasma treatment must be performed before spin-coating PI on top of a PDMS layer, to enrich the PDMS surface with polar-OH- groups and make it hydrophilic. Poor adhesion to the substrate will cause delamination and wrinkling of PI.

The development of exposed PI is also critical. If prolonged, it can lead to structure detachment from the PDMS layer. The development reaction ends by immersing the wafer with developed PI into the RER600 rinser. After this, the wafer should dry out by evaporating chemical residues, in air or nitrogen atmosphere. Removing the rinser with DI water causes cracks and wrinkles formation on the PI surface. This effect is visible in Fig.6.18A, B.

Another challenge encountered during PI processing on top of a PDMS layer is the stress in PDMS around the patterned PI structures. The cracking lines due to the stress release are formed immediately after PI coating, especially around sharp edges where stress concentration is high (Fig.6.18C). The cracks originating from the corners of e.g. square contact pads ended up at the interconnect area causing disruption in metal lines (Fig.6.18C). To solve this issue, the PI layer below the contact pads was redesigned into rounded corner structures with slight tapering to smoothen out the transition from a large contact pad area into a thin, serpentine interconnect. Such a design solved the issue of broken interconnects and reduced the stress in the PDMS layer around the sharp edges of PI structures, as visible in Fig.6.18D, E. Additionally, when patterning metal on top of the polymer layers such as PDMS and PI using dry etching, the timing of the etch-

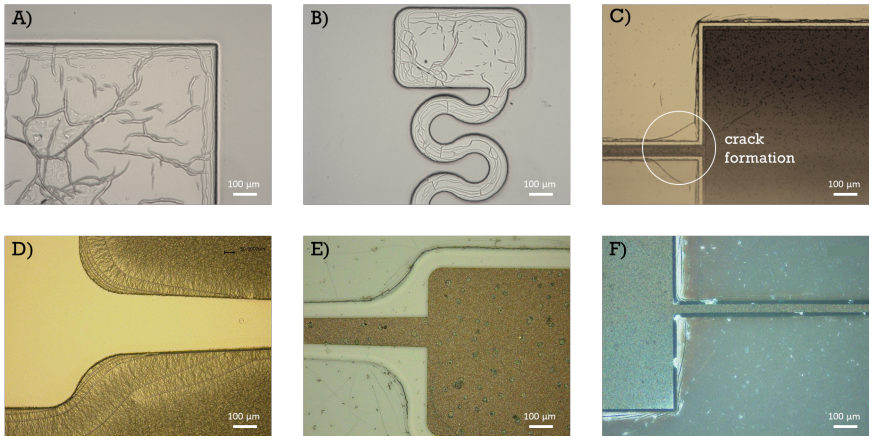

Figure 6.18: Examples of polyimide processing challenges.

ing process is crucial. In the case of even short overetching (10-15 s), both PI and PDMS get burned and result in a dark opaque layer as shown in Fig.6.18F.

PDMS ETCHING FOR CONTACT AND ELECTRODE OPENINGS

In the final fabrication process, electrode and contact openings were dry etched into a 20 µm-thick PDMS layer using a combination of SF_6, CF_4 and O_2 plasma. However, except for the dry etching, wet etching of PDMS was also explored. The benefits of wet etching are the speed of chemical reaction, good selectivity and lower cost than plasma etching. During dry etching SiO_2 is utilized as a landing layer, which is also etched by the chemistry used for PDMS etching, making the selective PDMS etching very challenging. Especially in the case of roller-coating of PDMS, the difference in layer thickness can reach up to 4μm from the center towards the wafer edges. This difference causes extensive overetching of the SiO_2 landing layer in the areas with thinner PDMS due to the poor etching selectivity, which is one of the main drawbacks of the dry etching process. On the other hand, a downside of wet etching is the use of very aggressive and dangerous chemicals which, if absorbed by PDMS, can be toxic to the cell culture. Nevertheless, with some fine-tuning, wet etching might be a good alternative for PDMS etching of small features and thin layers, such as contact openings, in the case when dry etching tools are not available.

PDMS was etched in a solution of tetrabutylammonium fluoride (TBAF) and N−methylpyrrolidinone (NMP) mixed in 3:1 ratio [149, 150]. The fluorine chemistry of TBAF is used to etch PDMS and form a complex, which is then removed using NMP as an organic solvent [151]. The etching solution reaches saturation after 35 min and the chemical reaction stops. Every 35 min of etching, the solution needs to be refreshed, which sets constraints on the PDMS thickness that can be etched in one go.

Similarly to the dry etching, regular photoresists cannot be used as the masking layers since they are dissolved in NMP. Two different geometries were patterned in 1 µm-thick Al hard mask for PDMS wet etching test. First, a wafer with large circular openings

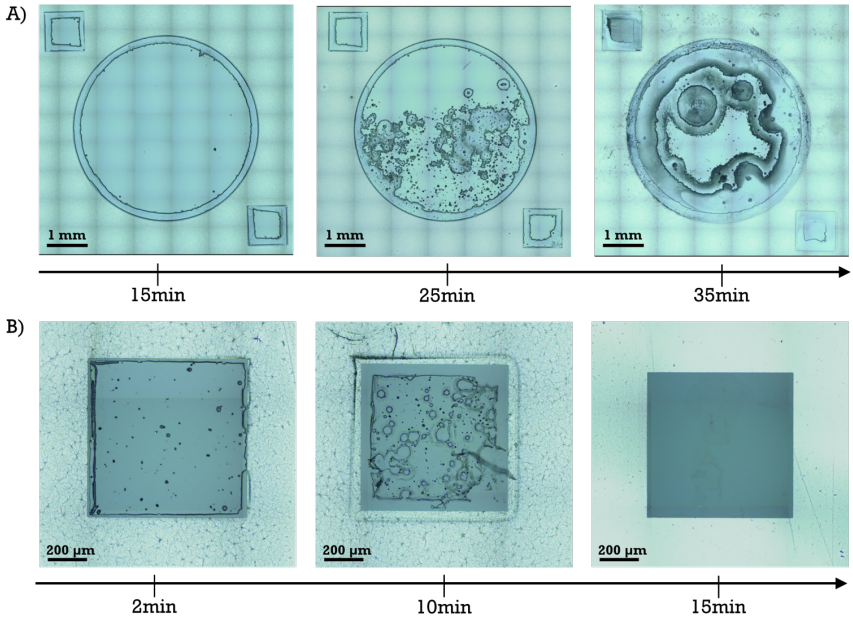

Figure 6.19: PDMS wet etching examples: A) timeline of large openings etching; B) timeline of etching contact openings.

was prepared to test the effect of PDMS etch of a large surface area and to find the etching limit regarding the thickness of the layer and the etching progress in time. The second example included a wafer with only contact openings to test the etching efficiency of small structures and etching selectivity.

It was found that the etching started from the structure edges and went non-uniformly towards the middle of the openings, as shown in Fig.6.19. Due to the nature of the process, the etch rate was very difficult to measure. It was demonstrated that the most suitable use of wet etching of PDMS is for the complete removal of the areas uncovered by the Al mask, and that precise patterning of delicate structures was not possible. Both etching examples are shown in Fig.6.19. In the first example with large circular structures, it was noticed that the etching saturates after ~ 30 min and that PDMS in this case cannot be completely removed without refreshing the solution. On the other hand, the second case (Fig.6.19B) demonstrated the complete removal of PDMS from the contact pad areas after 15 min, leaving a clean and smooth surface of SiO_2 landing layer below. Due to the process selectivity, the SiO_2 layer was not affected during the wet etching process.

FINAL STRUCTURE RELEASE

Finally, one of the most critical steps of the process flow was the release of the final PDMS structures from a Si mould by etching Si from the backside of the wafer. This was done using the Bosch process and 6 µm-thick SiO_2 layer as a hard mask. The most important parameters that are crucial for this process are the temperature of the process and the

thickness of the hard mask. Due to the presence of PDMS on the front side of the wafer, which is in direct contact with the bottom electrode during the Bosch process, helium cooling of the backside is less efficient. PDMS layer is an insulator, therefore the temperature of the silicon is higher than the temperature of the cooled-down chuck. This leads to low control of the etching process and faster consumption of the SiO_2 protective layer. To compensate for this effect, the process was performed at −10°C, to maintain the low temperature of the silicon wafer and assure that Si is completely etched from the big circular and contact openings before SiO_2 is entirely consumed. Fig.6.20. shows PDMS structure release from the backside of the wafer, where pillars and elliptic well are being protected by the layer of thermally grown SiO_2.

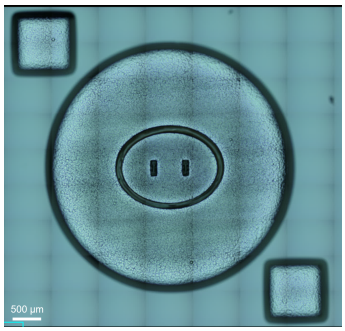

Figure 6.20: Final release of the test EHT platforms by backside silicon etching.

6.3.4. WIRE-BONDING

Once the final EHT platforms with integrated electrodes have been fabricated at a wafer level, they were cut or diced into single chips with dimensions of 9 x 9 mm^2, for further assembly and connection to the printed circuit board (PCB). Aluminum contact pads of the single chips were wire-bonded to the bond pads on the PCB. Similarly to the platform with integrated sensors, 1 µm-thin Al contact pads were suspended on top of the 80 µm thick PDMS layer. Wire-bonding on top of such a soft layer was performed using golden shims as a rigid support for the wire-bonding on top of the Al contact pads. The golden shims were attached to the pads using silver glue in a liquid form and baking it at 125 °C for 2h (Fig. 6.20A). Two joint points were made at the Al contact pad and at the PCB bond pad by welding the Al wire. Even with the addition of golden shims, bonding parameters had to be adjusted for this specific application, as the absorption of ultrasound energy was still higher than for the rigid substrates. An additional parameter to take into account is the force applied by the wire-bonding needle on the golden shim. If the applied force is too high, cracks are formed in the thin aluminum pads under the pressure. Optimized parameters used for wire-bonding are shown in Table 6.2. Fig. 6.20B, C shows single chips of EHT platforms with integrated electrodes, glued and wire-bonded to the gold-plated single-chip PCBs, to enable connection to the external pacing setup.

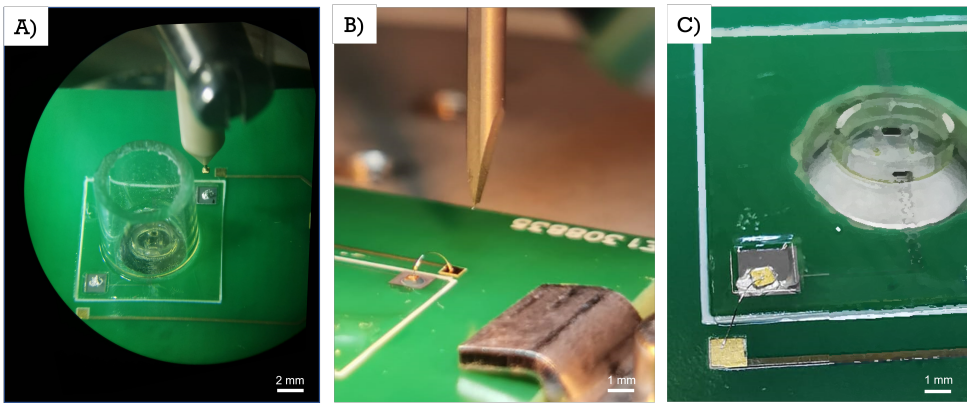

Figure 6.21: Wire-bonding of the single EHT platform with integrated pacing microelectrodes to a custom-designed PCB.

Table 6.2: Wire-bonding parameters for bonding the golden shims on Al pads, on top of a PDMS substrate, to the PCB contacts.

	US power [mW]	Time [ms]	Force [mN]
Bond 1 (chip)	1400	750	800
Bond 2 (PCB)	400	350	300

6.4. ELECTRICAL CHARACTERIZATION OF THE ELECTRODES

6.4.1. SHEET-RESISTANCE MEASUREMENTS

It is a good practice to inspect the quality of deposited layers during microfabrication processing. For conductive layers, a four-point measurement setup is typically used to obtain sheet resistance of sputtered metals on a wafer level, before patterning them (Fig.6.21). For this measurement, four probes are placed in line, equally distant from each other. The current is applied to the two outer probes (1,4), while the two inner ones (2,3) are connected to a high-impedance circuit and measure the voltage drop on a small part of the metal layer.

As mentioned previously, sputtering of Al/Ti/TiN was conducted at 25 °C, at 1 kW, after passing the LUR test. The low temperature is used to moderate the effect of wrinkle formation on the PDMS surface due to the large difference in thermal expansion coefficient between metal and polymer. The sheet resistance measurement of 1 µm of Al, 200 nm of Ti and 50 nm of TiN in 10 points on a wafer (Fig.6.22B) resulted in 29.522 ±1.5 mΩ/sq. Based on these measurements, and knowing the electrode dimensions, the resistance of patterned electrodes can be calculated in the following manner:

$$R_{sh} = \frac{\rho}{t} \tag{6.1}$$

$$R = \rho \frac{L}{A} = R_{sh} \frac{L}{w} \tag{6.2}$$

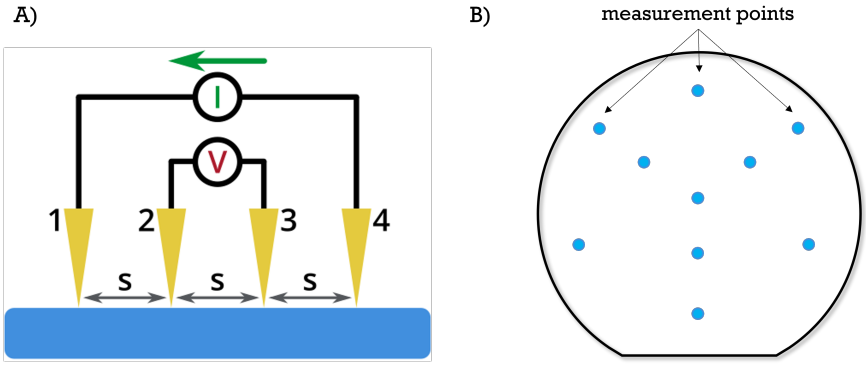

Figure 6.22: A) Illustration of four-point measurement setup; B) The ten measurement points on the wafer.

Here, R_{sh} is sheet resistance or resistance of the surface area of the electrode. When multiplied by the thickness of the metal layer $t = 1\mu$ m, it gives the resistivity of electrode ρ. Further on, R is the resistance of the electrode depending directly on electrode geometry and resistivity. L is the length of electrode and interconnects, A is cross-section area and w is the width of interconnects. All the dimensions were previously given in Table 6.1. Since R_{sh} is measured using the four-probe technique, the resistivity of the electrodes can now be calculated using Eq.6.2 and parameters from Table 6.1. Finally, the obtained value for resistivity is R = 6.5 Ω.

6.4.2. POST-FABRICATION RESISTANCE MEASUREMENTS

In addition to the characterization of metal layers during fabrication, the electrical characterization of the finalized platform with integrated pacing electrodes was also performed. Resistance of the fabricated chips was measured using the Cascade Microtech Summit 12k probe station. Two probes were brought into contact with the electrode and the contact pad to apply voltage in a range from -1 V to 1 V in 51 points. The resulting current was measured using the sensing functionality of the same probes.

Measurement results are shown in Fig.6.23. First, measurements were performed on diced chips, prior to wire-bonding. In this case, probe station needles were directly in contact with Al pads on PDMS. The second measurement was performed after the wire-bonding was completed and chips were transferred to individual PCBs. The idea was to test whether the contact between the golden shim and the Al contact pad through the conductive paste affects the resistance of the electrodes after the assembly process. However, what was noticed is that the resistance decreased in the second measurement, with wire-bonded chips. This happened due to the fact that the first measurements were done by gently scratching thin Al contacts on top of PDMS while trying to create electrical contact with the measurement probes. This made the measurement conditions quite challenging, as reflected in the variability of the results. On the other hand, the second measurement was performed by contacting golden pads on the PCB, which allowed easier and steady probing with the needles, good metal contact and more stable measurements. Wire-bonded chips have lower standard deviation and more repeatable

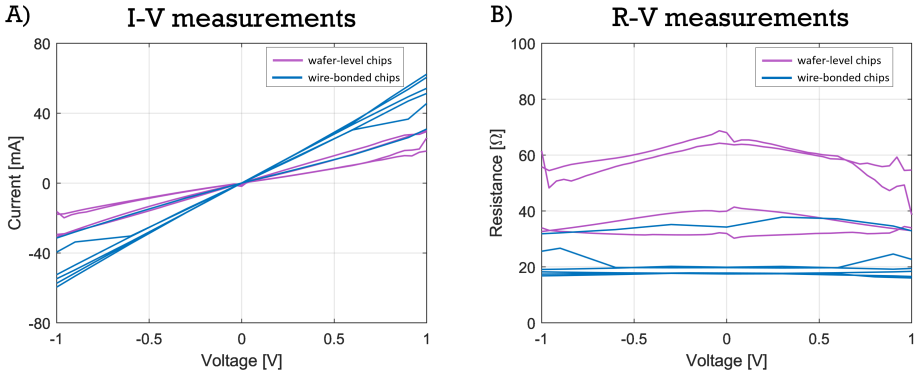

Figure 6.23: Electrical characterization of electrodes: A) I-V and B) R-V graphs for wafer-scale and wire-bonded platforms.

measurements with the resistance of R=21±6 Ω. For a single chip on a wafer level, more dispersed measurements were obtained with the average resistance of R=4±14 Ω. In total, 14 electrodes were characterized. Measurements were performed on the same samples, before and after wire-bonding.

The difference in the resistance values before and after the finalization of the fabrication can be attributed to the resistance introduced by measurement setup as well as the small variations in electrode dimensions during metal layer patterning.

6.5. DESIGN OF THE EXTERNAL PACING SETUP

As mentioned in the introduction, there are multiple ways of applying electrical simulations to the EHTs and the “optimal recipe” is yet to be found. For this reason, most of the currently used pacing systems come with parameters tunable within a range of interest, which gives a certain level of freedom in defining pacing experiments. Typical pacing systems use bipolar rectangular pulses of 1-25 V amplitude, up to 25 ms pulse width and up to 5 Hz stimulation frequency. For this specific EHT platform with integrated electrodes, the pacing circuitry was developed within the master thesis of Androniki Diakou [152]. The circuit generates short biphasic rectangular pulses with 15 V maximum peak-to-peak voltage, tunable pulse width from 0 to 25 ms and frequency in the range from 0.3 to 5 Hz. The maximum allowed current in the system is 12 mA. The output pacing signal is multiplexed to 16 individual channels to scale up the pacing capabilities and make it compatible with the future upgrade into a multi-well plate system (see Chapter 7). All the specifications of the pacing system are summarized in Table 6.3.

6.5.1. ELECTRICAL CIRCUIT MODEL OF EHT

An equivalent circuit of electrode/electrolyte interface has been used to estimate the expected load that cells within the cell culture medium represent in the pacing circuitry. The model consists of resistor R_p describing the polarization resistance of the electrode, in parallel to a capacitor-like "constant phase element" (CPE) [153] and the electrolyte

Table 6.3: Specifications of a pacing system.

Parameter	Description	Value
V	peak-to-peak voltage	30(±15) [V]
f	pacing frequency	0-5 [Hz]
I_{max}	maximum current	12 [mA]
T_{on}	pulse width	0-25 [ms]
N_{ch}	number of channels	16

resistance in series. The model is shown in Fig.6.24. For titanium nitride, it was found that $R_p = 4.68e^5 \Omega/cm^2$,$CPE = 2.66e^{-5} F/cm^2$, while the resistivity of human heart was found to be $R_t = 175 \Omega cm$ [154].

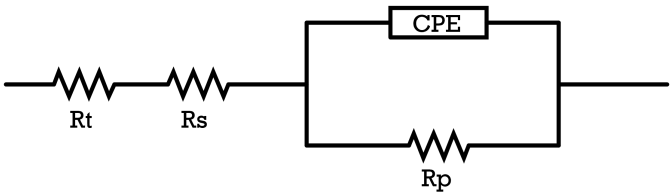

Figure 6.24: The equivalent circuit of electrode/electrolyte interface.

6.5.2. ELECTRONICS DESIGN

There are two common ways to implement electrical stimulation for biological tissues: voltage-controlled stimulation and current-controlled stimulation. The first method is more power-efficient because voltage remains stable while the current adapts to the load variation during the pacing experiment. The second method is less power efficient as the current control requires higher voltage, but provides good control of the current injected into the tissue. Both of these methods have been implemented into the pacing circuit design, whereby the selection of one or another can be made with a mechanical switch.

The developed pacing circuit can be divided into four units: the power management unit, a pulse generation unit, current and voltage measurement and signal demultiplexing. Each of these units will be briefly explained below. The block diagram of the pacing circuitry is shown in Fig.6.25.

POWER MANAGEMENT UNIT

The power management unit generates voltage levels required for the functioning of the pacing system. It receives 30 V DC from an external AC/DC converter, which is then converted into ± 15,± 12 and 8V, which are required voltage levels for all the other components in the circuit. The microcontroller unit (MCU) is supplied with 8 V, while operational amplifiers (OPAMPs) within the pulse-generation unit require ± 15 V to generate the maximum amplitude of the biphasic pulses. The voltage and current measure-

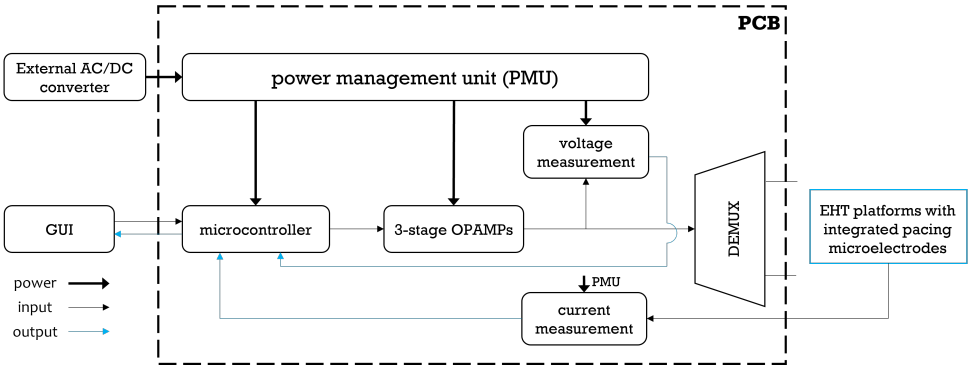

Figure 6.25: Block diagram of the entire pacing circuit system consisting of PMU, MCU, a pulse generation unit, voltage and current measurement modules, and demultiplexing unit.

ment circuits, as well as the demultiplexers and the Howland converter for the voltage-to-current stimulation mode, require ±15V.

The power supply system generates the required voltage levels using two converters. The first converter is a low-noise dual-supply inverting charge pump converter. It consists of an inverting charge pump with both linear positive and negative regulators. It converts 30 V of the external DC power supply to ± 15 V for all the above-mentioned units. The second converter is a DC-DC step-down converter, i.e. buck converter. It is the main supply for the microcontroller as it converts 30 V input voltage to 8 V at the output.

Both of these converters have safety capacitors, with a maximum working voltage of 50 V, between input signal lines and the ground, to assure the safe functioning of the power supply system and avoid sudden voltage drops. The block diagram of the power supply unit is shown in Fig.6.26.

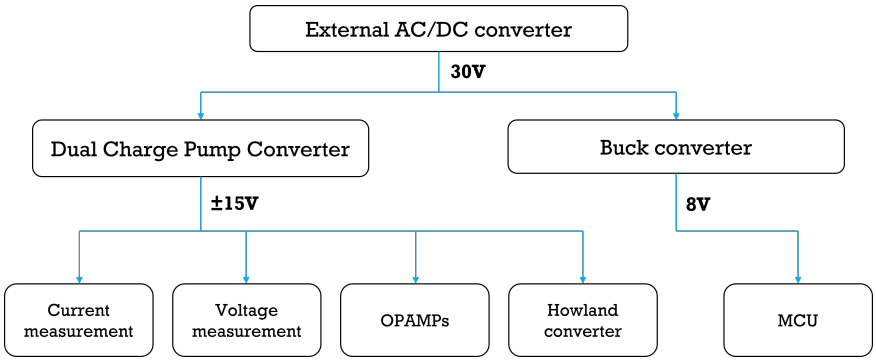

Figure 6.26: Block diagram of the power management unit: conversion of 30 V DC voltage to voltage levels required by the circuitry via dual and buck converters.

PULSE GENERATION UNIT

A system of three OPAMPs is used in sequence to generate bipolar rectangular pulses of desired properties. The input signals for the OPAMP sequence are two 5 V monophasic pulses generated by the MCU. These pulses were generated by implementing the pulse width modulation (PWM) method in the ATMEGA 328 microcontroller, to tune the pulse duty cycle according to the user input. The resulting two monophasic pulses, shifted in time by the single pulse duration, were the analog pin outputs of the MCU, sent further as inputs to the OPAMP sequence.

The first stage OPAMP is a differential amplifier that generated biphasic rectangular pulses of maximum ±15 V amplitude by subtracting two monophasic pulses coming from MCU. The second OPAMP functions as a buffer, improving the stability and consistency of the signal from the first amplifier. The third stage OPAMP is an inverting amplifier that defines the final shape of the pacing signal. In parallel to this output signal, there is a potentiometer that enables fine-tuning of the output signal amplitude in the specified range. The pulse generation unit is illustrated in Fig.6.27.

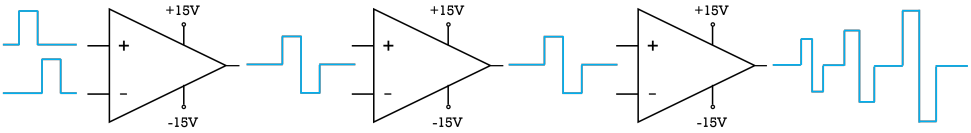

Figure 6.27: Schematics of bipolar pulse generation unit using three operational amplifiers.

CURRENT AND VOLTAGE MEASUREMENT

A very important requirement of the pacing system is to monitor and limit the current passing through the tissue during the entire duration of the pacing experiment. Indirect current measurement was implemented by measuring the voltage drop across a shunt resistor of a small resistance in the order of mOhm. Such implementation does not affect significantly the current flow, but due to a very small value of voltage drop, the measured signal requires amplification. The output of the current measurement circuit goes to the MCU analog input. This signal is further converted into a real current value and displayed in the GUI implemented in Matlab which will be explained in detail in the next Chapter. As the analog input of the microcontroller accepts 0-5 V, the voltage reference of 2.75 V was created in the middle of that range using a Zener diode.

Another relevant measurement that should be provided for the user is the output voltage measurement. The pulse amplitude is adjusted by the user with the potentiometer at the third stage OPAMP in the pulse generation unit. To make sure that the set voltage corresponds to the value generated at the output, a voltage measurement circuit is implemented. The output voltage is measured using an OPAMP with adjusted gain, which converts 0-15 V at the input to 2.75 – 5 V at the output. Similar to the current measurement, this output signal is connected to the analog input of the MCU, converted to the real voltage value and displayed to the user via GUI. The schematic of both current and voltage measurement circuits is shown in Fig.6.28.

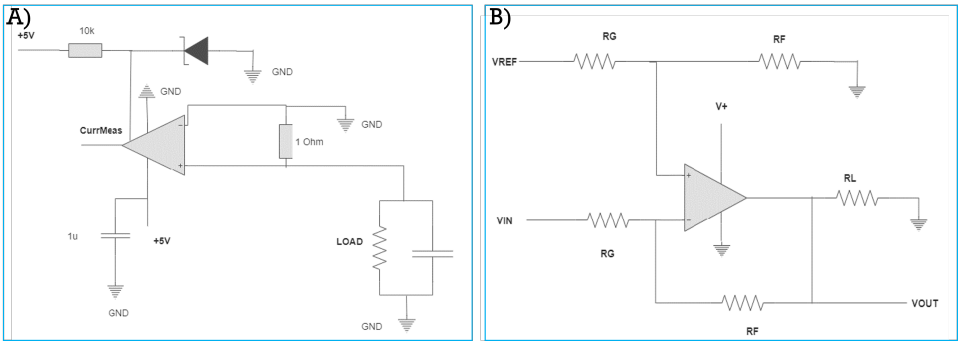

Figure 6.28: Schematics of current (A) and voltage (B) measurement circuits.

DEMULTIPLEXING

Demultiplexing of the output pacing signal is implemented in order to achieve selective stimulation of tissues in multiple EHT platforms. In this way, digitally controlling the selection signals of two demultiplexers (DEMUX) can deliver the pacing signal to 16 independent EHT platforms with integrated electrodes.

The generated biphasic pulse from the pulse generation unit is the input signal for two demultiplexers. Both DEMUXs are supplied with ± 15 V to be able to output the required pacing signals. Each DEMUX sends the input signal to one of the eight available output channels, which is controlled by selection via 3-bit address lines A0, A1, and A2 coming from the MCU.

6.5.3. TESTING

To verify the functionality and performance of the designed pacing circuit, several measurements were conducted. During the testing procedure, 30 V DC was applied to the board using Agilent 6613C DC Power Supply. In the later stage of the experiments, as well as during tests including EHTs, an external AC/DC converter was used to transform 220 V AC from the power grid to 30 V DC. As the initial verification, the voltage was measured at each testing point, at the outputs of the voltage converters, to make sure that all the components have the required voltage supply. Next, the circuit performance was tested with a digital oscilloscope, by monitoring the output signal of each OPAMP stage as well as the microcontroller outputs.

The voltage and current measurement circuitry were characterized by tuning the conversion coefficient used for the calculation of the measured signals based on the microcontroller analog inputs. The measured voltage is calculated based on Eq.6.3:

$$V_{real} = \frac{(V_{uC} - b)}{m} \tag{6.3}$$

where V_{real} is the voltage value applied to the tissue, V_{uC} is the voltage at the analog input of uC, and constants $m = 0.07$ and $b = 3.4V$ are desired gain and offset of the amplifier, respectively, set by resistors R_G, R_F and R_L in Fig.6.28B. The current is calculated

using Eq.6.4:

$$I_{real} = \frac{(V_{uC} - b)}{m \cdot R} \tag{6.4}$$

where I_{real} is the current going through the tissue, V_{uC} is the voltage at the analog input of uC, $m = 100$ and $b = 2.75V$ are gain and offset of the amplifier, respectively, and $R = 1\Omega$ is the resistivity of the shunt resistor from Fig.6.28A. The adjustments of the conversion equations from analog readout to the actual measured values are made by fitting the measured values to a second-order polynomial function in Matlab. This resulted in very precise real-time current and voltage measurements.

Finally, the performance of the pacing circuit by means of different pulse generation was tested by changing the frequency, pulse duration, and amplitude in the range defined by Table 6.3. Fig.6.29 shows the results of multiple frequency testing, where 0.5, 1, 2, and 4 Hz are presented. Variation of the pulse amplitude in the range from 12 to 4 V, for constant frequency, is shown in Fig.6.30.

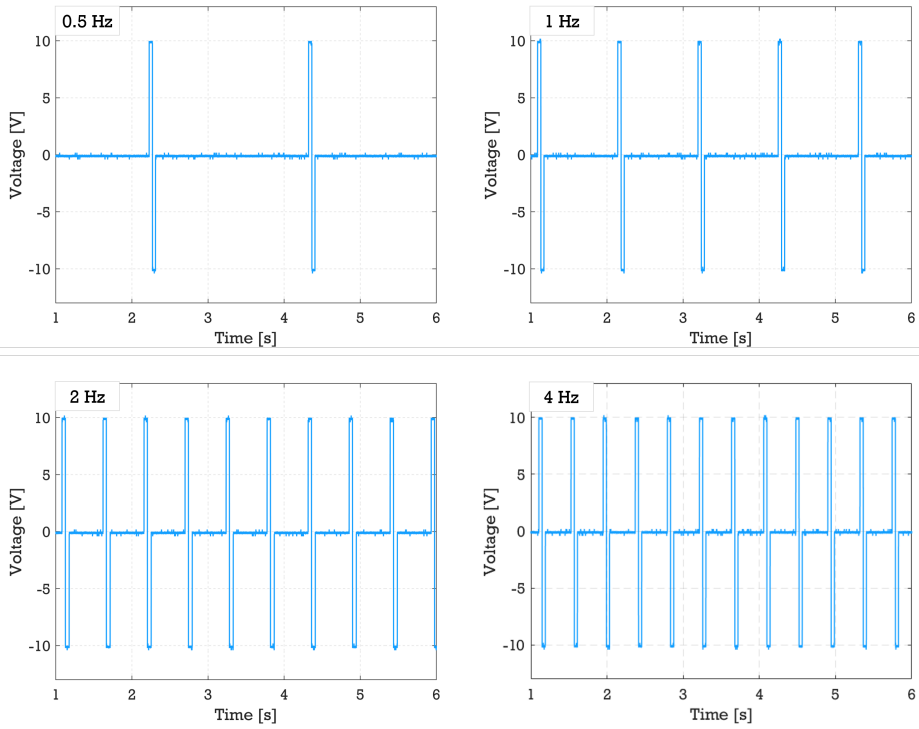

Figure 6.29: Demonstration of different frequency signals at the output of bipolar pulse generator.

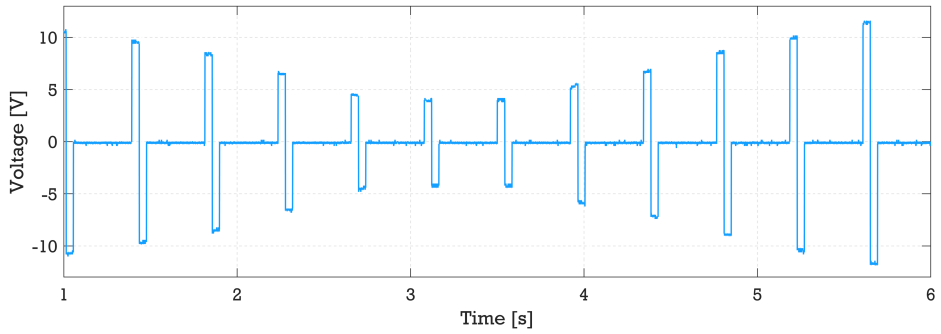

Figure 6.30: Demonstration of voltage sweep of the output signal of the bipolar pulse generator.

6.6. BIOLOGICAL VALIDATION OF THE PLATFORMS

Similarly to the previous cases, after the assembly of the entire platform with integrated pacing electrodes, biological validation followed. The cell culture was tested in single-chip PCBs with EHT platforms.

6.6.1. EHT GENERATION

Engineered heart tissues were made by mixing 70% cardiomyocytes (CMs), 15% of cardiac fibroblast (cFB) and 15% of endothelial cells (ECs). All three cell types were differentiated from iPSCs and kept in liquid nitrogen for up to 7 days prior to EHT seeding. ECM gel mixture was made using collagen I (3.3 mg/mL), DMEM (10X), NaOH, growth factor reduced Matrigel and formation medium in previously defined percentages (Chapter III). The EHTs were cultured in a formation medium for 72h combined with growth factors for endothelial cells and fibroblast (VEGF and FGF). After 72h the culture medium was switched to MBEL+ VEGF (50 ng/mL)+ FGF (5 ng/mL) and the same medium was used for refreshment until the end of the experiment. Since plastic circular wells around the EHT platforms for containing medium were smaller than standard 96-well plate compartments, less medium volume could fit in it and refreshment was done every two days instead of 3, as in the 96-well plate case. EHTs remained in culture for 14 days. During the entire experiment, tissues were kept in an incubator, except for brief periods for pacing experiments and measurement performance. Brightfield images were taken every day, following tissue formation, since the beginning of the experiment, with a Nikon Eclipse Ti2. Fig.6.31 shows tissues formed around PDMS pillars within the EHT platforms with integrated electrodes.

Tissues remained viable and functional for 14 days at least, demonstrating the biocompatibility of the novel platform with electrodes. The initial biocompatibility experiments were conducted on the single-chip level but the pacing was not tested on those due to issues with the structural integrity of electrodes and flaws in the assembly process. Upon solving the assembly issues, new experiments will be conducted to test pacing efficiency with the novel platform with integrated electrodes.

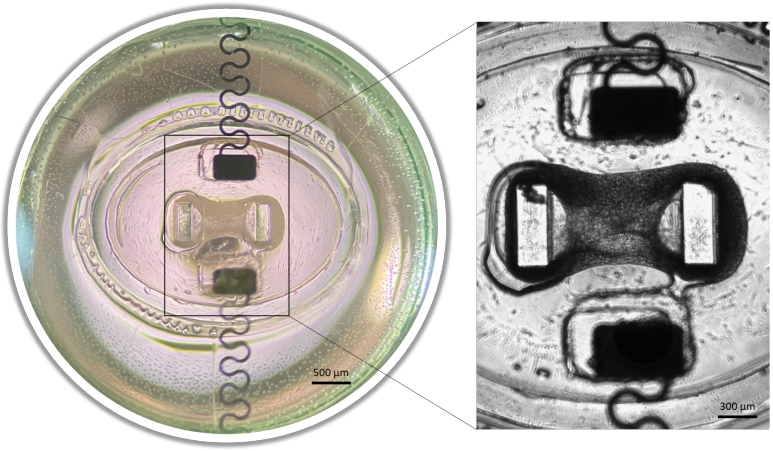

Figure 6.31: EHT culture on the platform with integrated pacing microelectrodes.

6.7. DISCUSSION AND CONCLUSIONS

In this Chapter, the design, fabrication and characterization of the EHT platform with integrated pacing microelectrodes were described. The pair of planar electrodes create a uniform electric field throughout most of the tissue area, perpendicular to the tissue formation direction. Numerical simulations using Comsol Multiphysics were carried out to determine the final design and position of the electrodes, placed at the bottom of the elliptic microwell, in close proximity to the tissue. Titanium nitride was selected as the electrode material due to its chemical inertness and non-faradaic charge transfer to the medium with tissues.

The platform was fabricated using a similar approach as before, combining standard silicon micromachining and polymer processing. Two fabrication strategies were developed for this purpose. The requirement of patterning metal on top of the polymer layer within deep Si cavities imposed significant challenges for both fabrication strategies. This issue was finally addressed with the inclusion of an additional stress-buffering layer. There might still be some air going out from the deep cavities with the polymer during pressure change prior to processing. This can generate small areas with inflating and deflating air bubbles. Even though, thanks to the PI layer, this trapped air does not harm metal lines, it can still interfere with the photolithography due to high topography.

Furthermore, for the first fabrication strategy, automation of the process was ensured with the final release of the structures with backside silicon etching and wafer dicing. Since initially the electrode integration process was developed for 3 µL platforms, 1mm-thick wafers were used for fabrication, making all the steps even more challenging. By switching to 500 µm-thick wafers and shorter pillars, the last fabrication step would become less challenging as it would require shorter etching steps. In this case, the first fabrication strategy would become preferable over the second one.

Nevertheless, even though being more manual, the second fabrication strategy proved to be very efficient. Optimization is required in all the wafer alignment steps, and a more

automated and custom-made system should be developed in the future specifically for this purpose. Standard available techniques for wafer alignment were not convenient for use in this case. Additionally, the second fabrication strategy is not optimal for future mechanical stimulation as substrate deformations are restricted due to the presence of the PSA layer. Still, the advantage of this approach is the compatibility with the fabrication of tapered pillars (Chapter 3), as there is no need for the backside structure release, which would anyway not be possible in the tapered pillar fabrication process.

Furthermore, custom-made pacing circuitry was developed for the generation of biphasic rectangular pulses for tissue stimulation, with tunable frequency, voltage and pulse duration. The circuit uses three-stage operational amplifiers to convert the monophasic rectangular pulses generated by a microcontroller into short, biphasic pulses of desired properties. The circuitry was designed to multiplex pacing signals and enable individual stimulation of 16 EHT platforms. As a future upgrade, the programming of the microcontroller can be modified to enable parallel stimulation of the tissues, by alternating signals between wells at high speed.

Finally, biological tests were performed to validate the novel EHT platforms with integrated electrodes. The initial tests proved the biocompatibility of the platforms, as tissues remained functional for 14 days. However, due to the failure in the electrical connection between electrodes and the PCB during the packaging process, pacing could not be tested. Future experiments will be conducted to test the efficiency of the electrical stimulation on tissues cultured in the developed EHT platform.

CHAPTER 7

A MULTI-WELL PLATE FOR SINGLE HEART-ON-CHIP PLATFORMS

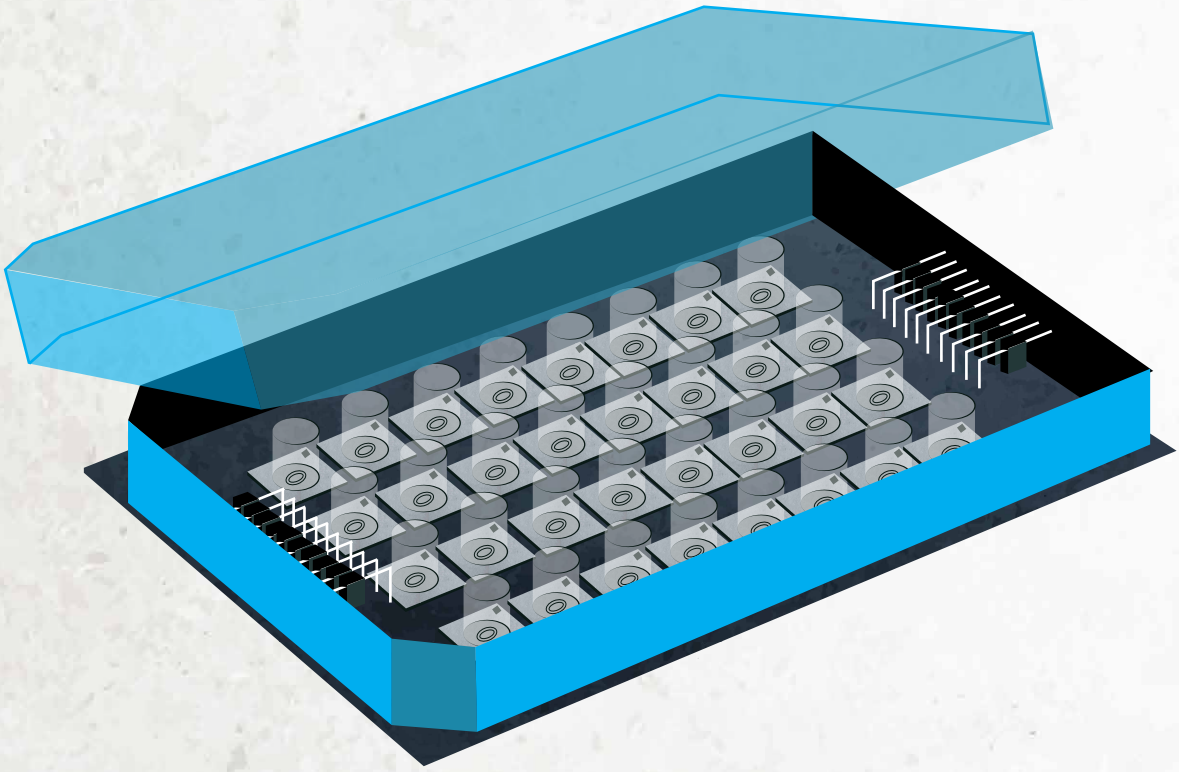

7.1. MULTIPLEXING SINGLE-CHIP OOC DEVICES

ONE of the big challenges of the OoC models that have been recently developed is the translation from research-based prototypes of single-chip models to multiplexed, upscaled systems used in high-throughput experiments and drug screening assays [12, 155–158]. Some of those chips reached the market as part of multi-well plate platforms and some of the examples of the ones that are commercially available are shown in Fig.7.1 [159–162]. Nevertheless, the commercialization and upscaled production of OoC systems are still at the starting phase. Most of the upscaled chips that reached the market in a multi-well plate format are relatively simple in design, containing static 3D topography and microfluidic integration, but with limited actuation and sensing capabilities. There is a lack of multi-functional platforms that would allow tissue culturing in a highly controlled and automated manner, including high-throughput analysis.

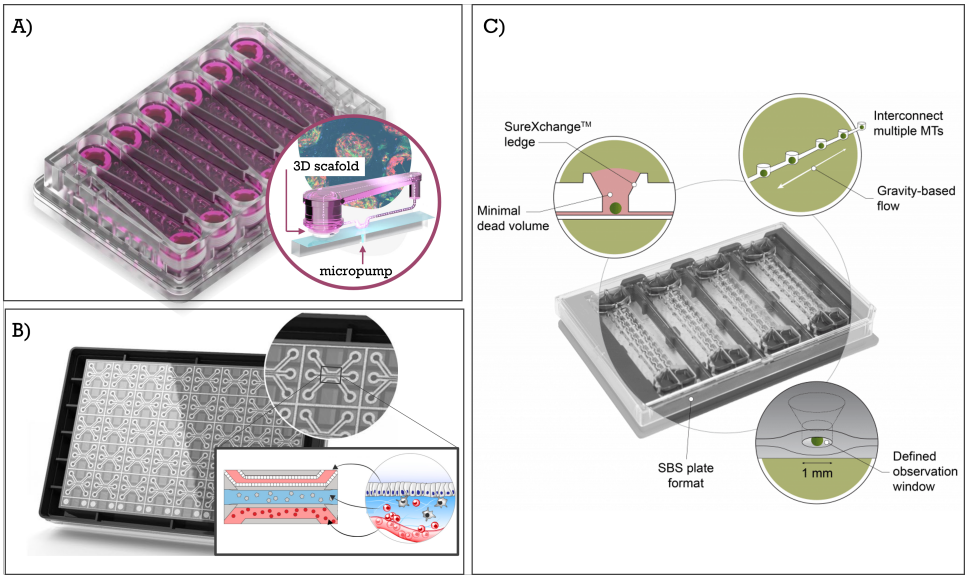

Figure 7.1: Examples of commercially available multi-well plate systems: A) PhysioMimix Liver plate by CN Bio for the culture of 3D liver organoids [163]; B) OrganoPlate by Mimetas for co-culture of different cell types [160]; C) Akura platform by InSphero for 3D microtissue culture [164].

In previous chapters, the focus has been on developing different versions of the platform for culturing engineered heart tissues and guiding their maturation by applying mechanical and electrical stimuli. All the platform functionalities were developed compatibly with a wafer-scale fabrication strategy, describing the design, fabrication and characterization of individual chips. However, as was already demonstrated in previously conducted experiments with cells, obtaining biologically and statistically-relevant results and conclusions required testing of at least several tissues per culture condition ($n > 3$) and repetition of the same experiment at least three times ($N = 3$). These numbers refer to the ideal case when the yield of the experiment is 100% and all the tissues can be used as relevant points in data analysis. In most cases, the number of cultured tissues is

much higher to make sure the minimum number of tissues reaches the end of the experiment. Going even further, when talking about drug assays and disease modeling, the number of chips per experiment quickly scales up.

Until now, with the fabrication at wafer-level exploited in this thesis, the number of single chips obtained per wafer is 69. However, an important step that was missing is the integration of single chips into a higher-level, multiplexed system. Therefore, in this chapter, the single EHT platforms with integrated pacing microelectrodes developed within Chapter 6 are assembled into a multi-well plate platform to enable multiplexing of the single-chip microenvironment for EHT culture and to address the need for high-throughput analysis in a reproducible and automated manner.

7.2. MULTIPLEXED PACING PLATFORM

7.2.1. PLATFORM ASSEMBLY

The previously developed EHT platforms with integrated pacing microelectrodes were assembled into a 96-well plate format for high-throughput experiments. The assembly process consists of several steps that will be described in detail. Briefly, the bottom of a 96-well plate was replaced with a custom-made printed circuit board (PCB) with the footprints of 32 single EHT platforms with electrodes. On top of the array of chips, an acrylic plate with wells for culture medium and pockets for wire-bonds was placed to enable cell culturing. The layers constituting the platform are illustrated in Fig.7.2.

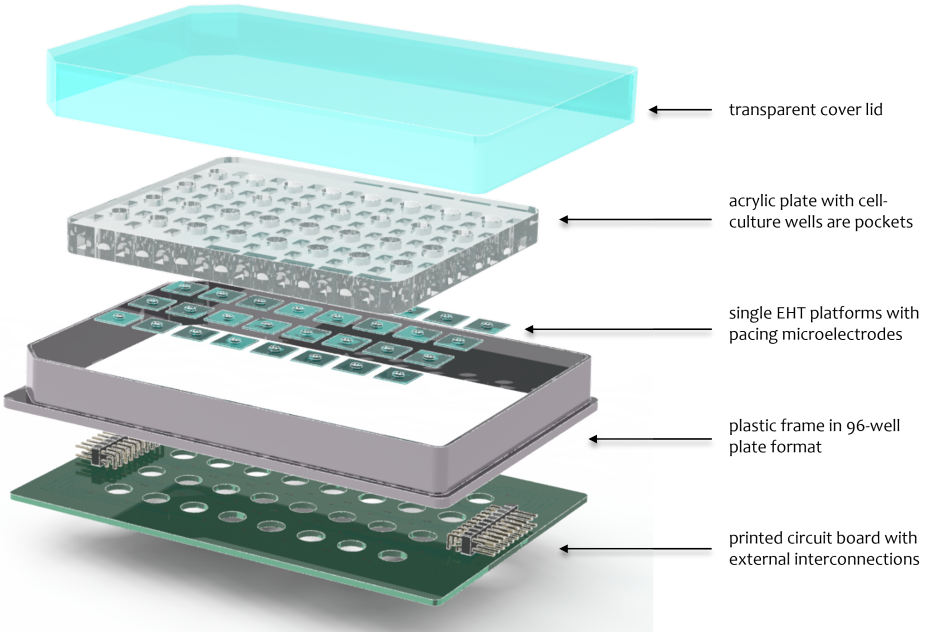

Figure 7.2: Exploded view of the functional layers making up the multi-well plate with EHT platforms with integrated pacing microelectrodes.

SINGLE-CHIP TRANSFER TO A CUSTOM-DESIGNED PCB

A custom-made PCB was designed to fit at the bottom of a 96-well plate, as this is the standard format plate used in biological laboratories. The PCB contains bond pads and traces for 32 single chips of EHT platforms with integrated electrodes. This PCB was meant to be connected to the separately designed PCB with pacing circuitry, which was described in Chapter VI. As explained previously, pacing circuitry contains a demultiplexer that enables pacing signal multiplication to 16 individual channels. For this reason, to host as many chips as possible, a multi-well plate PCB was designed with footprints and traces for 32 chips. Half of the PCB contains 16 chips and connectors to the pacing circuitry. The entire footprint is mirrored, including traces and connectors on the other side of the PCB to create a symmetrical layout. In this way, connections for 16 chips are provided on each side of the PCB. The PCB design is shown in Fig.7.3A.

Individual EHT platforms with integrated pacing microelectrodes were wire-bonded to the PCB as described previously. First, individual chips were glued to the PCB using uncured PDMS. After baking at 60°C for 2h, golden shims were glued to the Al contact pads using silver conductive paste. The glue solidified after 2h 30 min baking at 125°C, and the wire-bonding was performed using the same parameters as previously. Each bond was protected with an additional droplet of uncured PDMS for insulation and mechanical stability. Wire-bonding of 32 chips to the multi-well PCB, with the insert of single chip bonding, is shown in Fig.7.3B.

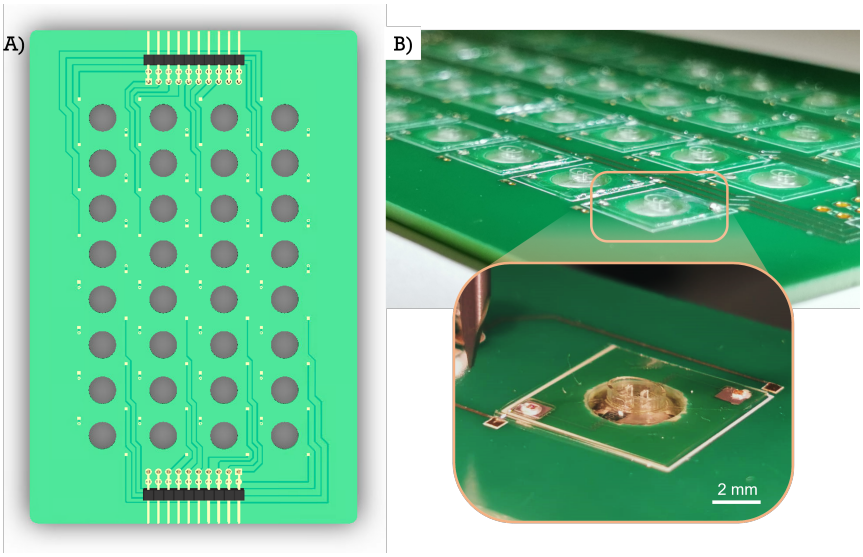

Figure 7.3: A) SolidWorks model of a PCB design as bottom layer of a 96-well plate; B) 32 EHT platforms with integrated pacing microelectrodes mounted and wire-bonded to the PCB in a multi-well plate format, with the enlarged single-chip bonding.

WELL BONDING

After wire-bonding of all the single EHT platforms, each wire-bond was protected with a droplet of the uncured PDMS for insulation and encapsulation. The next step in the assembly was the incorporation of wells for the cell culturing medium. For this purpose, an 8 mm-thick plate of acrylic was laser-cut to create 32 holes, 6 mm in diameter, for hosting cell culturing medium. Next to the holes, 4-mm deep pockets were created to fit the insulated wire-bonds. In this way, all the cell culturing wells were incorporated into the multi-well plate design as a single piece. SolidWorks design is shown in Fig.7.4A.

The acrylic plate was bonded to the PCB with individual wire-bonded chips using pressure-sensitive adhesive (PSA). PSA was also laser-cut into the patterns corresponding to the bottom of the acrylic plate. First, one side of the adhesive was aligned and glued to the acrylic. Using slight pressure, the acrylic was then attached to the PCB with PDMS chips on top, while placing wire-bonds in the small pockets. This assembly step is shown in Fig.7.4B. After gluing the acrylic wells to the PCB, a liquid leakage test was performed, by pouring DI water into all the wells and checking the leakage after 30 min. These tests gave positive results, as no leakage was noticed.

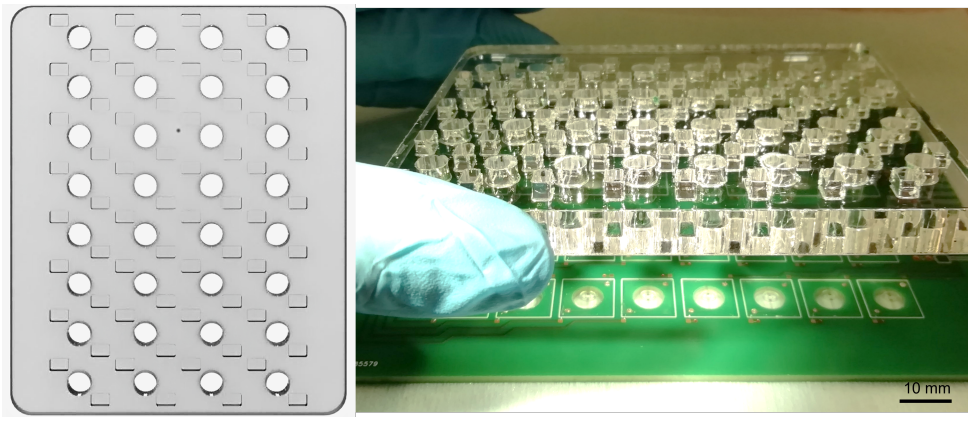

Figure 7.4: A) SolidWorks design of the acrylic plate with wells for cell culturing medium; B) Placement of the acrylic plate on top of the PCB with wire-bonded EHT platforms.

COMPLETE SYSTEM PACKAGING

The next step of the assembly was fitting into the 96-well plate frame and connecting it to the electronics. The wall of the standard 96-well plate was recreated using SolidWorks and adjusted to account for the thickness of the PCB at the bottom. Additionally, two openings were created on each side of the frame to create access for the pins of the connectors. This frame was 3D printed and bonded to the PCB with chips and acrylic using uncured PDMS. After placing the entire system into the frame, two connectors were soldered to the PCB to finalize the multi-well assembly. The completed multi-well plate with EHT platforms with integrated electrodes is shown in Fig.7.5.

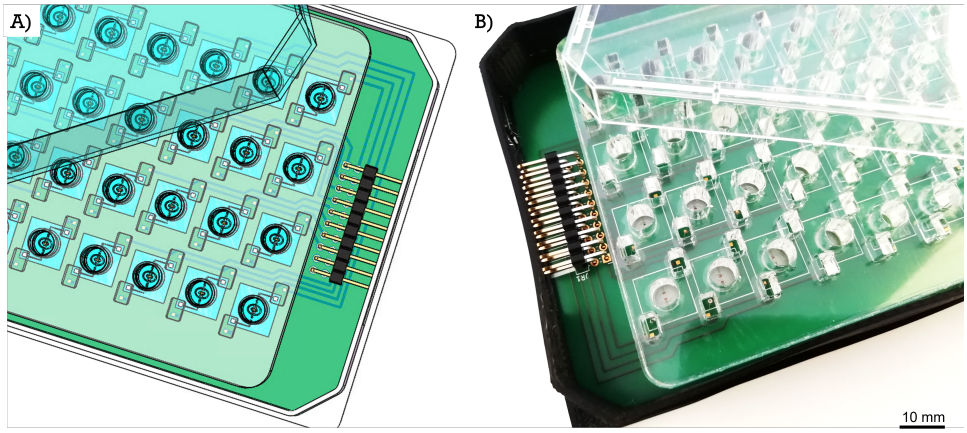

Figure 7.5: A) SolidWorks design of the assembled multi-well plate; B) The completed assembly of the multi-well plate with EHT platforms with integrated microelectrodes.

7.2.2. EXTERNAL ELECTRONIC CONNECTION AND USER INTERFACE PCB ASSEMBLY

After assembling the multi-well plate with EHT platforms, the connection with pacing circuitry was made. The designed PCB from the previous chapter was packaged into a custom-made 3D-printed plastic case, with openings for USB connection to a microcontroller (µC), a potentiometer knob for voltage tuning and a plug-in for the power supply. The case was designed using SolidWorks. Assembly of the pacing PCB is shown in Fig.7.6.

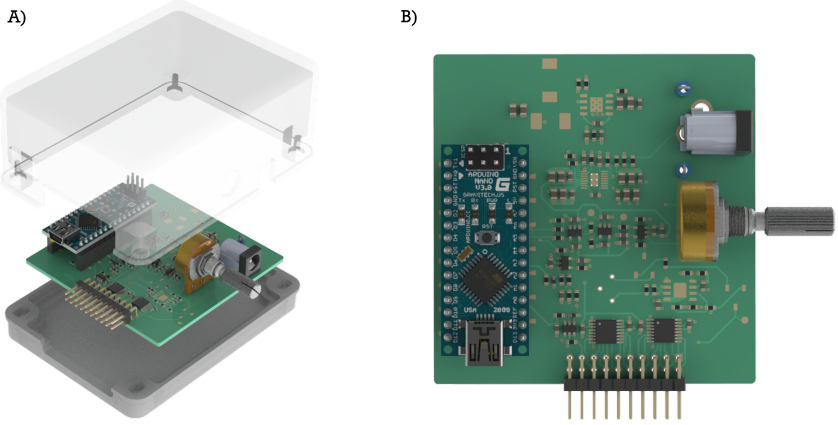

Figure 7.6: A) Assembly of the designed PCB containing pacing circuitry within the custom-made 3D-printed case; B) Top view of the SolidWorks model of a PCB for pacing signal generation.

USER-FRIENDLY CONTROL

A Matlab script was written to enable independent multiplexed stimulation of 16 out of 32 individual EHT platforms with integrated electrodes. The communication to the µC Arduino Mega of the pacing circuitry was established via the serial port of the PC. A graphical user interface (GUI) was generated using the Matlab AppBuilder tool to control pacing conditions and visualize measured signals. The user can set the pacing frequency, pulse duration and EHT platform selection via GUI and this information is transmitted to the µC before starting the stimulation. This data is sent only one time when the user changes settings or switches to a different EHT platform. Meanwhile, data from µC to Matlab with the analog readings of voltage and current going through the tissue (Section 6.5.2, Chapter 6) is sent to the GUI in real-time, during the period when voltage is zero.

The user interface contains one tab for connection set-up and a tab for stimulation control. In the connection tab, the user must select the serial port of the PC which is

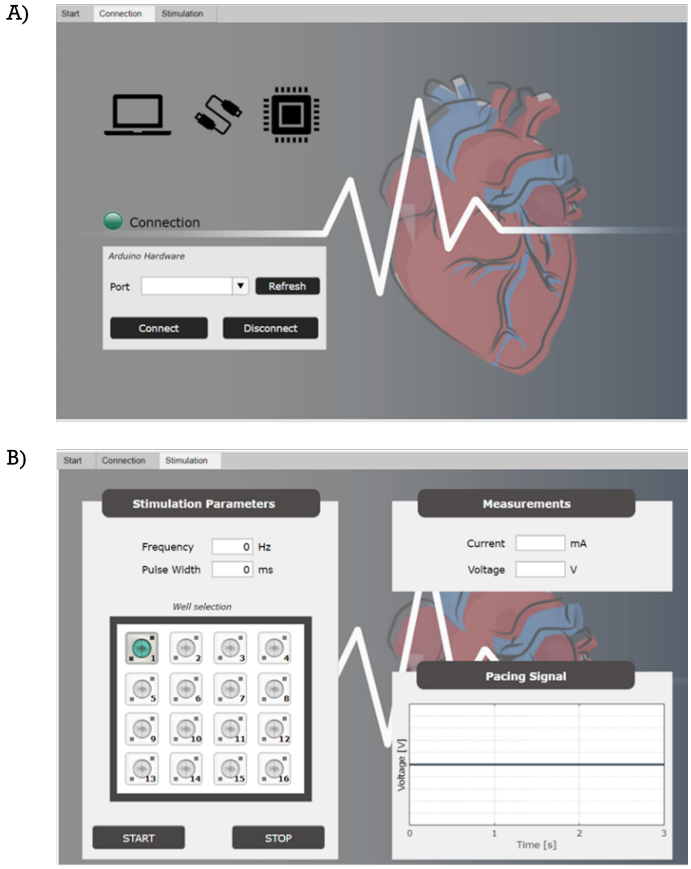

Figure 7.7: User-friendly interface of the app for pacing signal control: A) Tab for establishing a connection to the µC and pacing circuitry; B) Tab for a selection of pacing parameters and monitoring current and voltage applied to the tissues.

detected for the communication to the μC. Once the connection is established, a green LED indicator is switched on. The connection tab is shown in Fig.7.7A.

In the stimulation tab, the user can define stimulation parameters, as well as the platform selection. 16 channels can be stimulated separately using the developed circuit. Additionally, real-time measurements of the applied peak-to-peak voltage and corresponding current going through the tissue are displayed on the screen in this tab. There is shown also an artificially-generated pacing signal based on the pacing parameters selected by the user, for visualization purposes. The stimulation tab is shown in Fig.7.7B.

7.2.3. ASSEMBLY FLAWS

Each of the assembly steps could be further improved and optimized, as will be discussed below.

The design of the PCB can include in the future more than 32 chips, with the proper modification of multiplexing units, to host higher throughput simulation experiments. Furthermore, due to the imaging setup within the microscope with an incubator, it was shown that the electrical connection between the multi-well and the pacing circuit should be optimized by switching 90° pin connectors to the straight ones.

Currently, alignment of the individual chips to the PCB is conducted manually which requires a lot of time and results in alignment errors. Since the chips are large, the misalignment is not critical at this stage. However, in the future, a custom-designed pick-and-place tool could be used to automate the process and increase alignment precision.

Bonding of the acrylic plate to the PCB using PSA represents another challenge in the current system assembly process. The thickness of bonded individual PDMS chips varies significantly across the multi-well plate. These variations originate from the non-uniformity in layer thickness upon roller coating of PDMS (Section 6.3.3, Chapter 6), as well as from the gluing of the chips to the PCB with the uncured polymer. As a consequence, the PSA layer should compensate for all these thickness variations and ensure good adhesion with the PCB, while preventing any leakage. On the other hand, laser cutting of the acrylic plate results in surface roughness at the edges of the cuts. The roughness is reduced by sanding and polishing the cuts. However, it is still a source of defects that can cause leakage of the cell culture medium from the wells to the PCB and wire-bonds. Alternative processes can be used, such as micro-milling, to create smooth-edge openings for wells and wire-bonds in the acrylic plate.

Finally, the frame of a 96-well plate for packaging the PCB with bonded EHT platforms was 3D printed from plastic material. Even though this approach is good for prototyping, the material used for 3D printing was of low quality for this specific purpose, especially taking into account that the frame is a large, hollow structure with relatively thin walls. If exposed to higher temperatures during PDMS curing, (even at 60°) deformation of the material occurs. Once again, alternative fabrication methods can be used in the future to improve the quality of the multiwell plate frame concerning its mechanical and temperature stability.

7.2.4. TESTING OF THE PLATFORM

Validation of the platform was conducted by performing experiments with the inclusion of cardiac cells. The EHTs were generated using the same protocol previously described (Chapter 6). Briefly, 70% iPSC-derived cardiomyocytes (CMs), 15% of cardiac fibroblast (cFB), and 15% of endothelial cells (ECs) were mixed within ECM gel mixture made of collagen I (3.3 mg/mL), DMEM (10X), NaOH, growth factor reduced Matrigel and formation medium. The EHTs were cultured in a formation medium for 72h combined with growth factors for endothelial cells and fibroblast (VEGF and FGF). After 72h the culture medium was switched to MBEL+ VEGF (50 ng/mL)+ FGF (5 ng/mL).

The tissues were successfully formed after 72 hours, as demonstrated in Fig.7.8. However, after only 2 days in culture, platform leakage was noticed due to the poor adhesion of the PSA layer to the rough laser-cut surface of the acrylic plate. This leakage resulted in the complete removal of the cell culturing medium from the wells and the drying out of the tissues.

The only conclusion drawn from this experiment is the biocompatibility of the multi-well plate. Furthermore, before repeating the experiments with cells in the multi-well plate, the assembly flaws, particularly the leakage, need to be addressed.

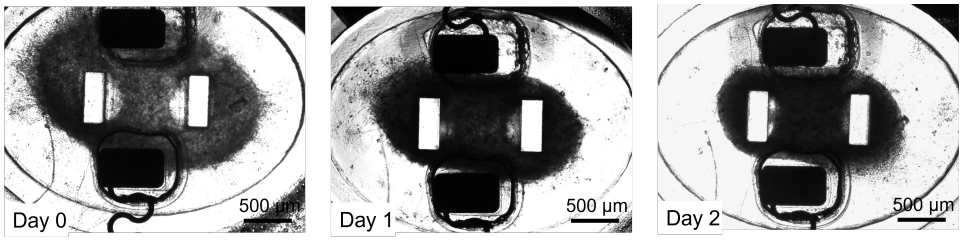

Figure 7.8: Timeline of the tissue formation within a single EHT platform with pacing microelectrodes as part of a multi-well plate.

7.3. MODULAR PLATFORM

The multi-well plate platform has been developed to be a modular system with tunable functionalities. Until now, only pacing electrodes are incorporated in a multiplexed manner to fit the platform layout. However, the design of both displacement sensors and tapered pillar platforms is also envisioned to be included in this system.

All the fabrication processes developed within this thesis were made compatible with the integration into the multi-well plate platform. Each process results in a 9x9 mm^2 chip size that could potentially fit the multi-well plate layout. Since the fabrication of both pacing electrodes and capacitive sensors uses a combination of two separate wafers, each of these processes is compatible with the integration with tapered pillars, without significant changes to the process flow. Furthermore, metal layers in the case of either sensors or electrodes can be easily adjusted to combine both functionalities in a single chip. However, in this case, the PCB design would still have to be adjusted to facilitate electrical connections to both chip functionalities. The illustration of different functionalities of the multi-well plate is shown in Fig.7.9.

Except for the currently available functionalities, additional sensing mechanisms can be explored and included in such a platform design. For example, by modifying metal patterning into a multielectrode array with functionalized electrode surface, electrochemical sensing can be incorporated into the platform, using previously developed highly-sensitive capacitive readout to extract change in capacitance between functionalized metal plates upon bonding of targeted cytokines.

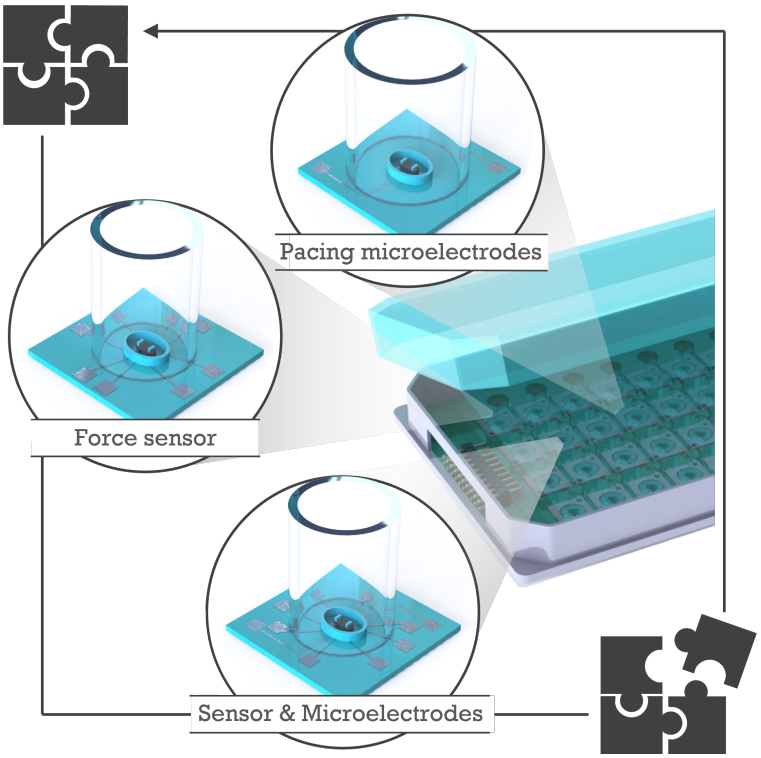

Figure 7.9: Illustration of different chip integration into the multi-well plate, as a future outlook.

7.4. DISCUSSION AND FUTURE OUTLOOK

In this Chapter, individual EHT platforms with integrated pacing microelectrodes were multiplexed and assembled into a multi-well plate format. The assembly included the design of a PCB with the footprint and interconnects for 32 single chips, laser cutting of the acrylic wells for cell culturing medium and 3D printing of the supportive frame in a 96-well plate layout for platform packaging. Additionally, a separate PCB with the pacing circuitry, developed in Chapter 6, was also assembled and packaged within a 3D-printed custom-made plastic case. A stand-alone app was developed using Matlab App Builder to control pacing parameters and monitor signals applied to the tissues during electrical stimulation. This app enables pacing control and selection of 16 individual EHT platforms.

The developed assembly process showed to be good for prototyping purposes, but it requires future optimization and automation of the assembly steps. Due to the leakage between the PSA layer and the acrylic wells during the cell culture experiments, tissues were left without the medium overnight and the experiment could not be concluded. Future assembly modification should address mentioned issues, prioritizing better methods for acrylic well cutting as well as the printing of high-quality plastic frames in the 96-well plate layout.

In the future, the developed multiplexed platform can be used to create a closed-loop system for tissue culture, with the automatic control of the tissue culturing environment and the possibility to tune the experiment conditions according to the obtained read-outs. For example, pacing parameters could be tuned based on the force read-out data from the displacement sensor. Ideally, such a system would provide full automation and precise engineering of the tissue microenvironment, where the experiment condition could be independently adjusted depending on the tissue's physiological responses and maturation stage.

CHAPTER 8

CONCLUSIONS AND FUTURE PERSPECTIVES

8.1. CONCLUSIONS

The death toll of cardiovascular diseases worldwide and the lack of effective treatments for them are the main motivation for developing alternative and more efficient models for drug development and investing in disease modeling research. The missing link between current laboratory research on static *in vitro* and animal models and the clinical stage research on human patients could be bridged using the rapidly emerging Organ-on-Chip (OOC) technology. The artificial microphysiological models developed within OoC research combine devices made of biocompatible polymers and human-induced pluripotent stem cell (hiPSC)-derived organ-specific cell cultures. The idea is to culture cells in a dynamic environment, including flow, chemical, electrical or bio-mechanical stimuli, to mimic the *in vivo* environment. For human cardiac tissue, such an *in vitro* model requires the interplay of different biomechanical and electrical cues within a platform made of soft, biocompatible material, to facilitate the growth and maturation of hiPSC-derived cardiac cell types, assembled into tissue-like bundles.

The work conducted within this thesis presented a step towards the development of such a dynamic artificial microenvironment suitable for the growth of hiPSC-based engineered cardiac tissues (EHTs). The developed platform and its variations can be utilized as a starting version of a 3D *in vitro* cardiac model for facilitating culture and improving maturation of EHTs, with integrated electrical stimulation and contraction force readouts.

The approach taken in this thesis was designing and fabricating a platform for EHT culture with simple topography, using wafer-level microfabrication techniques, followed by step-by-step platform upgrade and an increase in model complexity by the inclusion of electrical stimulation and readouts. The work on the platform development was done in parallel with the biological experiments on each version of the platform, conducted in close collaboration with researchers from Leiden University Medical Center.

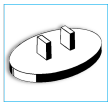

The first step in developing a microenvironment suitable for EHT culture was the search for optimal substrate and topography design to support the self-assembly of three different cardiac cell types into tissue-like bundles. In Chapter 2 an existing platform for EHT culture, composed of two micropillars with rectangular cross-sections, within an elliptic microwell, was taken as a starting point. The platform was anisometrically downscaled to facilitate 3, 2, and 1 µL volume of cell/extracellular matrix (ECM) mixture within the elliptic well. The entire platform was made by moulding PDMS into the deep reactive ion-etched cavities in the Si wafer. The well volume determined the final cell number within the tissue, hence downscaling of the pillars and wells resulted in a decrease in the number of cells used per tissue.

In this study, tissue performance was compared in all three platform sizes. The first outcome was that the downscaling of the platforms and tissue sizes did not affect negatively tissue formation and function. We showed that all the tissues expressed relevant cardiac markers and remained vital and functional for at least 14 days. The downscaling proved suitable for decreasing the number of cells used per tissue, consequently increasing the throughput of the experiment by means of the number of tissues that could be made using the same amount of cells. Additionally, downscaling enabled compatibility with wafer-level microfabrication technologies, which in turn enabled further platform upgrades.

The second goal of this study was to understand the relationship between the contraction force of the EHTs and the stiffness of the anchors upon which the force is applied. Anisometric downscaling resulted in three sizes of EHT platforms with the same stiffness of micropillars, which enabled different-sized tissues to experience the same load during formation and contraction cycles. In this regard, the results we obtained could only be used as proof that the tissues demonstrated similar contractile performance in a certain range of passive loads, which allowed certain freedom in the optimization of mechanical properties of the future platform design.

However, the direct comparison of tissue contractile behavior between different-sized platforms could not be performed. The reason was the high variability in the contraction force measurements and low yield of the experiment due to the "jumping off" of the tissues. These issues emerged as a consequence of the straight pillar geometry and the increase in tissue contraction force over time, which resulted in the EHTs climbing upward, along the length of the pillars, and finally jumping off them. Since the tissues were changing position during the experiments, the force of contraction could not be accurately measured, without precise information on the applied force position along the pillar length. The yield of experiments was also low since small percentage of tissues was reaching the end of the experiments and could be used for statistical analysis. Finally, the fact that tissues were able to change their position over time affected the reproducibility of the experimental conditions. Taking this into account, to answer the question of optimal substrate stiffness for EHT culture and its effect on tissue behavior, the first problem to address was the re-design of the tissue anchoring points, i.e. micropillars.

The problem of tissue position variation was addressed in Chapter 3, by introducing a novel tapered design of PDMS pillars. Since the previous analysis showed that tissues were successfully formed and functional in all three chip sizes, the 2µL-sized EHT platform was selected for further research and platform upgrades as a compromise between size downscaling and ease of use during cell seeding. To address the variation in tissue position, tissues were mechanically confined in the middle of pillars by their hourglass profile. Such a design was fabricated using a combination of anisotropic deep reactive ion etching (Bosch process) and isotropic etching of Si, where the tapering pillar angle was precisely controlled by fine-tuning the duration and alternation of mentioned processes. Two tapering angles were achieved using this staircase-like etching approach: 80° and 75°. Both designs were successfully fabricated, mechanically characterized, and used for EHT culture to test the confinement efficiency. Tissue behavior in the new tapered designs was compared to the previously made platform with straight pillars.

It was shown that the tissue spatial confinement was successful in both tapered designs, which resulted in accurate contraction force measurement and a significant decrease in the variability of contraction parameters. Additionally, the yield of the experiments increased to 100%, showing that the new pillar design is suitable for long-term experiments.

Even though the new design showed to be efficient in tissue spatial confinement, many fabrication challenges emerged with the hourglass etching profile. The limitations of the fine-tuning of the final dimensions of pillars and therefore of their stiffness were set by the nature of isotropic etching of narrow trenches. The non-uniform etching in

lateral directions on the narrow and wide sides of the rectangular windows resulted in different tapering angles on parallel sidewalls of cavities, affecting the final pillar stiffness. In the end, the stiffness of both 80° and 75° tapered pillars was higher than for corresponding straight pillars, which might have been the additional cause of contraction force decrease and lack of tissue movement outside of the confining regions.

The next step in the design of the controlled microenvironment for EHT culture was the inclusion of relevant readouts. As mentioned in the Introduction, one of the benefits of the EHT *in vitro* models is the ease of contractile force assessment by measuring the displacement of elastic anchors around which tissues compact. To achieve this, two different readout methods were implemented in this thesis: optical and electrical.

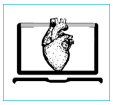

First, Chapter 4 described the development, implementation, and validation of a stand-alone software *ForceTracker* for monitoring tissue contractile properties. The software is based on a shape-tracking algorithm implemented in Python, which detects and tracks the movement of pillar tips across the frames in a video of contracting tissue. The software was developed for two different EHT platforms, with rectangular and circular pillar cross-sections, respectively, in collaboration with researchers from the University of Twente. By using a shape-independent algorithm and an easy-to-use user interface, the application has the advantage of automatically analyzing multiple videos in an unbiased way, taking into account the geometry and mechanical specifications of each platform. The software showed good performance in analyzing videos from both platforms in a time-efficient manner due to the implementation of a multi-threading approach. The main software outputs are pillar displacement, tissue force of contraction, speed of contraction and relaxation, and the force per tissue surface area. The software detection accuracy was validated using open-source image processing software ImageJ and showed to be in good agreement.

Even though the software performance and algorithm efficiency have been optimized, the main detection limitation is imposed by the poor quality videos, with low contrast, tilted tissues, or many visible artifacts. Even though the software can filter out and correct for the majority of mentioned defects, special instructions should be followed by users when recording videos for analysis in the first place.

Another drawback of the software is that all the videos of contracting tissues need to be recorded before analysis, meaning that the current version does not allow real-time measurement. However, even with the addition of the real-time force assessment, optical readout still requires an external camera within a bulky microscope setup and connection to a PC. Therefore, measurements still need to be performed outside of the incubator for a limited amount of time, or in microscopes equipped with incubation chambers.

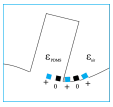

The mentioned issues were addressed by developing an alternative method to read out tissue contraction force from an EHT platform. In Chapter 5 a co-planar capacitive force sensor was integrated into the previously developed EHT platform with 3µL elliptic well volume. The pair of spiral co-planar capacitors was integrated into the substrate below the rectangular pillars. The working principle of the sensors is based on detecting the small compression and tension occurring in the substrate below PDMS pillars, upon tissue contraction and subsequent pillar displacement. The change in base capacitance due to the metal plate displacement was

measured and correlated to the applied force upon the pillars. Four different spiral geometries were analyzed using Comsol Multiphysics and implemented into the platform design to find the optimal dimensions and metallization ratio.

The sensors were successfully integrated into the EHT platform using a combination of micromachining and polymer processing. The fabrication consisted of a two-wafer process. PDMS pillars and wells were de-moulded from the deep reactive ion etched Si mould and bonded to the sensors patterned in Aluminum on top of a PDMS layer on a second silicon wafer. After successful fabrication, the base capacitance was measured in static conditions and it showed good agreement with the values from FEM and analytical models. For assessment of the dynamic behavior of the sensor during tissue contractions, a highly sensitive readout system was developed to measure base capacitance change in the aF range. The developed readout is based on a commercially available AD7746 component which uses capacitive-to-digital conversion to detect very small changes in capacitance. The dynamic behavior of the sensor was characterized by applying controlled force upon pillars with a nanoindentation tool and measuring electric response with the portable readout system. These measurements were performed only for one sensor type, due to the problems in the assembly process.

After addressing all the drawbacks of the assembly process of the EHT platforms with integrated sensors, more extensive electrical and biological characterization can be performed leading to the final choice of the sensor type for future upgrades.

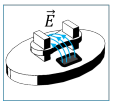

In parallel with the sensor design, integrated electrical stimulation was introduced into the EHT platform, whose significance for the maturation of hiPSC-CMs was described in the Introduction. The design, integration, and fabrication of a pair of microelectrodes into the EHT platform were described in Chapter 4. Two TiN microelectrodes were patterned at the bottom of the substrate of the elliptic microwell, in between the pillars, to provide uniform electric field stimulation to the tissue.

The platform with microelectrodes was fabricated using the same technology as in the case of capacitive sensors, with additional layers of polyimide for metal insulation and stress buffering. The platforms with pacing electrodes were successfully fabricated and wire-bonded to custom-designed PCBs. In parallel, electronic circuitry for the generation of biphasic rectangular pulses for tissue stimulation was developed and implemented. The circuitry enables tissue stimulation with a wide range of frequencies (1-5 Hz) and voltage amplitude up to ± 15V.

The electrical properties of the fabricated and wire-bonded platforms with electrodes were assessed upon the completed assembly process. Resistance of approximately 30 Ω was measured. Unfortunately, the efficiency of tissue pacing with the developed system could not be tested, as the experiments with cell inclusion were not successful due to platform leakage issues.

Hence, one of the main challenges with the current fabrication process is the system assembly in a leakage-free manner, together with the good alignment of two PDMS layers to the pressure-sensitive adhesive used for bonding.

Since the development of the force sensor and pacing microelectrodes and their integration into the EHT platform was done in parallel with the substrate optimization, both designs were made for 3 μL platforms with straight pillars. Later on, the flowchart

for the pacing electrode fabrication can be easily adjusted to the tapered pillar design, with a slight adjustment of the electrode positioning, and make it compatible with the integration. However, adjustment of the sensor design and corresponding photolithography mask requires more extensive FEM analysis with tapered pillars and is left for future work.

The natural follow-up on the single-chip development of the EHT platforms was upscaling and integration into a multi-well plate-like system for high-throughput experiments. For this purpose, single-chip EHT platforms with integrated electrodes were combined with a multiplexed pacing system. Chapter 7 introduced the development and assembly of a multi-well plate system that currently hosts 32 chips of EHT platforms with pacing electrodes and enables electrical stimulation of individual wells. The well plate is composed of a custom-made PCB as a bottom of a standard 96-well plate frame. This PCB contains single-chip footprints, contact pads and interconnects to the external pacing circuitry. The acrylic plate with laser-cut wells for the cell culture medium was glued on top of the wire-bonded EHT platform. The well plate is connected to the external pacing circuitry for the generation of rectangular bipolar pulses. Control of the pacing signal and individual well selection was realized via the user interface of a developed Matlab-based application.

Chapter 7 demonstrated a proof-of-concept multi-well plate system assembly, containing EHT platforms with integrated pacing electrodes. However, the process can benefit from substantial optimization of the assembly steps to enable leakage-free cell culture.

8.2. FUTURE WORK

8.2.1. FINDING THE OPTIMAL STIFFNESS OF PILLARS

One of the main goals of the research on the suitable substrate for EHT formation and culture was to find the optimal mechanical properties of the substrate by means of its topology and stiffness. Due to the issue with the variation of tissue position along pillar length during the experiments, the effect of pillar stiffness on tissue contractile performance could not be analyzed. The upgrade to a tapered pillar profile successfully addressed the issue of tissue confinement. However, due to the higher stiffness of tapered pillars compared to corresponding straight pillars, it is still to be found whether the tissue confinement is entirely a consequence of new pillar geometry. The alternative explanation is that the increase in pillar stiffness decreased the contractile performance of tissues, disabling tissue movement outside of the restricted region. To answer this question and unravel the reason behind pillar confinement efficiency, additional analysis needs to be performed. The stiffness of tapered pillars should be modified to match the straight pillar design to properly analyze confinement efficiency and choose between two tapered designs. Next, the stiffness of tapered pillars should be tuned further within a certain range, to study the effect of different passive loads on tissue formation and performance. Such a study could finally lead to a better understanding of the optimal mechanical properties of the substrate in the EHT models.

8.2.2. REAL-TIME FORCE ANALYSIS

In this thesis, two methods for tissue contractile force assessment were developed. As already mentioned in Chapter 5, real-time force analysis is very important for long-term assays or closed-loop systems for simultaneous tissue monitoring and stimulation. The integrated force sensor is specifically designed for the EHT platform developed in this Thesis. On the other hand, a stand-alone application for the assessment of tissue contractile properties, *ForceTracker*, is compatible with different EHT platforms of various pillar shapes and sizes. For this reason, it is relevant to mention that the implementation of the real-time force readout is an important future upgrade of the software. Such an addition would enable a time-efficient analysis of the tissue contractile performance, as the video recording of tissue contractions would be avoided. It would enable longer monitoring of the changes in tissue contraction due to the drug effect, for example, while enabling feedback to different stimulation setups.

8.2.3. IMPROVEMENTS OF THE ASSEMBLY PROCESS

Regarding the microfabrication of EHT platforms with microelectrodes and displacement sensors, some significant drawbacks in the assembly process were identified. For future fabrication optimization, alignment techniques and tools should be developed specifically for this application. One example would be using a dedicated wafer aligner system for flexible and optically transparent substrates to align the PSA layer to the PDMS structures. Further on, to improve wire-bonding and reduce contact disruption in the case of both designs, the interconnects should be modified into widely tapered metal lines at the connection with the contact pads.

Once the improvements in the assembly process are implemented, more platforms with capacitive sensors can be successfully fabricated and characterized. In the future, all four sensor types should be electrically characterized to obtain their sensitivity and compare it with the values from numerical analysis. Furthermore, since the characterization of dynamic sensors' behavior in a cell culturing environment could not be tested, the efficiency of the developed system for tissue contraction force measurement is yet to be proven. Also, the effect of the wet condition measurements on the signal-to-noise ratio should be assessed in future experiments. Based on all the pending analyses and characterizations, the final selection of one of the four types of sensors can be made.

8.2.4. MULTIPLEXING

Regarding the multi-well plate, parallel pacing of the multiple wells can be introduced as a future upgrade of single EHT platforms with microelectrodes. This could be realized by rapidly switching select signals of demultiplexer during the "off time" of the pulses, due to the low pacing frequency. Pacing parallelization would enable the long-term pacing of multiple tissues and the application of specific pacing regimes to all tissues simultaneously.

The same multiplexing should be applied in the case of displacement sensors. However, such implementation is more challenging than in the case of electrodes as it would require the development of a dedicated PCB with excitation signal multiplexing and connection to the developed AD7746 readout system. Low noise requirements impose an additional challenge in the case of multiplexing capacitive red-outs.

As envisioned at the beginning of the Thesis, the developed system can be further improved and upgraded to enable full automation and precise control of the EHT culture environment within a closed-loop system. This could be achieved by incorporating both sensors and electrodes into the multiwell-plate system. Software control of the setup would allow a simple combination of the pacing input with the electrical response from the force sensors, to develop a system in which pacing parameters could be tuned in real-time according to the force readout. As a final goal, the automated system can be created for researching the optimal microenvironment for tissue culture and maturation by applying different bio-mechanical stimuli to the tissue in an unbiased manner.

BIBLIOGRAPHY

[1] N Poulter. “Global risk of cardiovascular disease”. In: *Heart* 89.90002 (May 2003), pp. 2ii–5. DOI: 10.1136/heart.89.suppl_2.ii2.

[2] Adam Timmis et al. “European Society of Cardiology: cardiovascular disease statistics 2021”. In: *European Heart Journal* 43.8 (Feb. 2022), pp. 716–799. DOI: 10.1093/eurheartj/ehab892.

[3] Dolly A. Parasrampuria, Leslie Z. Benet, and Amarnath Sharma. “Why Drugs Fail in Late Stages of Development: Case Study Analyses from the Last Decade and Recommendations”. In: *The AAPS Journal* 20.3 (May 2018), p. 46. DOI: 10.1208/s12248-018-0204-y.

[4] Sarah A. Dugger, Adam Platt, and David B. Goldstein. “Drug development in the era of precision medicine”. In: *Nature Reviews Drug Discovery* 17.3 (Mar. 2018), pp. 183–196. DOI: 10.1038/nrd.2017.226.

[5] Andrew P. Voorhees and Hai-Chao Han. “Biomechanics of Cardiac Function”. In: *Comprehensive Physiology* 5.4 (Sept. 2015), pp. 1623–1644. ISSN: 2040-4603. DOI: 10.1002/cphy.c140070.

[6] Celinda M. Kofron and Ulrike Mende. “In vitro models of the cardiac microenvironment to study myocyte and non-myocyte crosstalk: bioinspired approaches beyond the polystyrene dish”. In: *The Journal of Physiology* 595.12 (June 2017), pp. 3891–3905. DOI: 10.1113/JP273100.

[7] John E. Hall. *Guyton and Hall textbook of medical physiology*. 13th edition. Philadelphia, PA: Elsevier, 2016.

[8] Rob F. Wiegerinck et al. “Force Frequency Relationship of the Human Ventricle Increases During Early Postnatal Development”. In: *Pediatric Research* 65.4 (Apr. 2009). Number: 4 Publisher: Nature Publishing Group, pp. 414–419. DOI: 10.1203/PDR.0b013e318199093c.

[9] Martina Brofiga et al. “On the road to the brain-on-a-chip: a review on strategies, methods, and applications”. In: *Journal of Neural Engineering* 18.4 (Aug. 2021), p. 041005. DOI: 10.1088/1741-2552/ac15e4.

[10] Sangeeta N. Bhatia and Donald E. Ingber. “Microfluidic organs-on-chips”. In: *Nature Biotechnology* 32.8 (Aug. 2014), pp. 760–772. DOI: 10.1038/nbt.2989.

[11] Uwe Marx et al. “’Human-on-a-chip’ developments: a translational cutting-edge alternative to systemic safety assessment and efficiency evaluation of substances in laboratory animals and man?” In: *Alternatives to laboratory animals: ATLA* 40.5 (Oct. 2012), pp. 235–257. DOI: 10.1177/026119291204000504.

[12] Boyang Zhang et al. “Advances in organ-on-a-chip engineering”. In: *Nature Reviews Materials* 3.8 (Aug. 2018). Number: 8 Publisher: Nature Publishing Group, pp. 257–278. DOI: 10.1038/s41578-018-0034-7.

[13] Chak Ming Leung et al. “A guide to the organ-on-a-chip”. In: *Nature Reviews Methods Primers* 2.1 (May 2022), pp. 1–29. DOI: 10.1038/s43586-022-00118-6.

[14] Dongeun Huh et al. “Reconstituting Organ-Level Lung Functions on a Chip”. In: *Science (New York, N.Y.)* 328.5986 (June 2010), pp. 1662–1668. DOI: 10.1126/science.1188302.

[15] Hyun Jung Kim et al. “Human gut-on-a-chip inhabited by microbial flora that experiences intestinal peristalsis-like motions and flow”. In: *Lab on a Chip* 12.12 (2012), p. 2165. DOI: 10.1039/c2lc40074j.

[16] David A. Soscia et al. “A flexible 3-dimensional microelectrode array for *in vitro* brain models”. In: *Lab on a Chip* 20.5 (2020), pp. 901–911. DOI: 10.1039/C9LC01148J.

[17] Jong Seob Choi et al. “Recent advances in three-dimensional microelectrode array technologies for in vitro and in vivo cardiac and neuronal interfaces”. In: *Biosensors and Bioelectronics* 171 (2021), p. 112687. DOI: https://doi.org/10.1016/j.bios.2020.112687.

[18] Kai-Hong Tu et al. “Development of Real-Time Transendothelial Electrical Resistance Monitoring for an In Vitro Blood-Brain Barrier System”. In: *Micromachines* 12.1 (Jan. 2021). Number: 1 Publisher: Multidisciplinary Digital Publishing Institute, p. 37. DOI: 10.3390/mi12010037.

[19] Chang Liu et al. “Generating 3D human cardiac constructs from pluripotent stem cells”. In: *eBioMedicine* 76 (2022), p. 103813. DOI: https://doi.org/10.1016/j.ebiom.2022.103813.

[20] Florian Weinberger, Ingra Mannhardt, and Thomas Eschenhagen. “Engineering Cardiac Muscle Tissue: A Maturating Field of Research”. In: *Circulation Research* 120.9 (Apr. 2017), pp. 1487–1500. DOI: 10.1161/CIRCRESAHA.117.310738.

[21] Richard Mills and James Hudson. “Bioengineering adult human heart tissue: How close are we?” In: *APL Bioengineering* 3 (Mar. 2019), p. 010901. DOI: 10.1063/1.5070106.

[22] Kazutoshi Takahashi and Shinya Yamanaka. “Induction of pluripotent stem cells from mouse embryonic and adult fibroblast cultures by defined factors”. In: *Cell* 126.4 (Aug. 2006), pp. 663–676. DOI: 10.1016/j.cell.2006.07.024.

[23] Kazutoshi Takahashi et al. “Induction of pluripotent stem cells from adult human fibroblasts by defined factors”. In: *Cell* 131.5 (Nov. 2007), pp. 861–872. DOI: 10.1016/j.cell.2007.11.019.

[24] Jeroen M. Stein, Christine L. Mummery, and Milena Bellin. “Engineered models of the human heart: Directions and challenges”. In: *Stem Cell Reports* 16.9 (Sept. 2021), pp. 2049–2057. DOI: 10.1016/j.stemcr.2020.11.013.

[25] Nicole T. Feric and Milica Radisic. “Towards adult-like human engineered cardiac tissue”. In: *Advanced drug delivery reviews* 96 (Jan. 2016), pp. 110–134. DOI: 10.1016/j.addr.2015.04.019.

[26] Chengyi Tu, Benjamin S. Chao, and Joseph C. Wu. "Strategies for Improving the Maturity of Human Induced Pluripotent Stem Cell-Derived Cardiomyocytes". In: *Circulation Research* 123.5 (Aug. 2018), pp. 512–514. DOI: 10.1161/CIRCRESAHA.118.313472.

[27] Sebastian Schaaf et al. "Human Engineered Heart Tissue as a Versatile Tool in Basic Research and Preclinical Toxicology". In: *PLoS ONE* 6.10 (Oct. 2011), e26397. DOI: 10.1371/journal.pone.0026397.

[28] Ignasi Jorba et al. "In Vitro Methods to Model Cardiac Mechanobiology in Health and Disease". In: *Tissue Engineering. Part C, Methods* 27.3 (Mar. 2021), pp. 139–151. DOI: 10.1089/ten.TEC.2020.0342.

[29] Kacey Ronaldson-Bouchard et al. "Engineering of human cardiac muscle electromechanically matured to an adult-like phenotype". In: *Nature protocols* 14.10 (Oct. 2019), pp. 2781–2817. DOI: 10.1038/s41596-019-0189-8.

[30] Scott D. Lundy et al. "Structural and Functional Maturation of Cardiomyocytes Derived from Human Pluripotent Stem Cells". In: *Stem Cells and Development* 22.14 (July 2013), pp. 1991–2002. DOI: 10.1089/scd.2012.0490.

[31] Kacey Ronaldson-Bouchard et al. "Advanced maturation of human cardiac tissue grown from pluripotent stem cells". In: *Nature* 556.7700 (Apr. 2018), pp. 239–243. DOI: 10.1038/s41586-018-0016-3.

[32] Xiulan Yang, Lil Pabon, and Charles E. Murry. "Engineering Adolescence: Maturation of Human Pluripotent Stem Cell-derived Cardiomyocytes". In: *Circulation research* 114.3 (Jan. 2014), pp. 511–523. DOI: 10.1161/CIRCRESAHA.114.300558.

[33] Elisa Giacomelli et al. "Human-iPSC-Derived Cardiac Stromal Cells Enhance Maturation in 3D Cardiac Microtissues and Reveal Non-cardiomyocyte Contributions to Heart Disease". In: *Cell Stem Cell* 26.6 (June 2020), 862–879.e11. DOI: 10.1016/j.stem.2020.05.004.

[34] Thomas Boudou et al. "A Microfabricated Platform to Measure and Manipulate the Mechanics of Engineered Cardiac Microtissues". In: *Tissue Engineering. Part A* 18.9-10 (May 2012), pp. 910–919. DOI: 10.1089/ten.tea.2011.0341.

[35] Marcelo C. Ribeiro et al. "A New Versatile Platform for Assessment of Improved Cardiac Performance in Human-Engineered Heart Tissues". In: *Journal of Personalized Medicine* 12.2 (Feb. 2022). Number: 2 Publisher: Multidisciplinary Digital Publishing Institute, p. 214. DOI: 10.3390/jpm12020214.

[36] Yimu Zhao et al. "A Platform for Generation of Chamber-Specific Cardiac Tissues and Disease Modeling". In: *Cell* 176.4 (Feb. 2019), 913–927.e18. DOI: 10.1016/j.cell.2018.11.042.

[37] Herman Vandenburgh et al. "Drug-screening platform based on the contractility of tissue-engineered muscle". In: *Muscle & Nerve* 37.4 (Apr. 2008), pp. 438–447. DOI: 10.1002/mus.20931.

[38] Norman Yu Liaw and Wolfram-Hubertus Zimmermann. "Mechanical stimulation in the engineering of heart muscle". In: *Advanced Drug Delivery Reviews* 96 (Jan. 2016), pp. 156–160. DOI: 10.1016/j.addr.2015.09.001.

[39] Jia-Ling Ruan et al. "Mechanical Stress Conditioning and Electrical Stimulation Promote Contractility and Force Maturation of Induced Pluripotent Stem Cell-Derived Human Cardiac Tissue". In: *Circulation* 134.20 (Nov. 2016), pp. 1557–1567. DOI: 10.1161/CIRCULATIONAHA.114.014998.

[40] Veniamin Y. Sidorov et al. "I-Wire Heart-on-a-Chip I: Three-dimensional cardiac tissue constructs for physiology and pharmacology". In: *Acta Biomaterialia* 48 (Jan. 2017), pp. 68–78. DOI: 10.1016/j.actbio.2016.11.009.

[41] Milica Dostanić et al. "A Miniaturized EHT Platform for Accurate Measurements of Tissue Contractile Properties". In: *Journal of microelectromechanical systems* 29.5 (Oct. 2020), pp. 881–887. ISSN: 1057-7157. DOI: 10.1109/JMEMS.2020.3011196.

[42] Michele A. Wozniak and Christopher S. Chen. "Mechanotransduction in development: a growing role for contractility". In: *Nature Reviews Molecular Cell Biology* 10.1 (Jan. 2009), pp. 34–43. DOI: 10.1038/nrm2592.

[43] Deok-Ho Kim et al. "Microengineered Platforms for Cell Mechanobiology". In: *Annual Review of Biomedical Engineering* 11.1 (2009), pp. 203–233. DOI: 10.1146/annurev-bioeng-061008-124915.

[44] A. C. C. van Spreeuwel et al. "The influence of matrix (an)isotropy on cardiomyocyte contraction in engineered cardiac microtissues". In: *Integrative Biology: Quantitative Biosciences from Nano to Macro* 6.4 (Apr. 2014), pp. 422–429. DOI: 10.1039/c3ib40219c.

[45] Hesam Parsa, Bryan Z. Wang, and Gordana Vunjak-Novakovic. "A microfluidic platform for the high-throughput study of pathological cardiac hypertrophy". In: *Lab on a Chip* 17.19 (Sept. 2017), pp. 3264–3271. DOI: 10.1039/c7lc00415j.

[46] Wolfram-Hubertus Zimmermann et al. "Engineered heart tissue grafts improve systolic and diastolic function in infarcted rat hearts". In: *Nature Medicine* 12.4 (Apr. 2006), pp. 452–458. DOI: 10.1038/nm1394.

[47] Jacqueline M. Bliley et al. "Dynamic loading of human engineered heart tissue enhances contractile function and drives a desmosome-linked disease phenotype". In: *Science Translational Medicine* 13.603 (July 2021), eabd1817. DOI: 10.1126/scitranslmed.abd1817.

[48] J. van der Velden et al. "Force production in mechanically isolated cardiac myocytes from human ventricular muscle tissue". In: *Cardiovascular Research* 38.2 (May 1998), pp. 414–423. DOI: 10.1016/s0008-6363(98)00019-4.

[49] George Kensah et al. "A Novel Miniaturized Multimodal Bioreactor for Continuous In Situ Assessment of Bioartificial Cardiac Tissue During Stimulation and Maturation". In: *Tissue Engineering. Part C, Methods* 17.4 (Apr. 2011), pp. 463–473. DOI: 10.1089/ten.tec.2010.0405.

[50] Richard J. Mills et al. “Functional screening in human cardiac organoids reveals a metabolic mechanism for cardiomyocyte cell cycle arrest”. In: *Proceedings of the National Academy of Sciences of the United States of America* 114.40 (Oct. 2017), E8372–E8381. DOI: 10.1073/pnas.1707316114.

[51] J. P. Ward. *Solid Mechanics: An Introduction*. English. 1992nd edition. Dordrecht ; Boston: Springer, Aug. 1992. ISBN: 978-0-7923-1949-8.

[52] Meredith Metzler and Raj Patel. “Plasma Enhanced Chemical Vapor Deposition (PECVD) of Silicon Dioxide (SiO2) Using Oxford Instruments System 100 PECVD”. In: ().

[53] Regina Luttge. “Chapter 2 - Basic Technologies for Microsystems”. In: *Microfabrication for Industrial Applications*. Ed. by Regina Luttge. Micro and Nano Technologies. Boston: William Andrew Publishing, Jan. 2011, pp. 13–54. DOI: 10.1016/B978-0-8155-1582-1.00002-2.

[54] Yogesh B. Gianchandani, Osamu Tabata, and Hans Zappe, eds. *Comprehensive Microsystems*. English. 1st edition. Elsevier Science, Dec. 2007.

[55] Alfred J. van Roosmalen. “Review: dry etching of silicon oxide”. In: *Vacuum*. Vacuum Special Issue: Proceedings of the SIRA International Seminar on Film Preparation and Etching using Vacuum or Plasma Technology, University of Suzzex, Brighton, UK 22-24 March 1983 34.3 (Mar. 1984), pp. 429–436. DOI: 10.1016/0042-207X(84)90079-4.

[56] Franz Laermer. “1.08 - Dry Etching”. In: *Comprehensive Microsystems*. Ed. by Yogesh B. Gianchandani, Osamu Tabata, and Hans Zappe. Oxford: Elsevier, Jan. 2008, pp. 217–233. DOI: 10.1016/B978-044452190-3.00009-4.

[57] P. Galambos. “Microelectromechanical Systems, Principles of”. In: *Encyclopedia of Materials: Science and Technology*. Ed. by K. H. Jürgen Buschow et al. Oxford: Elsevier, Jan. 2001, pp. 5598–5609. DOI: 10.1016/B0-08-043152-6/00979-7.

[58] Richard J. Mills et al. “Drug Screening in Human PSC-Cardiac Organoids Identifies Pro-proliferative Compounds Acting via the Mevalonate Pathway”. In: *Cell Stem Cell* 24.6 (June 2019), 895–907.e6. DOI: 10.1016/j.stem.2019.03.009.

[59] *LUMCi028-A · Cell Line · hPSCreg*. URL: https://hpscreg.eu/cell-line/LUMCi028-A.

[60] Milica Dostanic et al. “Highly Reproducible Tissue Positioning with Tapered Pillar Design in Engineered Heart Tissue Platforms”. In: *2023 IEEE 36th International Conference on Micro Electro Mechanical Systems (MEMS)*. Jan. 2023, pp. 374–377. DOI: 10.1109/MEMS49605.2023.10052166.

[61] J. A. Alfaro-Barrantes et al. “Highly-Conformal Sputtered Through-Silicon Vias With Sharp Superconducting Transition”. In: *Journal of Microelectromechanical Systems* 30.2 (Apr. 2021). Conference Name: Journal of Microelectromechanical Systems, pp. 253–261. DOI: 10.1109/JMEMS.2021.3049822.

[62] Niclas Roxhed, Patrick Griss, and Göran Stemme. “A method for tapered deep reactive ion etching using a modified Bosch process”. In: *Journal of Micromechanics and Microengineering* 17.5 (May 2007), pp. 1087–1092. DOI: 10.1088/0960-1317/17/5/031.

[63] R. Li et al. “Continuous deep reactive ion etching of tapered via holes for three-dimensional integration”. In: *Journal of Micromechanics and Microengineering* 18.12 (Nov. 2008), p. 125023. DOI: 10.1088/0960-1317/18/12/125023.

[64] Zhong Ren and Mark E. McNie. “Inductively coupled plasma etching of tapered via in silicon for MEMS integration”. In: *Microelectronic Engineering*. Micro/Nano Fabrication 2014 141 (June 2015), pp. 261–266. DOI: 10.1016/j.mee.2015.03.071.

[65] Kuo-Shen Chen et al. “Effect of process parameters on the surface morphology and mechanical performance of silicon structures after deep reactive ion etching (DRIE)”. In: *Journal of Microelectromechanical Systems* 11.3 (June 2002), pp. 264–275. DOI: 10.1109/JMEMS.2002.1007405.

[66] I. U. Abhulimen et al. “Effect of process parameters on via formation in Si using deep reactive ion etching”. In: *Journal of Vacuum Science & Technology B: Microelectronics and Nanometer Structures Processing, Measurement, and Phenomena* 25.6 (Oct. 2007), p. 1762. DOI: 10.1116/1.2787869.

[67] Deginet Admassu et al. “Adhesive wafer bonding of micro-actuators with SU-8 photoresist”. In: *Microsystem Technologies* 27.9 (Sept. 2021), pp. 3293–3297. DOI: 10.1007/s00542-020-05097-w.

[68] Khalil Najafi et al. “1.09 - Wafer Bonding”. In: *Comprehensive Microsystems*. Ed. by Yogesh B. Gianchandani, Osamu Tabata, and Hans Zappe. Oxford: Elsevier, Jan. 2008, pp. 235–270. DOI: 10.1016/B978-044452190-3.00008-2.

[69] M. Boufnichel et al. “Profile control of high aspect ratio trenches of silicon. II. Study of the mechanisms responsible for local bowing formation and elimination of this effect”. In: *Journal of Vacuum Science & Technology B: Microelectronics and Nanometer Structures Processing, Measurement, and Phenomena* 21.1 (Jan. 2003), pp. 267–273. DOI: 10.1116/1.1539063.

[70] Thomas Dawson. *Theory and Practice of Solid Mechanics*. Springer Science & Business Media, Dec. 2012.

[71] *Introduction to Stress and Equations of Motion*.

[72] Husain Jubran Al-Gahtani. “Exact Stiffnesses for Tapered Members”. In: *Journal of Structural Engineering* 122.10 (Oct. 1996). Publisher: American Society of Civil Engineers, pp. 1234–1239. DOI: 10.1061/(ASCE)0733-9445(1996)122:10(1234).

[73] D. L. Karabalis and D. E. Beskos. “Static, dynamic and stability analysis of structures composed of tapered beams”. In: *Computers & Structures* 16.6 (Jan. 1983), pp. 731–748. DOI: 10.1016/0045-7949(83)90064-0.

[74] Si-Wei Liu, Rui Bai, and Siu-Lai Chan. “Second-order analysis of non-prismatic steel members by tapered beam–column elements”. In: *Structures* 6 (May 2016), pp. 108–118. DOI: 10.1016/j.istruc.2016.02.006.

[75] Demeter G. Fertis and Michael E. Keene. “Elastic and Inelastic Analysis of Non-prismatic Members”. In: *Journal of Structural Engineering* 116.2 (Feb. 1990), pp. 475–489. DOI: 10.1061/(ASCE)0733-9445(1990)116:2(475).

[76] Oscar J. Abilez et al. “Passive Stretch Induces Structural and Functional Maturation of Engineered Heart Muscle as Predicted by Computational Modeling”. In: *Stem Cells* 36.2 (Feb. 2018), pp. 265–277. DOI: 10.1002/stem.2732.

[77] Ingra Mannhardt et al. “Human Engineered Heart Tissue: Analysis of Contractile Force”. In: *Stem Cell Reports* 7.1 (May 2016), pp. 29–42. DOI: 10.1016/j.stemcr.2016.04.011. URL: https://www.ncbi.nlm.nih.gov/pmc/articles/PMC4944531/ (visited on 07/10/2022).

[78] Ana Maria Gracioso Martins et al. “Microphysiological System for High-Throughput Computer Vision Measurement of Microtissue Contraction”. In: *ACS Sensors* 6.3 (Mar. 2021), pp. 985–994. DOI: 10.1021/acssensors.0c02172.

[79] Grant Mathews et al. “Computational Analysis of Contractility in Engineered Heart Tissue”. In: *IEEE Transactions on Biomedical Engineering* 59.5 (May 2012), pp. 1429–1435. DOI: 10.1109/TBME.2012.2187899.

[80] Arne Hansen et al. “Development of a drug screening platform based on engineered heart tissue”. In: *Circulation Research* 107.1 (July 2010), pp. 35–44. DOI: 10.1161/CIRCRESAHA.109.211458.

[81] Himanshu Singh. *Practical Machine Learning and Image Processing: For Facial Recognition, Object Detection, and Pattern Recognition Using Python*. Berkeley, CA: Apress, 2019. DOI: 10.1007/978-1-4842-4149-3.

[82] Sylvain Paris et al. “Bilateral Filtering: Theory and Applications”. In: (), p. 10.

[83] M.Ajay Kumar et al. “Image Processing based on Adaptive Morphological Techniques”. In: *2019 International Conference on Emerging Trends in Science and Engineering (ICESE)*. Vol. 1. Sept. 2019, pp. 1–4. DOI: 10.1109/ICESE46178.2019.9194641.

[84] Nobuyuki Otsu. “A Threshold Selection Method from Gray-Level Histograms”. In: *IEEE Transactions on Systems, Man, and Cybernetics* 9.1 (Jan. 1979), pp. 62–66. DOI: 10.1109/TSMC.1979.4310076.

[85] Jun Zhang and Jinglu Hu. “Image Segmentation Based on 2D Otsu Method with Histogram Analysis”. In: *2008 International Conference on Computer Science and Software Engineering*. Vol. 6. 2008, pp. 105–108.

[86] Xin-Yi Gong et al. “An Overview of Contour Detection Approaches”. en. In: *International Journal of Automation and Computing* 15.6 (Dec. 2018), pp. 656–672. DOI: 10.1007/s11633-018-1117-z.

[87] Kanagamalliga S. and Vasuki S. “Contour-based object tracking in video scenes through optical flow and gabor features”. In: *Optik* 157 (Mar. 2018), pp. 787–797. DOI: 10.1016/j.ijleo.2017.11.181.

[88] Harsha D Devalla and Robert Passier. "Cardiac differentiation of pluripotent stem cells and implications for modeling the heart in health and disease." In: *Science translational medicine* 10.435 (Apr. 2018), eaah5457. DOI: 10.1126/scitranslmed.aah5457.

[89] Paul M. L. Janssen. "Myocardial contraction-relaxation coupling". In: *American Journal of Physiology-Heart and Circulatory Physiology* 299.6 (Dec. 2010), H1741–H1749. DOI: 10.1152/ajpheart.00759.2010.

[90] Malte Tiburcy et al. "Defined Engineered Human Myocardium With Advanced Maturation for Applications in Heart Failure Modeling and Repair". In: *Circulation* 135.19 (May 2017), pp. 1832–1847. DOI: 10.1161/CIRCULATIONAHA.116.024145.

[91] Daisuke Sasaki et al. "Contractile force measurement of human induced pluripotent stem cell-derived cardiac cell sheet-tissue". In: *PloS One* 13.5 (2018), e0198026. DOI: 10.1371/journal.pone.0198026.

[92] Hidetoshi Masumoto et al. "The myocardial regenerative potential of three-dimensional engineered cardiac tissues composed of multiple human iPS cell-derived cardiovascular cell lineages". In: *Scientific Reports* 6 (July 2016), p. 29933. DOI: 10.1038/srep29933.

[93] Nathaniel L. Tulloch et al. "Growth of engineered human myocardium with mechanical loading and vascular coculture". In: *Circulation Research* 109.1 (June 2011), pp. 47–59. DOI: 10.1161/CIRCRESAHA.110.237206.

[94] *PySimpleGUI*. URL: https://www.pysimplegui.org/en/latest/.

[95] *Nuitka the Python Compiler — Nuitka the Python Compiler documentation*. URL: https://www.nuitka.net/.

[96] *MinGW-w64*. URL: https://www.mingw-w64.org/ (visited on 09/10/2022).

[97] José M. Rivera-Arbeláez et al. "Contractility analysis of human engineered 3D heart tissues by an automatic tracking technique using a standalone application". In: *PLOS ONE* 17.4 (Apr. 2022), e0266834. DOI: 10.1371/journal.pone.0266834.

[98] Alessandro Iuliano et al. "Coupling 3D Printing and Novel Replica Molding for In House Fabrication of Skeletal Muscle Tissue Engineering Devices". In: *Advanced Materials Technologies* 5.9 (2020), p. 2000344. DOI: 10.1002/admt.202000344.

[99] Mohammad E. Afshar et al. "A 96-well culture platform enables longitudinal analyses of engineered human skeletal muscle microtissue strength". In: *Scientific Reports* 10.1 (Apr. 2020), p. 6918. DOI: 10.1038/s41598-020-62837-8.

[100] Johan U. Lind et al. "Instrumented cardiac microphysiological devices via multimaterial three-dimensional printing". In: *Nature Materials* 16.3 (Mar. 2017), pp. 303–308. DOI: 10.1038/nmat4782.

[101] Kevin S. Bielawski et al. "Real-Time Force and Frequency Analysis of Engineered Human Heart Tissue Derived from Induced Pluripotent Stem Cells Using Magnetic Sensing". In: *Tissue Engineering Part C: Methods* 22.10 (Oct. 2016), pp. 932–940. DOI: 10.1089/ten.tec.2016.0257.

[102] J. Virtanen et al. “Direct measurement of contraction force in human cardiac tissue model using piezoelectric cantilever sensor technique”. In: *Current Applied Physics* 20.1 (Jan. 2020), pp. 155–160. DOI: 10.1016/j.cap.2019.10.020.

[103] Mutsuhito Sakamiya et al. “A heart-on-a-chip platform for online monitoring of contractile behavior via digital image processing and piezoelectric sensing technique”. In: *Medical Engineering & Physics* 75 (Jan. 2020), pp. 36–44. DOI: 10.1016/j.medengphy.2019.10.001.

[104] Ingmar Schoen et al. “Probing Cellular Traction Forces by Micropillar Arrays: Contribution of Substrate Warping to Pillar Deflection”. In: *Nano Letters* 10.5 (May 2010), pp. 1823–1830. DOI: 10.1021/nl100533c.

[105] A. Kajzar et al. “Toward Physiological Conditions for Cell Analyses: Forces of Heart Muscle Cells Suspended Between Elastic Micropillars”. In: *Biophysical Journal* 94.5 (Mar. 2008), pp. 1854–1866. DOI: 10.1529/biophysj.107.115766.

[106] Androniki Diakou. “Design and Fabrication of Electrical Stimulation Set Up for EHT platform”. MA thesis. 2020.

[107] Yongdae Kim et al. “Thin Polysilicon Gauge for Strain Measurement of Structural Elements”. In: *IEEE Sensors Journal* 10.8 (Aug. 2010), pp. 1320–1327. DOI: 10.1109/JSEN.2009.2039565.

[108] Antonino D’Alessandro, Salvatore Scudero, and Giovanni Vitale. “A Review of the Capacitive MEMS for Seismology”. In: *Sensors* 19.14 (July 2019), p. 3093. DOI: 10.3390/s19143093.

[109] Denivaldo P. da Silva and Sérgio F. Pichorim. “Modeling of Open Square Bifilar Planar Spiral Coils”. In: *Journal of Microwaves, Optoelectronics and Electromagnetic Applications* 17.3 (Sept. 2018), pp. 319–339. DOI: 10.1590/2179-10742018v17i31254.

[110] Shixuan Yang and Nanshu Lu. “Gauge factor and stretchability of silicon-on-polymer strain gauges”. In: *Sensors (Basel, Switzerland)* 13.7 (July 2013), pp. 8577–8594. DOI: 10.3390/s130708577.

[111] Klaas Hauke Baumgärtel, Daniel Zöllner, and Karl-Ludwig Krieger. “Classification and Simulation Method for Piezoelectric PVDF Sensors”. In: *Procedia Technology*. 3rd International Conference on System-Integrated Intelligence: New Challenges for Product and Production Engineering 26 (Jan. 2016), pp. 491–498. DOI: 10.1016/j.protcy.2016.08.062.

[112] Sang Min Won et al. “Piezoresistive Strain Sensors and Multiplexed Arrays Using Assemblies of Single-Crystalline Silicon Nanoribbons on Plastic Substrates”. In: *IEEE Transactions on Electron Devices* 58.11 (Nov. 2011), pp. 4074–4078. DOI: 10.1109/TED.2011.2164923.

[113] Tao Han et al. “Multifunctional Flexible Sensor Based on Laser-Induced Graphene”. In: *Sensors (Basel, Switzerland)* 19.16 (Aug. 2019), p. 3477. DOI: 10.3390/s19163477.

[114] *Coplanar Waveguide with Finite-Width Ground Planes*. John Wiley & Sons, Ltd, 2001, pp. 112–126. DOI: 10.1002/0471224758.ch4.

[115] E. Carlsson and S. Gevorgian. “Conformal mapping of the field and charge distributions in multilayered substrate CPWs”. In: *IEEE Transactions on Microwave Theory and Techniques* 47.8 (), pp. 1544–1552. DOI: 10.1109/22.780407.

[116] H. Hillborg et al. “Crosslinked polydimethylsiloxane exposed to oxygen plasma studied by neutron reflectometry and other surface specific techniques”. In: *Polymer* 41.18 (Aug. 2000), pp. 6851–6863. DOI: 10.1016/S0032-3861(00)00039-2.

[117] Filippo Pfaiffer. “Towards a read-out for capacitive displacement sensor in an engineered heart tissue device”. MA thesis. 2022.

[118] Pietro Ciccarella et al. “Multichannel 65 zF rms Resolution CMOS Monolithic Capacitive Sensor for Counting Single Micrometer-Sized Airborne Particles on Chip”. In: *IEEE Journal of Solid-State Circuits* 51.11 (Nov. 2016), pp. 2545–2553. DOI: 10.1109/JSSC.2016.2607338.

[119] Javier Pérez Sanjurjo et al. “A Capacitance-To-Digital Converter for MEMS Sensors for Smart Applications”. In: *Sensors (Basel, Switzerland)* 17.6 (June 2017), p. 1312. DOI: 10.3390/s17061312.

[120] Longjie Zhong, Xinquan Lai, and Donglai Xu. “Oversampling Successive Approximation Technique for MEMS Differential Capacitive Sensor”. In: *IEEE Journal of Solid-State Circuits* 53.8 (Aug. 2018), pp. 2240–2251. DOI: 10.1109/JSSC.2018.2827922.

[121] Yuming He et al. “27.7 A 0.05mm^2 1V capacitance-to-digital converter based on period modulation”. In: *2015 IEEE International Solid-State Circuits Conference - (ISSCC) Digest of Technical Papers* (Feb. 2015), pp. 1–3. DOI: 10.1109/ISSCC.2015.7063138.

[122] Giuseppe Scotti et al. “88-μ A 1-MHz Stray-Insensitive CMOS Current-Mode Interface IC for Differential Capacitive Sensors”. In: *IEEE Transactions on Circuits and Systems I: Regular Papers* 61.7 (July 2014), pp. 1905–1916. DOI: 10.1109/TCSI.2014.2298275.

[123] Dezhi Lin. “An atto-Farad resolution closed loop impedance measurement bridge for capacitive sensors”. In: (2018).

[124] F. M. L. Van der Goes. “Low-cost smart sensor interfacing”. PhD thesis. 1996.

[125] *UTI datasheet_Smartec*.

[126] *AD7746 datasheet_Analog Devices*.

[127] G. Harman. *Wire Bonding in Microelectronics, Third Edition*. McGraw-Hill, 2010. URL: https://books.google.nl/books?id=827MwgEACAAJ.

[128] Hyejun Kang, Ashutosh Sharma, and Jae Pil Jung. “Recent Progress in Transient Liquid Phase and Wire Bonding Technologies for Power Electronics”. In: *Metals* 10.7 (), p. 934. DOI: 10.3390/met10070934.

[129] Milica Radisic et al. “Functional assembly of engineered myocardium by electrical stimulation of cardiac myocytes cultured on scaffolds”. In: *Proceedings of the National Academy of Sciences* 101.52 (Dec. 2004), pp. 18129–18134. DOI: 10.1073/pnas.0407817101.

8

[130] Loraine L.Y. Chiu et al. “Biphasic Electrical Field Stimulation Aids in Tissue Engineering of Multicell-Type Cardiac Organoids”. In: *Tissue Engineering Part A* 17.11-12 (June 2011), pp. 1465–1477. DOI: 10.1089/ten.tea.2007.0244.

[131] Nina Tandon et al. “Electrical stimulation systems for cardiac tissue engineering”. In: *Nature Protocols* 4.2 (Feb. 2009), pp. 155–173. DOI: 10.1038/nprot.2008.183.

[132] Sara S. Nunes et al. “Biowire: a new platform for maturation of human pluripotent stem cell derived cardiomyocytes”. In: *Nature methods* 10.8 (Aug. 2013), pp. 781–787. DOI: 10.1038/nmeth.2524.

[133] Marc N. Hirt et al. “Functional improvement and maturation of rat and human engineered heart tissue by chronic electrical stimulation”. In: *Journal of Molecular and Cellular Cardiology* 74 (Sept. 2014), pp. 151–161. DOI: 10.1016/j.yjmcc.2014.05.009.

[134] Whitney L. Stoppel, David L. Kaplan, and Lauren D. Black. “Electrical and mechanical stimulation of cardiac cells and tissue constructs”. In: *Advanced drug delivery reviews* 96 (Jan. 2016), pp. 135–155. DOI: 10.1016/j.addr.2015.07.009.

[135] N. Tandon et al. “Design of Electrical Stimulation Bioreactors for Cardiac Tissue Engineering”. In: *Conference proceedings : ... Annual International Conference of the IEEE Engineering in Medicine and Biology Society. IEEE Engineering in Medicine and Biology Society. Conference* 2008 (2008), pp. 3594–3597. DOI: 10.1109/IEMBS.2008.4649983.

[136] Robert Maidhof et al. “Biomimetic perfusion and electrical stimulation applied in concert improved the assembly of engineered cardiac tissue”. In: *Journal of Tissue Engineering and Regenerative Medicine* 6.10 (2012), e12–e23. DOI: 10.1002/term.525.

[137] Ning Zhang et al. “Multifunctional 3D electrode platform for real-time in situ monitoring and stimulation of cardiac tissues”. In: *Biosensors and Bioelectronics* 112 (July 2018), pp. 149–155. DOI: 10.1016/j.bios.2018.04.037.

[138] Junqing Liu et al. “High-throughput rhythmic regulation of cardiomyocytes by integrated electrical stimulation and video-based automated analysis biosensing platform”. In: *Biosensors and Bioelectronics* 209 (Aug. 2022), p. 114252. DOI: 10.1016/j.bios.2022.114252.

[139] Richard A Lasher et al. “Electrical stimulation directs engineered cardiac tissue to an age-matched native phenotype”. In: *Journal of Tissue Engineering* 3.1 (July 2012), p. 2041731412455354. DOI: 10.1177/2041731412455354.

[140] Nina Tandon et al. “Optimization of electrical stimulation parameters for cardiac tissue engineering”. In: *Journal of Tissue Engineering and Regenerative Medicine* 5.6 (2011), e115–e125. DOI: 10.1002/term.377.

[141] Manuel Alejandro Tamargo et al. “milliPillar: A Platform for the Generation and Real-Time Assessment of Human Engineered Cardiac Tissues”. In: *ACS Biomaterials Science & Engineering* 7.11 (Nov. 2021), pp. 5215–5229. DOI: 10.1021/acsbiomaterials.1c01006.

[142] Daniel R. Merrill, Marom Bikson, and John G. R. Jefferys. “Electrical stimulation of excitable tissue: design of efficacious and safe protocols”. In: *Journal of Neuroscience Methods* 141.2 (Feb. 2005), pp. 171–198. DOI: 10.1016/j.jneumeth.2004.10.020.

[143] Neelesh K. Jain et al. “Metal Deposition: Plasma-Based Processes”. In: *Encyclopedia of Plasma Technology - Two Volume Set*. Num Pages: 19. CRC Press, 2016.

[144] D. Depla, S. Mahieu, and J. E. Greene. “Chapter 5 - Sputter Deposition Processes”. In: *Handbook of Deposition Technologies for Films and Coatings (Third Edition)*. Ed. by Peter M. Martin. Boston: William Andrew Publishing, Jan. 2010, pp. 253–296. DOI: 10.1016/B978-0-8155-2031-3.00005-3.

[145] Nina Tandon and Gordana Vunjak-Novakovic. “Characterization of Electrical Stimulation Electrodes for Cardiac Tissue Engineering”. In: (), p. 4.

[146] Xuezeng Dai et al. “Meniscus fabrication of halide perovskite thin films at high throughput for large area and low-cost solar panels”. In: *International Journal of Extreme Manufacturing* 1.2 (June 2019), p. 022004. DOI: 10.1088/2631-7990/ab263e.

[147] Miao Liu, Jianren Sun, and Quanfang Chen. “Influences of heating temperature on mechanical properties of polydimethylsiloxane”. In: *Sensors and Actuators A: Physical* 151.1 (Apr. 2009), pp. 42–45.

[148] T. S. Radhakrishnan. “Thermal degradation of poly(dimethylsilylene) and poly (tetra-methyldisilylene-co-styrene)”. In: *Journal of Applied Polymer Science* 99.5 (Mar. 2006), pp. 2679–2686. DOI: 10.1002/app.22813.

[149] B. Balakrisnan, S. Patil, and E. Smela. “Patterning PDMS using a combination of wet and dry etching”. In: *Journal of Micromechanics and Microengineering* 19.4 (Mar. 2009), p. 047002. DOI: 10.1088/0960-1317/19/4/047002.

[150] Yu-Luen Deng and Yi-Je Juang. “Polydimethyl siloxane wet etching for three dimensional fabrication of microneedle array and high-aspect-ratio micropillars”. In: *Biomicrofluidics* 8.2 (Mar. 2014), p. 026502. DOI: 10.1063/1.4871038.

[151] A. Kakati, D. Maji, and S. Das. “Unveiling the wet chemical etching characteristics of polydimethylsiloxane film for soft micromachining applications”. In: *Journal of Micromechanics and Microengineering* 27.1 (Dec. 2016), p. 015033. DOI: 10.1088/1361-6439/27/1/015033.

[152] Mahdieh Shojaei Baghini. “Design and Development of Integrated Displacement Sensors for Engineered Heart Tissue Platforms”. MA thesis. 2020.

[153] R. L. Magin and M. Ovadia. “MODELING THE CARDIAC TISSUE ELECTRODE INTERFACE USING FRACTIONAL CALCULUS”. In: *IFAC Proceedings Volumes*. 2nd IFAC Workshop on Fractional Differentiation and its Applications 39.11 (Jan. 2006), pp. 302–307. DOI: 10.3182/20060719-3-PT-4902.00056.

[154] T. J. Faes et al. “The electric resistivity of human tissues (100 Hz-10 MHz): a meta-analysis of review studies”. In: *Physiological Measurement* 20.4 (Nov. 1999), R1–10. DOI: 10.1088/0967-3334/20/4/201.

8

[155] Lucie A. Low et al. “Organs-on-chips: into the next decade”. In: *Nature Reviews Drug Discovery* 20.5 (May 2021), pp. 345–361. ISSN: 1474-1784. DOI: 10.1038/s41573-020-0079-3.

[156] Eva-Maria Dehne, Tobias Hasenberg, and Uwe Marx. “The ascendance of microphysiological systems to solve the drug testing dilemma”. In: *Future Science OA* 3.2 (Mar. 2017), FSO185. DOI: 10.4155/fsoa-2017-0002.

[157] DoYeun Park et al. “Integrating Organs-on-Chips: Multiplexing, Scaling, Vascularization, and Innervation”. In: *Trends in Biotechnology* 38.1 (Jan. 2020), pp. 99–112. DOI: 10.1016/j.tibtech.2019.06.006.

[158] Benjamin Fook Lun Lai et al. “A well plate–based multiplexed platform for incorporation of organoids into an organ-on-a-chip system with a perfusable vasculature”. In: *Nature Protocols* 16.4 (Apr. 2021), pp. 2158–2189. DOI: 10.1038/s41596-020-00490-1.

[159] Karel Domansky et al. “Perfused Multiwell Plate for 3D Liver Tissue Engineering”. In: *Lab on a chip* 10.1 (Jan. 2010), pp. 51–58. DOI: 10.1039/b913221j.

[160] Xandor M. Spijkers et al. “A directional 3D neurite outgrowth model for studying motor axon biology and disease”. In: *Scientific Reports* 11.1 (Jan. 2021), p. 2080. DOI: 10.1038/s41598-021-81335-z. (Visited on 01/14/2023).

[161] Thomas D. Lewin et al. “An in silico Model of T Cell Infiltration Dynamics Based on an Advanced in vitro System to Enhance Preclinical Decision Making in Cancer Immunotherapy”. In: *Frontiers in Pharmacology* 13 (2022), p. 837261. DOI: 10.3389/fphar.2022.837261.

[162] Nienke R. Wevers et al. “High-throughput compound evaluation on 3D networks of neurons and glia in a microfluidic platform”. In: *Scientific Reports* 6 (Dec. 2016), p. 38856. DOI: 10.1038/srep38856.

[163] Dharaminder Singh et al. “A microfluidic system that replicates pharmacokinetic (PK) profiles in vitro improves prediction of in vivo efficacy in preclinical models”. In: *PLoS biology* 20.5 (May 2022), e3001624. DOI: 10.1371/journal.pbio.3001624.

[164] Przemysław Błyszczuk et al. “Activated Cardiac Fibroblasts Control Contraction of Human Fibrotic Cardiac Microtissues by a -Adrenoreceptor-Dependent Mechanism”. In: *Cells* 9.5 (May 2020), p. 1270. DOI: 10.3390/cells9051270.

List of Publications

Journal Papers

1. **M. Dostanić**, L.M. Windt, J.M. Stein, B.J. van Meer, M. Bellin, V. Orlova, C.L. Mummery, P.M. Sarro, M. Mastrangeli, *A Miniaturized EHT Platform for Accurate Measurements of Tissue Contractile Properties*,Journal of Microelectromechanical Systems **29**,5, 881-887 (2020).

2. J.M. Rivera-Arbelaez*, **M. Dostanić***, L.M. Windt, J.M. Stein, C. Cofino-Fabres, T. Boonen, M. Wiendels, A. van den Berg, L.I. Segerink, C.L. Mummery, P.M. Sarro, B.J. van Meer, M.C. Ribeiro, M. Mastrangeli, R. Passier, *ForceTracker: A versatile tool for standardized assessment of tissue contractile properties in 3D Heart-on-Chip platforms*, Submitted to ACS Biomaterials Science & Engineering.

3. J.M. Rivera-Arbelaez*, D. Keekstra*, C. Cofino-Fabres, T. Boonen, **M. Dostanić**, S.A. ten Den, K. Vermeul, M. Mastrangeli, A. van den Berg, L.I. Segerink, M.C. Ribeiro, N. Strisciuglio#, R. Passier#, *Automated assessment of human engineered heart tissues using deep learning and template matching for segmentation and tracking*, Bioengineering & Translational Medicine p. e10513, doi: 10.1002/btm2.10513.

4. D. Nahon*, R. Moerkens*, H. Aydogmus**, B. Lendemeijer**, A. Martinez-Silgado**, J.M. Stein**, **M. Dostanić**, J.P. Frimat, C. Gontan, M. de Graaf, M. Hu, D. Kasi, L.S. Koch, K. Le, S. Lim, H. Middelkamp, J. Mooiweer, P. Motreuil-Ragot, E. Niggl, C. Pleguezuelos, J. Puschhof, N. Revyn, J.M. Rivera-Arbelaez, J. Slager, L.M. Windt, M. Zakharova, B.J. van Meer, V. Orlova, F. de Vrij, S. WIthoff, M. Mastrangeli, A.D. van der Meer, C.L. Mummery, *Taking microphysiological systems to the next level: Why quantification of physiological features is essential*, Accepted to Nature Biomedical Engineering.

Conference Papers

1. **M. Dostanić**, F. Pfaiffer, M. S. Baghini, L. M. Windt, M. Wiendels, B. J. van Meer, C. L. Mummery, P. M. Sarro, M. Mastrangeli, *A highly sensitive capacitive displacement sensor for force measurement integrated in an engineered heart tissue platform*, In 22nd Int. Conf. on Solid-State Sensors, Actuators and Microsystems (TRANSDUCERS 2023).

2. **M. Dostanić**, L. M. Windt, M. Wiendels, B. J. van Meer, C. L. Mummery, P. M. Sarro, M. Mastrangeli, *Highly reproducible tissue positioning with tapered pillar design in engineered heart tissue platforms*, In IEEE 36th Int. Conf. on Micro Electro Mechanical Systems (MEMS2023).

3. M. Mastrangeli, H. Aydogmus, **M. Dostanić**, P. Motreuil-Ragot, N. Revyn, B. de Wagenaar, R. Dekker; P.M. Sarro, *Microelectronmechanical organs-on-chip*, In 21st Int. Conf. on Solid-State Sensors, Actuators and Microsystems (TRANSDUCERS 2021)

4. H. Aydogmus, **M. Dostanić**, M. Jahangiri, R. Sinha, W. F. Quiros-Solano, M. Mastrangeli, P. M. Sarro, *FET-based integrated charge sensor for organ-on-chip applications*, In IEEE Sensors 2020.

CONFERENCE PRESENTATIONS AND POSTERS

1. **M. Dostanić**, L. M. Windt, J. M. Stein, B. J. Van Meer, C. L. Mummery, P. M. Sarro, M. Mastrangeli, *Tapered pillars increase tissue position reproducibility in engineered heart tissue platforms*, In EUROoCS Conference 2022, 4-5 July 2022.

2. **M. Dostanić**, L. Windt, J. Stein, B. van Meer, A. Diakou, C. L. Mummery, P. M. Sarro, M. Mastrangeli, *An engineered heart tissue platform with integrated pacing microelectrodes*, In EUROoCS Conference 2021, online, 1-2 July, 2021.

3. J. M. Rivera-Arbelaez, **M. Dostanić**, J. M. Stein, A. van den Berg, L. I. Segerink, C. L. Mummery, P. M. Sarro, M. Mastrangeli, M. C. Ribeiro, R. Passier, *ForceTracker: A versatile tool for contractile force assessment in 3D organ-on-chip platforms*, In EUROoCS Conference 2021, online, 1-2 July, 2021.

4. L. Windt, **M. Dostanić**, J. Stein, V. Meraviglia; G. Campostrini, M. Bellin, V. Orlova, M. Mastrangeli, P. M. Sarro, B. van Meer, C. Mummery,*Miniaturized engineered heart tissues from human induced pluripotent cell-derived co-culture* , In EUROoCS Conference 2020

5. **M. Dostanić**, L. Windt, J. Stein, B. van Meer, M. Mastrangeli, C. Mummery, P. M. Sarro, *A miniaturized EHT platform for contractile tissue measurements*,In International Micro-NanoConference, Utrecht (NL), December 10-11, 2019.

6. H. Aydogmus, **M. Dostanić**, M. Jahangiri, R. Sinha, W. F. Quiros-Solano, M. Mastrangeli, P. M. Sarro, *Sensor applications for organ-on-chip platforms*, In International MicroNanoConference, Utrecht (NL), December 10-11, 2019.

ACKNOWLEDGEMENTS

The work presented in this thesis was certainly not a one-man show. Instead, it was one big collaboration, mutual effort, and contribution of many people.

First, I would like to thank my promotor, Prof. Sarro, for giving me the opportunity to be part of the NOCI project and to work on introducing the Organ-on-Chip technology into the MEMS processing flows. Massimo, my co-promotor and daily supervisor, thank you for all the feedback, advice, and guidance over the past years. I appreciate a lot the trust and support I got from you in all the ideas and research paths I took along the way.

Next, I would like to thank all the committee members: Prof. Dekker, Prof. Mummery, Prof. van der Meer, Prof. den Toonder, Prof. Rasponi and Prof. French for accepting to be part of the promotion committee and for taking the time to read my thesis.

It was truly a unique experience exploiting microfabrication technology, using very toxic gasses and strong acids for processing silicon wafers, to create soft, biocompatible "homes" for extremely sensitive human-origin cells. As challenging as it sounds, it was still possible to do it thanks to the great team of people: technicians, students, postdocs, and researchers, who worked with me at the Else Kooi laboratory on a daily basis. Mario, Johannes, Silvana, Joost, Robert, Hitham, Koos, Tom, Jord, Gregory, Sten, Paolo, Bruno, Lovro, Juan, Roberto, Shriya, Leandro, Nikolas, Bjorn I have a big appreciation for all of you, for both the technical and scientific support I got over the years. Thank you for all the jokes, talks, help, and support in the downtimes (of both humans and machines). It made the long hours in the space suit very fun. Also, a big thank you to the rest of the ECTM colleagues, working inside and outside of the cleanroom, for the many coffees, lunches, and birthday cakes we shared. I am very grateful for all the master students I had the pleasure of working with: Anita, Maddy, Jilian, Laurens, and Filippo. Thanks a lot for your dedication, patience, and hard work. I learned a lot from each one of you.

One special group of people to thank is Bioelectronics, the group that adopted us as honorary members: Ronaldo, Nasim, Gandhi, Cesc, and the Berlin part: Andra, Konstantina, and Raphael. Thank you, lovely people, for all the great times in Delft, Berlin, and Tirol!

This thesis is a testimony of a close collaboration between biology and engineering that I'm very happy to be part of. My deepest gratitude to Prof. Christine Mummery for the opportunity to do my entire research in collaboration with her group at LUMC. Berend, it was amazing having you as someone who understands both fields, a mastermind with impressive communication skills, to be that bridge between biology and technology and always help us find common ground. Thank you for all the support. My dear Laura and Jeroen, who patiently watched me pipetting for the first time and allowed me to create art instead of the EHTs. Such a pleasure working with you! Laura, thank you for your everlasting enthusiasm for our research and every new chip design. A big thanks to my new ANA group at LUMC for making the transition from microfabrication to cell biology very exciting and fun. Special thanks to Maury and Mervyn for a loooot of patience

in guiding me through the cell culturing lab.

Behind this collaboration is the Netherlands Organ on Chip consortium, which provided the opportunity for all of us to work together. NOCIIIIIIz, what an experience being part of such a fun and cheerful community, full of brilliant people! Thank you for all the great times during our meetings, inspiring talks, and all the effort put into understanding each other's research and finding possibilities to collaborate. Thank you for all the parties and hangovers. With such a nice environment that we created, I'm sure we will be gathering for many more years.

Of course, every gastarbeiter has its own 'second home' community outside of their country. I have to thank all the members of my small Balkan group that helped me feel close to home over the past years. My big Serbian brother and sister, Aleksandar and Violeta. Aleksandar, thank you for all the help and support from day 0, inside and outside of the lab. Not to mention that you were the one welcoming me to this country. Violeta, you are such a role model on how broad, curious, and versatile a person should be. Thank you for all the great times in Delft, and now is your turn to be the cool friend from Amsterdam. Vukan and David, thank you for all the fun, colors, arts, and laughs. Filip, your contagious positive energy is a great asset to have around. Thanks for all the care and support. Elida, my dearest Bosnian mama, and such an amazing lady, thank you for embracing me so openly into both of your families. You are the true soul of our warm culture.

Finally, my paranymphs, my two fellow musketeers, and beautiful human beings. I am sooo lucky to have shared these past four years with you and many more to come. I could not imagine doing this otherwise. What were the chances that the three of us will end up in the same office? From that first party in Utrecht to partying in Belgrade..we came such a long way. Handić, my ex-fellow countrywoman, it is unbelievable how you can understand another person so well without even having to speak. You are such an inspiration and synonym for resilience and rightfulness. And Paul, our little rebel. I am so lucky to be part of your PhD journey and to have witnessed the "growing up" part in both professional and personal ways. Thank you both for being my rock all these years. I'm so proud of both of you and happy that we did this together. House of Delft!

Cmicojkice, Katice, and Miks, the distance could not even slightly affect the impact and contribution you have in my life. You are the true core of my happiness and everything that friendship should be about. Thank you for always being there and for believing that I'm competent enough for proper adulting in another country, even when I doubted. Thank you for balancing out all the stress and pressure with the long talks, unconditional support, love, and care. I am very grateful for your patience with all the chaos we go through every time I'm home. A big thanks to the rest of my Serbian family Irina, Zuca, Miloš, Ivan, Daca, Boki, and Andrija. Even from far, you were always a great support during past years.

The deepest gratitude goes to my closest family, mom and dad, for all the love and immeasurable support.